

VOLUME II

Final Report on

Multiple Beam Torus Antenna Study

Prepared for

Defense Communications Agency

Under

Contract DCA100-76-C-0050

March 1977

by

COMSAT Laboratories

Clarksburg, Maryland 20734

DDC
RECEIVED
DEC 1 1977
REGISTERED
F

Carol Rieger

Carol Rieger
Principal Mechanical/
Structures Engineer

William J. English

William J. English
Principal RF Engineer

Paul Schrantz

Paul Schrantz
Manager, Stabilization
and Structures

Randall Kreutel
Randall Kreutel
Manager, Antenna
Department

ACCESSION NO.	
NTIS	
DOC	
ADVIS	
BY	
DISTRIBUTION/AVAIL. ADVICE	
REMARKS	
PK	

DISTRIBUTION STATEMENT A
Approved for public release
Distribution Unlimited

REPORT DOCUMENTATION PAGE

READ INSTRUCTIONS
BEFORE COMPLETING FORM

1. REPORT NUMBER	2. GOVT ACCESSION NO.	3. RECIPIENT'S CATALOG NUMBER
4. TITLE (and Subtitle) Final Report on Multiple Beam Torus Antenna Study, Volume II.		5. TYPE OF REPORT & PERIOD COVERED Final Report covering Jul 76 through Feb 77
6. AUTHOR(s) William J. English Carol Rieger	7. CONTRACT OR GRANT NUMBER(s) DCA100-76-C-0050	
8. PERFORMING ORGANIZATION NAME AND ADDRESS CONSAT Laboratories Clarksburg, MD 20734		9. PROGRAM ELEMENT, PROJECT, TASK AREA & WORK UNIT NUMBERS P.E. 33126K
10. CONTROLLING OFFICE NAME AND ADDRESS Defense Communications Engineering Center, DCA 1860 Wiehle Avenue Reston, VA 22090		11. REPORT DATE March 1977
12. MONITORING AGENCY NAME & ADDRESS (if different from Controlling Office) 238p.		13. NUMBER OF PAGES Vol I - 42 pgs. Vol II - 170 pgs.
		14. SECURITY CLASSIFICATION (of this report) Unclassified
15. DISTRIBUTION STATEMENT (of this Report) Approved for Public Release -- Distribution Unlimited SBIE		
16. DISTRIBUTION STATEMENT (of the abstract entered in Block 20, if different from Report) AD-E1001001		
17. SUPPLEMENTARY NOTES		
18. KEY WORDS (Continue on reverse side if necessary and identify by block number) Multiple Beam Torus Antennas (MBTA), Satellite Communications, Satellite earth terminal, Multibeam/Multifrequency		
19. ABSTRACT (Continue on reverse side if necessary and identify by block number) Offset-fed multiple beam torus antennas (MBTA) provide exceptional wide-angle sidelobe characteristics as a result of a blockage-free aperture. The formation of multiple beams at one or more frequency bands using shared apertures on a fixed reflector structure can result in significant cost savings in a DSCS system in which satellites are constrained to a fixed portion of the geosynchronous arc.		

Handwritten initials/signature

Table of Contents (Continued)

	<u>Page No.</u>
5.10 Spherical Generating Curve MBTA	5-56
5.11 Illumination Gain of Front-Fed MBTA	5-63
5.12 Offset MBTA Field of View and Scanned Feed Parameters	5-68
5.13 Patterns and Polarization	5-76
5.14 Noise Temperature and Feed Spillover	5-81
5.15 Aberration-Correcting Subreflectors	5-94
5.16 Aberration-Correcting Feeds	5-99
 6. MECHANICAL AND STRUCTURAL CHARACTERISTICS OF THE UNCORRECTED FRONT-FED MBTA	 6-1
6.1 Worldwide Deployment Considerations	6-1
6.2 Mechanical Considerations	6-7
6.3 Structural Design Considerations	6-13
6.4 Applied Loads Analysis	6-18
6.4.1 Gravity	6-18
6.4.2 Wind	6-18
6.4.3 Temperature	6-20
6.5 Allowable Deformation and Tilt Error Budget	6-20
6.5.1 Surface rms	6-20
6.5.2 Pointing Error	6-21
6.6 Structural Model	6-22
6.6.1 Panels	6-22
6.6.2 Backup Structure	6-26
6.6.3 Support Points	6-29
6.7 Structural Layout	6-33
6.8 Load Analysis	6-36
6.9 Static Analysis	6-41

Table of Contents (Continued)

	<u>Page No.</u>
6.10 Dynamic Analysis	6-44
6.11 Error Analysis	6-44
7. COST ESTIMATES FOR A RECOVERABLE MBTA	7-1
8. REFERENCES	8-1
APPENDIX A. PROGRAM DESCRIPTIONS	A-1

List of Illustrations

<u>Figure No.</u>	<u>Title</u>	<u>Page No.</u>
VOLUME II		
4-1	MBTA Beam Elevation Angle vs Latitude and Differential Longitude	4-3
4-2	Sum of Beam Elevation and Latitude Angles $81.3^\circ \leq \epsilon + \nu \leq 90^\circ$ at Co-longitude Position	4-4
4-3	Local MBTA Beam Pointing Azimuth Angle	4-4
4-4	Right Spherical Triangle Relationships	4-5
4-5	Plane Geometry Angle Relationships	4-7
4-6	Horizon Vector \hat{q} and Scan "Plane" Vector \hat{p} in MBTA Aperture Plane	4-8
4-7	Geometry for Beam Pointing Vector, \bar{R}	4-9
4-8	MBTA Local North Vector	4-12
4-9	Local Orientation of \hat{p} and \hat{q} Unit Vectors	4-13
4-10	Conical Beam Scan Locus	4-15
4-11	Map of Optimum MBTA Generating Axis Angles, ϕ_0	4-19
4-12	Optimum ϕ_0 Angle vs Latitude at Co-longitude Position	4-20
4-13	Rotation Axis Inclination Angle	4-21
4-14	Rotation Axis Inclination Angle vs Lati- tude at the Co-longitude Position	4-22
4-15	Beam Pointing Loci with Scan	4-23
4-16	Beam Pointing Locus with ϕ_0 Fixed	4-25
4-17	$\phi(\phi_s)$ for $\phi_0 = 90^\circ$, $\lambda = 0^\circ$	4-29
4-18	$\phi(\phi_s)$ for $\phi_0 = 93^\circ$, $\lambda = 0^\circ$	4-30

List of Illustrations (Continued)

<u>Figure No.</u>	<u>Title</u>	<u>Page No.</u>
4-19	$\phi(\phi_s)$ for $\phi_0 = 93.5^\circ$, $\lambda = 0^\circ$	4-31
4-20	$\phi(\phi_s)$ for $\phi_0 = 94^\circ$, $\lambda = 0^\circ$	4-32
4-21	$\phi(\phi_s)$ for $\phi_0 = 95.5^\circ$, $\lambda = 0^\circ$	4-33
4-22	$\phi(\phi_s)$ for $\phi_0 = 93.5^\circ$, $\lambda = 40^\circ$	4-34
4-23	$\phi(\phi_s)$ for $\phi_0 = 93.5^\circ$, $\lambda = -70^\circ$	4-35
4-24	Rotation Axis Inclination in Co-longitude Plane with Fixed ϕ_0	4-37
4-25	Rotation Axis Vector Components	4-38
5-1	Illumination Gain and Beamwidth vs D/λ	5-4
5-2	MBTA Diameter vs D/λ at X-Band	5-6
5-3	Diameter vs D/λ at Specified Frequencies ..	5-7
5-4	Symmetrical MBTA Field of View Parameters	5-8
5-5	Symmetrical MBTA Field of View vs W/D at Specified Radius of Curvature (R/D)	5-10
5-6	Spherical Reflector Focusing	5-11
5-7	Symmetrical MBTA Feed Illumination Angle vs D/R	5-14
5-8	Projected Length of Feed Arc for 27-ft- Diameter Symmetrical MBTA	5-16
5-9	Offset MBTA Feed Illumination and Point- ing Angles	5-18
5-10	Feed Illumination Angle	5-19
5-11	Feed Offset Angle [$\theta_{osf} = \theta_2$ + $(\theta_2 - \theta_1)/2$]	5-20
5-12	Feed Offset Angle (θ_{osf} + center of projected aperture)	5-21
5-13	Minimum MBTA Beam Spacing	5-24
5-14	Corrugated Feed Horn Patterns	5-25

List of Illustrations (Continued)

<u>Figure No.</u>	<u>Title</u>	<u>Page No.</u>
5-15	Feed Power Patterns [$-P(\theta) = \cos^2 \theta$ (x2)] ..	5-26
5-16	6-GHz Corrugated Horn Antenna System	5-27
5-17	4-GHz Lightweight Corrugated Horn	5-28
5-18	Gain Loss vs Normalized rms Surface Toler- ance for Fixed Feed Offset Angles	5-30
5-19	Gain Loss of Baseline MBTA vs rms Surface Tolerance	5-31
5-20	Geometry for MBTA Reflector Equation	5-32
5-21	Symmetrical Spherical Reflector Geometry ..	5-35
5-22	Offset MBTA Reflector Geometry ($\phi_0 = 90^\circ$)	5-38
5-23	Symmetrical MBTA (D/R = 0.4) Aperture Plane Phase Errors	5-42
5-24	Symmetrical MBTA (D/R = 0.4) Gain vs F/R ..	5-43
5-25	Offset (114) MBTA (D/R = 0.4) Aperture Plane Phase Errors	5-44
5-26	Offset (116) MBTA Aperture Illumination Gain vs (F/R)	5-46
5-27	Offset (228) MBTA (D/R = 0.4) Aperture Plane Phase Errors	5-47
5-28	Offset (118) MBTA (D/R = 0.3) Aperture Plane Phase Errors	5-48
5-29	Offset (118) MBTA (D/R = 0.4) Aperture Plane Phase Errors with Optimum Focusing ..	5-49
5-30	Gain vs Feed Illumination Angle at 30 GHz (baseline MBTA)	5-50
5-31	Offset (118) MBTA (D/R = 0.5) Aperture Plane Phase Errors with Optimum Focusing ..	5-51

List of Illustrations (Continued)

<u>Figure No.</u>	<u>Title</u>	<u>Page No.</u>
5-32	Gain vs Feed Illumination Angle at 30 GHz (D/R = 0.5 geometry)	5-52
5-33	Geometry for General ϕ_0 Reflector Surface	5-54
5-34	Scanned Beam Feed Positions for Baseline MBTA	5-57
5-35	Parabolic Plane Beam Scan Loss for Base- line MBTA at 8.15 GHz	5-58
5-36	MBTA with Spherical Generating Curve	5-59
5-37	Aperture Plane Phase Error vs Feed Focus- ing with Spherical Generating Curve (D/R = 0.4)	5-61
5-38	Aperture Plane Phase Error vs Feed Focus- ing with Spherical Generating Curve (D/R = 0.3)	5-62
5-39	MBTA Illumination Gain vs D/1	5-64
5-40	Aperture Illumination Gain vs Feed Edge Taper	5-65
5-41	Aperture Illumination Gain vs Feed Offset Angle	5-65
5-42	Aperture Illumination Gain (D = 27 ft) vs Frequency	5-66
5-43	Projected Aperture Area of MBTA	5-68
5-44	Illumination Gain with Equal Projected Area Contours	5-69
5-45	Feed Pointing Parameters for Offset MBTA ..	5-71
5-46	10-Percent Offset MBTA Field of View vs (W/D)	5-72
5-47	Scanned Beam Feed Position Geometry	5-74

List of Illustrations (Continued)

<u>Figure No.</u>	<u>Title</u>	<u>Page No.</u>
5-48	Baseline MBTA Pattern ($\theta = 90^\circ$)	5-77
5-49	Baseline MBTA Pattern ($\theta = 0^\circ$)	5-78
5-50	Baseline MBTA Receive Band Pattern at 7.5 GHz ($\theta = 90^\circ$)	5-79
5-51	Baseline MBTA Receive Band Pattern at 7.5 GHz ($\theta = 0^\circ$)	5-80
5-52	Baseline MBTA Receive Band Pattern at 3.95 GHz ($\theta = 90^\circ$)	5-82
5-53	Baseline MBTA Receive Band Pattern at 3.95 GHz ($\theta = 0^\circ$)	5-83
5-54	Baseline MBTA Receive Band Pattern at 11 GHz ($\theta = 90^\circ$)	5-84
5-55	Baseline MBTA Receive Band Pattern at 11 GHz ($\theta = 0^\circ$)	5-85
5-56	Baseline MBTA Receive Band Pattern at 20.7 GHz ($\theta = 90^\circ$)	5-86
5-57	Baseline MBTA Receive Band Pattern at 20.7 GHz ($\theta = 0^\circ$)	5-87
5-58	48-ft-Diameter MBTA (D/R = 0.3) Pattern at 8.15 GHz ($\theta = 90.2^\circ$)	5-88
5-59	48-ft-Diameter MBTA (D/R = 0.3) Pattern at 8.15 GHz ($\theta = 0^\circ$)	5-89
5-60	Offset MBTA D/R = 0.3 Geometry	5-90
5-61	Spillover Characteristics of Corrugated Feed Horn for Baseline MBTA	5-92
5-62	Extended MBTA Aperture Area Decreases Feed Spillover	5-93
5-63	MBTA Antenna Temperature at X-Band	5-94

List of Illustrations (Continued)

<u>Figure No.</u>	<u>Title</u>	<u>Page No.</u>
5-64	MBTA with Phase Corrective Subreflector ...	5-95
5-65	Correcting Subreflector Diameter in Geo- synchronous Plane Limits Minimum Beam Spacing	5-97
5-66	Phase-Corrective Subreflector Designed and Tested at COMSAT Laboratories	5-98
5-67	Primary Pattern Characteristics of Aberration-Correcting Feed System	5-100
5-68	3-Element Aberration-Correcting Feed Array	5-101
5-69	Primary Pattern Characteristics of 3- Element Aberration-Correcting Feed	5-103
5-70	7- (or 5-) Element Aberration-Correcting Feed Array	5-104
5-71	Symmetrical MBTA Patterns ($D/R = 0.4$, $D/\lambda = 1000$) with 5-Element Aberration- Correcting Feed	5-105
5-72	Offset MBTA Patterns ($D/R = 0.4$, D/λ $= 820$) with 4-Element Aberration- Correcting Feed	5-106
6-1	Offset Feed Configuration	6-3
6-2	Circular Angle of Generation	6-3
6-3	Typical 4-Panel Generating Truss	6-4
6-4	Coordinate System Rotation Angles	6-6
6-5	Gain Loss of MBTA vs rms Surface Tolerance, ϵ	6-9
6-6	MBTA with Radome Environmental Protection	6-10

List of Illustrations (Continued)

<u>Figure No.</u>	<u>Title</u>	<u>Page No.</u>
6-7	Existing Feed Transport Mechanism Support	6-11
6-8	Orthogonal View of Feed Transport Mechanism Support	6-12
6-9	Reflector Geometry	6-13
6-10	27-ft MBTA Reflector Panel Configuration ..	6-14
6-11	Detail of Backup Truss Members	6-16
6-12	4-Point Pickup Support Structure	6-17
6-13	6-Point Pickup Support Structure	6-17
6-14	Normalized Projected Area $[A/(W \times D)]$	6-19
6-15	Equivalent Plate Thickness	6-25
6-16	Reflector Panel Cross Section	6-27
6-17	Panel Configurations	6-28
6-18	Vertical Truss Configurations	6-30
6-19	Typical Panel Layout	6-31
6-20	NASTRAN Plot of Backup Structure	6-32
6-21	View of COMSAT UET Torus Antenna During Construction	6-34
6-22	Normalized Wind Moment Area $\{(A \times H)/(W \times D^2)\}$	6-35
6-23	NASTRAN Plate Element Numbering	6-37
6-24	NASTRAN Backup Truss Grid Point Numbering Scheme	6-38
6-25	NASTRAN Foundation Grid Point Layout	6-39
6-26	Flow Chart of Design Iterations	6-43
6-27	Surface Tilt and rms Deformation	6-47
7-1	Fabrication Costs vs Surface Area	7-2
7-2	Erection Costs vs Surface Area	7-3
7-3	Width vs Location	7-5

List of Illustrations (Continued)

<u>Figure No.</u>	<u>Title</u>	<u>Page No.</u>
7-4	Height vs Location	7-6
7-5	De-icing Costs per Square Foot vs Surface Area	7-7
7-6	Sizes of Several MBTA Reflectors at COMSAT Labs	7-10
7-7	Antenna Cost vs Surface Area	7-11
7-8	Views of 27-ft MBTA at Locations 1 and 2 ..	7-13
7-9	Views of 27-ft MBTA at Locations 3 and 4 ..	7-14

List of Tables

<u>Table No.</u>	<u>Title</u>	<u>Page No.</u>
VOLUME II		
4-1	Summary of Spherical Scan Beam Pointing Errors vs Field of View and Latitude ($\phi_0 = 93.5^\circ$)	4-34
5-1	Multiple Frequency Band Summary	5-3
6-1	Representative Sites for Worldwide MBTA Deployment	6-7
6-2	NASTRAN Load Cases	6-40
7-1	MBTA Dimensions and Cost (FOV = 30° , center frequency = 7.25 GHz)	7-9
7-2	27-ft MBTA Dimensions and Cost at Several Locations	7-12

4. GEOMETRICAL AND BEAM POINTING CONSIDERATIONS

This section develops the MBTA mounting and beam pointing parameters and derives the optimum rotation axis angle for matching the conical scan surface capability of the MBTA to the geosynchronous arc. The derived results are a function of the latitude and differential longitude of the antenna. The effect of fixing the rotation axis angle to one value independent of antenna location for a DCSC system deployed worldwide is also evaluated.

4.1 LOCAL ELEVATION AND AZIMUTH ANGLES FOR BEAM POINTING

For a geosynchronous satellite, all MBTA antenna mounting and pointing parameters may be expressed⁹ in terms of two independent variables (ν , λ), where

$$\nu = \text{MBTA (north) latitude} \quad (4-1a)$$

$$\lambda = \text{MBTA (east) longitude} - \text{satellite (east) longitude} \quad (4-1b)$$

and $m \equiv 6.61 = \text{satellite radius/earth radius}$.

The local elevation of the beam pointing direction is

$$\epsilon = \tan^{-1} \left[\frac{m \cos(\nu) \cos(\lambda) - 1}{m \sqrt{1 - \cos^2(\nu) \cos^2(\lambda)}} \right] \quad (4-2)$$

Several special cases of interest are as follows:

a. $\epsilon = 0^\circ$ when $m \cos(\nu) \cos(\lambda) = 1$. If $\lambda = 0^\circ$ then $\cos(\nu) = 1/m$ and $\nu = 81.3^\circ$. (Note that ν and λ are interchangeable.) If $\lambda = \nu$, then $\cos^2(\nu) = 1/m$ and $\nu = 67.1^\circ$.

b. $\epsilon = 5^\circ$ when $\cos(\nu) \cos(\lambda) = 0.2363$. If $\lambda = 0^\circ$, then $\nu = 76.332^\circ$; if $\lambda = \nu$, then $\nu = 60.915^\circ$.

Figure 4-1 shows the local beam elevation angle for the MBTA as a function of its latitude and differential longitude. When the differential longitude, λ , is zero, then

$$81.3^\circ \leq (\epsilon + \nu) \leq 90^\circ \quad (4-3)$$

as shown in Figure 4-2.

The local azimuth of the beam pointing direction is measured clockwise from a north reference, as shown in Figure 4-3. The equations for the northern and southern hemisphere local azimuth differ by 180° :

$$AZ_{N.H.} = 180^\circ + \tan^{-1} \left[\frac{\tan \lambda}{\sin \nu} \right] \quad (4-4a)$$

$$AZ_{S.H.} = \tan^{-1} \left[\frac{\tan \lambda}{\sin \nu} \right] \quad (4-4b)$$

where $AZ_{N.H.} = 180^\circ$ and $AZ_{S.H.} = 0^\circ$ if $\lambda = 0^\circ$. Also shown in Figure 4-3 is the satellite angle (relative to the subsatellite axis) to the MBTA:

$$\alpha = \tan^{-1} \left[\frac{\sqrt{1 - \cos^2(\nu) \cos^2(\lambda)}}{\sin \nu \cos(\lambda)} \right] \quad (4-5)$$

Figure 4-4 shows several additional angle relationships that exist when the MBTA and satellite position have been specified. The following are derived from the identities for a right spherical triangle:

- a. $\cos \psi = \cos \lambda \cos \nu$,
- b. $\cos \Omega' = \sin \nu / \sin \psi$,

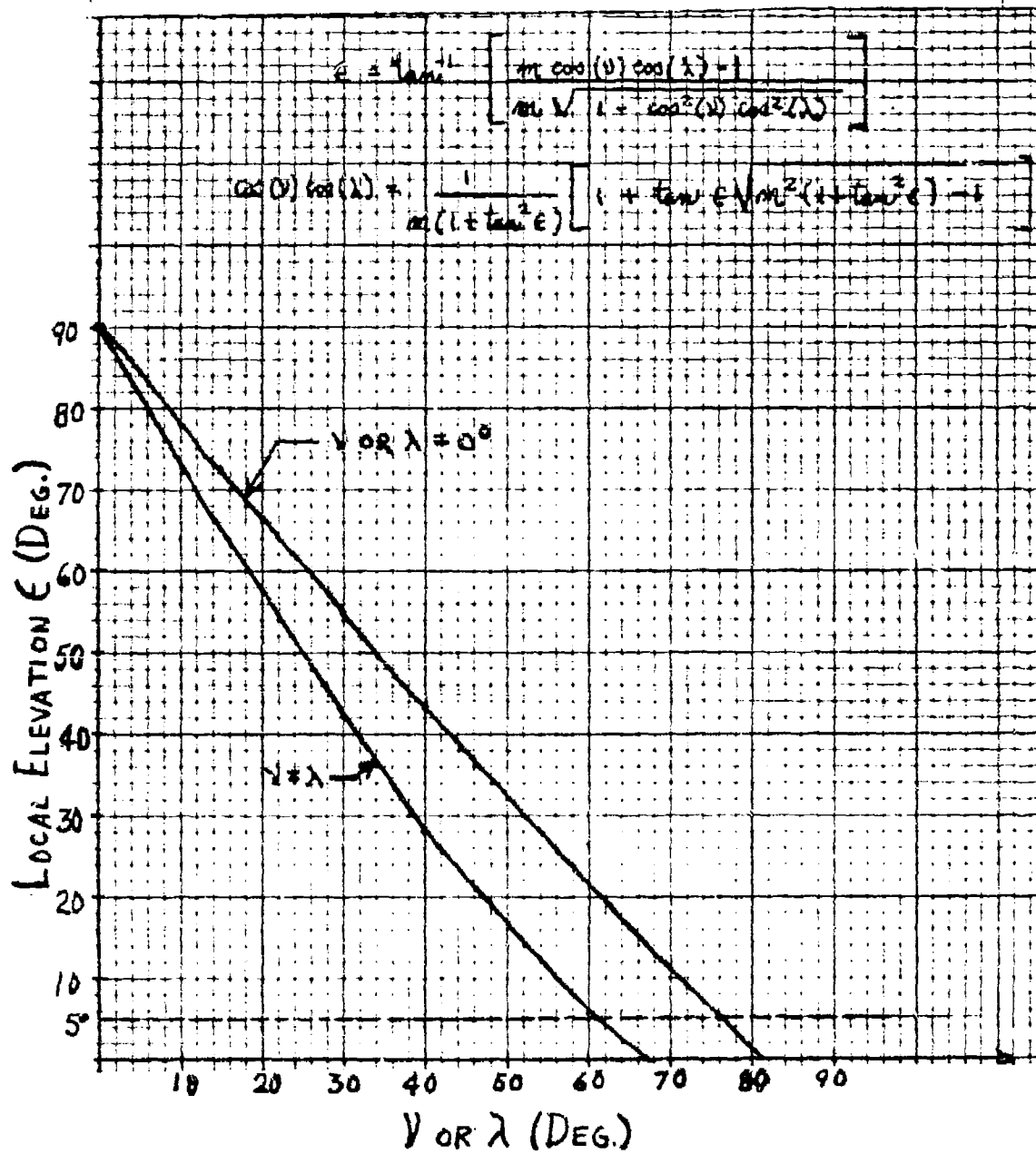


Figure 4-1. MBTA Beam Elevation Angle vs Latitude and Differential Longitude

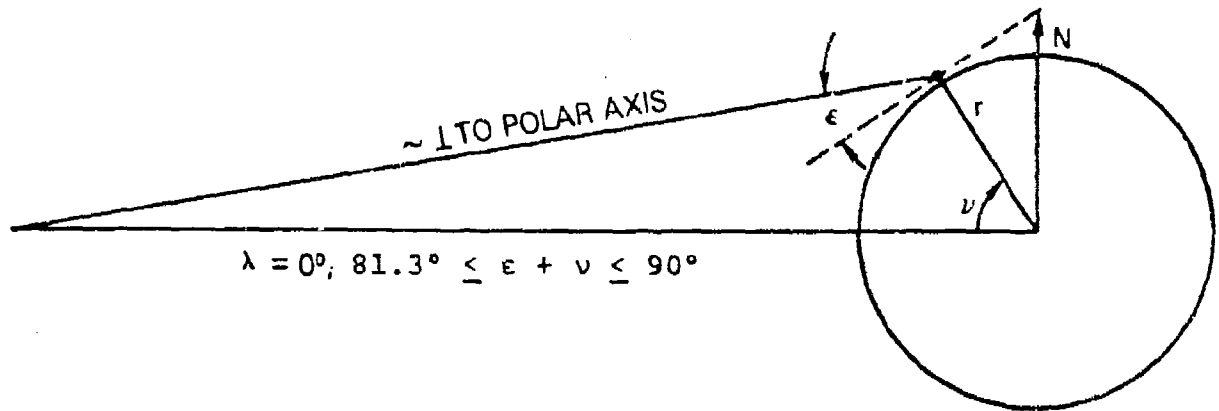


Figure 4-2. Sum of Beam Elevation and Latitude Angles
 $81.3^\circ \leq \epsilon + \nu \leq 90^\circ$ at Co-longitude Position

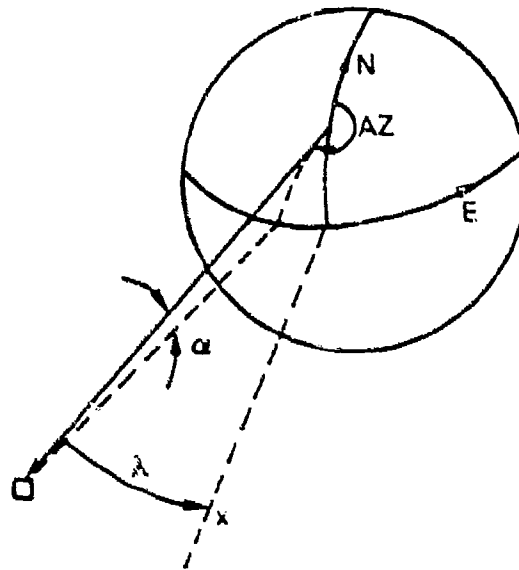


Figure 4-3. Local MBTA Beam
Pointing Azimuth Angle

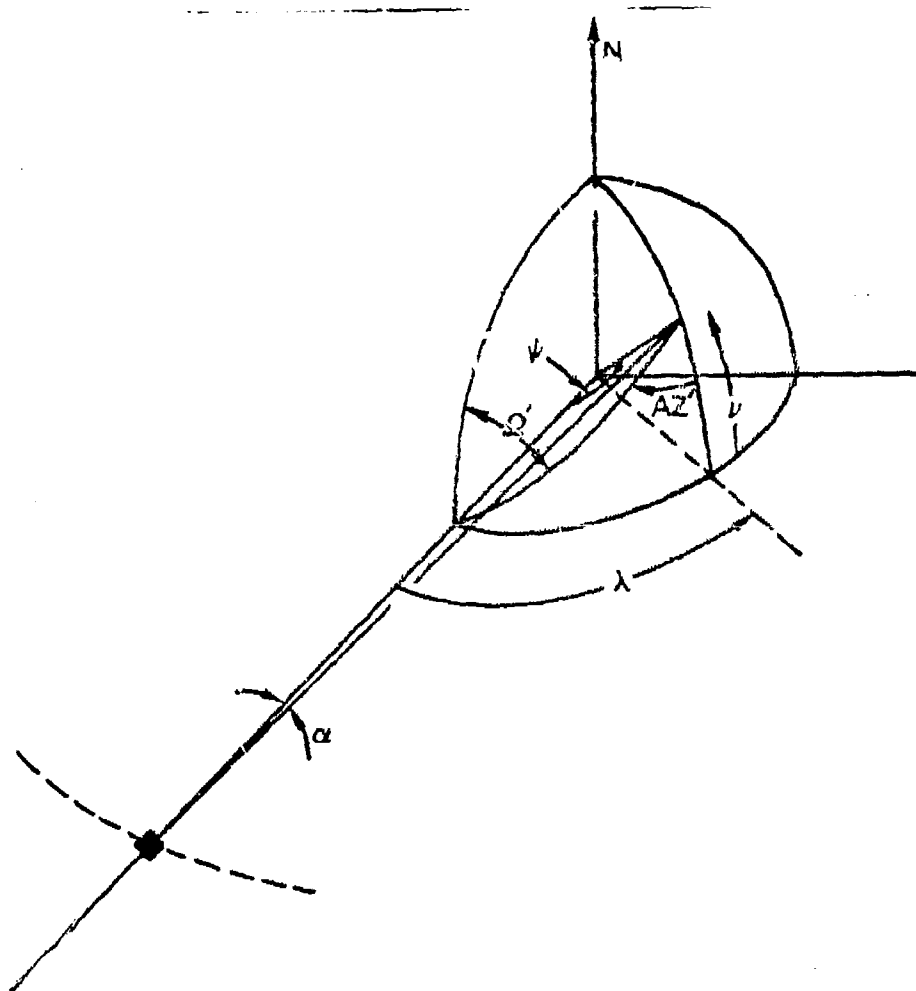


Figure 4-4. Right Spherical Triangle Relationships

- c. $\sin (AZ') = \sin \lambda / \sin \psi,$
- d. $\tan \alpha = r \sin \psi / (h - r \cos \psi) = \sin \psi / (m - \cos \psi),$
- e. $\tan \Omega' = \sin \lambda / \tan \nu,$ and
- f. $90^\circ - \epsilon = (\psi + \alpha).$

Figure 4-5 shows the geometrical basis for d and f.

4.2 MBTA LOCAL HORIZON AND SCAN "PLANE" VECTORS

Two additional unit vectors are used to describe the mounting and pointing of the MBTA:

- a. \hat{p} = MBTA scan "plane" vector, and
- b. \hat{q} = horizon vector in the aperture plane.

Both of these unit vectors lie in the aperture plane, as shown in Figure 4-6. The local horizon vector \hat{q} can be defined as

$$\hat{q} \perp \text{to } \bar{R}; \quad \hat{q} \cdot \bar{R} = 0 \quad (4-6)$$

$$\hat{q} \perp \text{to } \bar{r}; \quad \hat{q} \cdot \bar{r} = 0 \quad (4-7)$$

where \bar{r} is the radius vector from the earth center to the MBTA location and \bar{R} is the beam pointing vector from the MBTA to the satellite position (in this case, assumed to be at the center of the defined field of view), as shown in Figure 4-7.

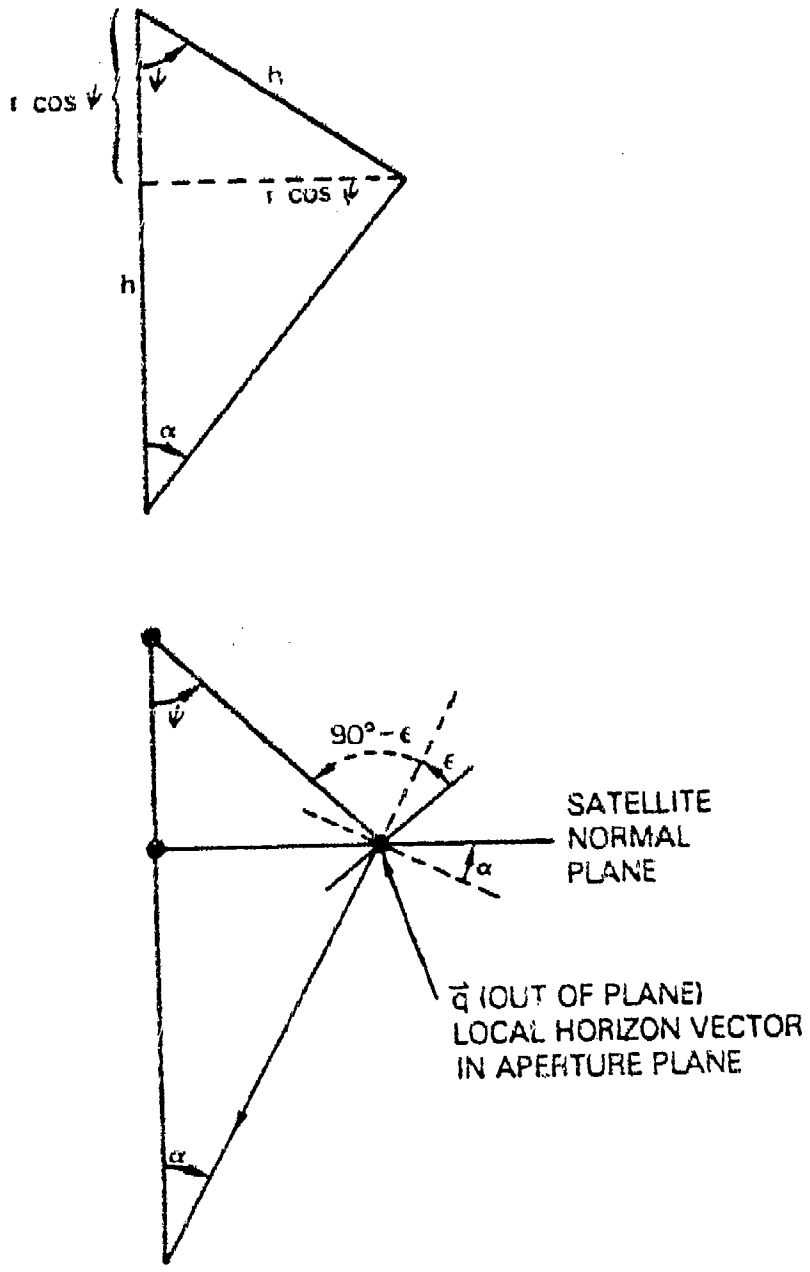
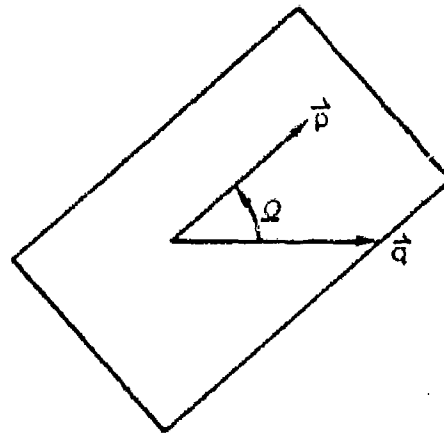


Figure 4-5. Plane Geometry Angle Relationships



\hat{p} = SCAN PLANE VECTOR OF TORUS

\hat{q} = HORIZON VECTOR IN APERTURE PLANE

Figure 4-6. Horizon Vector \hat{q} and
Scan "Plane" Vector \hat{p} in MBTA
Aperture Plane

The vector relationships are

$$\bar{r} = r[\hat{i} \cos v \cos \phi_A + \hat{j} \cos v \sin \phi_A + \hat{k} \sin v] \quad (4-8a)$$

$$\bar{h} = h[\hat{i} \cos \phi_s + \hat{j} \sin \phi_s] \quad (4-8b)$$

$$\bar{R} = \bar{h} - \bar{r} \quad (4-8c)$$

$$|\bar{R}| = r \sqrt{m^2 + 1 - 2m \cos v \cos \lambda} \quad (4-8d)$$

$$\bar{T} = h[-\hat{i} \sin \phi_s + \hat{j} \cos \phi_s] \quad (4-8e)$$

The scan "plane" vector \hat{p} is defined as

$$\hat{p} \perp \text{to } \bar{R}; \quad \hat{p} \cdot \bar{R} = 0 \quad (4-9)$$

where \hat{p} lies in the plane of \bar{R} and \bar{T} , and $\hat{p} \cdot \bar{R} \times \bar{T} = 0$.

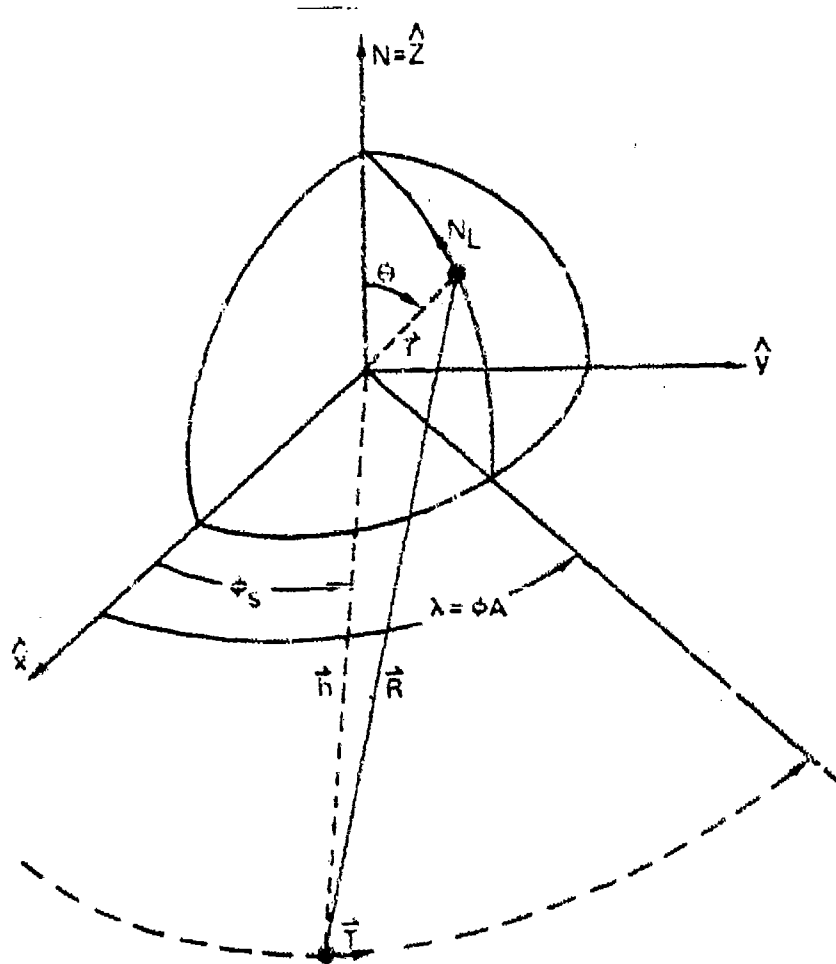


Figure 4-7. Geometry for Beam Pointing
Vector, \vec{R}

The last important geometrical relationship can now be given as

$$\tan \Omega = \tan \Omega' \cos \alpha = \left(\frac{\sin \lambda}{\tan \nu} \right) \left(\frac{m - \cos \psi}{\sqrt{m^2 - 2m \cos \psi + 1}} \right) \quad (4-10)$$

This relationship is derived by noting that

$$\tan \Omega = \left(\frac{|\hat{q} \times \hat{p}|}{\hat{q} \cdot \hat{p}} \right) \quad (4-11)$$

Further, noting that

$$\hat{q} \times \hat{a} \times \hat{r} = -(\hat{r} \times \hat{r}) \quad (4-12a)$$

$$\hat{p} \times \hat{a} (\hat{r} \times \hat{t}) \times \hat{r} = -(\hat{r} \times \hat{r} \times \hat{t}) \quad (4-12b)$$

gives

$$\begin{aligned} \tan \Omega &= \frac{|(\hat{r} \times \hat{r}) \times (\hat{r} \times \hat{r} \times \hat{t})|}{(\hat{r} \times \hat{r}) \cdot (\hat{r} \times \hat{r} \times \hat{t})} \\ &= \frac{|(\hat{r} \times \hat{r}) \times [(\hat{r} \cdot \hat{r}) \hat{t} - (\hat{t} \cdot \hat{r}) \hat{r}]|}{(\hat{r} \times \hat{r}) [(\hat{r} \cdot \hat{r}) \hat{t} - (\hat{t} \cdot \hat{r}) \hat{r}]} \\ &= \frac{|(\hat{r} \cdot \hat{r}) (\hat{r} \times \hat{r} \times \hat{t}) - (\hat{t} \cdot \hat{r}) (\hat{r} \times \hat{r} \times \hat{r})|}{- (\hat{r} \cdot \hat{r}) (\hat{r} \times \hat{r} \cdot \hat{t}) + (\hat{t} \cdot \hat{r}) (\hat{r} \times \hat{r} \cdot \hat{r})} \quad (4-13) \\ &= 0 \end{aligned}$$

and since

$$\hat{r} \times \hat{r} \times \hat{r} = (\hat{r} \cdot \hat{r}) \hat{r} - (\hat{r} \cdot \hat{r}) \hat{r}$$

$$\begin{aligned} \tan \Omega &= \frac{|(\hat{r} \cdot \hat{r}) [(\hat{r} \cdot \hat{t}) \hat{r} - (\hat{r} \cdot \hat{r}) \hat{t}] - (\hat{t} \cdot \hat{r}) [(\hat{r} \cdot \hat{r}) \hat{r} - (\hat{r} \cdot \hat{r}) \hat{r}]|}{- (\hat{r} \cdot \hat{r}) (\hat{r} \times \hat{r} \cdot \hat{t})} \\ &= \frac{|\hat{r}|}{|\hat{r}|^2} \left[\frac{(\hat{t} \cdot \hat{r}) (\hat{r} \cdot \hat{r}) - (\hat{r} \cdot \hat{r}) (\hat{r} \cdot \hat{t})}{- (\hat{r} \times \hat{r} \cdot \hat{t})} \right] \end{aligned}$$

then

$$\bar{K} \times \bar{r} \cdot \bar{T} = -h^2 r \sin \nu$$

$$\bar{r} \cdot \bar{T} = -\bar{T} \cdot \bar{R} \text{ (since } \bar{T} \cdot \bar{h} = 0) = hr \cos \nu \sin \lambda$$

$$\bar{r} \cdot \bar{R} = \bar{r} \cdot \bar{h} - \bar{r} \cdot \bar{k} = (m \cos \nu \cos \lambda - 1) r^2$$

Thus,

$$\begin{aligned} \tan \Omega &= \frac{(\bar{T} \cdot \bar{R})}{|\bar{R}| h^2 r \sin \nu} \\ &= \frac{\{ (m \cos \nu \cos \lambda - 1) r^2 + r^2 (m^2 + 1 - 2m \cos \nu \cos \lambda) \}}{(hr \cos \nu \sin \lambda) (r^2) (m^2 - m \cos \nu \cos \lambda)} \\ &= \frac{(h^2 r \sin \nu) r \sqrt{m^2 + 1 - 2m \cos \nu \cos \lambda}}{(\sin \lambda) [m - \cos(\psi)]} \\ &= \left[\frac{\sin(\lambda)}{\tan(\nu)} \right] \frac{[m - \cos(\psi)]}{\sqrt{m^2 + 1 - 2m \cos(\psi)}} \end{aligned} \quad (4-14)$$

The local horizon vector may be determined by applying equations (4-6) and (4-7) or (4-12) (normalized) as follows:

$$\hat{q} = \frac{-\sin(\psi_B) \hat{i} + \cos(\psi_B) \hat{j} - \cotan(\nu) \sin(\lambda) \hat{k}}{\sqrt{1 + \cotan^2(\nu) \sin^2(\lambda)}} \quad (4-15)$$

The azimuth angle of \hat{q} differs from that of the beam pointing [e.g., equation (4-4)] by 90° . The local north vector at an MBTA site, shown in Figure 4-8, is given by

$$\hat{N}_L = \hat{i} \sin \nu \cos \epsilon_A - \hat{j} \sin \nu \sin \epsilon_A + \hat{k} \cos \nu \quad (4-16)$$

and the local azimuth angle defined by $\hat{\epsilon}$ is

$$\cos \epsilon = \hat{N}_L \cdot \hat{q} = \frac{-\sin \lambda}{\sqrt{\sin^2 \nu + \cos^2 \nu \sin^2 \lambda}} \quad (4-17)$$

Thus,

$$\phi = AZ - 90^\circ$$

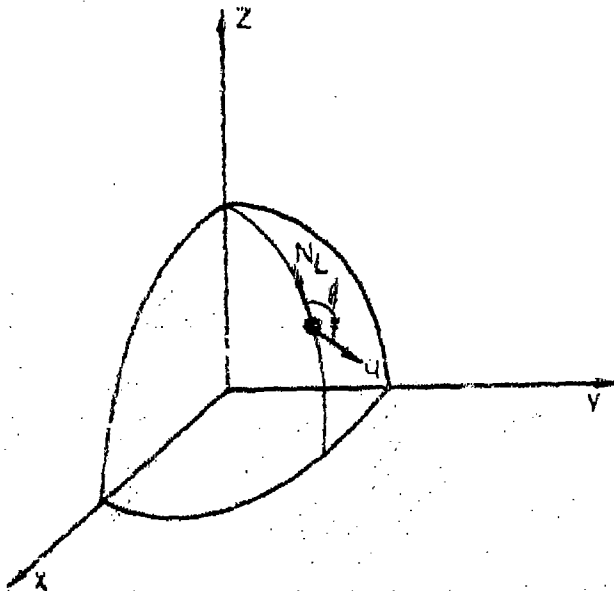


Figure 4-8. MBTA Local North
Vector

The orientation of the \hat{q} and \hat{p} vectors is shown in Figure 4-9. Note that the angle Ω is negative for a U.S. MBTA torus position viewing an Atlantic region satellite.

The unit scan "plane" vector \hat{p} is derived from

$$\hat{p} = \frac{(\bar{R} \times \bar{T}) \times \bar{R}}{|(\bar{R} \times \bar{T}) \times \bar{R}|} \quad (4-18)$$

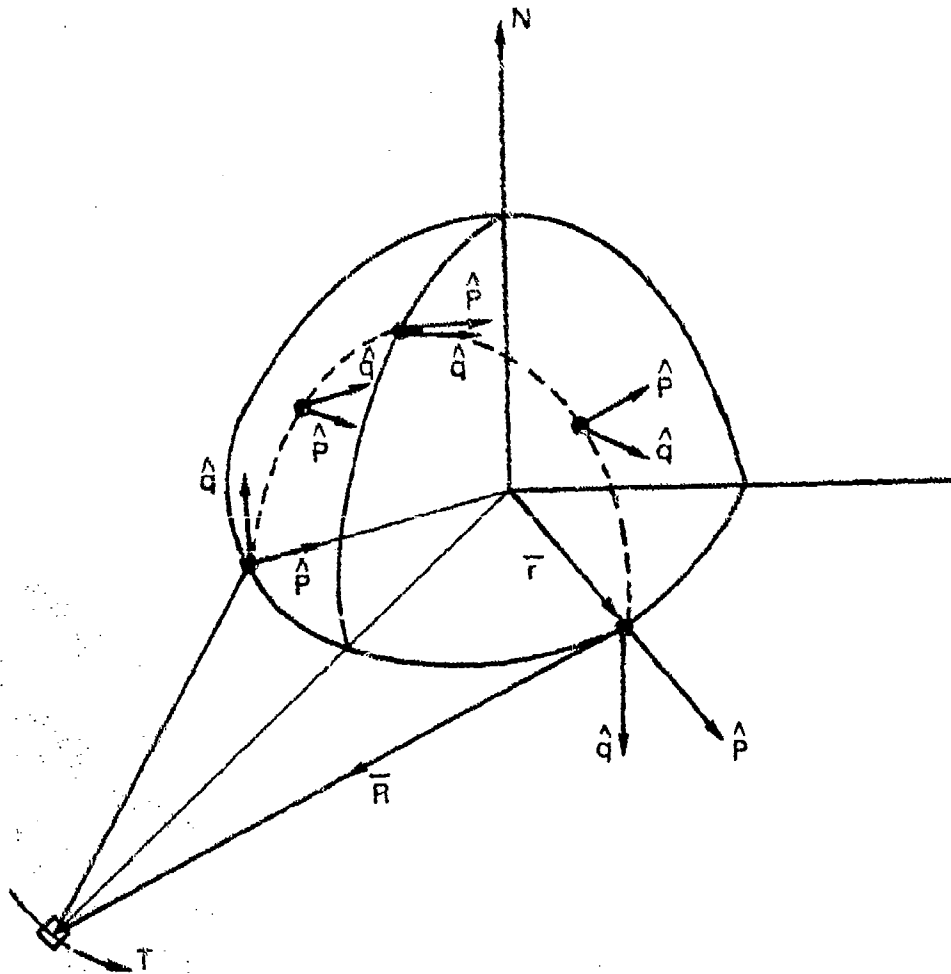


Figure 4-9. Local Orientation of \hat{p} and \hat{q}
Unit Vectors

The unnormalized vector expression is

$$\begin{aligned} \bar{p} = & \hat{i}[-\sin \phi_s (m^2 + 1 - 2m \cos \nu \cos \lambda) + \cos \phi_s (m \cos \nu \sin \lambda) \\ & - \cos^2 \nu \sin \lambda \cos \phi_A] + j[\cos \phi_s (m^2 + 1 - 2m \cos \nu \cos \lambda) \\ & + \sin \phi_s (m \cos \nu \sin \lambda) - \cos^2 \nu \sin \lambda \sin \phi_A] \\ & + \hat{k}[-\cos \nu \sin \nu \sin \lambda] \end{aligned} \quad (4-19)$$

A computer program (Program MBTA-1) for calculating the pointing and geometrical parameters given ν and λ is included in the appendix.

4.3 DERIVATION OF OPTIMUM ROTATION AXIS ANGLE, ϕ_0

The beam of the MBTA scans over a conical surface, as shown in Figure 4-10. The rotation axis angle, ϕ_0 , is established by

$$\phi_0 = \cos^{-1} \left[\frac{\bar{R} \cdot \bar{u}}{|\bar{R}| |\bar{u}|} \right] \quad (4-20)$$

where \bar{R} is the pointing vector (beam axis) from the MBTA to the satellite and \bar{u} is the rotation axis for generating the spherical portion of the MBTA. A given antenna system at a specific latitude, ν , and differential longitude, λ , is defined by one fixed ϕ_0 value. With the antenna support structure adjusted to place the beam on the geosynchronous arc at one location, exact beam pointing with scan (or equivalently satellite motion) would require all derivatives of ϕ_0 with respect to ϕ_s (satellite motion along the geosynchronous arc) to be zero.

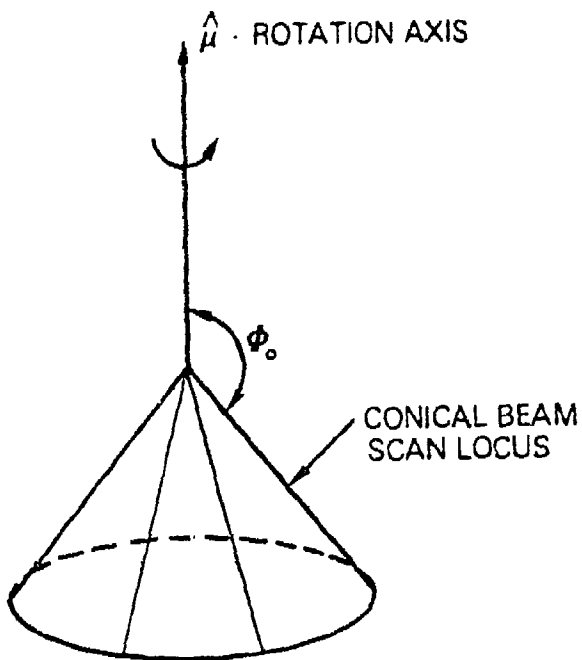


Figure 4-10. Conical Beam Scan Locus

The MBTA geometrical degrees of freedom permit the first two derivatives¹⁰ to be set at zero for an optimum solution:

$$\frac{\delta\phi_0}{\delta\phi_s} = \frac{\delta^2\phi_0}{\delta\phi_s^2} = 0 \quad (4-21)$$

The rotation axis \bar{u} is specified as

$$\bar{u} = a\hat{i} + b\hat{j} + c\hat{k} \quad (4-22)$$

Then

$$\phi_0 = \cos^{-1} \left[\frac{a(m \cos \phi_s - \cos v \cos \phi_A) + b(m \sin \phi_s - \cos v \sin \phi_A) - c \sin v}{\sqrt{m^2 + 1 - 2m \cos v \cos \lambda} \sqrt{a^2 + b^2 + c^2}} \right] \quad (4-23)$$

Application of the derivative conditions [equation (4-21)] and the normalization condition

$$|\bar{u}| = 1; \quad \sqrt{a^2 + b^2 + c^2} = 1 \quad (4-24)$$

is sufficient to determine $\bar{u} = (a, b, c)$ and the resulting optimum generating axis angle

$$\phi_0 = \cos^{-1} (a, b, c) \quad (4-25)$$

A useful identity is

$$\frac{\delta}{\delta x} (\cos^{-1} w) = \frac{-1}{\sqrt{1-w^2}} \frac{\delta w}{\delta x} = 0 \quad (4-26)$$

Thus, in general $\delta w / \delta x = 0$ unless $w^2 = 1$.

By symmetry, the first derivative of ϕ_0 is equal to zero for the co-longitude case ($\lambda = 0$). Application of the first derivative condition yields

$$\begin{aligned} & a \left\{ -\sin \phi_s (m^2 + 1 - 2m \cos v \cos \lambda) \right. \\ & \quad \left. + m \cos \phi_s \cos v \sin \lambda - \cos^2 v \cos \phi_A \sin \lambda \right\} \\ & + b \left\{ \cos \phi_s (m^2 + 1 - 2m \cos v \cos \lambda) \right. \\ & \quad \left. + m \sin \phi_s \cos v \sin \lambda \right. \\ & \quad \left. - \cos^2 v \sin \phi_A \sin \lambda \right\} + c \left\{ -\sin v \cos v \sin \lambda \right\} = 0 \quad (4-27) \end{aligned}$$

while application of the second derivative condition yields

$$\begin{aligned}
 & a \left\{ -\cos \phi_s (m^2 + 1 - m \cos v \cos \lambda) \right. \\
 & \quad \left. + \sin \phi_s (m \cos v \sin \lambda) + \cos^2 v \cos \phi_A \cos \lambda \right\} \\
 & + b \left\{ -\sin \phi_s (m^2 + 1 - m \cos v \cos \lambda) \right. \\
 & \quad \left. - \cos \phi_s (m \cos v \sin \lambda) \right. \\
 & \quad \left. + \cos^2 v \sin \phi_A \cos \lambda \right\} + c \left\{ \sin v \cos v \cos \lambda \right\} = 0 \quad (4-28)
 \end{aligned}$$

Then

$$ax_1 + bx_2 + cx_3 = 0 \quad (\text{first derivative}) \quad (4-29a)$$

$$ax_4 + bx_5 + cx_6 = 0 \quad (\text{second derivative}) \quad (4-29b)$$

$$a^2 + b^2 + c^2 = 1 \quad (\text{normalization}) \quad (4-29c)$$

Since

$$x_3 = -\tan \lambda x_6 \quad (4-30)$$

solving yields

$$\frac{a}{c} = -\frac{x_6}{(x_4 + x_5 h)} \quad (4-31a)$$

$$\frac{b}{c} = -x_6 \frac{h}{(x_5 h + x_4)} \quad (4-31b)$$

$$c = \pm \frac{x_4 + x_5 h}{\sqrt{x_6^2 (1 + h^2) + (x_4 + x_5 h)^2}} \quad (4-31c)$$

where

$$h = \frac{(x_1 x_6 - x_3 x_4)}{(x_3 x_5 - x_2 x_6)}$$

Program MBTA-3 in the appendix provides the optimum generating axis angle and the corresponding rotation axis unit vector components as a function of the antenna longitude and the MBTA latitude and differential longitude.

Figure 4-11 is a map of the optimum MBTA generating angle as a function of differential longitude and latitude coordinates. Results for the northern and southern hemispheres are the same. The spacecraft position is at the center of the map. The optimum ϕ_0 angle is essentially a function of only the antenna latitude. The optimum MBTA generating axis angle at the co-longitude point, shown in Figure 4-12, varies from 90° at the equator to 97.8° over the present latitude range of DSCS antenna locations. The rotation axis inclination angle relative to the polar axis is

$$\phi_i = \cos^{-1}(\bar{k} \cdot \bar{u}) = \cos^{-1}(c) \quad (4-32)$$

as shown in Figure 4-13. The magnitude of the inclination angle is shown in Figure 4-14. At latitudes of 0° and 90° , \bar{u} is identical to the polar axis; at intermediate latitude positions it departs only slightly from this orientation.

Worldwide deployment of the MBTA antenna to view synchronous satellites from all elevation angles $\geq 5^\circ$ requires identification of the minimum number of different reflector designs (defined by the angle ϕ_0 between the beam pointing direction and the axis of rotation) and their corresponding region of applicability. If the angle ϕ_0 is fixed for a multitude of MBTA locations, some amount of orthogonal plane (parabolic) beam scan loss

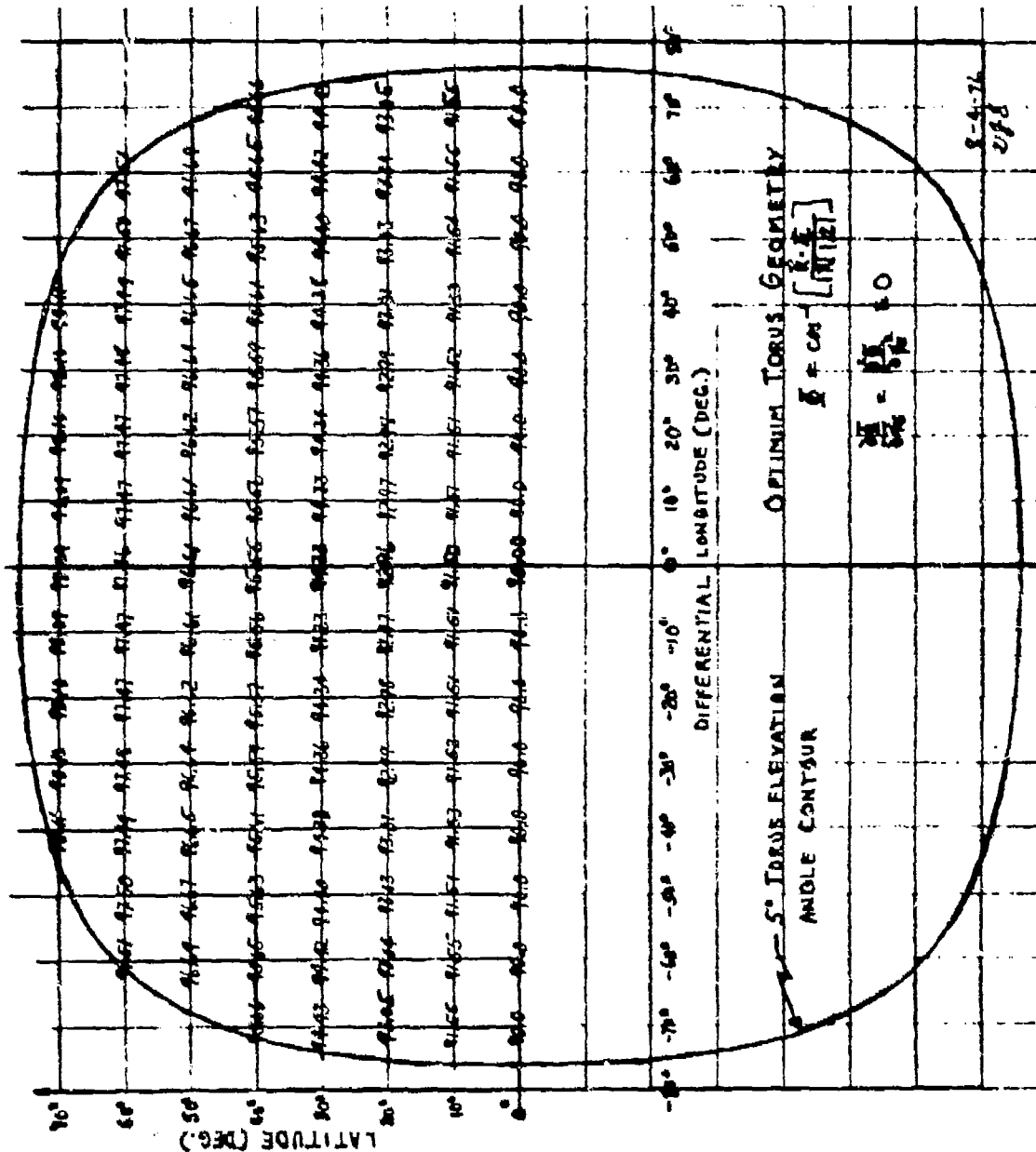


Figure 4-11. Map of Optimum MBTA Generating Axis Angles, ϕ_0

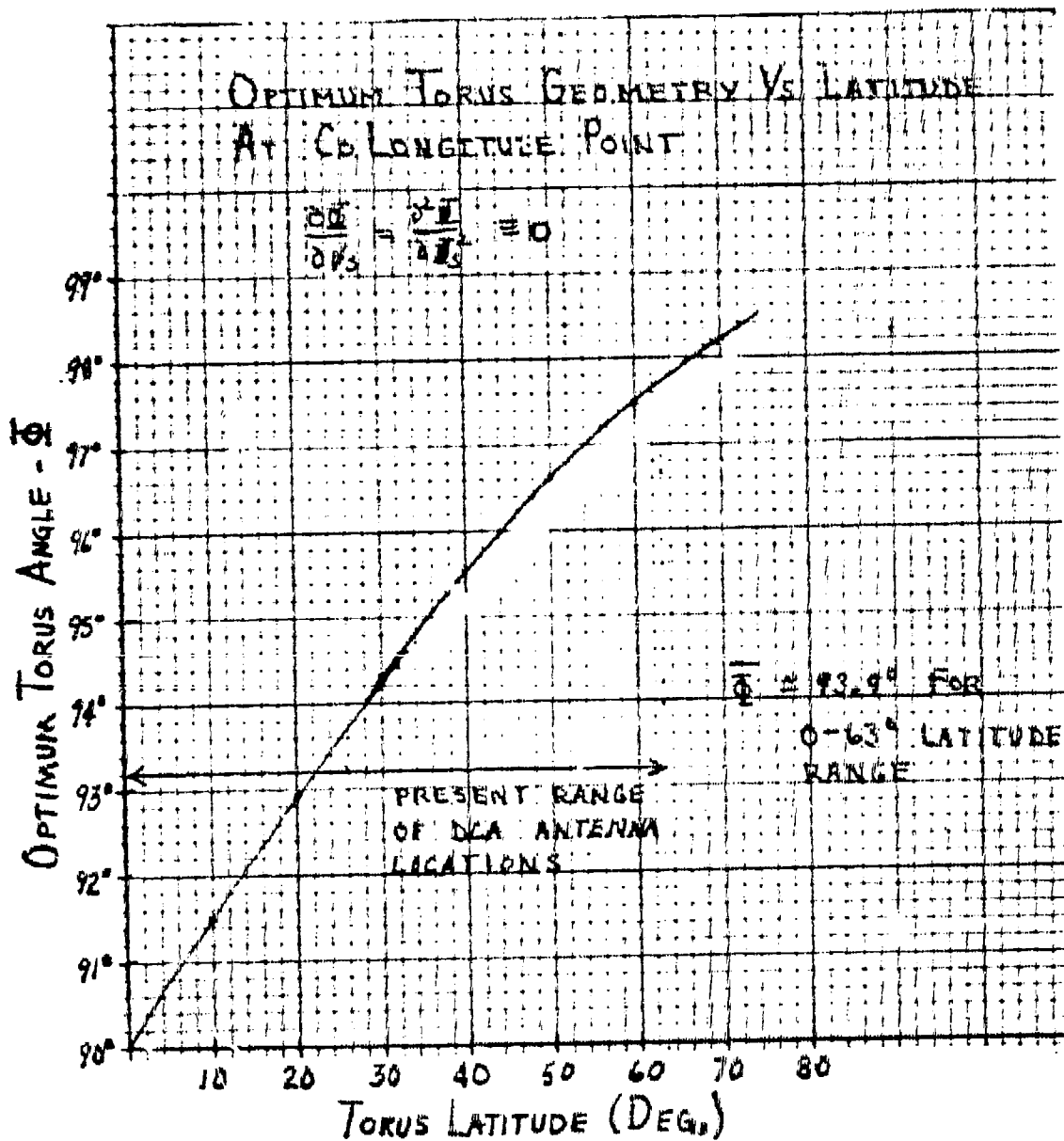


Figure 4-12. Optimum Φ_0 Angle vs Latitude at Co-longitude Position

is required to scan and reposition the beam along the geostationary arc. The antenna mount positions the beam exactly at the center of the field of view or at two symmetrically displaced angular positions about the center of the field of view, as shown in Figure 4-15. The scanned beam position(s) will then depart somewhat from the locus of pointing directions defining the geosynchronous arc. The beam is repositioned onto the geosynchronous arc by scanning the beam in the parabolic plane of the MBTA.

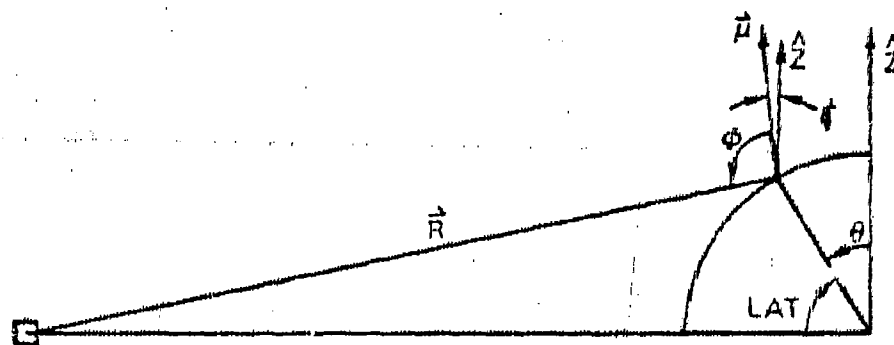


Figure 4-13. Rotation Axis Inclination Angle

In terms of economy, it is important to minimize the number of different reflector geometries required for a system. One major objective of this study program was to verify that a single reflector geometry would provide sufficient performance margins for DSCS applications. Use of a single reflector geometry for all DSCS MBTA locations, with only the reflector support structures varying to accommodate different latitude and differential longitude positions, results in considerable simplification for the overall antenna system and minimizes the resultant antenna fabrication costs.

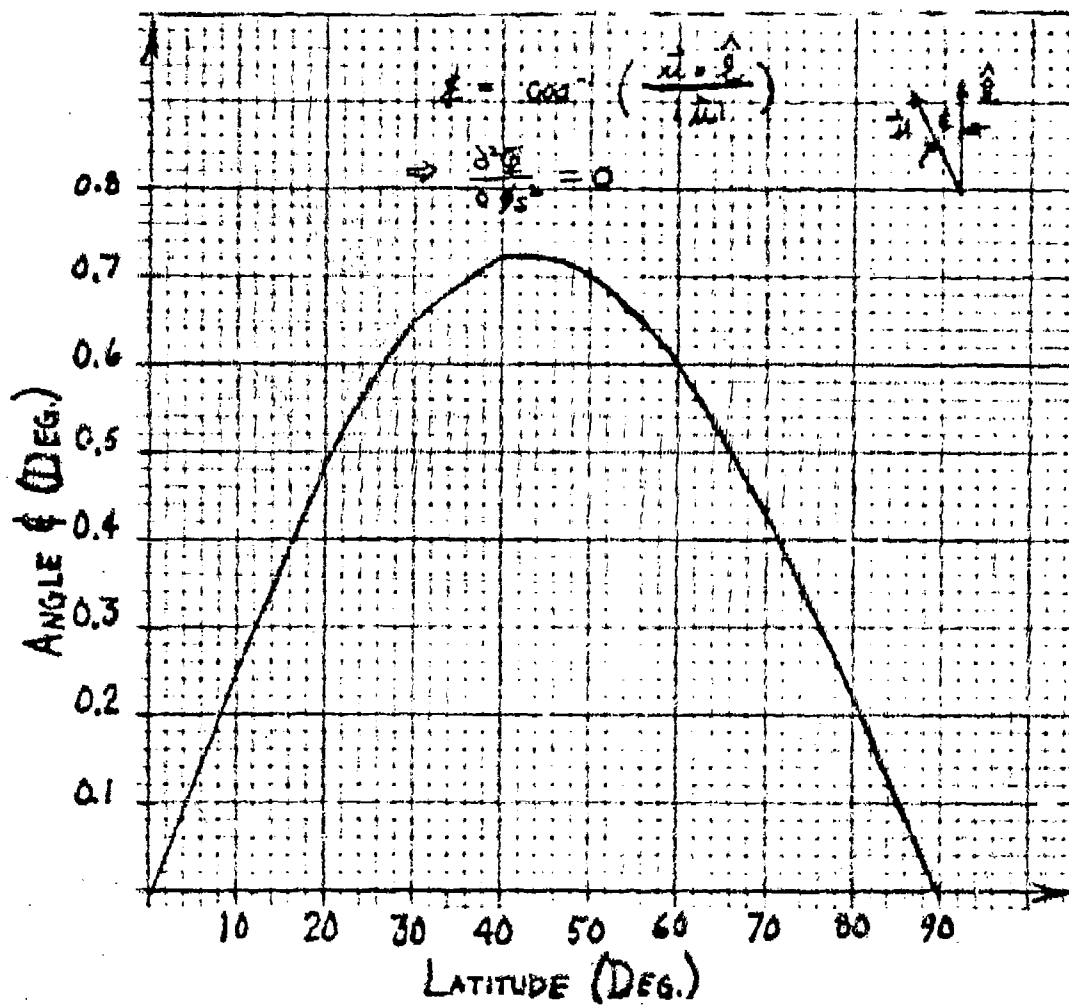
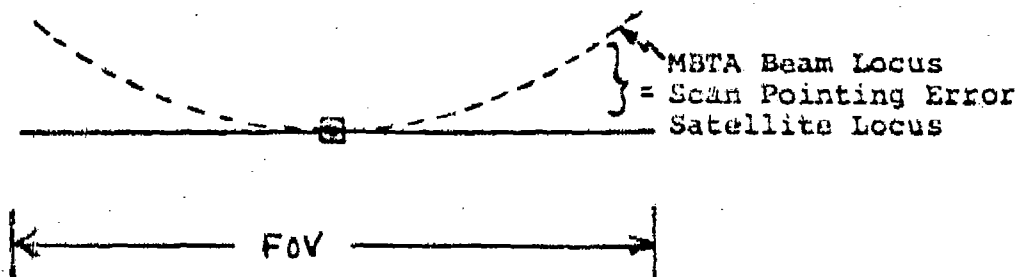


Figure 4-14. Rotation Axis Inclination Angle vs Latitude at the Co-longitude Position

- a) Exact beam pointing with spherical scan at center of FOV



- b) Exact beam pointing with spherical scan at two positions over FOV

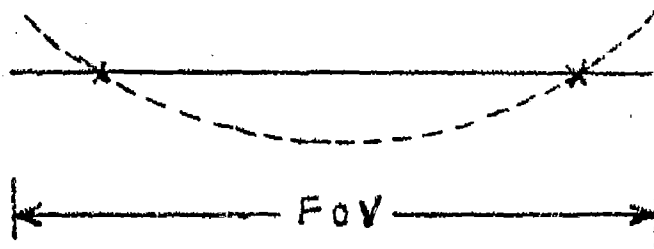


Figure 4-15. Beam Pointing Loci with Scan

4.4 POINTING EFFECTS OF A SINGLE FIXED ϕ_0 GEOMETRY

When the reflector generating axis angle, ϕ_0 , is fixed, the amount of pointing error with beam scan is

$$(\text{desired} - \text{actual}) \text{ beam pointing} = \phi(\phi_s) - \phi_0(\phi_s) \quad (4-33)$$

as shown in Figure 4-16. The angle $\phi(\phi_s)$ is the exact angle between the fixed \bar{u}_0 rotation axis and the \bar{R} pointing vector between the MBTA and the geosynchronous satellite position. The antenna geometry fixes $\phi = \phi_0$ independent of the satellite position ϕ_s as the beam or satellite angle changes. Hence, the difference between the two is essentially the beam pointing error that must be corrected by providing some amount of beam scan in the parabolic plane of the MBTA. Fixing ϕ_0 results in the following set of defining equations for the MBTA reflector rotation axis. For the first derivative condition [equation (4-27)],

$$ax_1 + bx_2 + cx_3 = 0 \quad (4-34a)$$

for a fixed ϕ_0 design [equation (4-23)],

$$ax_7 + bx_8 + cx_9 = \cos \phi_0 \sqrt{m^2 + 1} - 2m \cos v \cos \lambda = x_{10} \quad (4-34b)$$

and for the normalization condition [equation (4-24)],

$$a^2 + b^2 + c^2 = 1 \quad (4-34c)$$

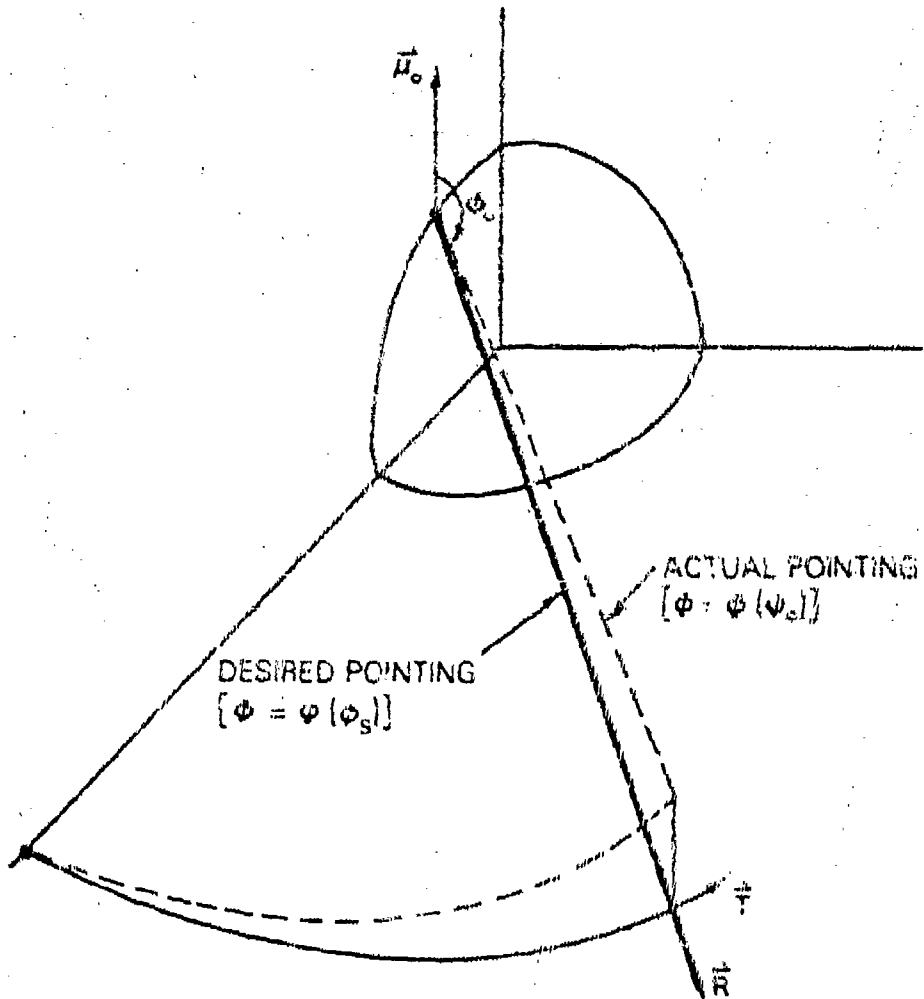


Figure 4-13. Beam Pointing Locus with ϕ_p Fixed

This set of equations specifies the rotation axis parameters (a_0, b_0, c_0) as a function of antenna and satellite positions. They are returned to the expression

$$\phi = \phi(\phi_s) = \cos^{-1} \left[\hat{R}(\phi_s) \cdot \hat{u}_0 \right] \quad (4-35)$$

to evaluate the ϕ angle associated with exact beam positioning over the geosynchronous arc.

Solving the preceding set of equations as follows:

$$ax_1x_5 + bx_2x_5 + cx_3x_5 = 0$$

$$ax_2x_7 + bx_2x_8 + cx_2x_9 = x_2x_{10}$$

and subtracting yields

$$a(x_1x_8 - x_2x_7) + c(x_3x_8 - x_2x_9) = -x_3x_{10}$$

or

$$ax_{11} + bx_{12} = x_{13} \quad (4-36a)$$

$$ax_1x_7 + bx_2x_7 + cx_3x_7 = 0 \quad (4-36b)$$

$$ax_7x_1 + bx_8x_1 + cx_9x_1 = x_{10}x_1 \quad (4-36c)$$

Further subtraction yields

$$b(x_2x_7 - x_1x_8) + c(x_3x_7 - x_1x_9) = -x_1x_{10}$$

or

$$bx_{14} + cx_{15} = x_{16} \quad (4-37)$$

Therefore,

$$a = \left(\frac{x_{13}}{x_{11}} \right) - c \left(\frac{x_{12}}{x_{11}} \right) = x_{17} + cx_{18} \quad (4-38)$$

$$b = \left(\frac{x_{16}}{x_{14}} \right) - c \left(\frac{x_{15}}{x_{14}} \right) = x_{19} + cx_{20} \quad (4-39)$$

To find c ,

$$a^2 + b^2 + c^2 = 1$$

where

$$a^2 = x_{17}^2 + 2x_{17}x_{18}c + x_{18}^2c^2 \quad (4-40a)$$

$$b^2 = x_{19}^2 + 2x_{19}x_{20}c + x_{20}^2c^2 \quad (4-40b)$$

Thus,

$$\begin{aligned} & c^2(1 + x_{18}^2 + x_{20}^2) + 2c(x_{17}x_{18} + x_{19}x_{20}) + (x_{17}^2 + x_{19}^2 - 1) \\ &= c(uu) + 2c(vv) + rr \\ &= 0 \end{aligned}$$

and

$$c = \left[\frac{-vv \pm \sqrt{vv^2 - 4uu(rr)}}{2uu} \right] \quad (4-42)$$

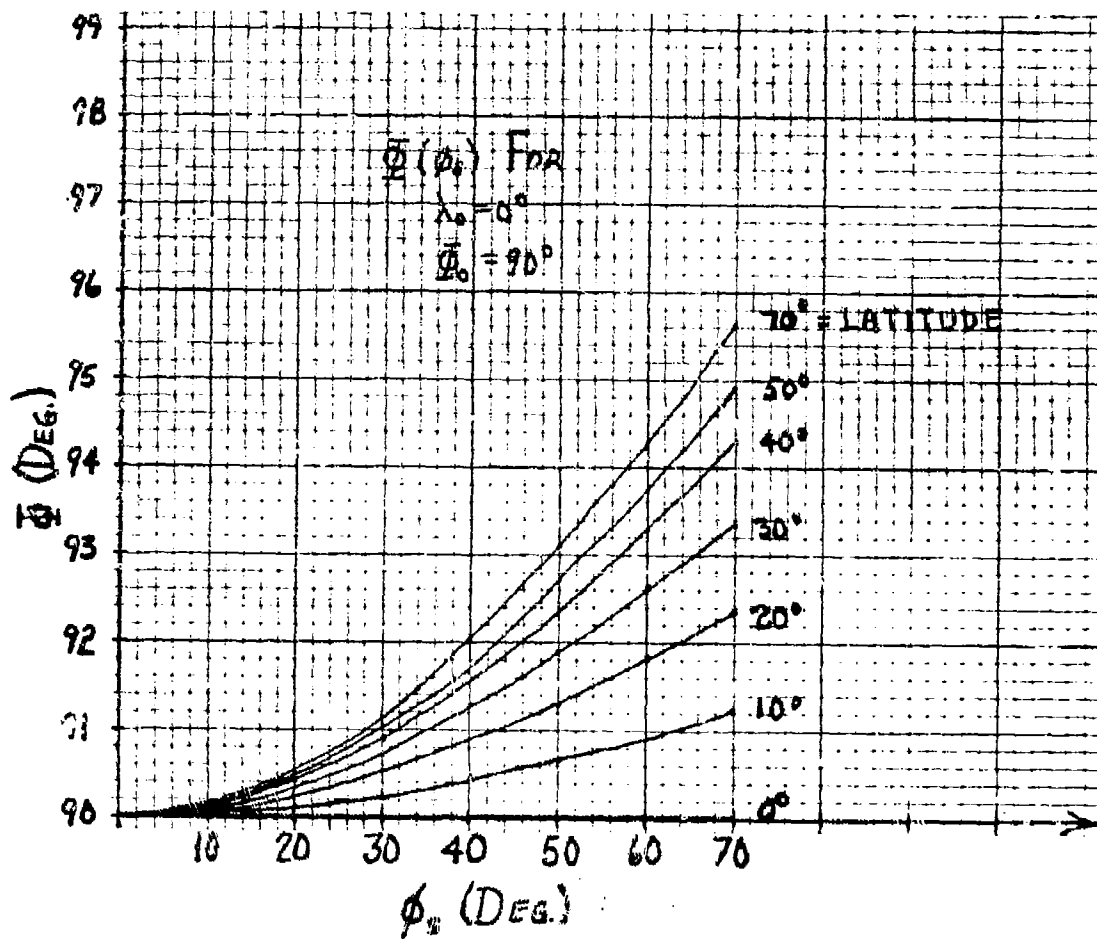
The two solutions obtained above both satisfy the first derivative conditions. Although the antenna scan performance over a limited range ($\leq 20^\circ$ field of view) is virtually identical, the "+" solution provides a better optimum over a wide field of view.

The beam pointing angle $\phi(\phi_s)$ is plotted in Figures 4-17 through 4-21 as a function of ϕ_s at fixed latitudes for fixed generating axis angles of 90° , 93° , 93.5° , 94° , and 95.5° , respectively, with exact pointing at $\lambda = 0^\circ$. The difference between $\phi(\phi_s)$ and ϕ_0 is the error between the actual and desired beam pointing directions. This error is compensated by scanning the beam in the parabolic plane of the MBTA. A reflector surface defined by

$$\phi_0 = 93.5^\circ \quad (4-43)$$

which symmetrizes the orthogonal plane scan error characteristics for antenna locations at 0° and 70° latitude, is chosen as the optimum solution for the DSCS application. A field of view of $\pm 20^\circ$ requires less than 0.3° of parabolic plane beam scan (no more than one beamwidth of scan at 54-dB gain, and no more than two beamwidths of scan at 59-dB gain) for $\nu = 0^\circ$ and 70° latitudes. Negligible beam scan error occurs for $\nu = 20^\circ$ - 30° latitudes.

The scanned beam pointing error characteristics for the optimum $\phi_0 = 93.5^\circ$ geometry with exact beam pointing at $\lambda = +40^\circ$ and -70° are shown in Figures 4-22 and 4-23. The scan characteristics as a function of differential longitude are nearly identical in each case. Note that when $\lambda = -70^\circ$ the beam can be scanned only in one direction to satisfy the constraint that the local elevation angle must be greater than 5° . This constraint also affects the range of useful latitude positions (0° to $\sim \pm 44^\circ$ for $\lambda = \pm 70^\circ$). Table 4-1 summarizes the scanned beam pointing error (in degrees) as a function of latitude and field of view for the optimum $\phi_0 = 93.5^\circ$ geometry. For fields of view up to 40° and antenna beamwidths corresponding to gains up to 60 dB,

Figure 4-17. $\phi_s(\phi_e)$ for $\phi_0 = 90^\circ$, $\lambda = 0^\circ$

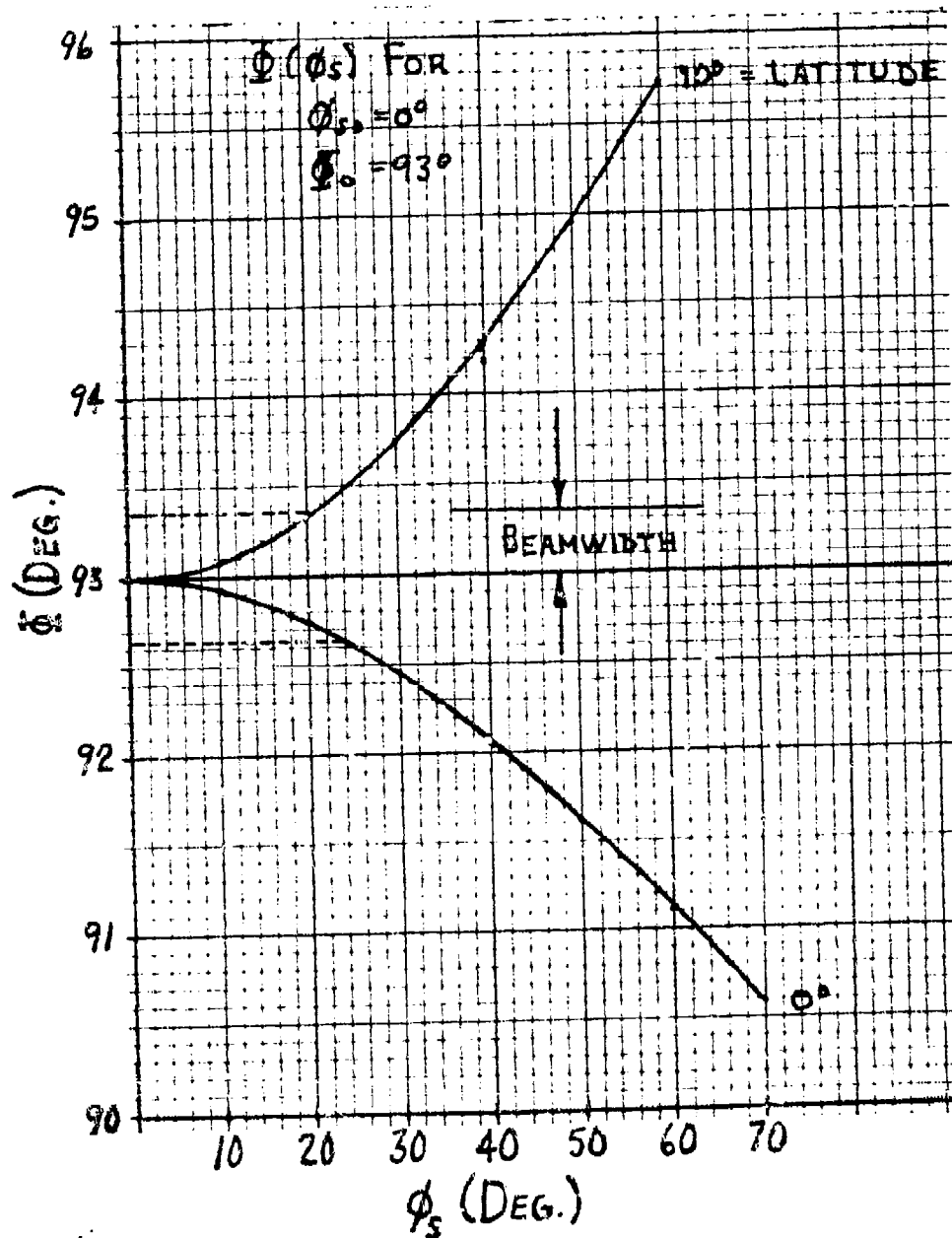
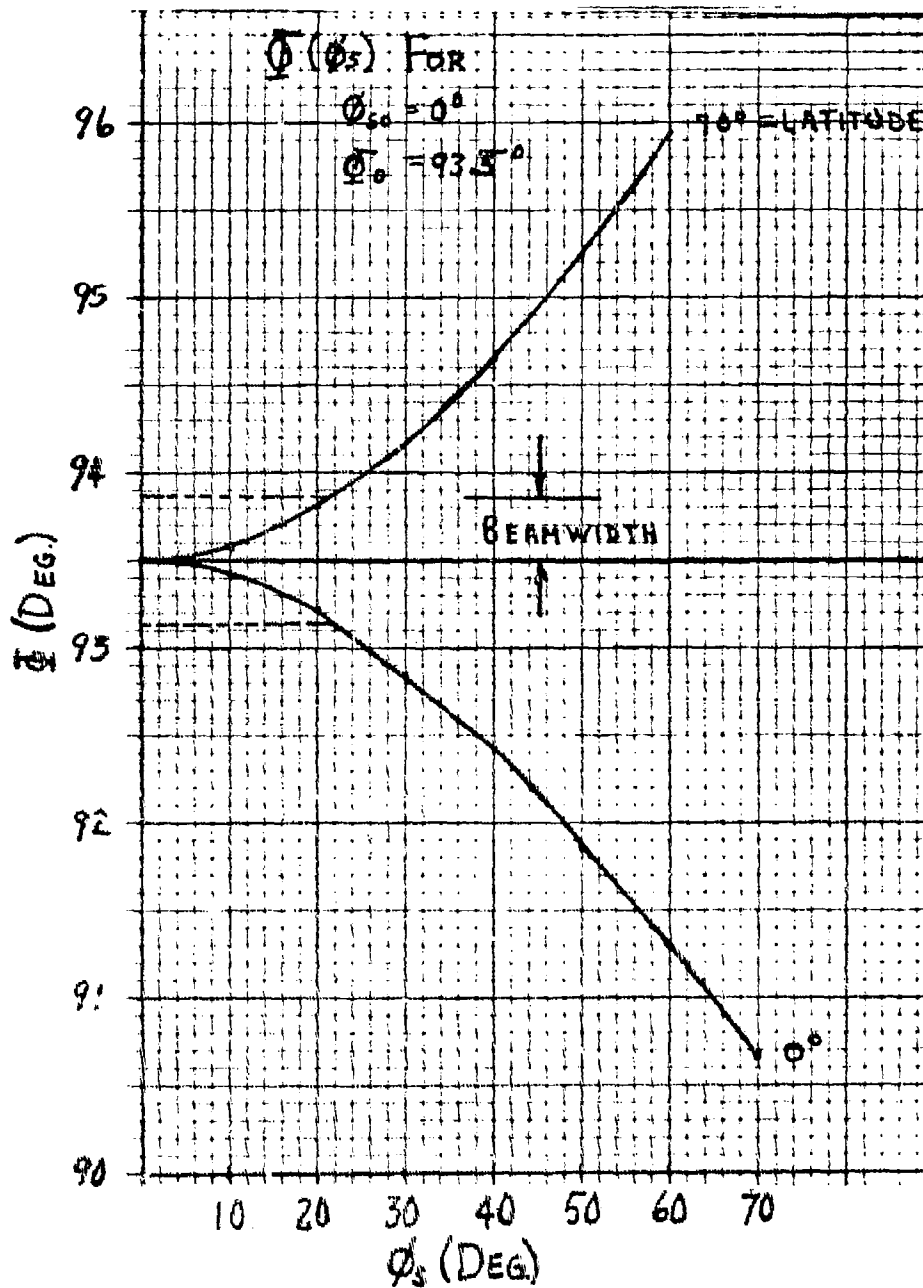


Figure 4-18. $\phi(\phi_s)$ for $\phi_0 = 93^\circ$, $\lambda = 0^\circ$

Figure 4-19. $\Phi(\phi_s)$ for $\phi_0 = 93.5^\circ$, $\lambda = 0^\circ$

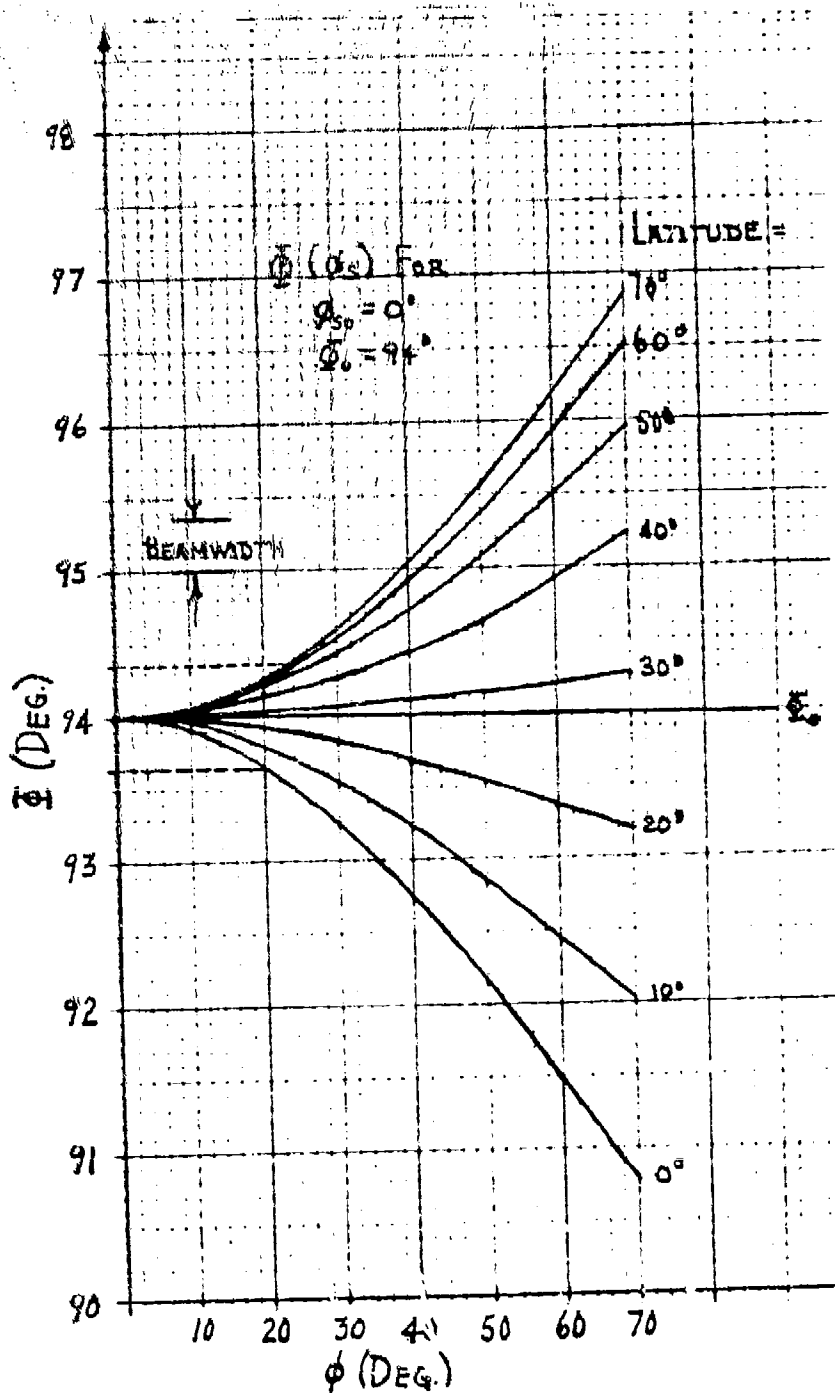


Figure 4-20. $\theta_s(\phi_s)$ for $\phi_0 = 94^\circ$, $\lambda = 0^\circ$

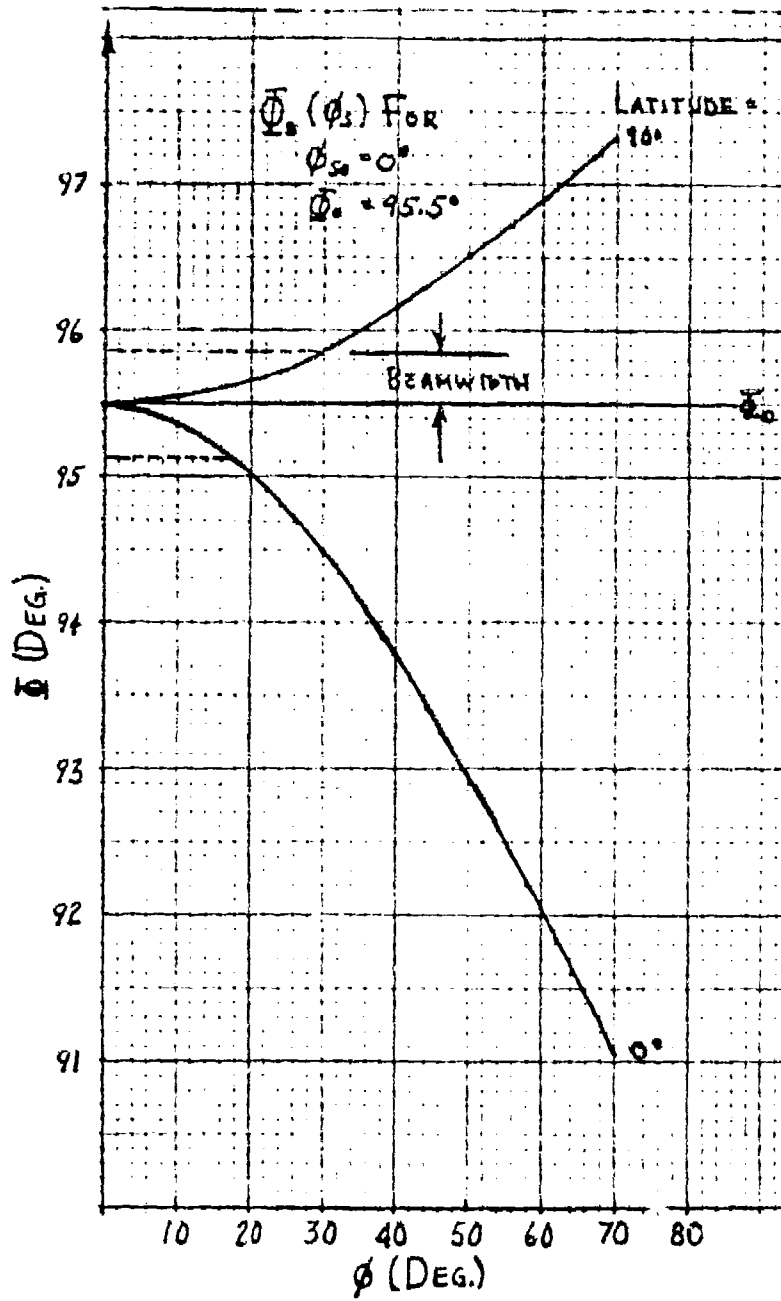


Figure 4-21. $\bar{\Phi}(\phi_s)$ for $\phi_0 = 95.5^\circ$, $\lambda = 0^\circ$

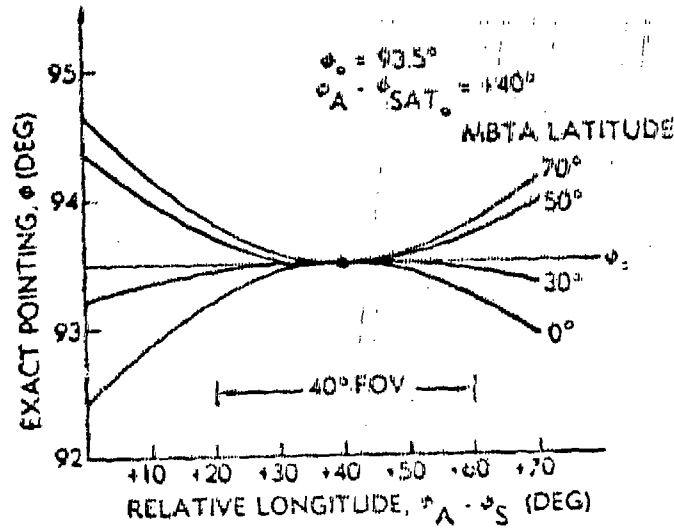


Figure 4-22. $\phi(\phi_S)$ for $\phi_0 = 93.5^\circ$,
 $\lambda = 40^\circ$

Table 4-1. Summary of Spherical Scan Beam Pointing
Errors vs Field of View and Latitude ($\phi_0 = 93.5^\circ$)

Field of View	Latitude, ν							
	0°	10°	20°	30°	40°	50°	60°	70°
10°	-0.019°	-0.01°	0.003°	0.004°	0.01°	0.01°	0.02°	0.02°
20°	-0.07°	-0.04°	-0.01°	0.02°	0.04°	0.06°	0.07°	0.07°
30°	-0.16°	-0.09°	-0.02°	0.037°	0.09°	0.13°	0.16°	0.17°
40°	-0.29°	-0.16°	-0.04°	0.07°	0.16°	0.23°	0.28°	0.30°

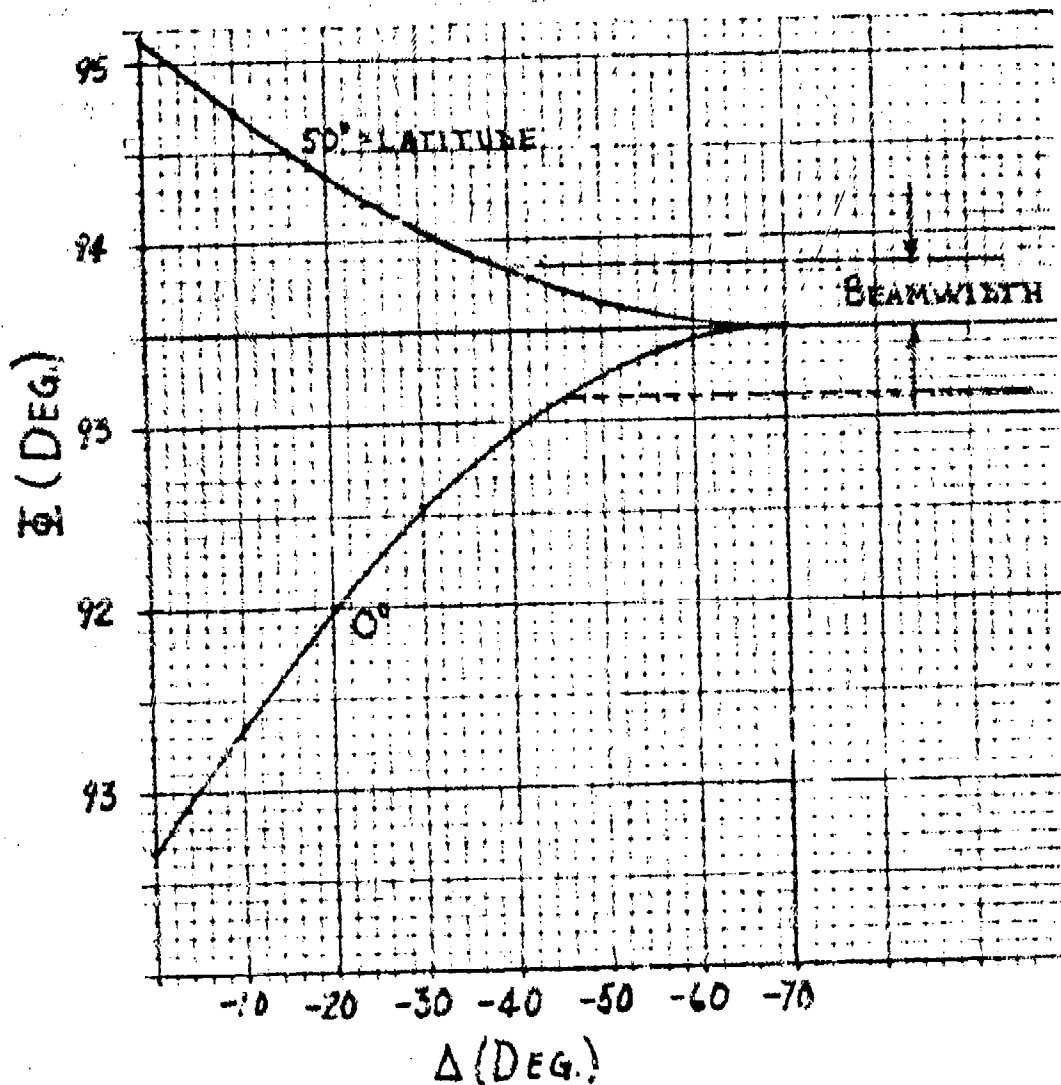


Figure 4-23. $\Phi(\phi_s)$ for $\phi_0 = 93.5^\circ$, $\lambda = -70^\circ$

the performance impact of orthogonal (parabolic) plane scan requirements is negligible. The narrower beamwidths associated with the 20/30-GHz bands require three to five beamwidths of orthogonal plane scan and some performance impact is noted. If the antenna reflector surface is mounted to provide two exact pointing positions over the field of view, as shown in Figure 4-15, the maximum beam pointing errors are halved. The choice between the two antenna mounting arrangements which provide either of the beam scanning loci shown in Figure 4-15 depends upon the system definition, i.e., a system in which all satellite positions over the field of view are equally likely or a system in which the mid-point of the field of view represents a favored beam pointing direction.

The rotation axis inclination in the co-longitude plane ($\lambda = 0$) is shown in Figure 4-24 as a function of latitude for fixed ϕ_0 angles. The components of the rotation axis vector \hat{u} are shown in Figure 4-25 as a function of v and λ for an antenna at $\phi_A = 0^\circ$ with $\phi_0 = 93.5^\circ$. Program MBTA-4 in the appendix provides the beam pointing $\phi(\phi_s)$ and rotation vector \hat{u} characteristics as a function of ϕ_0 , ϕ_A , v , and λ .

The important conclusions are that, for DSCS applications with a field of view up to 40° , a single reflector surface geometry ($\phi_0 = 93.5^\circ$) is sufficient for a system deployed worldwide, and that beam pointing errors associated with scan have a negligible impact on RF performance.

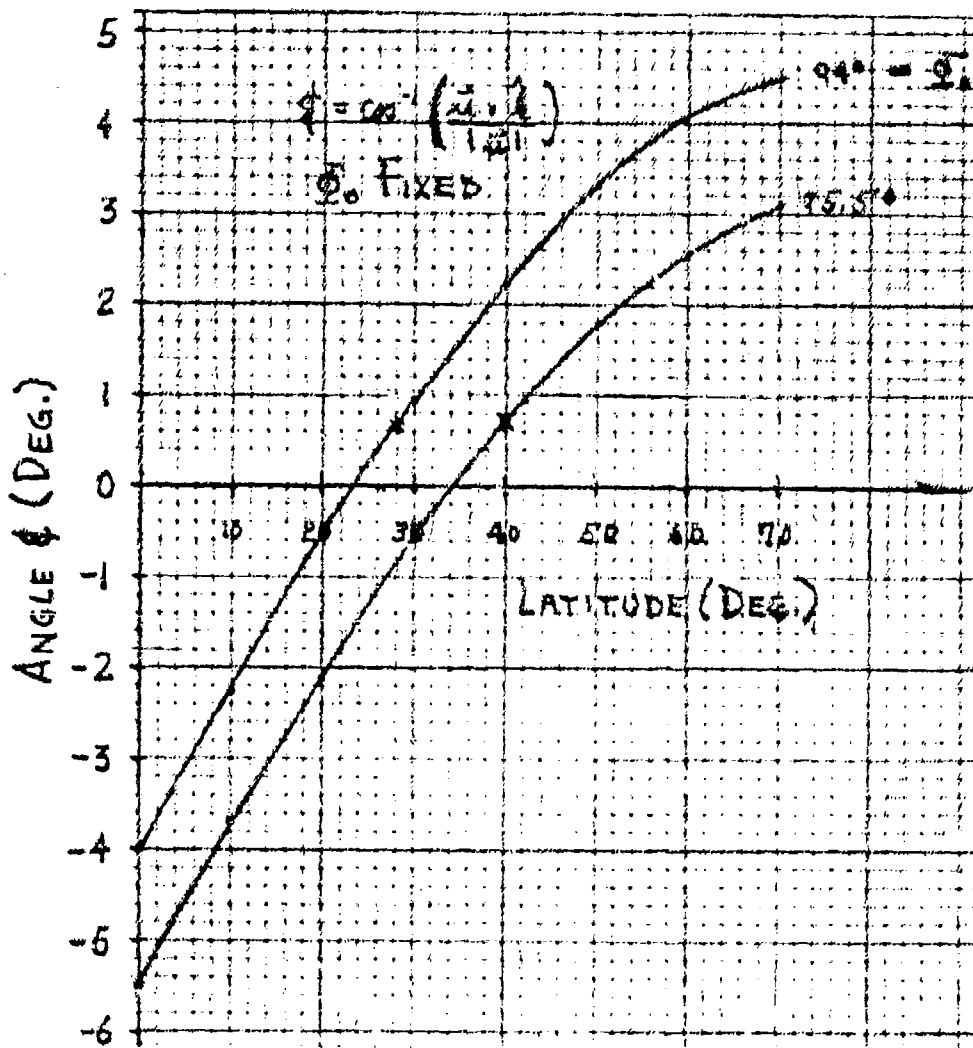


Figure 4-24. Rotation Axis Inclination in Co-longitude Plane with Fixed ϕ_0

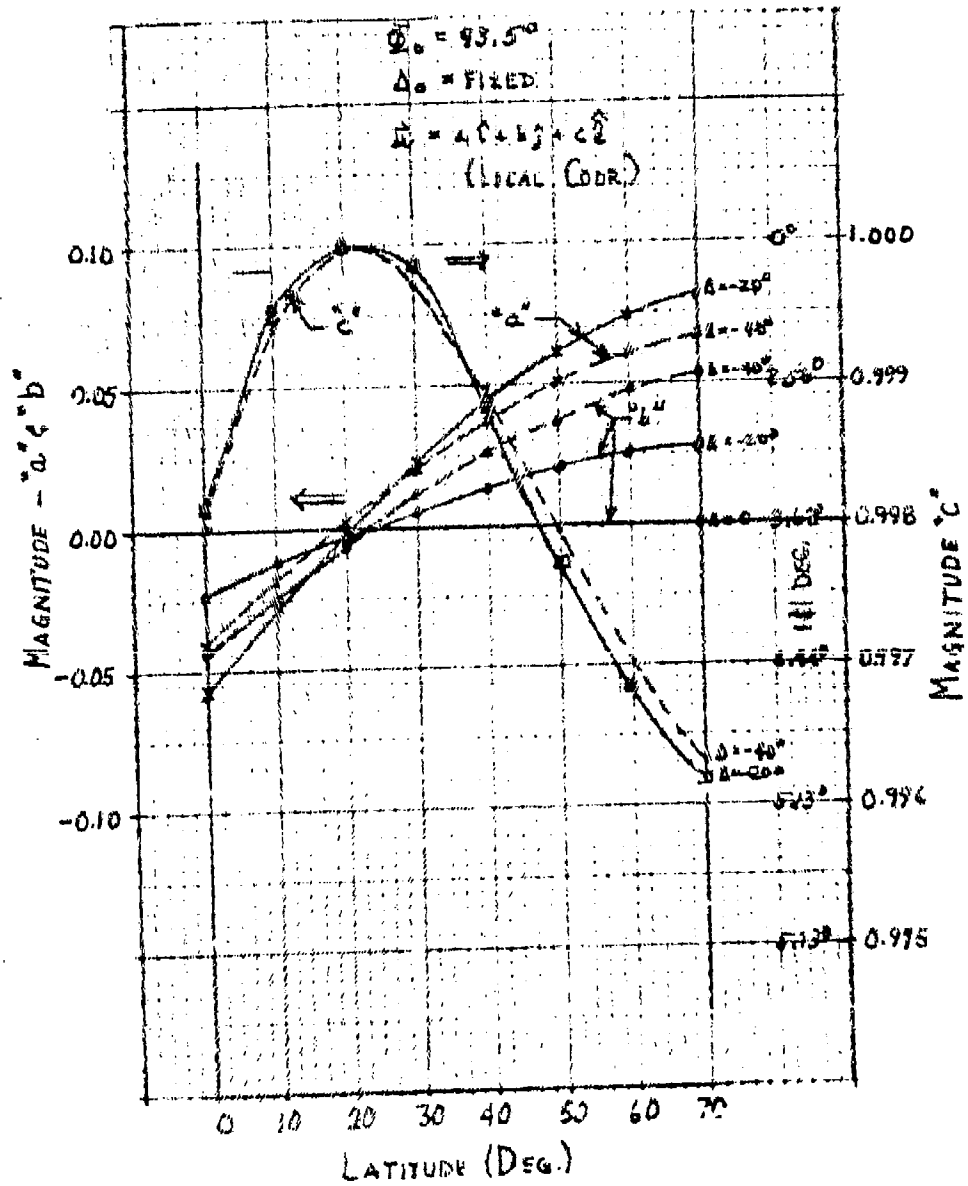


Figure 4-25. Rotation Axis Vector Components

5. ELECTRICAL (RF) PERFORMANCE CHARACTERISTICS

This section develops and details the electrical performance characteristics of the MBTA. The major part of the study analysis focuses on the front-fed offset geometry that is not compensated for spherical aberration. However, phase corrected MBTA systems utilizing either an aberration-correcting subreflector or an aberration-correcting feed array are addressed in the latter part of this section.

5.1 BASIC FREQUENCY CONSIDERATIONS

The Government X-band frequencies are considered to be the primary frequencies for optimizing the MBTA design. The X-band up- and down-link bands are summarized in the following. For the up-link X-band:

$$\begin{aligned} 7.9 &\leq \text{frequency (GHz)} \leq 8.4 \\ \Delta f &= 500 \text{ MHz} \\ \Delta f/\bar{f} &= 6.13\% \\ 1.494 &\geq \lambda \text{ (in.)} \geq 1.406 \\ 3.795 &\geq \lambda \text{ (cm)} \geq 3.569 \end{aligned}$$

and for the down-link X-band,

$$\begin{aligned} 7.25 &\leq \text{frequency (GHz)} \leq 7.75 \\ \Delta f &= 500 \text{ MHz} \\ \Delta f/\bar{f} &= 6.67\% \\ 1.629 &\geq \lambda \text{ (in.)} \geq 1.524 \\ 4.125 &\geq \lambda \text{ (cm)} \geq 3.868 \end{aligned}$$

The minimum separation between the transmit and receive frequency bands is

$$\Delta f_{\min}(\text{TRANSMIT} \rightarrow \text{RECEIVE}) = 150 \text{ MHz} \quad (5-1)$$

This separation imposes special requirements on the necessary filtering and isolation between the transmit and receive frequency bands. In addition, as a result of this separation, any nonlinear junction effects in the feed or antenna system can give rise to intermodulation products that cause transmit band energy to appear in the receive frequency band spectrum. The total X-band frequency range gives a design bandwidth of

$$\frac{\Delta f_{\max}}{f_{\text{ave}}} = 14.27\% \quad (5-2)$$

The average wavelength over the X-band frequency range is

$$\lambda_{\text{ave}}(\text{X-band}) = 1.5 \text{ in.} \quad (5-3)$$

The designs are also evaluated at the commercial frequency bands 4/6, 11/14, and 20/30 GHz. The characteristics of these frequency bands are summarized in Table 5-1.

5.2 BASIC APERTURE DIAMETER, GAIN, AND BEAMWIDTH CONSIDERATIONS

Figure 5-1 summarizes the illumination gain and beamwidth of a reference circular aperture antenna system as a function of the diameter-to-wavelength ratio (D/λ). The gain curves

Table 5-1. Multiple Frequency Band Summary

Band (GHz)	Frequency (GHz)		Δf (MHz)		λ_{ave} (in.)	
	Down-Link	Up-Link	Down-Link	Up-Link	Down-Link	Up-Link
4/6	3.7-4.2	5.925-6.425	500	500	2.88	1.91
7/8	7.25-7.75	7.9-8.4	500	500	1.57	1.45
11/14	10.95-11.2 11.45-11.7	14.0-14.5	500	500	1.04	0.83
20/30	20.2-21.2	30-31	1000	1000	0.57	0.39

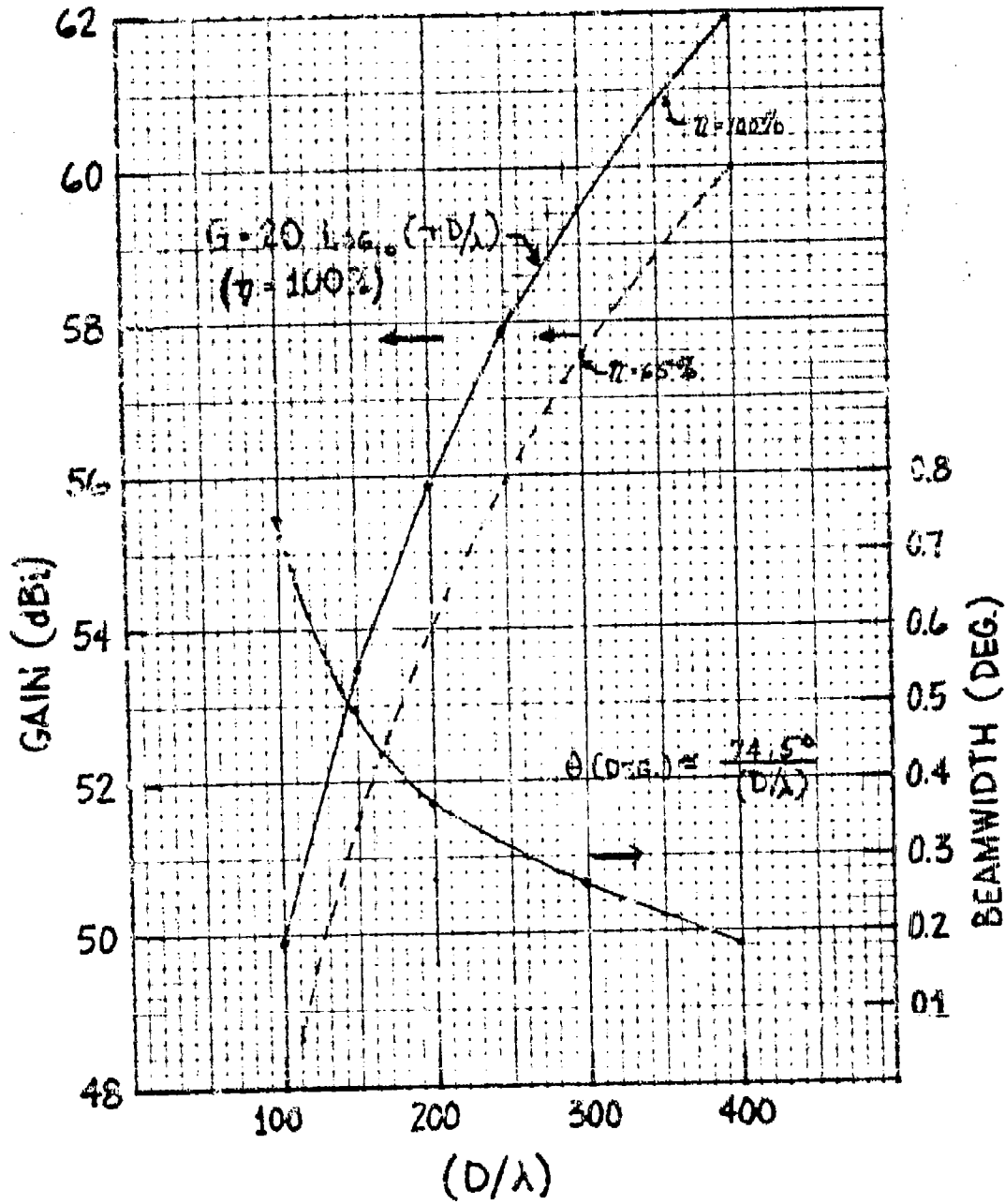


Figure 5-1. Illumination Gain and Beamwidth vs D/λ

correspond to 65- and 100-percent aperture efficiency. The illumination gain curves do not include feed or reflector rms surface tolerance losses. In this study two cases at the X-band frequencies are of particular interest:

- a. $G = 54$ dB, $(D/\lambda) = 220$, and $\theta_0 = 0.35^\circ$; and
- b. $G = 59$ dB, $(D/\lambda) = 380$, and $\theta_0 = 0.18^\circ$.

The diameter, D , versus D/λ at the minimum down-link and maximum up-link X-band frequencies is shown in Figure 5-2. Figure 5-3 shows D versus D/λ at the minimum down-link and maximum up-link frequencies for all the frequency bands of interest in the study.

5.3 SYMMETRICAL MBTA FIELD OF VIEW, FOCUSING, AND FEED ILLUMINATION ANGLE PARAMETERS

A symmetrical MBTA geometry with a 90° angle between the rotation axis and beam pointing direction provides an excellent starting point for deriving several basic relationships. Figure 5-4, which is a cross section through the center of the MBTA, indicates the derivation of the MBTA field of view or scan range in terms of the width, W , of the reflector aperture. In this figure,

$$\alpha = \sin^{-1} \left(\frac{D/2}{R} \right) \quad (5-4)$$

is half the included angle from the rotation axis to the edge of the feed illuminated area of the reflector and

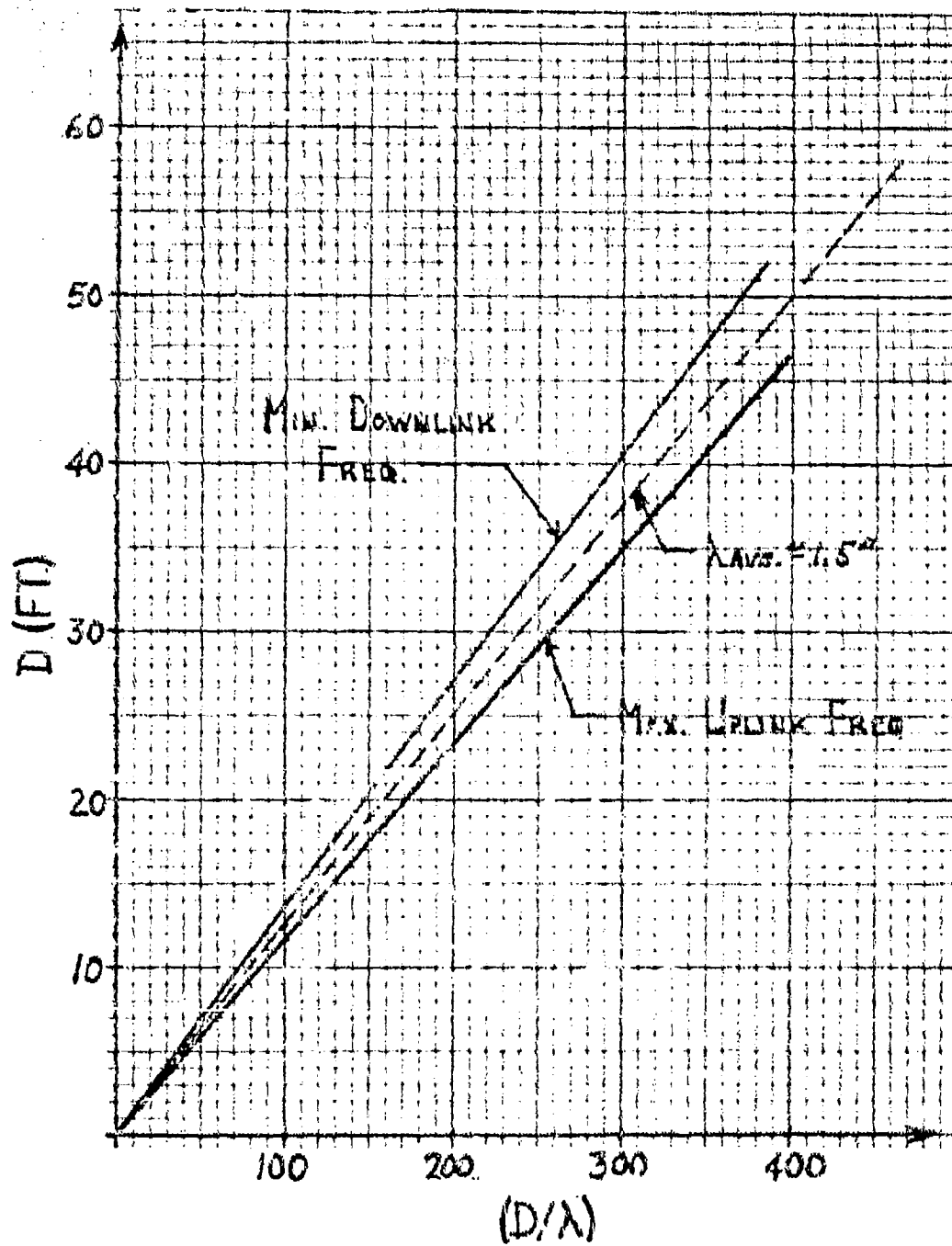


Figure 5-2. MBTA Diameter vs D/λ at x-Band

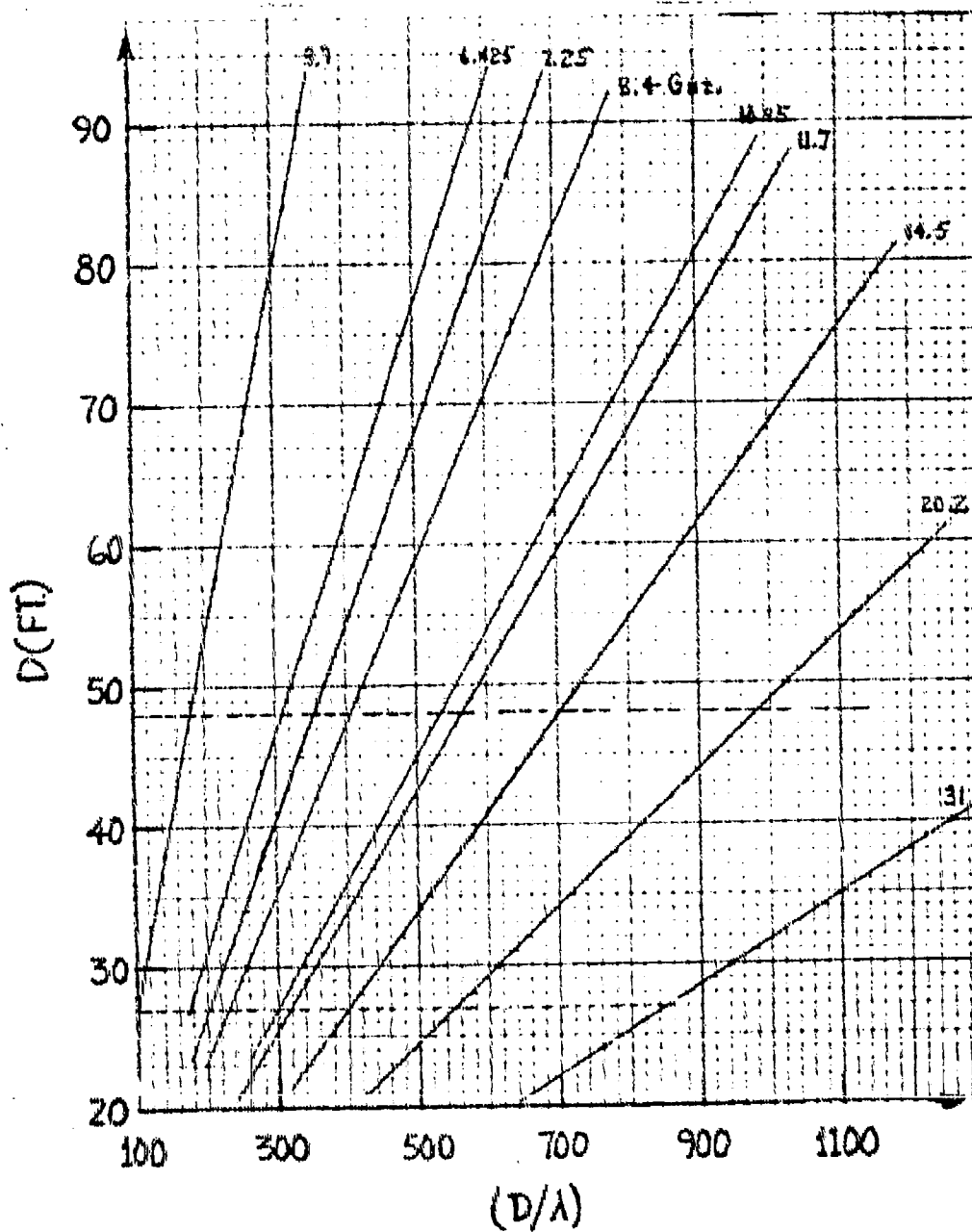
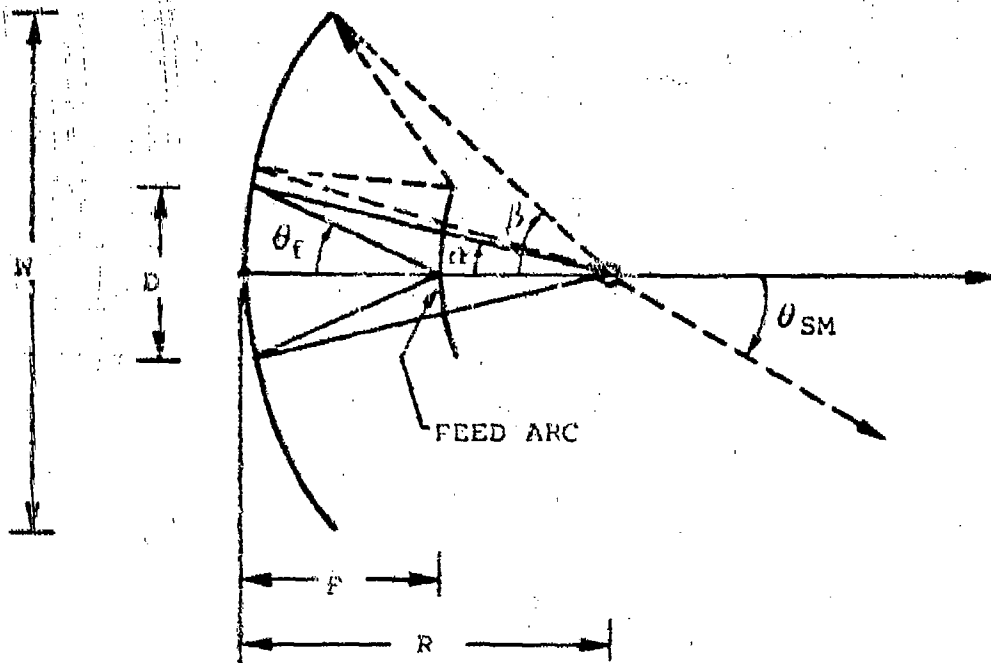


Figure 5-3. Diameter vs D/λ at Specified Frequencies



$$\alpha = \sin^{-1} \left(\frac{D/2}{R} \right)$$

$$\beta = \sin^{-1} \left(\frac{W/2}{R} \right)$$

$$2 \theta_{SM} = \text{FOV} - 2 \left[\sin^{-1} \left(\frac{W}{2R} \right) - \sin^{-1} \left(\frac{D}{2R} \right) \right]$$

Figure 5-4. Symmetrical MBTA Field of View Parameters

$$\beta = \sin^{-1} \left(\frac{W/2}{R} \right) \quad (5-5)$$

is half the included angle from the rotation axis to the edge of the reflector aperture. The maximum scan angle is:

$$\theta_{\text{max}} = (\beta - \alpha) = \sin^{-1} \left(\frac{W}{2R} \right) - \sin^{-1} \left(\frac{D}{2R} \right) \quad (5-6)$$

The symmetrical MBTA field of view is then

$$\text{FOV} = 2\theta_{\text{max}} = 2 \left[\sin^{-1} \left(\frac{W}{2R} \right) - \sin^{-1} \left(\frac{D}{2R} \right) \right] \quad (5-7)$$

$$\text{FOV} = \left(\frac{180^\circ}{\pi} \right) \left(\frac{D}{R} \right) \left(\frac{W}{D} - 1 \right) \quad (5-8)$$

Figure 5-5 shows the field of view versus the ratio of aperture plane dimensions (W/D) for fixed D/R ([normalized radius of curvature]⁻¹) values. Spherical aberration phase errors decrease with a larger radius of curvature (decreasing D/R), but the field of view also decreases if W/D remains fixed.

The paraxial focus of a spherical reflector is defined as

$$F_{\text{paraxial}} = 0.5R \quad (5-9)$$

This spherical reflector focal position is shown in Figure 5-6. Using ray optics, the problem is to determine the feed position, F, which is required to provide an axially directed ray. The solution depends upon the rays position in the aperture plane.

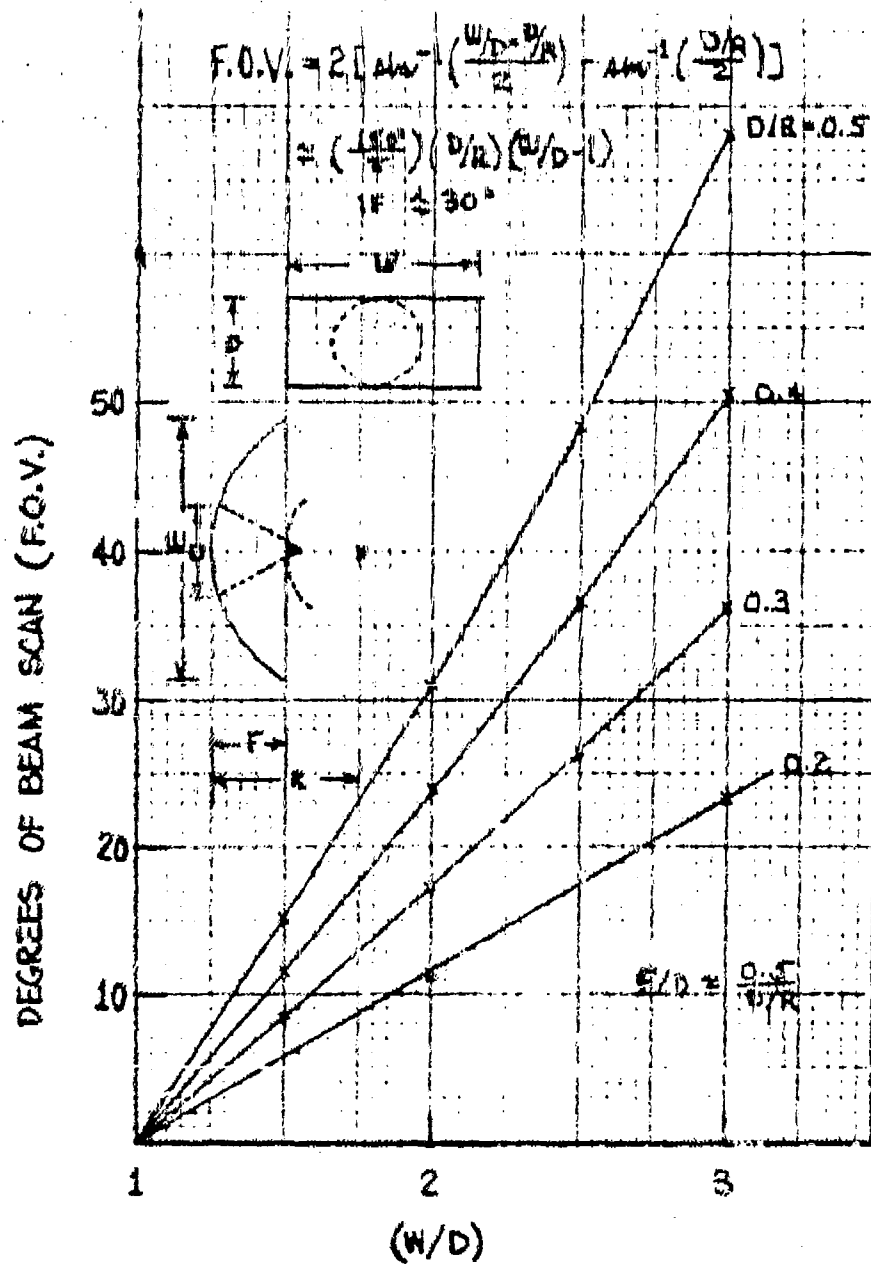


Figure 5-5. Symmetrical MBTA Field of View vs W/D at Specified Radii of Curvatures (R/D)

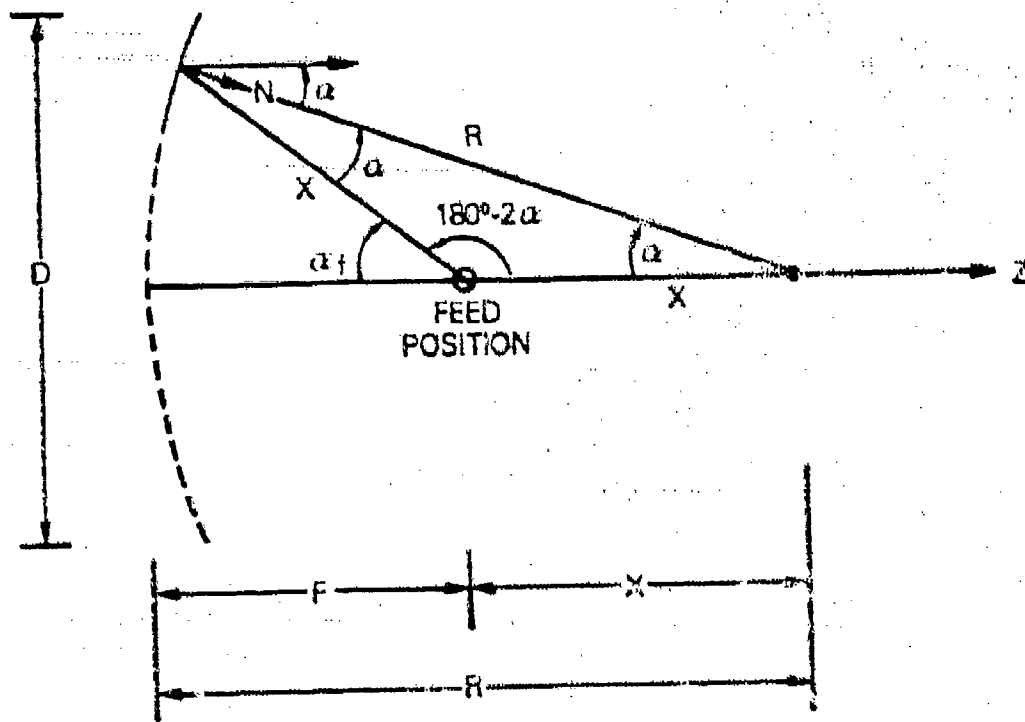


Figure 5-6. Spherical Reflector Focusing

The distance $x = f(\alpha)$ which provides a \hat{z} directed re-
flected wave from the spherical reflector is determined by

$$R^2 = 2x^2 [1 - \cos (180^\circ - 2\alpha)] = 2x^2 [1 + \cos (2\alpha)] \quad (5-10)$$

Thus,

$$\frac{x}{R} = \frac{1}{\sqrt{2[1 + \cos (2\alpha)]}} \quad (5-11)$$

or

$$\cos \alpha = \sqrt{1 - \frac{1}{4} \left(\frac{D}{R}\right)^2} \quad (5-12)$$

and

$$F = R - x \quad (5-13)$$

Solving yields

$\alpha = \alpha_E/2$	$\frac{F}{R}$	$\frac{F}{D}$
0°	0.5	0.5
10°	0.509	0.492
20°	0.531	0.468
30°	0.577	0.423

(5-14)

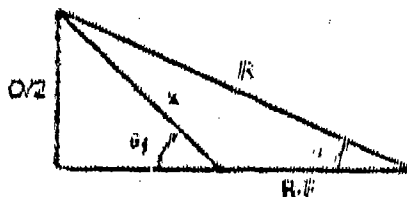
Thus, the best fit focal position for a feed in the spherical reflector is

$$\frac{F}{R} \leq 0.5 \quad (5-15)$$

where the exact number depends upon the particular geometry and feed edge taper. Thus, for the spherical reflector,

$$\frac{F}{D} = \frac{F/R}{D/R} = \left(\frac{0.5}{D/R} \right) \quad (5-16)$$

The feed illumination half angle $-\theta_2$ can be determined from



as

$$x^2 = R^2 + (R - F)^2 - 2R(R - F) \cos \alpha$$

For the MBTA,

$$F = \frac{D}{2} \tag{5-17a}$$

$$x^2 = R^2 \left[\frac{5}{4} - \cos \alpha \right] \tag{5-17b}$$

$$x = R \sqrt{\frac{5}{4} - \cos \alpha} \tag{5-17c}$$

and

$$\cos \alpha = \sqrt{1 - \frac{1}{4} \left(\frac{D}{R} \right)^2} \tag{5-17d}$$

Therefore,

$$\theta_f = \sin^{-1} \left(\frac{D/2}{x} \right) = \sin^{-1} \left(\frac{D/R}{2\sqrt{5/4 - \cos \alpha}} \right) \tag{5-18}$$

Since

$$\cos \alpha = 1 \left(\frac{D}{R} \right) \leq 0.5$$

$$\theta_f = \sin^{-1} \left(\frac{D}{R} \right)$$

then

$$2\theta_g = \left(\frac{360^\circ}{\pi}\right)\left(\frac{D}{R}\right) \quad (5-19)$$

is the required feed illumination angle for the aperture diameter, D . Figure 5-7 shows the feed illumination angle for the symmetrical MBTA as a function of D/R .

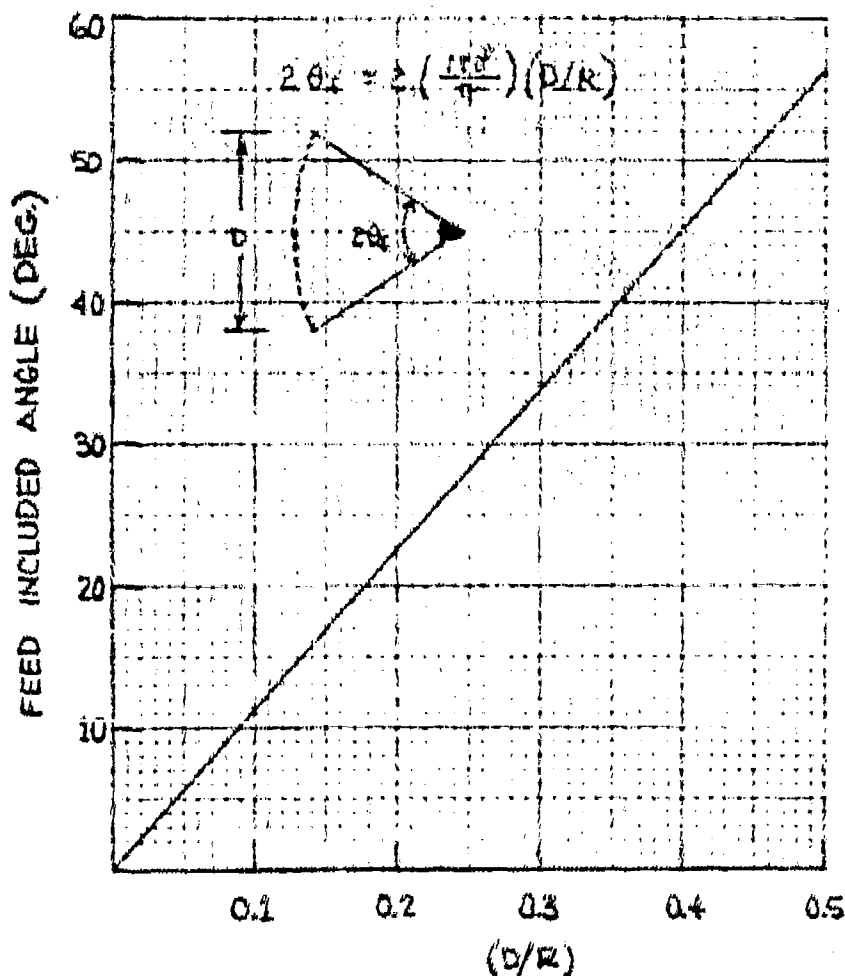
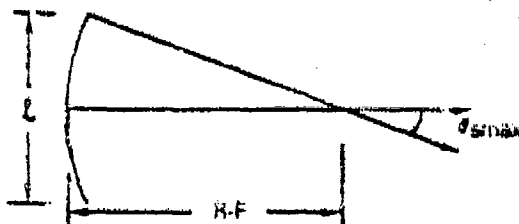


Figure 5-7. Symmetrical MBTA Feed Illumination Angle vs D/R

For the symmetrical MBTA, the projected length of the feed arc, i.e., the length of the window size in the feed house, is



where

$$L = 2(R - F) \sin \theta_{\max} \quad (5-20)$$

or

$$\frac{L}{D} = \frac{1}{D/R} \sin \left(\frac{FOV}{2} \right) \quad (5-21)$$

Figure 5-8 shows the projected length of the feed arc with a 27-ft aperture diameter as a function of the field of view for fixed D/R values.

5.4

OFFSET REFLECTOR FEED POINTING AND ILLUMINATION ANGLES

The feed illumination angles and pointing directions (direction cosines) for the offset MBTA geometry are shown in

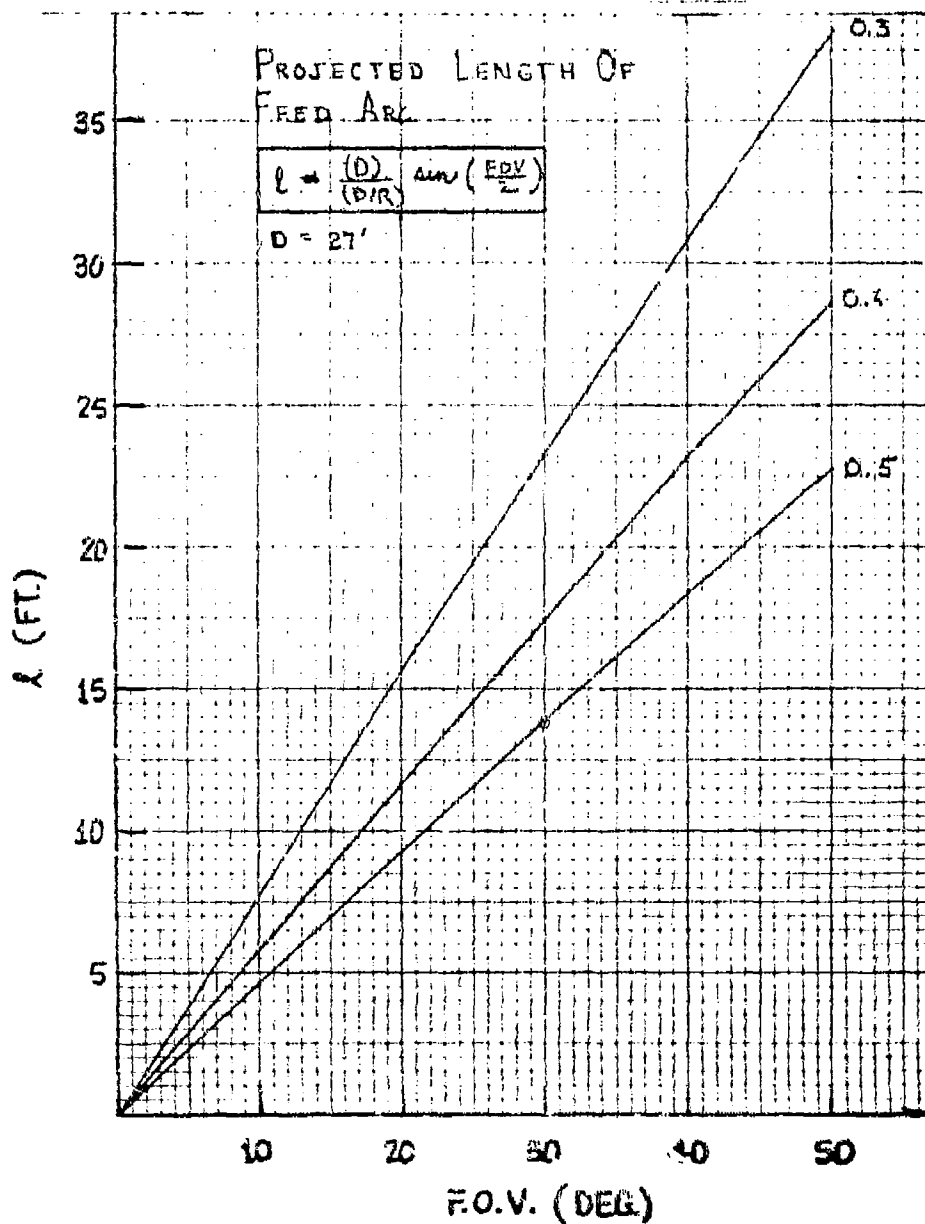


Figure 5-8. Projected Length of Feed Arc for
27-ft-Diameter Symmetrical MBTA

Figure 5-9. The angle to the bottom portion of the offset section is

$$\theta_1 = \tan^{-1} \left[\frac{d}{F - d^2/4F} \right] \quad (5-22)$$

and the angle to the top portion of the offset section is

$$\theta_2 = \tan^{-1} \left[\frac{d + D}{F - (d + D)^2/4F} \right] \quad (5-23)$$

Using the relationship

$$F = 0.5R$$

yields

$$\theta_1 = \tan^{-1} \left[\frac{\left(\frac{2}{D/R \times d/D} \right)}{\left(\frac{1}{D/R \times d/D} \right)^2 - 1} \right] \quad (5-24)$$

$$\theta_2 = \tan^{-1} \left\{ \frac{\left[\frac{2}{D/R \times (1 + d/D)} \right]}{\left[\frac{1}{D/R \times (1 + d/D)} \right]^2 - 1} \right\} \quad (5-25)$$

Note that $d/D = -0.5$ yields the symmetrical MBTA geometry. The feed illumination angle is defined as

$$\theta_{inc} = (\theta_2 - \theta_1) \quad (5-26)$$

as shown in Figure 5-10.

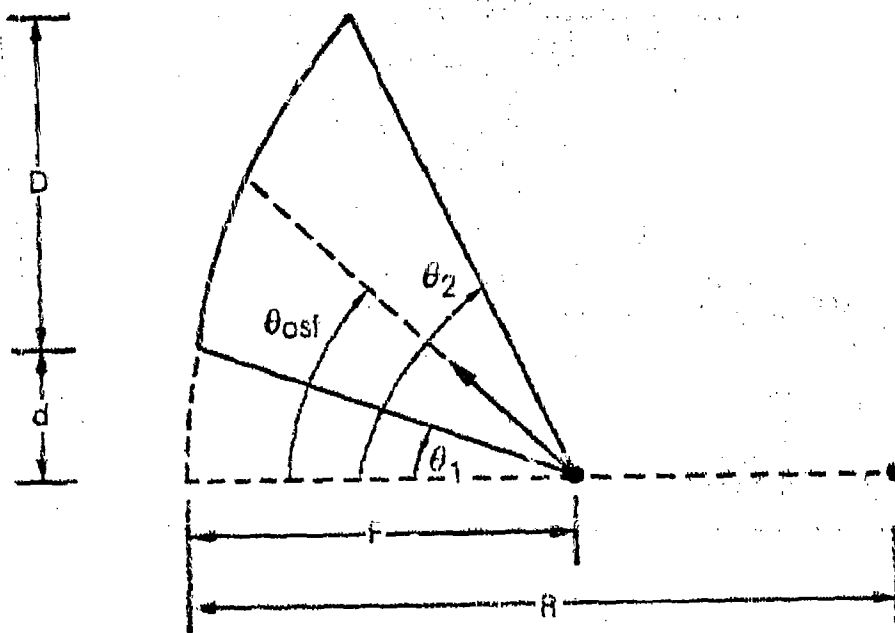


Figure 5-9. Offset MBTA Feed Illumination and Pointing Angles

The feed offset angle, θ_{osf} , can be defined in two different but useful ways. The first definition is

$$\theta_{osf} = \frac{(\theta_1 + \theta_2)}{2} \quad (5-27)$$

which is shown in Figure 5-11. Alternatively, θ_{osf} may be defined to the center of the projected aperture plane as shown in Figure 5-12. Then,

$$\theta_{osf} = \tan^{-1} \left[\frac{4 \left(\frac{F}{d + D/2} \right)}{4 \left(\frac{F}{d + D/2} \right)^2 - 1} \right] \quad (5-28)$$

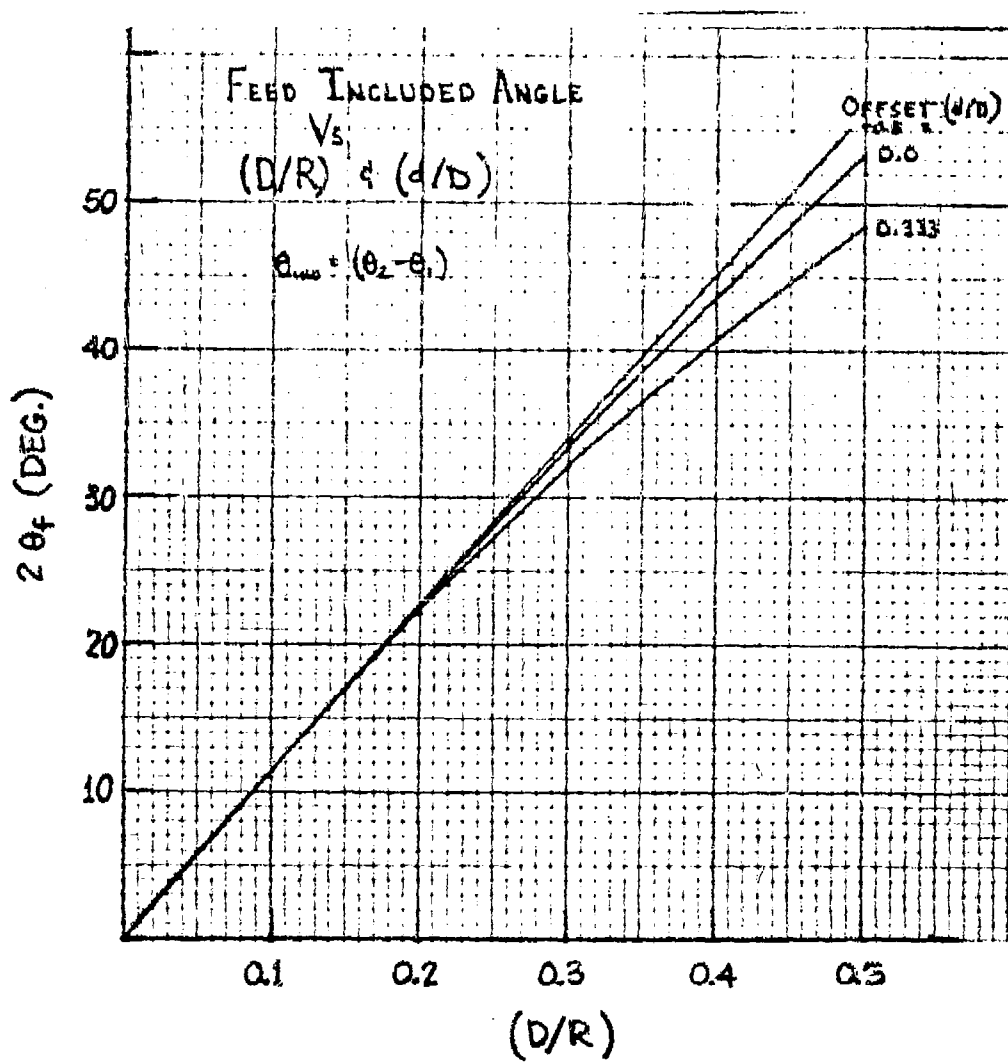


Figure 5-10. Feed Illumination Angle

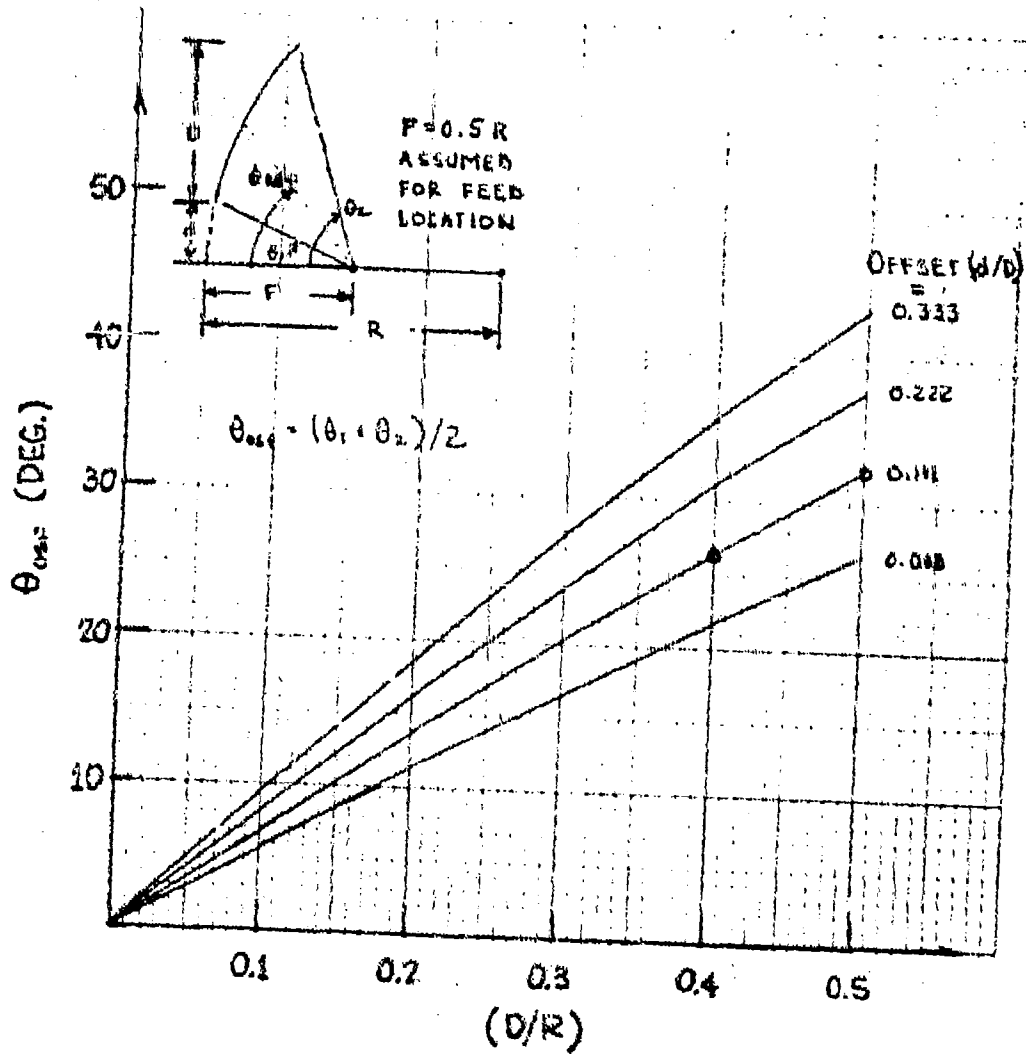


Figure 5-11. Feed Offset Angle
 $[\theta_{offset} = \theta_1 + (\theta_2 - \theta_1) / 2]$

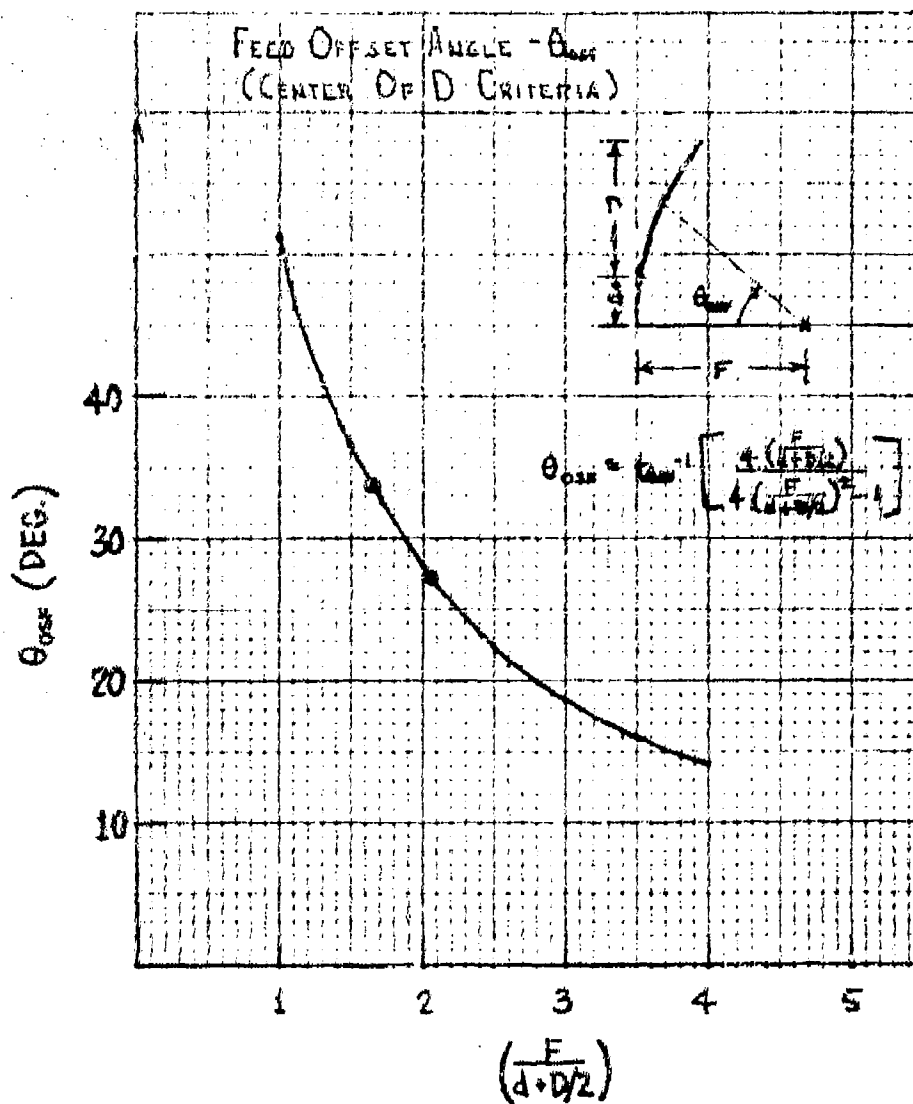
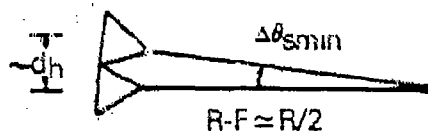


Figure 5-12. Feed Offset Angle (θ_{osf} + center of projected aperture)

The increased "space taper" attenuation to the top edge of the reflector suggests that an angle slightly larger than that given by equation (5-26) would yield optimum gain. The angle defined by equation (5-28) is closer to optimum although the differences are small.

5.5. FEED CHARACTERISTICS AND MINIMUM BEAM SPACINGS

The minimum spacing between adjacent beams in the front-fed MBTA configuration is determined by the diameter of the feed horn:



where

$$\Delta\theta_{smin} = \tan^{-1} \left(\frac{2d_h}{R} \right) = \frac{360^\circ}{\pi} \left(\frac{d_h}{R} \right) \quad (5-29)$$

which can be expressed as

$$\Delta\theta_{smin} = \frac{(360^\circ/\pi) (d_h/\lambda) (D/R)}{D/\lambda} \quad (5-30)$$

The required feed horn aperture diameter to wavelength ratio (d_h/λ) is determined from the desired edge of reflector illumination taper. For a simple circular aperture TE_{11} mode feed, the -10-dB E- and H-plane beamwidths are related to the feed horn diameter as follows:

$$\theta_{0E}(-10 \text{ dB}) = 100^\circ \left(\frac{\lambda}{d_h} \right) \quad (5-31a)$$

$$\theta_{0H}(-10 \text{ dB}) = 130^\circ \left(\frac{\lambda}{d_h} \right) \quad (5-31b)$$

For corrugated horn feeds,

$$\theta_0(-10 \text{ dB}) = 160^\circ \left(\frac{\lambda}{d_h} \right) \quad (5-32)$$

Assuming a -10-dB edge illumination with a corrugated feed horn and a feed illumination angle

$$2\theta_f = \left(\frac{360^\circ}{\pi} \right) \left(\frac{D}{R} \right) = 160^\circ \left(\frac{\lambda}{d_h} \right) \quad (5-33)$$

and given that the half-power beamwidth of the MBTA is

$$\theta_{HP} = \frac{70^\circ}{D/\lambda} \quad (5-34)$$

yields

$$\Delta\theta_{\text{min}} = 2.3 \theta_{HP} \quad (5-35)$$

Allowance for different feed types and extra structural material around the feed horn aperture yields

$$\Delta\theta_{\text{min}} = (2 - 4) \theta_{HP} \quad (5-36)$$

The minimum beam spacing for the front-fed MBTA as a function of D/λ with -10- and -20-dB edge tapers from a corrugated horn is shown in Figure 5-13.

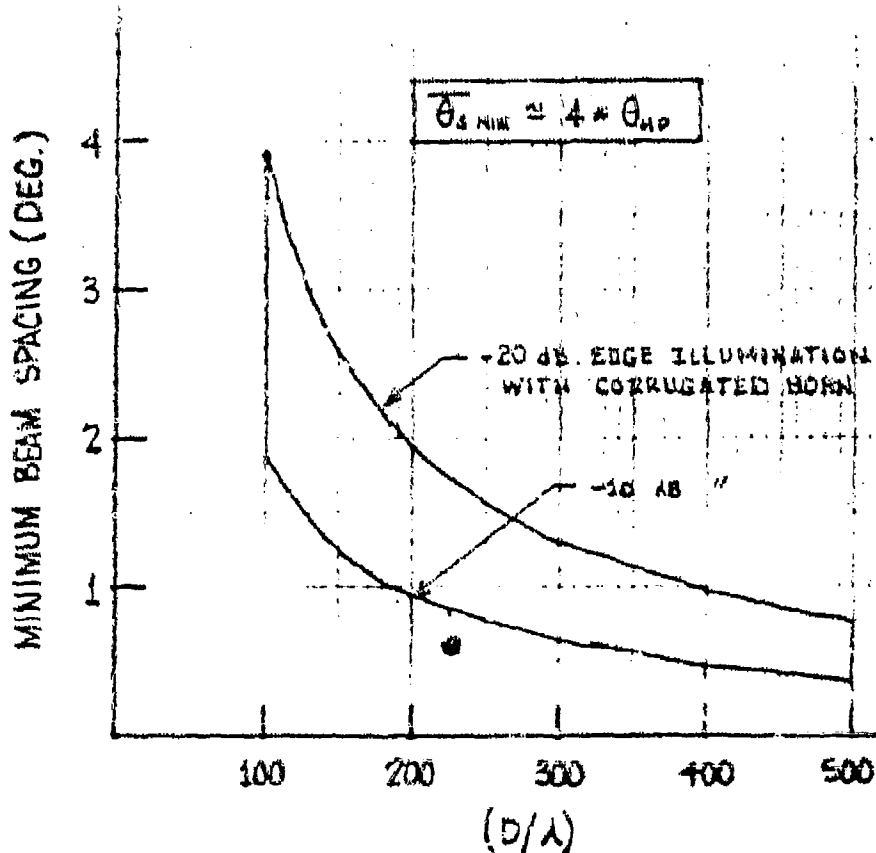


Figure 5-13. Minimum MBTA Beam Spacing

The measured complex radiation patterns of a well-designed corrugated horn are rotationally symmetric and provide an excellent feed illumination for the MBTA.^{11,12} The aperture diameter of the corrugated horn is typically oversized relative to that of a conventional conical horn for a specified feed illumination angle, but the minimum beam spacings achieved are acceptable for most applications.

Measured E- and H-plane radiation patterns for a corrugated feed horn at 3.95 GHz are shown in Figure 5-14. The Gaussian-shaped pattern has virtually no sidelobes, which helps

to minimize both coupling to adjacent beams and reflector spill-over. In addition, the aperture fields of a corrugated horn are sharply tapered. The low field strength at the edges of the aperture results in both exceptionally low coupling to adjacent feed horns and a lack of spurious radiating currents on the exterior walls of the feed horn.

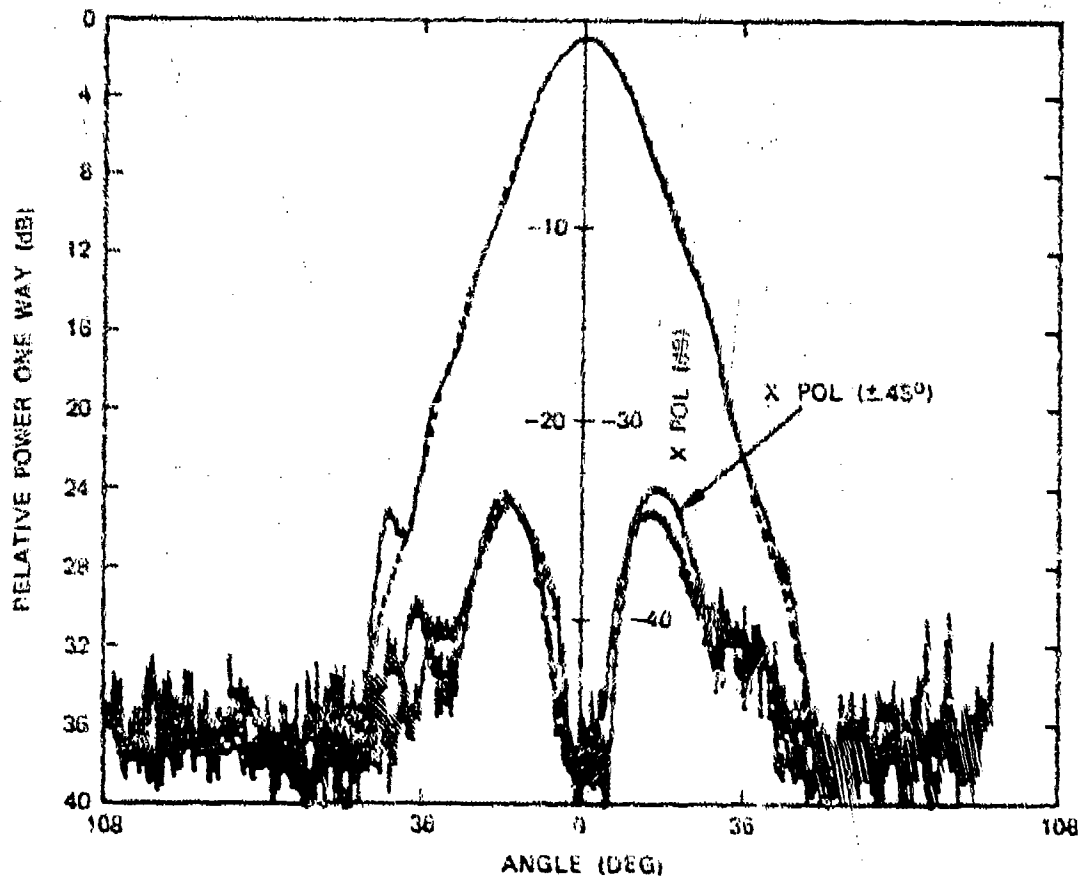


Figure 5-14. Corrugated Feed Horn Patterns

The electrical characteristics of the MBTA have been evaluated using conventional circular and square aperture feeds as well as corrugated horns. A convenient mathematical feed pattern description for the corrugated horn is

$$P(\theta) = \cos^2(x_1\theta) \quad (5-37)$$

or

$$P(\theta) = \cos^4(x_2\theta) \quad (5-38)$$

where x_1 and x_2 are chosen to provide the desired amplitude taper at a specified off-axis angle θ_0 . The edge of reflector amplitude taper in terms of parameter $(x\theta)$ is shown in Figure 5-15.

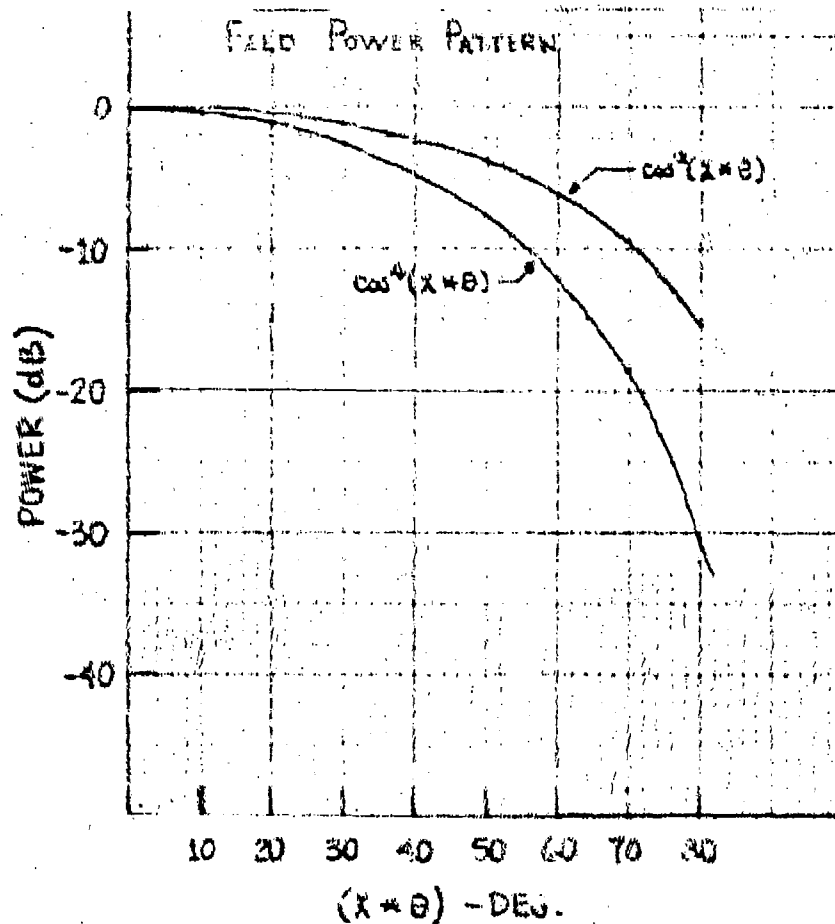


Figure 5-15. Feed Power Patterns
[$P(\theta) = \cos^{2n}(x\theta)$]

The -10-dB beamwidths of each of the patterns defined above are

$$\theta_{-10}^{(2)} = \left(\frac{2}{x_1} \right) \cos^{-1} (10^{-0.5}) = \frac{143.2^\circ}{x_1} \quad (5-39)$$

and

$$\theta_{-10}^{(4)} = \left(\frac{2}{x_2} \right) \cos^{-1} (10^{-0.25}) = \frac{111.6^\circ}{x_2} \quad (5-40)$$

Figures 5-16 and 5-17 are photographs of corrugated feed horns at 6 and 4 GHz.

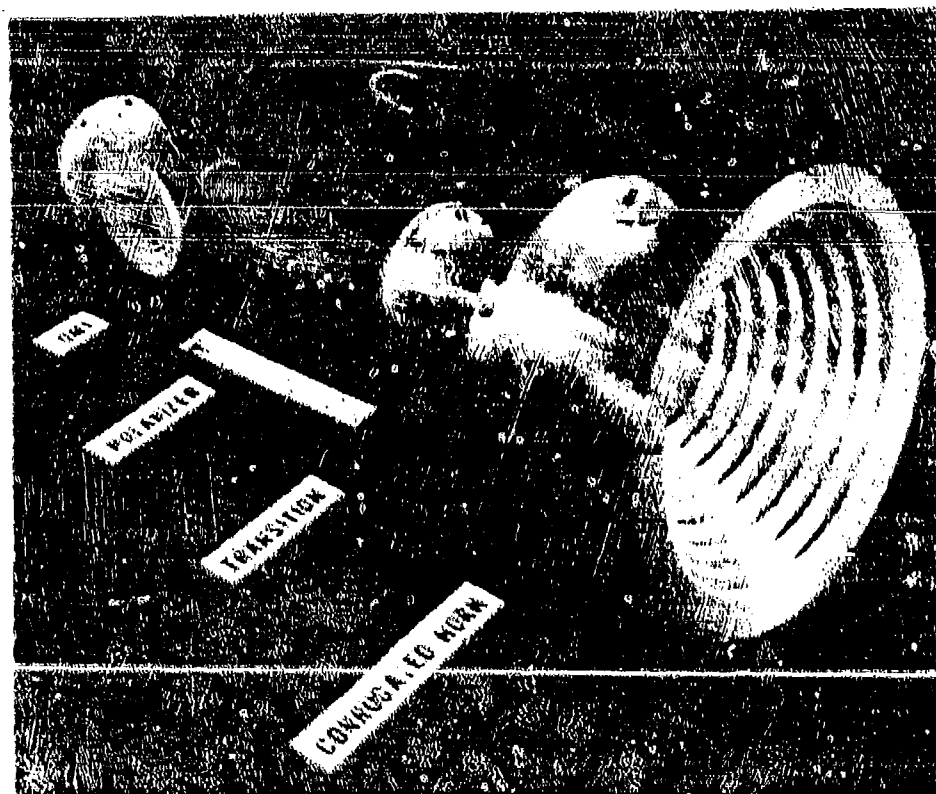


Figure 5-16. 6-GHz Corrugated Horn Antenna System.

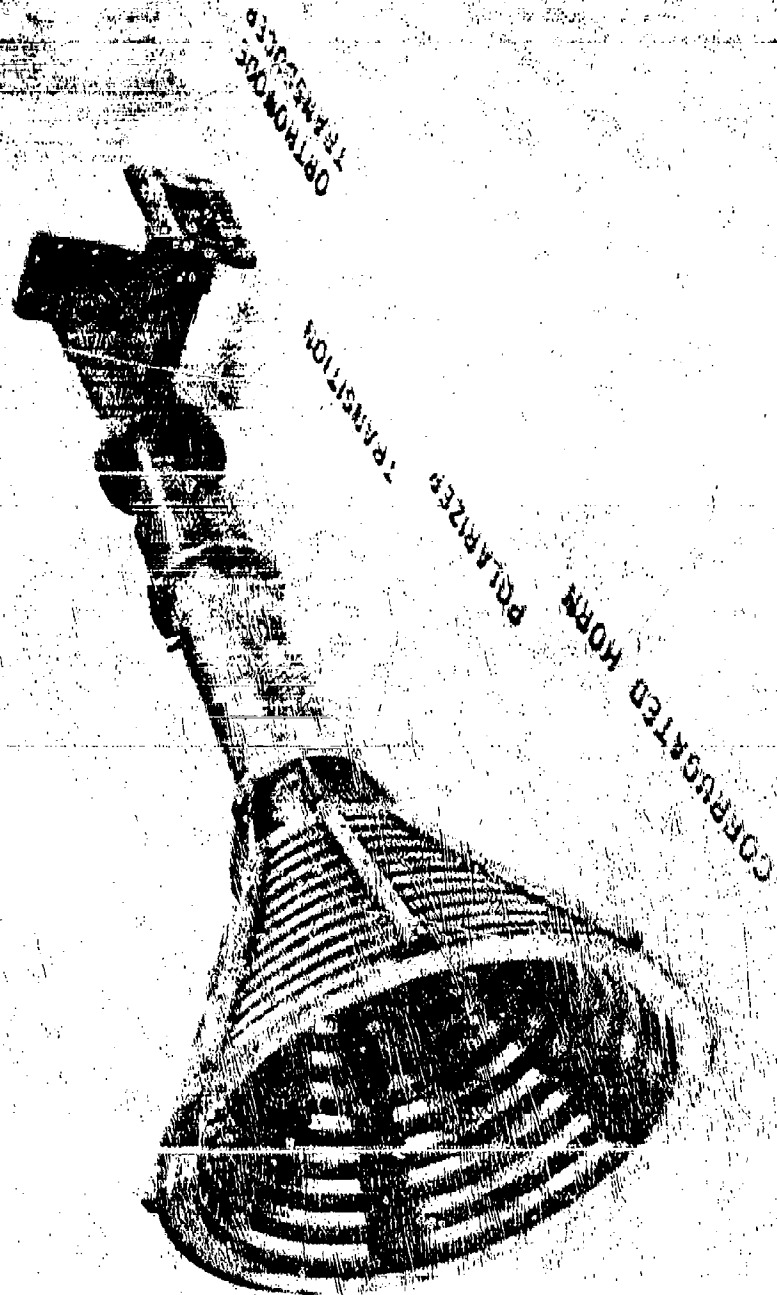


Figure 5-17. 4-GHz Lightweight Corrugated Horn

5.6 RMS SURFACE TOLERANCE LOSSES

The gain loss associated with MBTA surface tolerance, ϵ , measured normal to the reflecting surface is given by¹³

$$G_L = 10 \log_{10} \exp \left[- \frac{4\pi^2}{\lambda} \cos(\theta_{\text{osf}}) \right]^2 \quad (5-41)$$

This equation accounts for an effective tolerance in the beam direction of

$$\epsilon_{\text{eff}} = \epsilon \cos(\theta_{\text{osf}}) \quad (5-42)$$

Thus, with the same rms surface tolerance specification, the gain loss associated with an offset MBTA is reduced somewhat relative to that for a symmetrical MBTA configuration, as shown in Figure 5-18. The gain loss of an offset MBTA geometry ($\theta_{\text{osf}} = 25^\circ$) is shown in Figure 5-19 as a function of the rms surface tolerance, ϵ (mils), in each of the specified frequency bands.

Program MBTA-5 calculates the gain loss versus normalized surface tolerance (ϵ/λ) for fixed feed offset angles. Program MBTA-6 calculates the gain loss of the MBTA versus rms surface tolerance, ϵ (mils), for the fixed feed offset angles.

5.7 MATHEMATICAL EXPRESSION FOR ROTATED PARABOLIC SECTION

Figure 5-20 shows the coordinate system used to derive the mathematical expression $f(x,y,z) = 0$ or $f(u,v,w) = 0$ for the MBTA reflector surface.

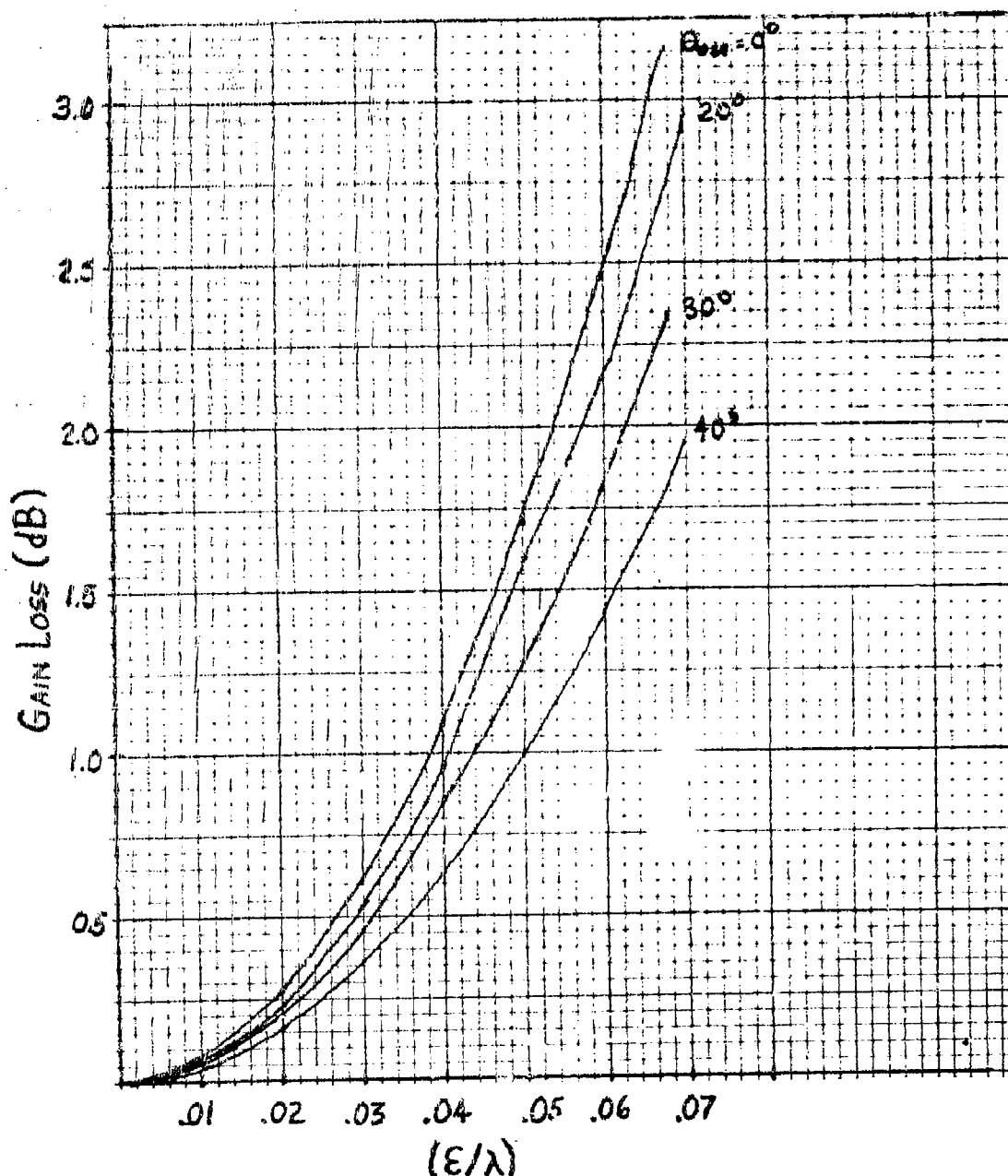


Figure 5-18. Gain Loss vs Normalized rms Surface Tolerance for Fixed Feed Offset Angles

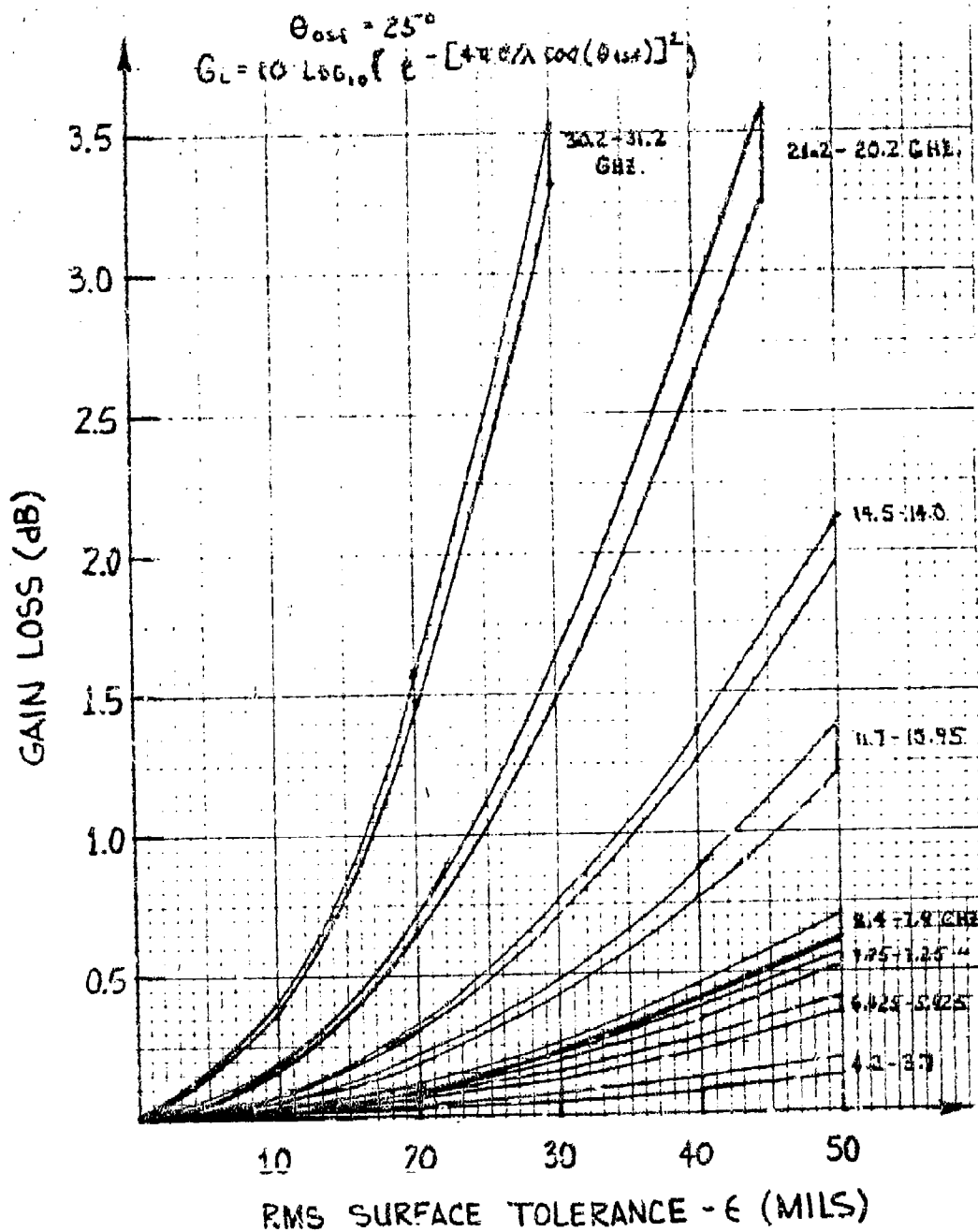


Figure 5-19. Gain Loss of Baseline MBTA vs rms Surface Tolerance

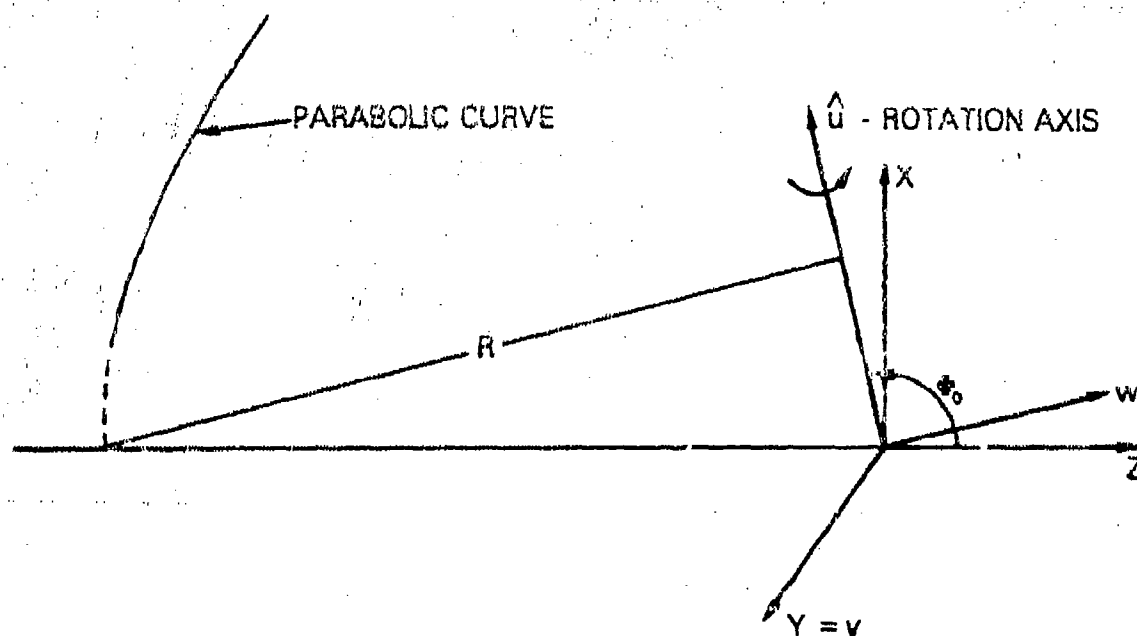


Figure 5-20. Geometry for MBTA Reflector Equation

The equation of the parabolic section in the $(x-z)$ plane is

$$x^2 - 4F \left(z + \frac{R}{\sin \phi_0} \right) = f(x, z) = 0. \quad (5-43)$$

The transformations between the (x, y, z) and (u, v, w) coordinates are

$$\begin{bmatrix} u \\ v \\ w \end{bmatrix} = \begin{bmatrix} \sin \phi_0 & 0 & \cos \phi_0 \\ 0 & 1 & 0 \\ -\cos \phi_0 & 0 & \sin \phi_0 \end{bmatrix} \begin{bmatrix} x \\ y \\ z \end{bmatrix} \quad (5-44)$$

and

$$\begin{bmatrix} x \\ y \\ z \end{bmatrix} = \begin{bmatrix} \sin \phi_0 & 0 & -\cos \phi_0 \\ 0 & 1 & 0 \\ \cos \phi_0 & 0 & \sin \phi_0 \end{bmatrix} \begin{bmatrix} v \\ v \\ w \end{bmatrix} \quad (5-45)$$

The equation of the parabolic section expressed in the (u-w) plane becomes

$$\begin{aligned} & (u \sin \phi_0 - w \cos \phi_0)^2 \\ & - 4F(u \cos \phi_0 + w \sin \phi_0) - \frac{4FR}{\sin \phi_0} = 0 \end{aligned} \quad (5-46)$$

The equation of the rotated curve is generally

$$v^2 + w^2 - (rr)^2 = 0 \quad (5-47)$$

where rr is the radius from the \hat{u} axis [determined from equation (5-46)]. Note that

$$rr = w \quad (5-48)$$

when $v = 0$. When $\phi_0 = 90^\circ$, the equations are somewhat simplified to result in

$$u^2 - 4Fw - 4FR = 0 \quad (5-49)$$

$$v^2 + w^2 - \left[\frac{u^2 - 4FR}{4F} \right]^2 = 0 \quad (5-50)$$

Then, since $(x, y, z) = (u, v, w)$,

$$f(x, y, z) = x^4 - 8x^2(FR) - 16F^2(y^2 + z^2) + 16F^2R^2 = 0 \quad (5-51)$$

Note that the rotated curve description is not equivalent to a general second-order polynomial.

For the general angle ϕ_0 case, the equation of the reflector surface is obtained by using the same derivation procedure, but the resulting equation

$$f(x, y, z) \equiv 0 \text{ (general } \phi_0) \quad (5-52)$$

is cumbersome.

5.8 APERTURE PLANE SPHERICAL ABERRATION PHASE ERRORS

Inspection of the aperture plane phase error characteristics provided a great deal of insight into the RF characteristics of the MBTA. In fact, the antenna system focal position (F/R) as a function of offset and D/R is most economically optimized by inspecting the aperture plane phase error magnitudes for various F/R positions.

First consider the path length differences over the aperture of a symmetrical spherical section shown in Figure 5-21. The path length from the feed, F, to the center of the reflector and back to the center of the aperture plane is a reference:

$$L_0 = \overline{FO} + \overline{OF} = 2F \quad (5-53)$$

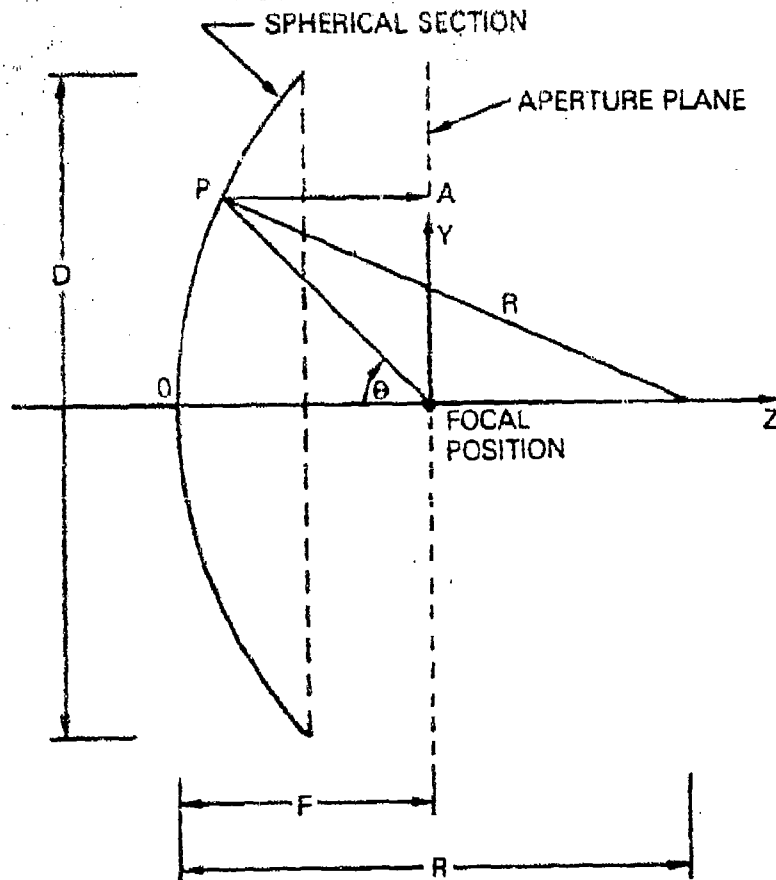


Figure 5-21. Symmetrical Spherical Reflector Geometry

The path length to an arbitrary position P on the spherical reflector and back to the aperture plane at A is

$$l(y) = \overline{FP} + \overline{PA} \quad (5-54)$$

It is assumed that reflected rays arrive normal to the aperture plane, which is very nearly exact for the range of geometrical parameters considered in this study. The equation of the reflector is

$$y^2 + [z - (R - F)]^2 = R^2 \quad (5-55)$$

That

$$\overline{FP} = \sqrt{y^2 + y^2} \quad (5-56)$$

$$\overline{PA} = |z| \quad (5-57)$$

$$z = (R - F) - \sqrt{R^2 - y^2} \quad (5-58)$$

Thus,

$$\begin{aligned} \overline{FP} &= \sqrt{y^2 + (R - F)^2 + (R^2 - y^2) - 2(R - F) \sqrt{R^2 - y^2}} \\ &= \sqrt{R^2 + (R - F)^2 - 2(R - F) \sqrt{R^2 - y^2}} \end{aligned} \quad (5-59)$$

and

$$\overline{PA} = \sqrt{R^2 - y^2} - (R - F) \quad (5-60)$$

The phase path length difference between the general and central rays, converted into degrees, is

$$\begin{aligned} \psi(0, y, 0) &= 360^\circ \frac{[\rho(y) - \rho_0]}{\lambda} \\ &= 360^\circ \left(\frac{D/\lambda}{D/R} \right) \left\{ \sqrt{1 + \left(1 - \frac{F}{R}\right)^2} - 2 \left(1 - \frac{F}{R}\right) \sqrt{1 - \left(\frac{Y}{D} \frac{D}{R}\right)^2} \right. \\ &\quad \left. + \sqrt{1 - \left(\frac{Y}{D} \frac{D}{R}\right)^2} - \left(1 + \frac{F}{R}\right) \right\} \end{aligned} \quad (5-61)$$

For the offset MBTA geometry shown in Figure 5-22 with $\phi_0 = 90^\circ$, the path length to the approximate center $(x_0, 0, 0)$ of the projected aperture plane,

$$l_0 = \overline{FC} + \overline{CA}_1 \quad (5-62)$$

is taken as a reference. The equation of the parabolic curve section described in a coordinate system centered at F is

$$x^2 - 4F(z + F) = 0 \quad (5-63)$$

$$\overline{FC} = \sqrt{x^2 + z^2} = \sqrt{x^2 + \left(\frac{x^2}{4F} - F\right)^2} \quad (5-64)$$

and

$$\overline{CA}_1 = |z| = \left(F - \frac{x^2}{4F}\right) \quad (5-65)$$

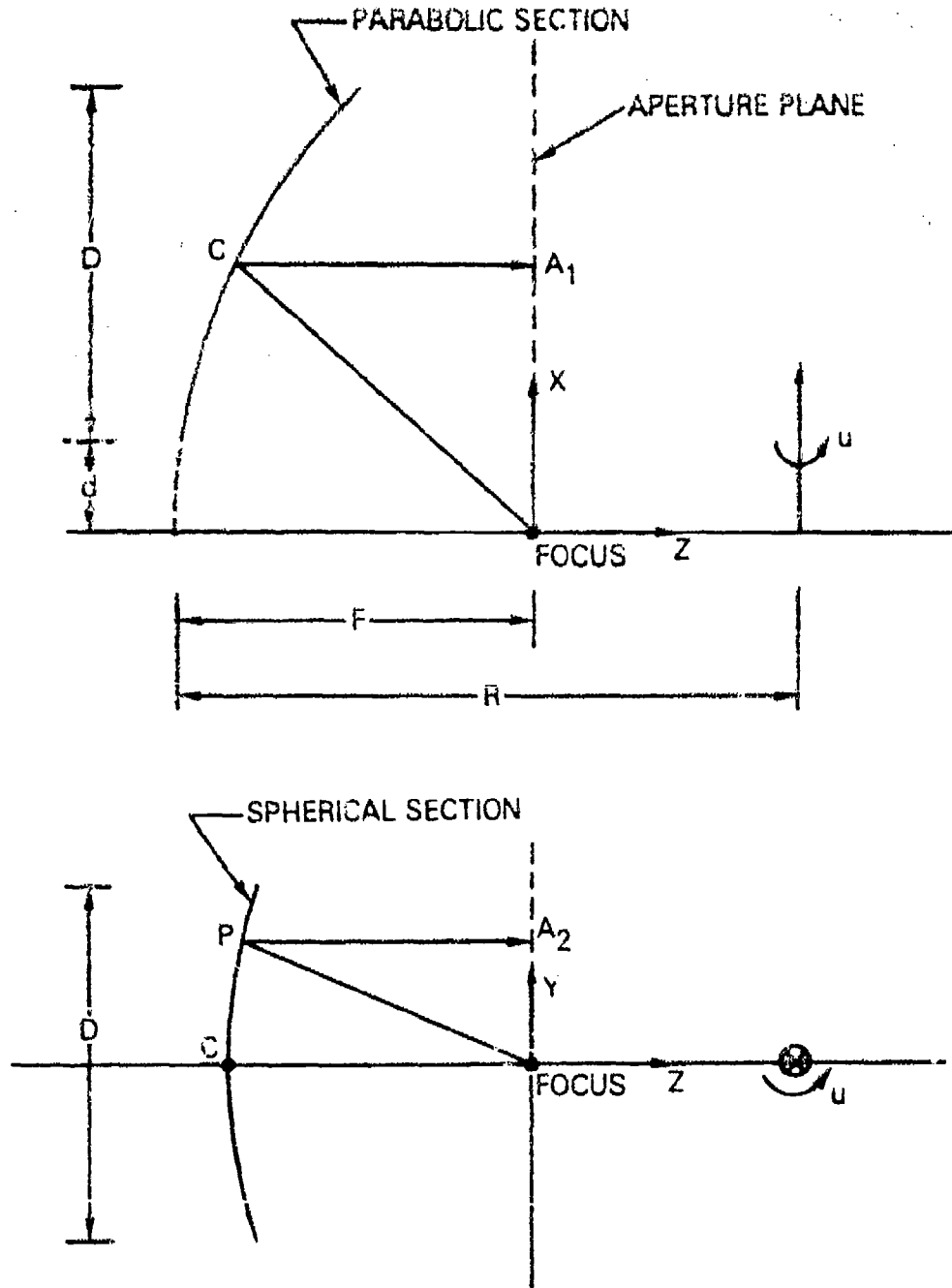


Figure 5-22. Offset MBTA Reflector Geometry ($\phi_0 = 90^\circ$)

which yields

$$z_0(x_0, 0, 0) = \sqrt{x_0^2 + \left(\frac{x_0^2}{4F} - F\right)^2} + \left(F - \frac{x_0^2}{4F}\right) \quad (5-68)$$

At the center of the aperture,

$$z_0 = \left(d + \frac{D}{2}\right) \quad (5-67)$$

The equation of the surface is determined from

$$y^2 + [z - (R - F)]^2 = R^2(x) \quad (5-68)$$

$$R(x) = \left(R - \frac{x^2}{4F}\right) \quad (5-69)$$

Solving yields

$$z(x, y) = (R - F) - \sqrt{R^2(x) - y^2} \quad (5-70)$$

which is the equation of the surface expressed in aperture plane coordinates.

The path length to an arbitrary aperture plane location is

$$L(x, y) = \overline{FP} + \overline{PA_2} \quad (5-71)$$

$$\overline{FP} = \sqrt{x^2 + y^2 + z^2} \quad (5-72)$$

and

$$\overline{PA_2} = |z| \quad (5-73)$$

THAZP

$$\begin{aligned}
 \Delta(x, y, 0) = & \sqrt{x^2 + y^2 + \left\{ (R - F) - \sqrt{\left[R - \left(\frac{x^2}{4F} \right) \right]^2 - y^2} \right\}^2} \\
 & + \sqrt{\left[R - \frac{x^2}{4F} \right]^2 - y^2} - (R - F)
 \end{aligned} \quad (5-74)$$

The path length difference between the aperture reference position $(x_c, 0, 0)$ and an arbitrary aperture location $(x, y, 0)$ converted to degrees becomes

$$\begin{aligned}
 \phi(x, y, 0) = & 360 \cdot \left(\frac{D}{\lambda} \right) \left[\frac{\Delta(x, y, 0) - \Delta(x_c, 0, 0)}{D} \right] \\
 = & 360 \cdot \left(\frac{D}{\lambda} \right) \\
 & \times \left\{ \sqrt{\left(\frac{x}{D} \right)^2 + \left(\frac{y}{D} \right)^2} + \left\{ \frac{R}{D} \left(1 - \frac{F}{R} \right) - \sqrt{\left[\frac{R}{D} - \frac{(x/D)^2}{4F/R \times R/D} \right]^2 - \left(\frac{y}{D} \right)^2} \right\}^2 \right. \\
 & + \sqrt{\left[\frac{R}{D} - \frac{(x_c/D)^2}{4F/R \times R/D} \right]^2 - \left(\frac{y}{D} \right)^2} - \left(\frac{R}{D} \right) \\
 & \left. - \sqrt{\left(\frac{x_c}{D} \right)^2 + \left[\frac{(x_c/D)^2}{4F/R \times R/D} - \frac{F}{R} \right]^2} - \frac{(x_c/D)^2}{4F/R \times R/D} \right\}
 \end{aligned} \quad (5-75)$$

For a generalized feed location (x_F, y_F, z_F) measured from the parabolic focus,

$$\overline{FC} = \sqrt{(x - x_F)^2 + (z - z_F)^2} \quad (5-76)$$

and

$$\overline{FP} = \sqrt{(x - x_F)^2 + (y - y_F)^2 + (z - z_F)^2} \quad (5-77)$$

and the generalized expression for the aperture plane phase error becomes

$$W(x,y,z) = 100 \cdot \left(\frac{D}{\lambda}\right)$$

$$\begin{aligned} & \cdot \sqrt{\left(\frac{x - x_c}{D}\right)^2 + \left(\frac{y - y_c}{D}\right)^2 + \left[\frac{z}{D} \left(1 - \frac{z}{2D}\right) - \sqrt{\left(\frac{z}{D} - \frac{(x/D)^2 + (y/D)^2}{4F/R \times R/D}\right)}\right]^2} - \left(\frac{z}{D}\right)^2 - \frac{z}{D} \\ & \cdot \sqrt{\left[\frac{R}{D} - \frac{(x/D)^2 + (y/D)^2}{4F/R \times R/D}\right]^2} - \left(\frac{z}{D}\right)^2 - \left(\frac{z}{D}\right) \\ & - \sqrt{\left(\frac{x_c - x_c}{D}\right)^2 + \left[\frac{(x_c/D)^2 + (y_c/D)^2}{4F/R \times R/D} - \frac{F/R}{R/D} - \frac{z_c}{D}\right]^2} + \frac{(x_c/D)^2}{4F/R \times R/D} \end{aligned} \quad (5-78)$$

Program MBTA-7 calculates the aperture plane phase error using this expression. Results for the symmetrical MBTA geometry can be obtained by using

$$x_c = 0 \quad (5-79)$$

and

$$x_c = \frac{D}{2} \quad (5-80)$$

gives the center of the offset projected aperture.

Figure 5-23 shows the calculated aperture plane phase errors for a symmetrical MBTA geometry with different focusing parameters (F/R). Since the feed horn would place a specified amplitude distribution over the aperture plane, an F/R ratio between 0.495 and 0.5 would minimize the amplitude weighted phase errors over the aperture plane. Figure 5-24 represents the calculated peak gain of the same symmetrical MBTA (from COMSAT's GAP Program¹⁴) as a function of F/R with a specified feed illumination, P(6). As expected from the phase error diagrams, peak

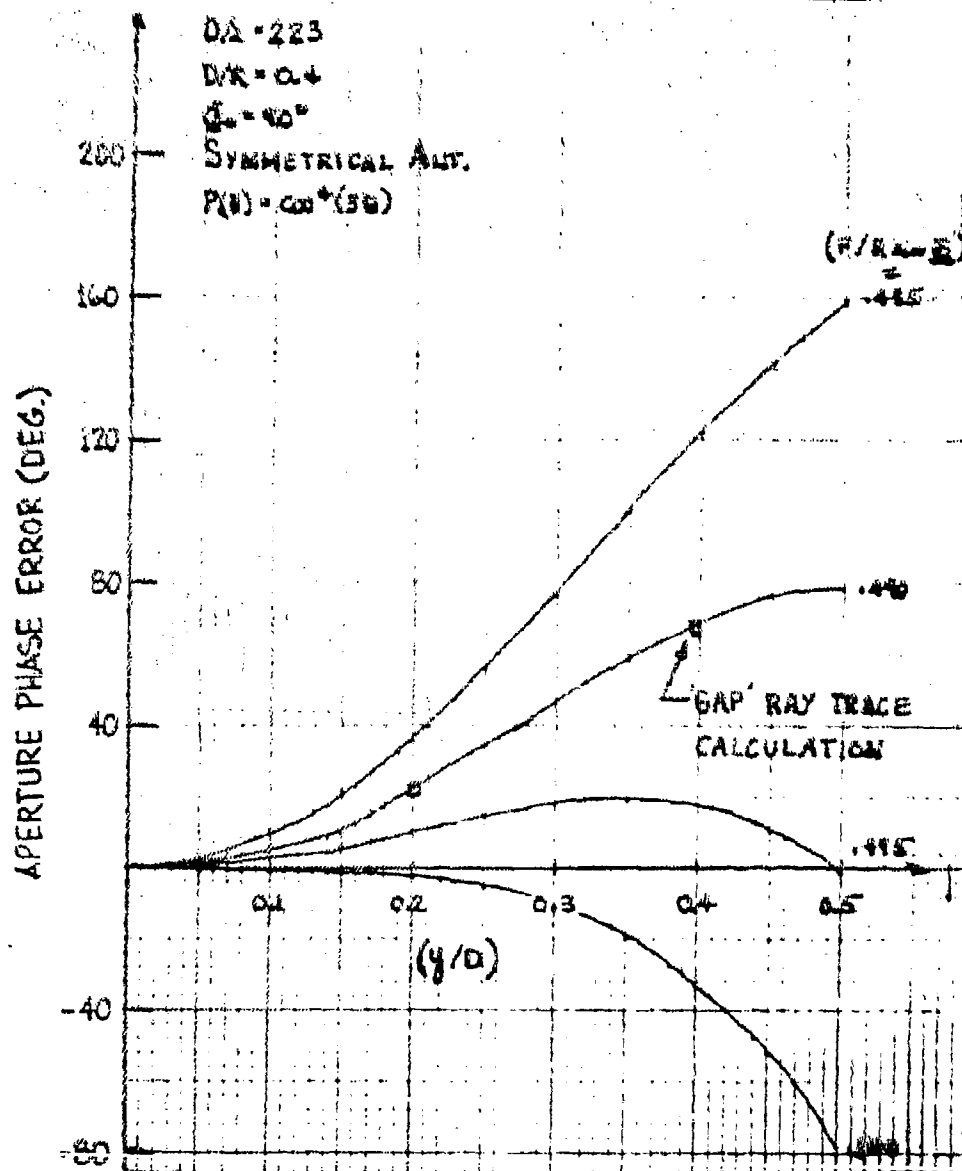


Figure 5-23. Symmetrical MBTA ($D/R = 0.4$) Aperture Plane Phase Errors

gain occurs for F/R between 0.495 and 0.5. Figure 5-23 also compares the aperture plane phase error calculated using COMSAT's GAP Program and equation (5-73).

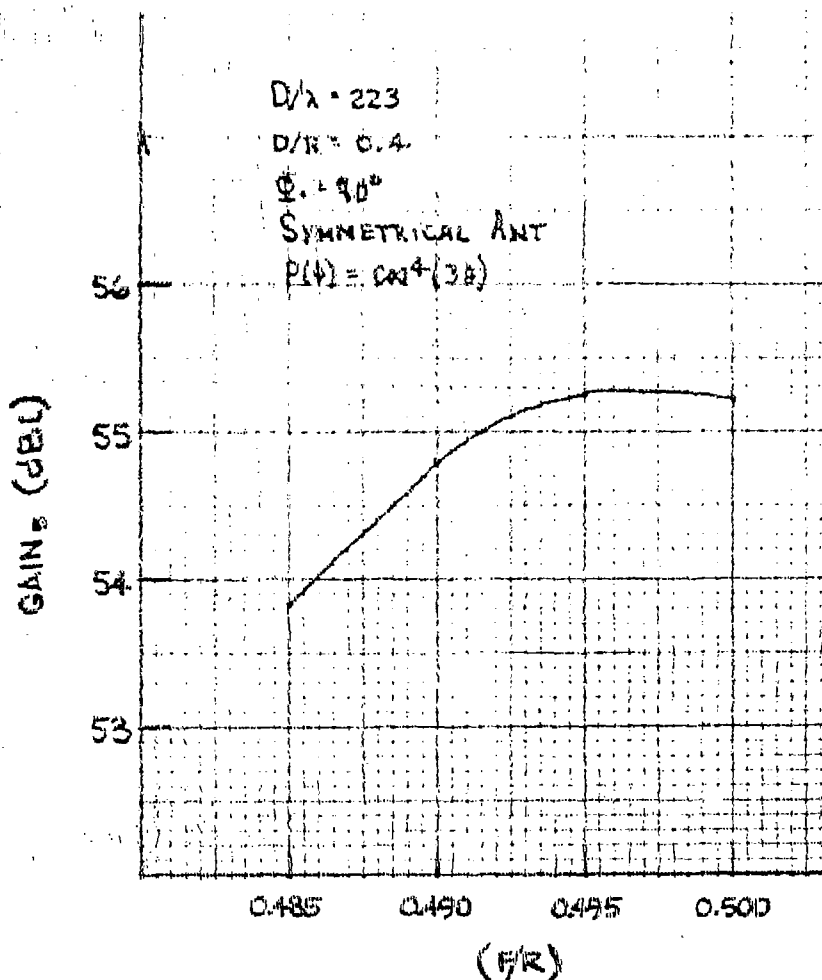


Figure 5-24. Symmetrical MBTA ($D/R = 0.4$)
Gain vs F/R

Figure 5-25 shows the center of aperture plane phase errors for an offset MBTA geometry ($D/R = 0.4$, $d/D = 1/9 = 11$ percent) as a function of the feed position (F/R). Again, when feed amplitude weightings are considered, the maximum gain

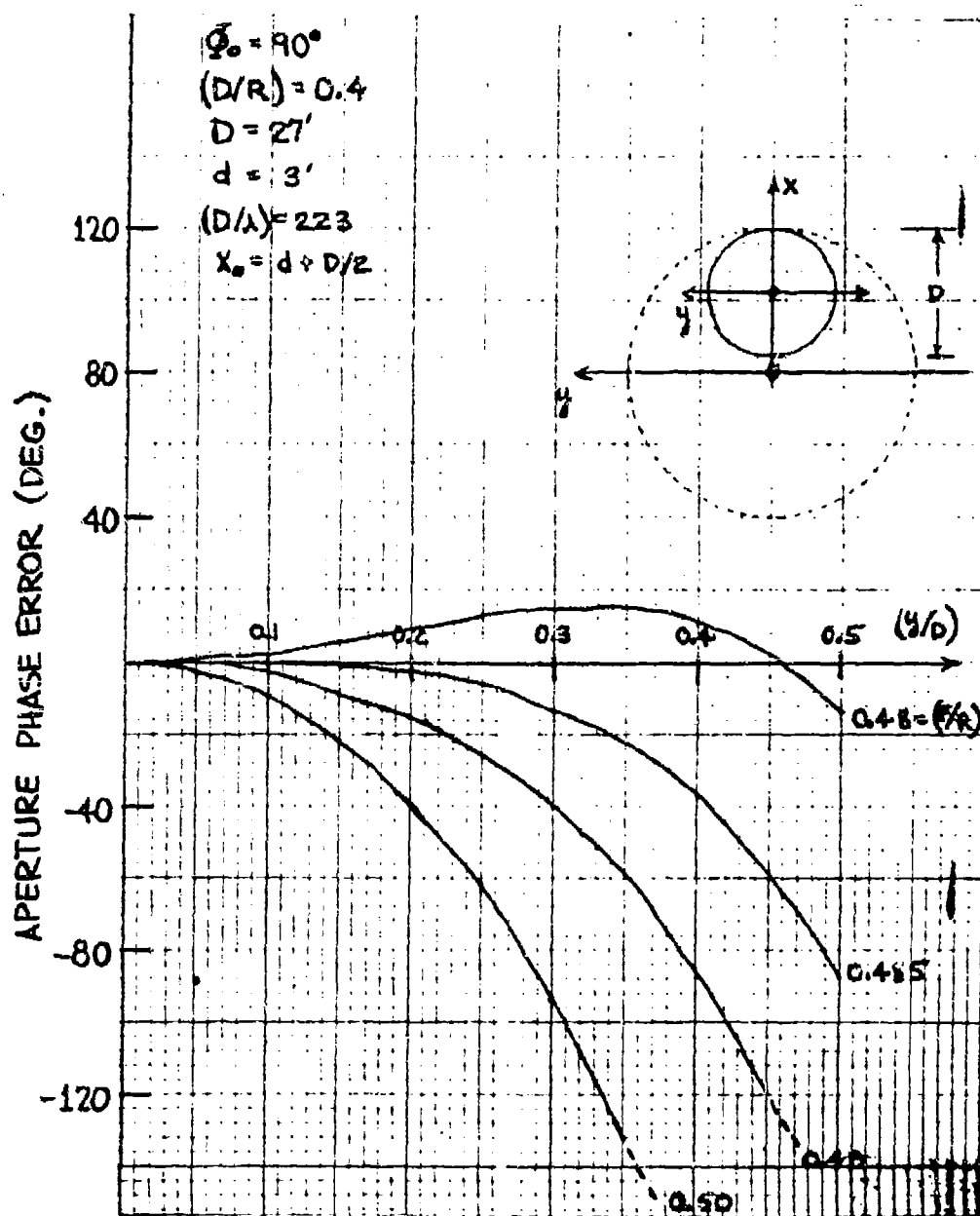


Figure 5-25. Offset (11%) MBTA ($D/R = 0.4$) Aperture Plane Phase Errors

(minimum weighted phase error) is expected for $0.48 \leq F/R \leq 0.485$. In Figure 5-26, which shows the calculated gain of an offset MBTA with a specified feed amplitude taper, the middle curve ($D/R = 0.4$) indicates a maximum gain at $F/R = 0.483$. The generating axis angle, ϕ_0 , is slightly different for the antenna geometries ($\phi_0 = 90 + 93.5^\circ$) compared in these two figures. The conclusion, which will also be demonstrated later, is that small changes in ϕ_0 do not markedly affect the aperture plane phase error distribution.

Figure 5-27 shows the center of aperture plane phase errors when the offset distance, d , is increased to 6 ft ($d/D = 22$ percent). A comparison of Figures 5-25 and 5-27 indicates that the F/R optimization is quite sensitive to the offset distance. Figure 5-28 shows the center of aperture plane phase errors for the $D/R = 0.3$ geometry. Comparison with Figure 5-25 again demonstrates that the feed positioning (F/R) can be optimized on the basis of a relatively simple aperture phase error expression.

The full aperture plane phase errors for the baseline MBTA configuration are shown in Figure 5-29. The phase error distribution is symmetrical in y , but the offset configuration gives rise to an asymmetrical distribution in x (except at the center of the aperture, since the feed is at the focus of the parabolic section). The effective radius of the curvature is changing as a function of x [equation (5-69)] over the aperture. The path lengths to positions on the top portion of the aperture are shorter than those to the bottom portion of the aperture. Hence, the parabolic plane pattern tends to be scanned somewhat in the $(-\theta)$ direction.

The aperture plane phase errors can be directly scaled by D/λ . As the frequency increases the edge of aperture phase errors increase in magnitude until voltage contributions from the edge of the aperture actually cause a decrease in peak gain.

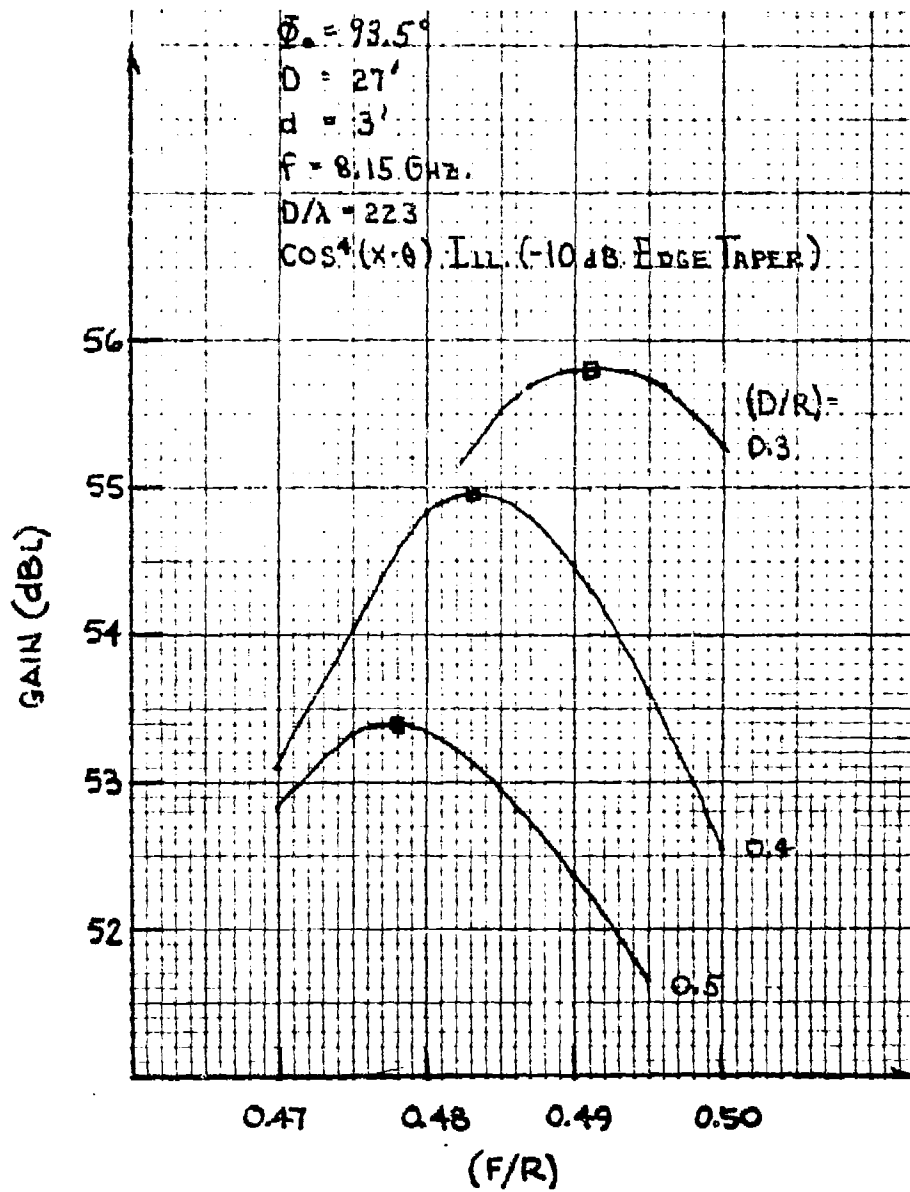


Figure 5-26. Offset (11%) MBTA Aperture
Illumination Gain vs (F/R)

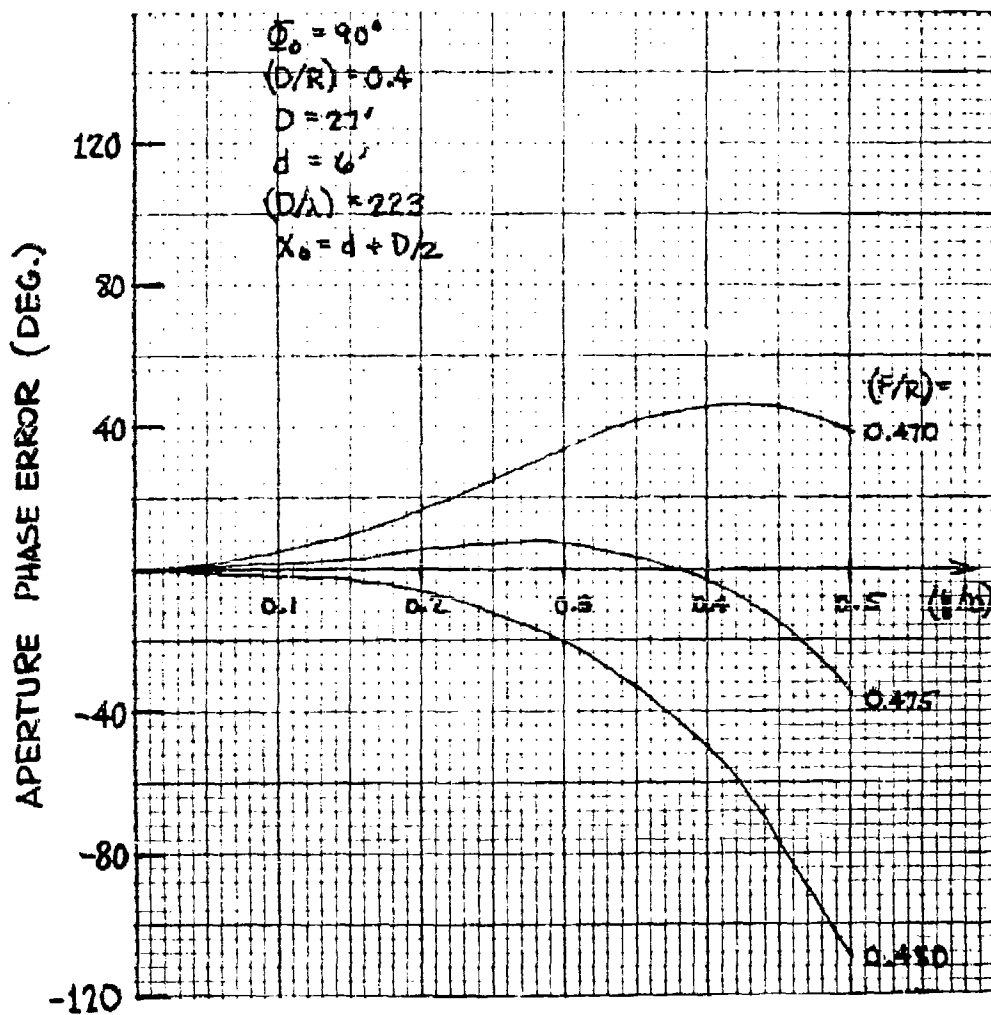


Figure 5-27. Offset (22%) META ($D/R = 0.4$) Aperture Plane Phase Errors

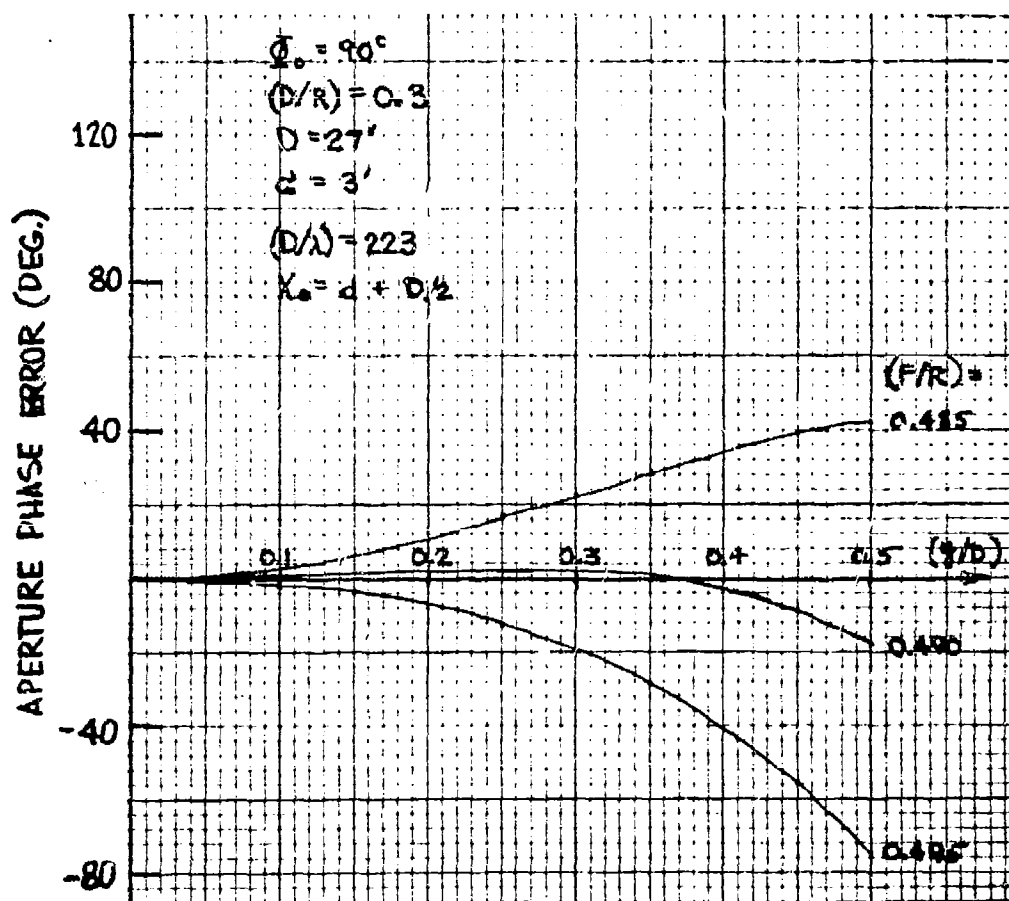


Figure 5-28. Offset (11%) MBTA ($D/R = 0.3$) Aperture Plane Phase Errors

APERTURE PHASE ERRORS

$\phi_0 = 90^\circ$ $F/R = 0.483$
 $D = 21'$ $D/R = 0.4$
 $H = 3'$
 $D/\lambda = 223$

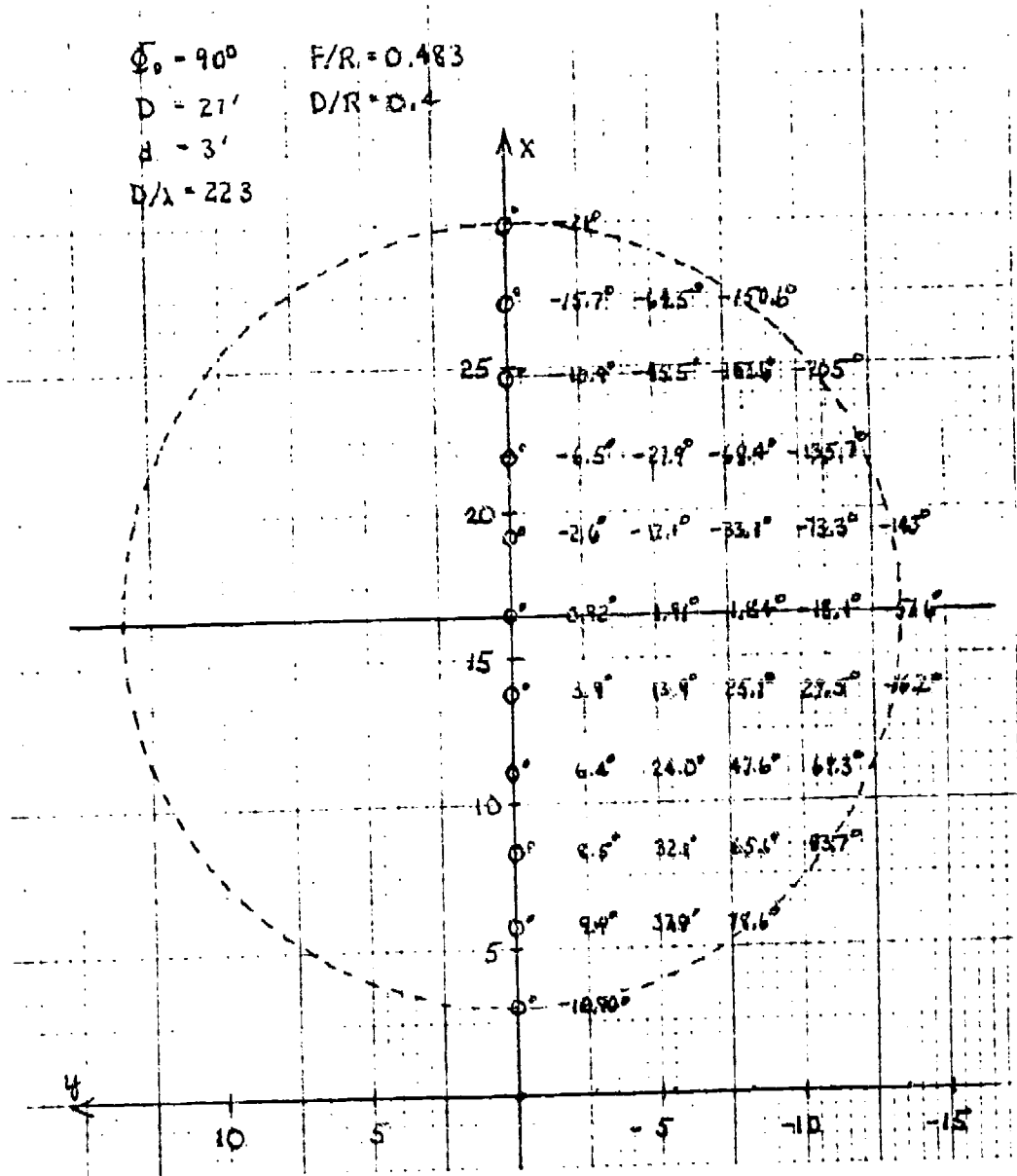


Figure 5-29. Offset (11%) MBTA ($D/R = 0.4$) Aperture Plane Phase Errors with Optimum Focusing

Maximum gain is then achieved by illuminating only an inner portion of the physical aperture, D . Figure 5-30 shows the calculated gain of the baseline offset MBTA geometry at 30 GHz as a function of the -10 -dB feed beamwidth. Maximum gain occurs when the -10 -dB feed illumination angle is $2 \times 13^\circ = 26^\circ$. If the full physical aperture is illuminated with a feed illumination angle of $2 \times 21^\circ = 42^\circ$, the peak gain is reduced by 0.9 dB.

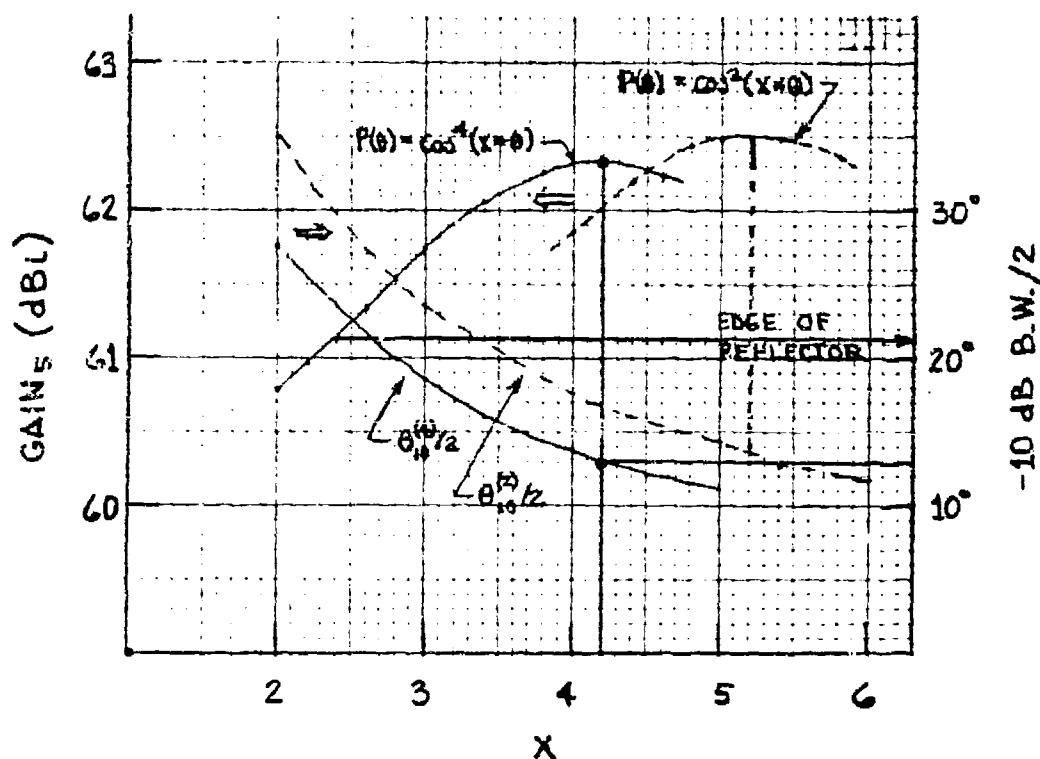


Figure 5-30. Gain vs Feed Illumination Angle at 30 GHz (baseline MBTA)

The full aperture plane phase error distribution for a $D/R = 0.5$ offset geometry is shown in Figure 5-31. Peak gain occurs when the -10 -dB feed illumination angle projects to the

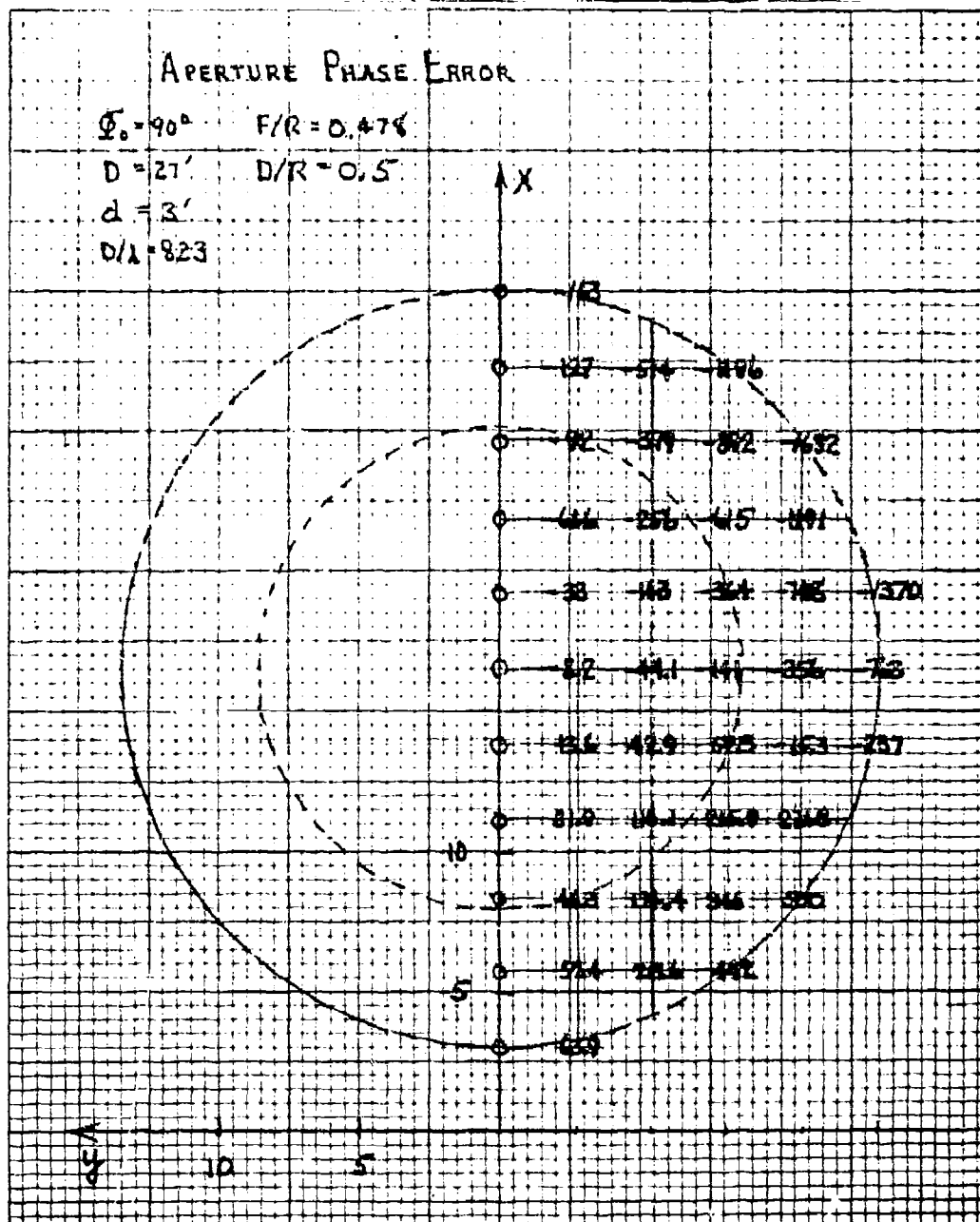


Figure 5-31. Offset (11%) MBTA ($D/R = 0.5$) Aperture Plane Phase Errors with Optimum Focusing

dashed circular aperture shown in the figure. The average edge of aperture phase error on the dashed optimum aperture is $\approx 120^\circ$. The peak gain versus the -10 -dB beamwidth is plotted in Figure 5-32. If the full aperture is illuminated, the peak gain is reduced by 1.4 dB.

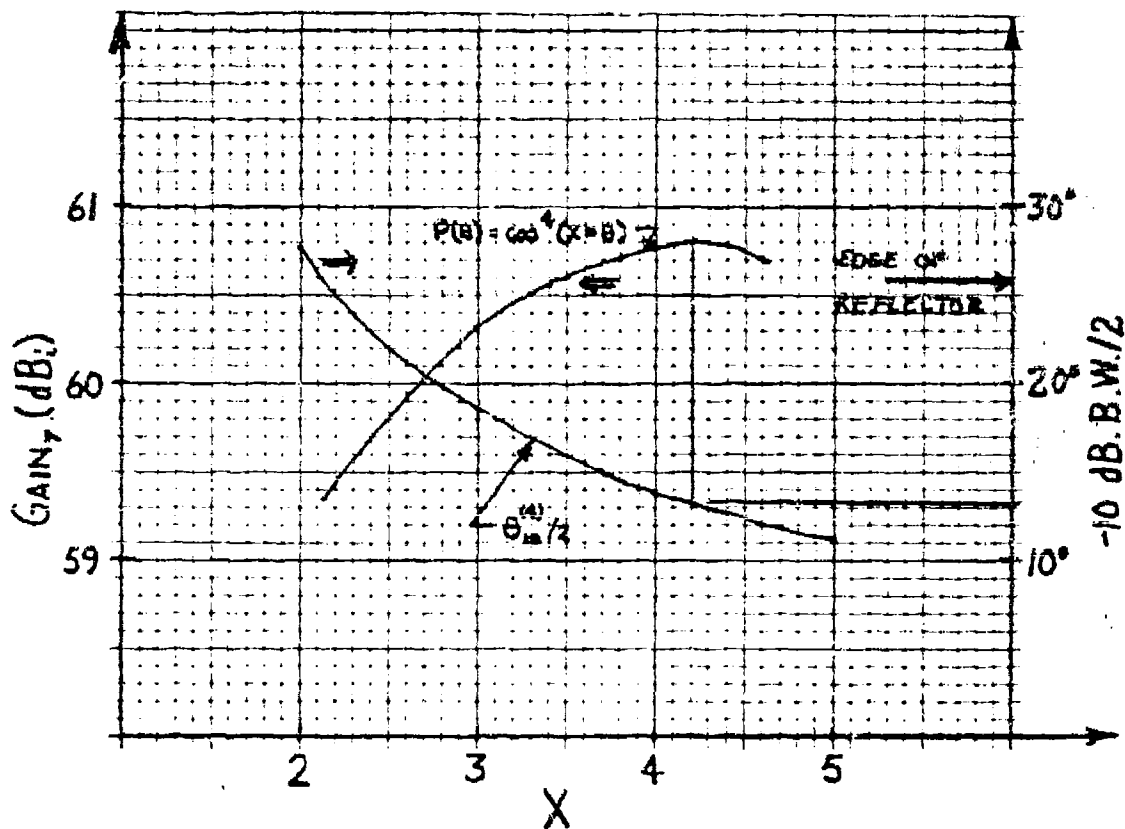


Figure 5-32. Gain vs Feed Illumination Angle at 30 GHz
($D/R = 0.5$ geometry)

The aperture plane phase error expression for an MBTA with a general ϕ_0 angle is derived by using the geometry shown in

Figure 5-33. The description of the central path length ray ϕ_0 is identical to the previous results derived for the special case of $\phi_0 = 90^\circ$ [equation (5-66)]. The equation of the rotated parabolic section is

$$v^2 + w^2 - R^2(u) = 0 \quad (5-81)$$

or

$$y^2 + \left[-\cos \phi_0 x + \sin \phi_0 \left(z - \frac{R}{\sin \phi_0 - F} \right) \right]^2 = R^2(u) \quad (5-82)$$

and

$$R(u) = w \quad (5-83)$$

(when $v = y = 0$) is obtained from the equation for the parabolic section:

$$x^2 - 4F(z + F) = 0 \quad (5-84)$$

or

$$(\sin \phi_0 u - \cos \phi_0 w)^2 - 4F(\cos \phi_0 u + \sin \phi_0 w + F) = 0 \quad (5-85)$$

as the general equation of the MBTA rotated surface.

where z is found from the reflector surface equation $f(x,y,z) = 0$.

5.9 PARABOLIC PLANE SCANNED BEAM FEED POSITIONS AND SCAN GAIN LOSS

The aperture plane phase error expressions derived in the previous subsection can be utilized to determine to a first order the feed positions $(x_{fs}, 0, z_{fs})$ required to scan the parabolic plane pattern. The sum of the phase errors at the top and bottom of the aperture plane in the $y = 0$ (parabolic) plane is equated to zero:

$$\text{Err}(x_{fs}, z_{fs}) = \psi(x = d + D, 0, 0) + \psi(x = d, 0, 0) = 0 \quad (5-87)$$

A family of (x_{fs}, z_{fs}) feed positions which satisfy this equation is obtained. Each set is associated with an absolute phase error difference across the aperture plane that corresponds to the scanned beam location. If the aperture phase errors at the top and bottom of the aperture are $\Delta\psi$ and $-\Delta\psi$, respectively, the scanned beam position is

$$\theta_s = \tan^{-1} \left(\frac{\Delta\psi}{180^\circ \times D/\lambda} \right) \quad (5-88)$$

Since the expression for $\Delta\psi$ is directly proportional to D/λ , the scanned beam location is independent of frequency.

For small scan angles,

$$\Delta\psi \text{ (deg)} = \theta_s \text{ (deg)} \approx \frac{D}{\lambda} \quad (5-89)$$

Program MBTA-9 calculates the scanned beam feed positions and associated scan angle.

Figure 5-34 shows the locus of scanned beam feed positions calculated by using equation (5-87) and the corresponding parabolic plane scan angle for the baseline MBTA geometry. The calculated scan beam feed positions were then verified using COMSAT's GAP program. The full aperture integration (GAP) includes the effects of feed amplitude weighting. The peak gain as a function of parabolic plane beam scan is shown in Figure 5-35 for the baseline MBTA. Note that the scan gain loss characteristic is not symmetrical as a result of differential feed amplitude weighting effects.

The space taper amplitude varies differentially with scan. The maximum loss at $\pm 2.5^\circ$ is 2 dB at $D/\lambda = 223$.

5.10 SPHERICAL GENERATING CURVE MBTA

For applications which require a considerable amount of scan (or beamwidths of scan) in a plane perpendicular to the geosynchronous arc, the use of a spherical generating curve for the MBTA may prove useful. The reflector system can then be designed to have a constant gain for a specified out-of-plane scan requirement. This constant gain will be lower than the gain achieved with the parabolic generating curve when there is no scan. In addition, it requires the reflector diameter to be increased to provide a full aperture illumination with the maximum scan angles. The geometry of an offset MBTA using a spherical generating section with a generating axis angle, $\phi_0 = 90^\circ$ is shown in Figure 5-36.

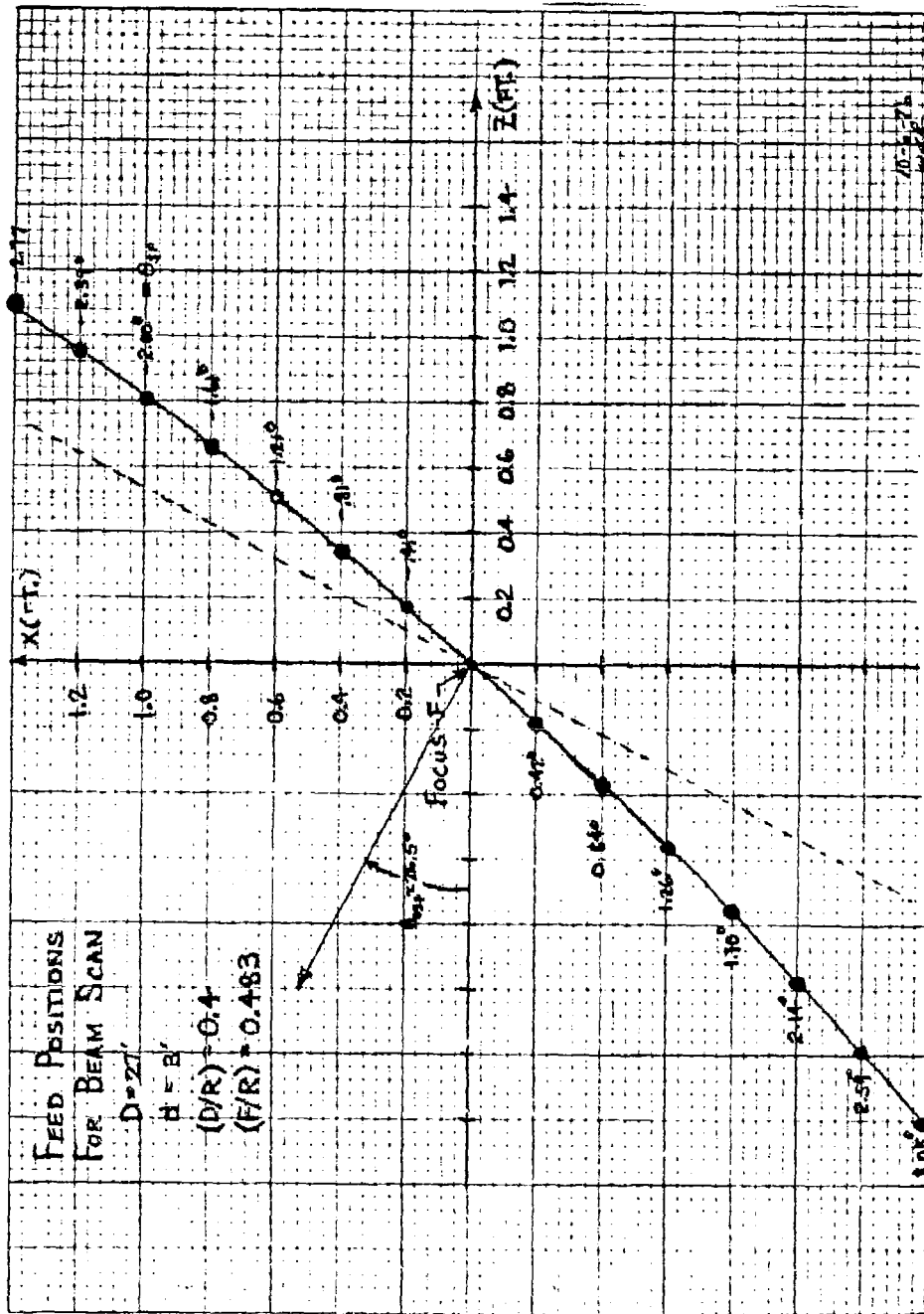


Figure 5-34. Scanned Beam Feed Positions for Baseline MBTA

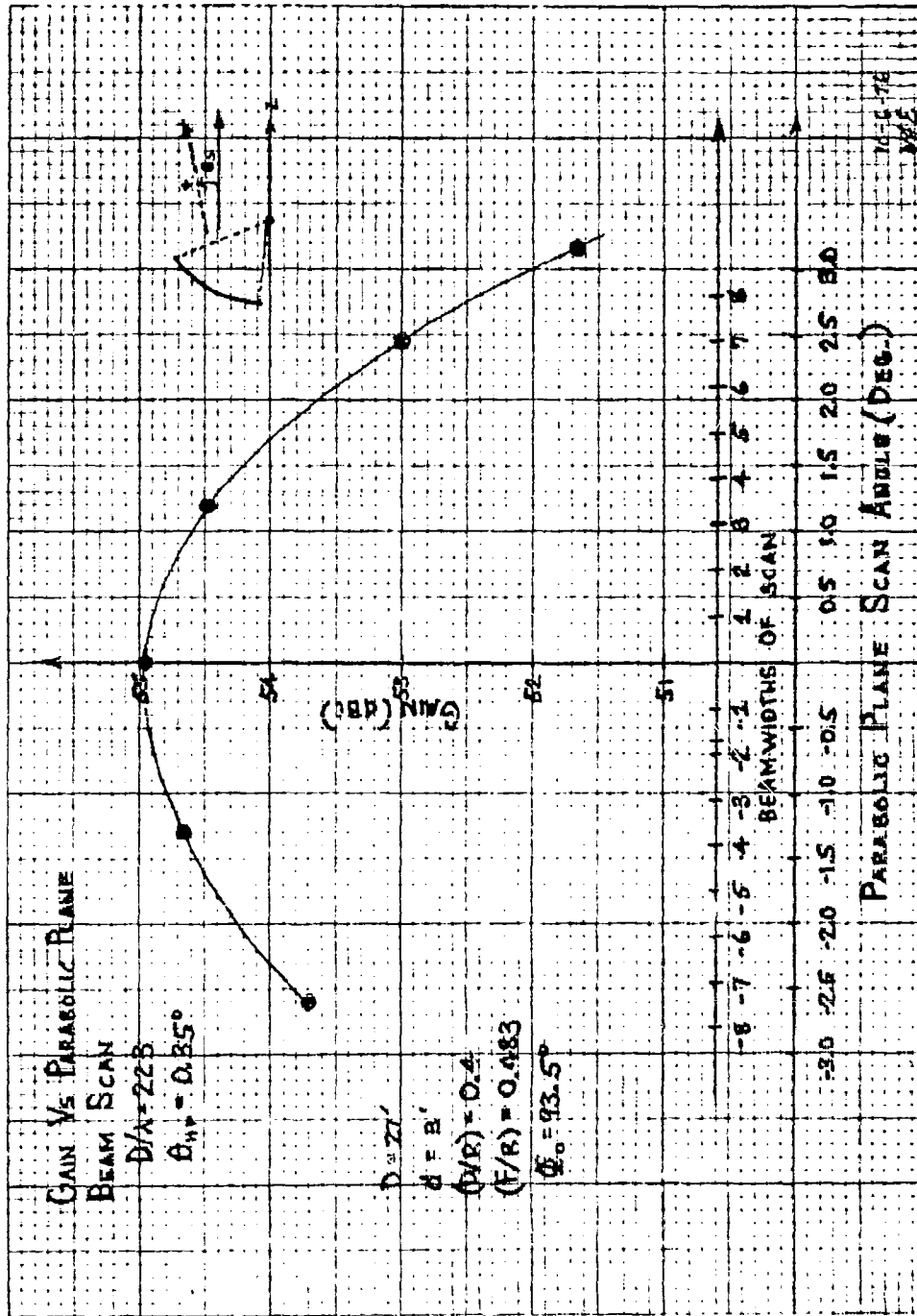


Figure 5-35. Parabolic Plane Beam Scan Loss for Baseline MBTA at 8.15 GHz

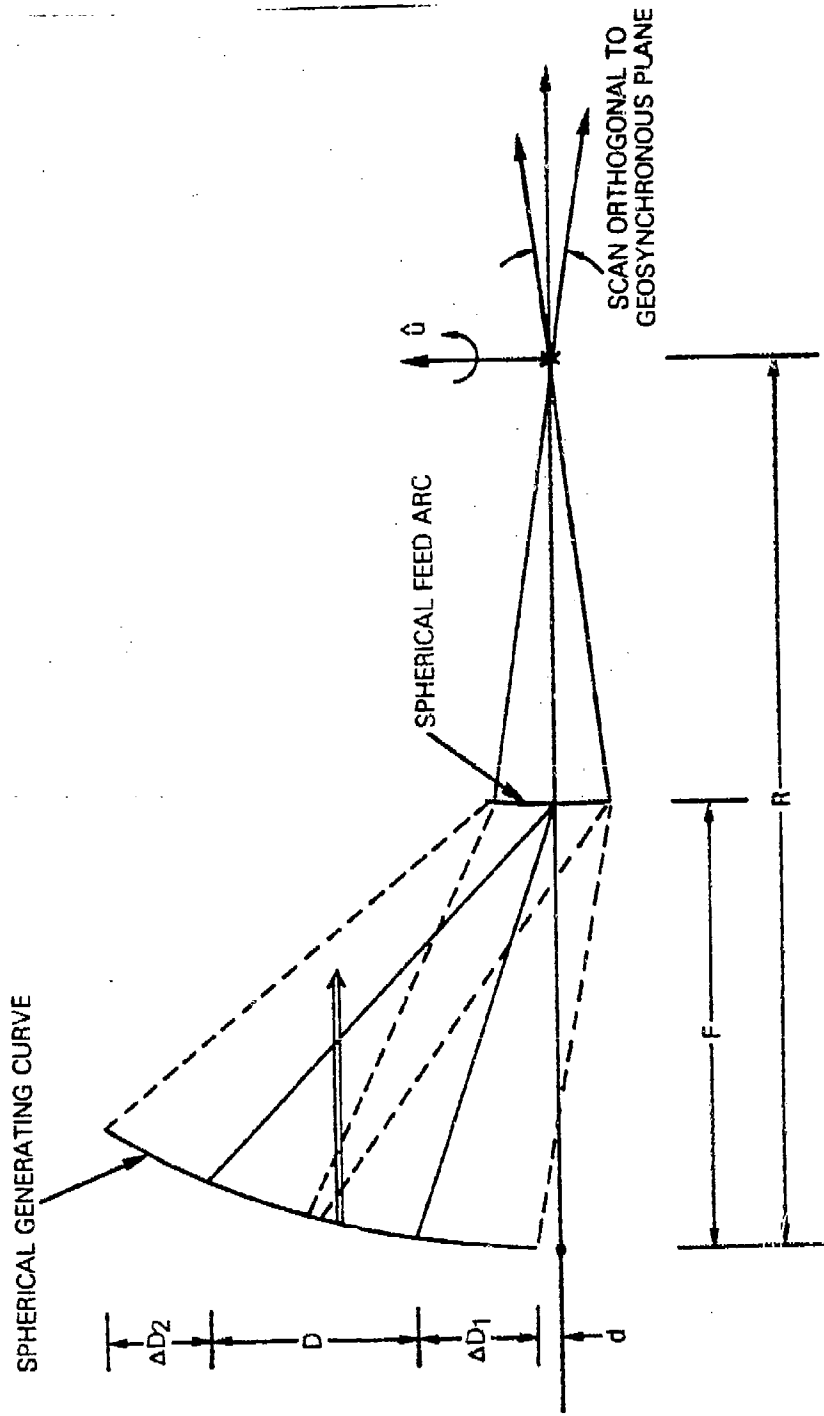


Figure 5-36. MBTA with Spherical Generating Curve

The equation of the spherical cross section in the $y = 0$ plane is

$$x^2 + [z - (R - F)]^2 = R^2 \quad (5-90)$$

or

$$z = (R - F) - \sqrt{R^2 - x^2} \quad (5-91)$$

The radius of curvature about the rotation axis, \hat{u} , is

$$R(x) = \sqrt{R^2 - x^2} \quad (5-92)$$

The general rotated plane curve is described by

$$z = (R - F) - \sqrt{R^2 - x^2 - y^2} \quad (5-93)$$

The path length for a ray from a general feed position (x_F, y_F, z_F) relative to F into the aperture plane $(x, y, 0)$ is

$$\begin{aligned} \ell(x, y, 0) = & \sqrt{(x - x_F)^2 + (y - y_F)^2 + \left[(R - F) - \sqrt{R^2 - x^2 - y^2} - z_F \right]^2} \\ & + \sqrt{R^2 - x^2 - y^2} - (R - F) \end{aligned} \quad (5-94)$$

and the aperture plane phase error expression is

$$\psi(x, y, 0) = 360^\circ \left(\frac{D}{\lambda} \right) \left[\frac{\ell(x, y, 0) - \ell(x_0, 0, 0)}{D} \right] \quad (5-95)$$

The aperture plane phase errors in the $y = 0$ plane, are plotted in Figures 5-37 and 5-38 for two geometries that are similar to those considered for the MBTA baseline configuration.

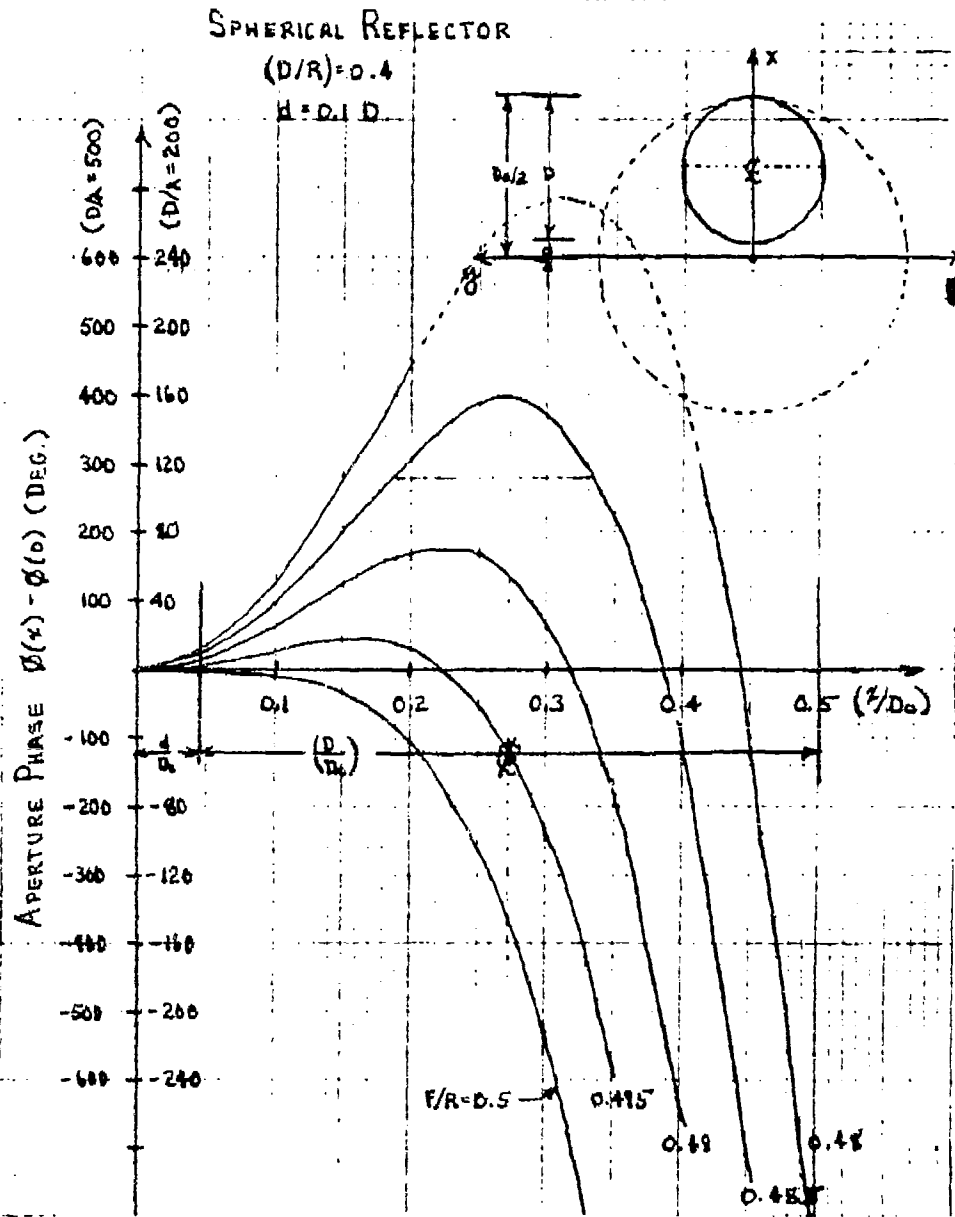


Figure 5-37. Aperture Plane Phase Error vs Feed Focusing with Spherical Generating Curve (D/R = 0.4)

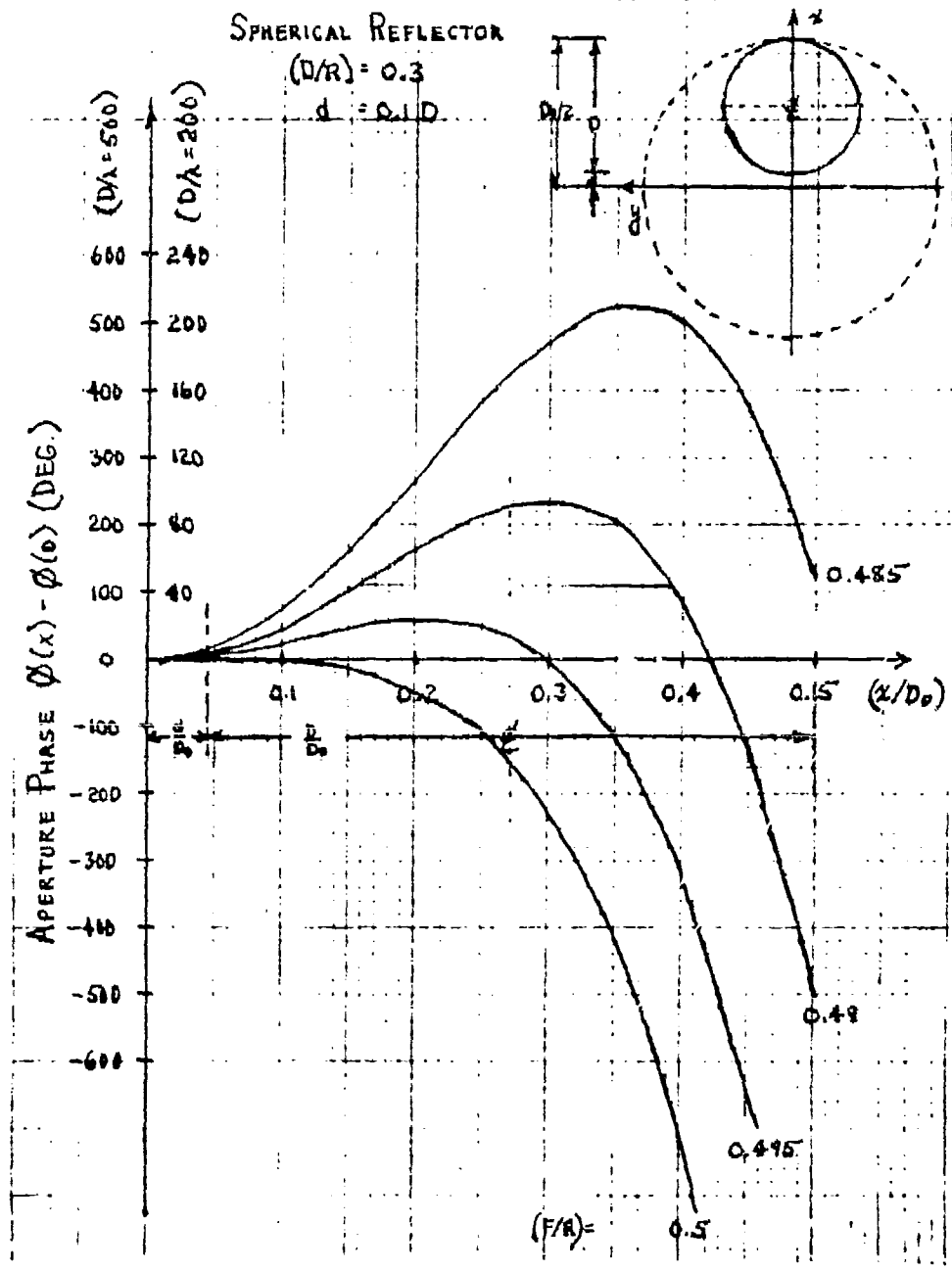


Figure 5-38. Aperture Plane Phase Error vs Feed Focusing with Spherical Generating Curve (D/R = 0.3)

5.11 ILLUMINATION GAIN OF FRONT-FED MBTA

The illumination gain of the front-fed offset reflector MBTA, excluding feed system or reflector rms surface tolerance losses, is summarized in Figure 5-39. The gain for a 10-percent offset ($d/D = 0.1$) and a 93.5° generating angle is shown as a function of D/λ for fixed D/R values. Gain increases as the radius of curvature increases. Because of edge-of-aperture phase errors, the tradeoff between peak gain and feed illumination taper is slower for the MBTA than for a conventional parabola. The aperture illumination gain versus feed edge taper is shown in Figure 5-40 for the baseline MBTA geometry. A feed edge taper of -15 dB virtually eliminates feed spillover past the reflector with little impact on peak gain.

The aperture illumination gain versus errors in the feed offset angle, θ_{osf} , is shown in Figure 5-41 for the baseline antenna. Variation of θ_{osf} produced no changes in the beam pointing direction. A $\pm 2^\circ$ variation about the calculated θ_{osf} angle is required before a decrease in gain is noted.

The illumination gain of the baseline 27-ft-diameter MBTA as a function of frequency from 3.7 to 31 GHz is shown in Figure 5-42. An 11-percent offset is utilized to ensure that the aperture plane is unblocked by the feed (or feed house) at the extreme parabolic plane scan position. The horn diameter must be used in conjunction with Figure 5-34 to determine the minimum offset distance. In addition, an allowance for the roof of the

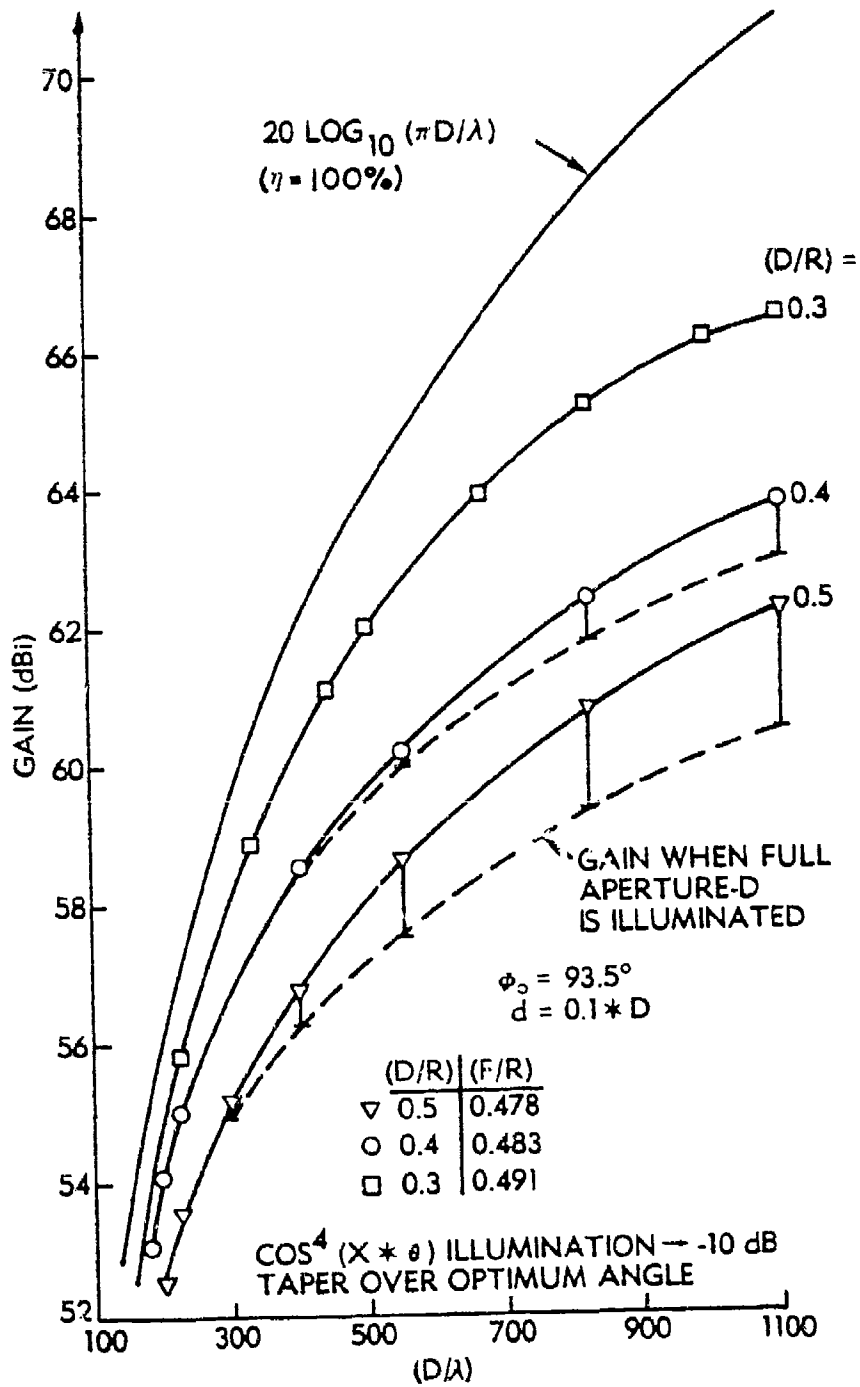


Figure 5-39. MBTA Illumination Gain vs D/λ

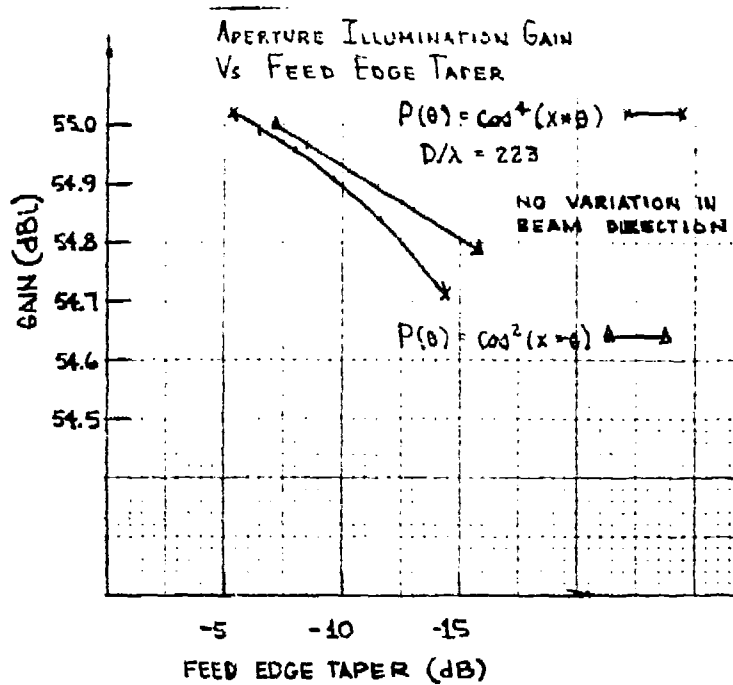


Figure 5-40. Aperture Illumination Gain vs Feed Edge Taper

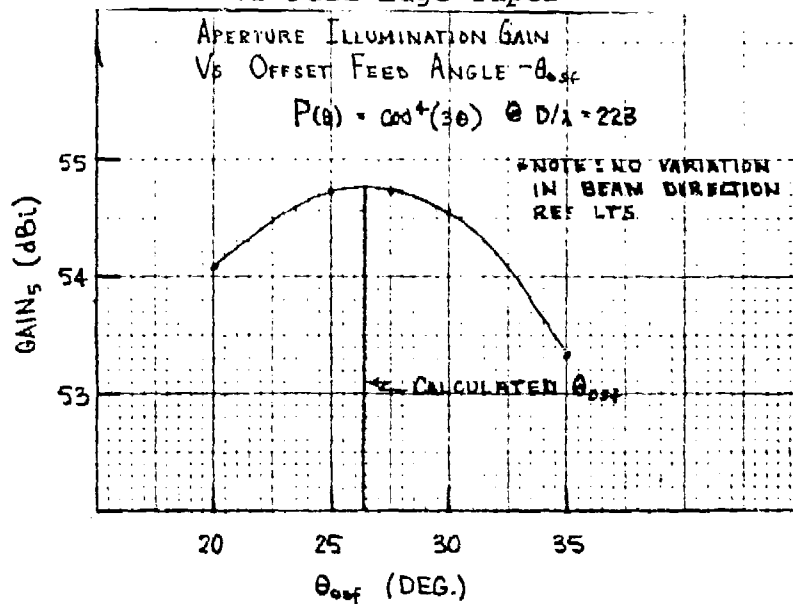


Figure 5-41. Aperture Illumination Gain vs Feed Offset Angle

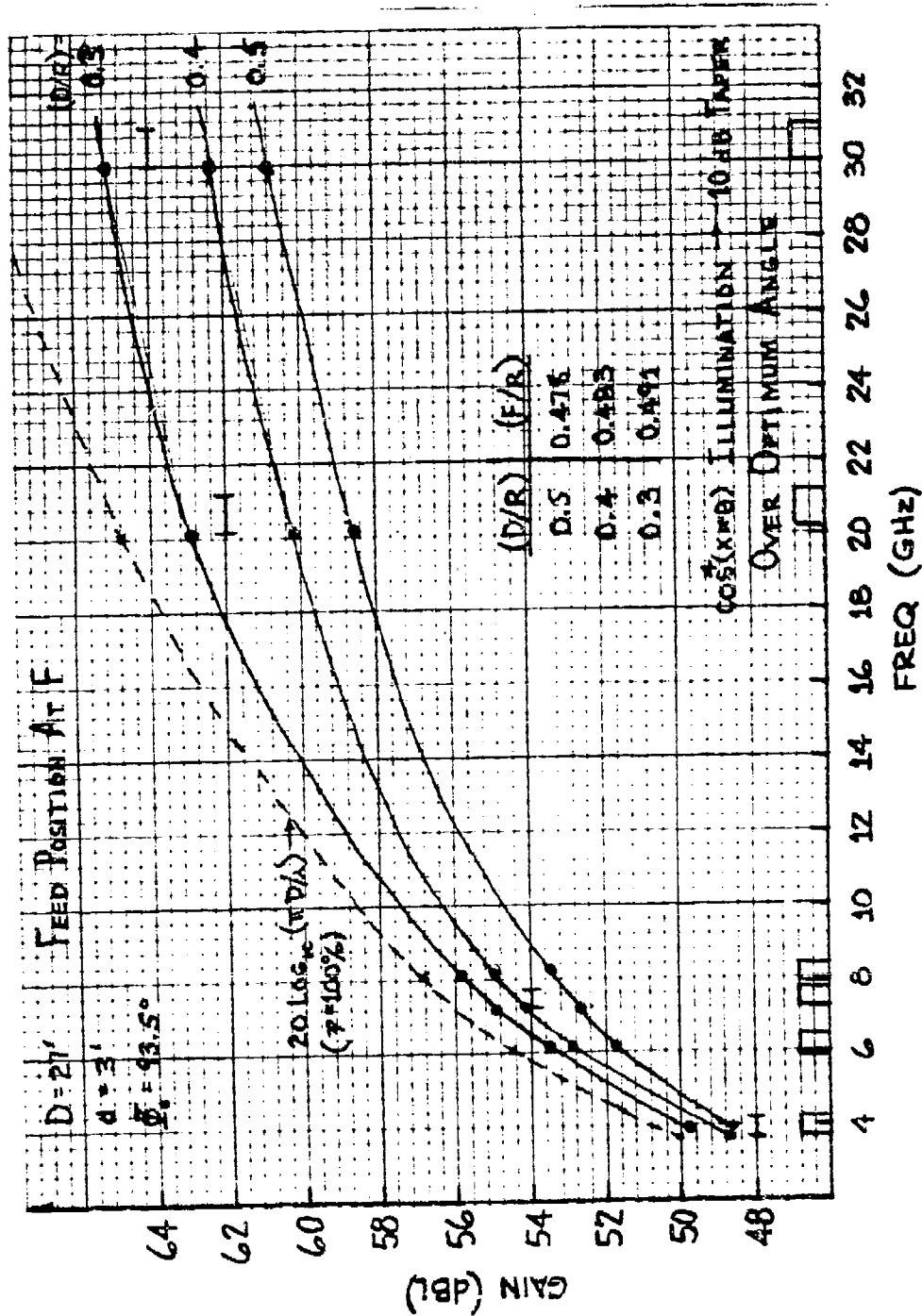


Figure 5-42. Aperture Illumination Gain (D = 27 ft) vs Frequency

room housing the feed/rail structure must be included. The $D/R = 0.4$ geometry provides an optimum 54-dB X-band gain solution for a 20° - 40° field of view. [The solution is optimum in the sense of minimizing the overall reflector area and ratio of reflector aperture dimensions (W/D) and ultimately cost.]

The relative projected aperture area of the MBTA is

$$\text{area} = WD \quad (5-96)$$

if the corner panels are not rounded. Since

$$\text{FOV} = \left(\frac{\pi}{180^\circ} \right) \left(\frac{D}{R} \right) \left(\frac{W}{D} - 1 \right) \quad (5-97)$$

then

$$\frac{\text{area}}{D^2} = \frac{(\pi/180^\circ)}{(D/R)} \text{FOV} + 1 \quad (5-98)$$

The projected aperture area¹⁵ of the MBTA as a function of D/R for fixed field of view requirements is shown in Figure 5-43. Contours of equal projected aperture areas can be placed on the illumination gain curves for a fixed field of view requirement, as shown in Figure 5-44. The relationship between D/λ and D/R , given a fixed area and field of view, is

$$\frac{D}{\lambda} = \sqrt{\frac{(\text{area}/\lambda^2)}{[(\pi/180^\circ)/(D/R)] \text{FOV}_0 + 1}} \quad (5-99)$$

These curves are quite helpful in arriving at a first-order optimum MBTA solution. Given a specified gain and field of view at a design frequency, the contours of equal projected aperture area identify the optimum D/R geometry.

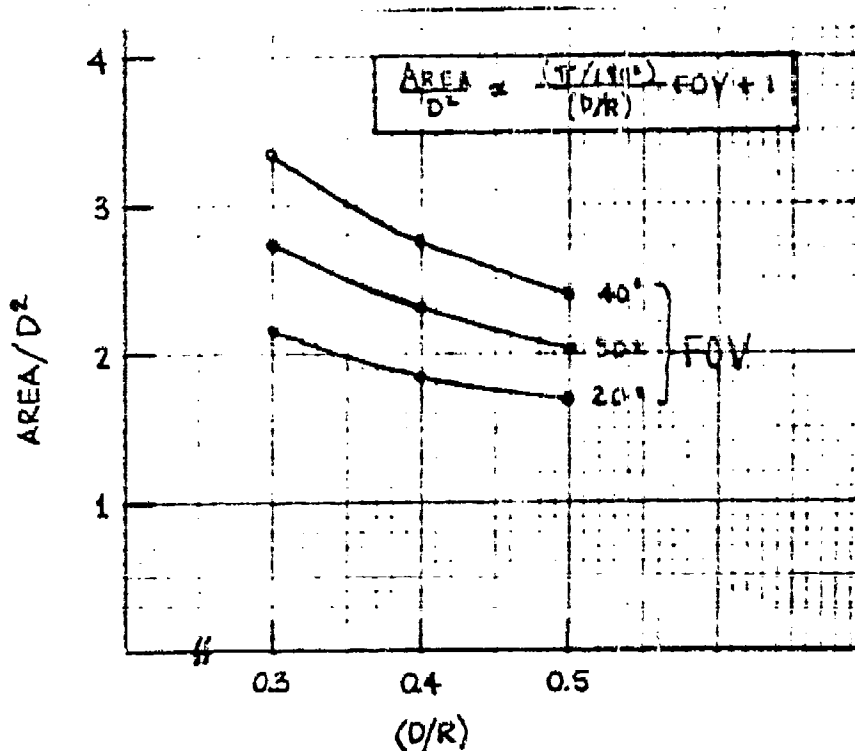


Figure 5-43. Projected Aperture Area of MBTA

5.12

OFFSET MBTA FIELD OF VIEW AND SCANNED
FEED PARAMETERS

The relationship between the MBTA field of view and the ratio of aperture plane dimensions for the offset geometry is

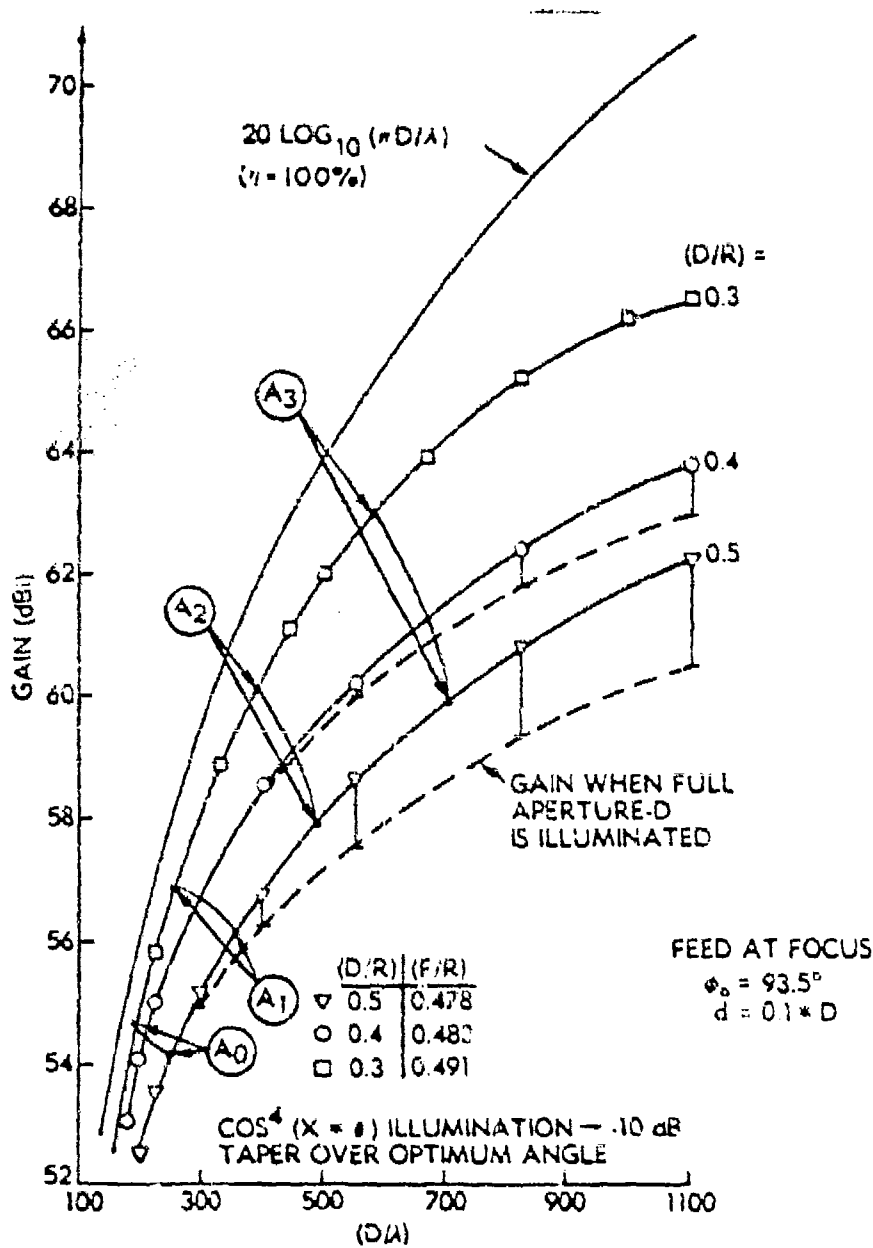


Figure S-44. Illumination Gain with Equal Projected Area Contours

$$\text{FOV} = 2 \left[\sin^{-1} \left(\frac{W}{2D} \frac{D}{R} \frac{R}{R_c} \right) - \sin^{-1} \left(\frac{D}{2R} \frac{R}{R_c} \right) \right] \quad (5-100)$$

$$\text{FOV} \approx \left(\frac{180^\circ}{\pi} \right) \left(\frac{D}{R} \right) \left(\frac{W}{D} - 1 \right) \left(\frac{R}{R_c} \right) \quad (5-101)$$

where the ratio of the radius at the center of the aperture plane, R_c , to the radius, R , shown in Figure 5-45 is

$$\frac{R_c}{R} = 1 + \cos \phi_0 \left(\frac{D}{R} \right) \left(\frac{x_c}{D} \right) - \sin \phi_0 \frac{(D/R)^2 \left(\frac{x_c}{D} \right)^2}{4(F/R)} \quad (5-102)$$

The field of view versus W/D for the 10-percent offset geometry is shown in Figure 5-46. Comparison of the field of view in this figure with that for a symmetrical MBTA (Figure 5-5) indicates that the shorter radius of curvature at the center of the aperture for an offset geometry increases the field of view for a fixed W/D ratio. Program MBTA-2 calculates the field of view versus reflector parameters.

The locus of feed phase center positions as a function of spherical scan is derived from the geometry in Figure 5-47. The feed arc is defined in the v - w plane as the feed revolves around the rotation axis, \hat{u} . The scanned beam locus does not lie in the v - w plane, but the maximum angular deviation out of this plane is $2(\phi_0 - 90^\circ)$ for a full $\pm 180^\circ$ field of view. The beam scan angle, θ_s , is assumed to be the beam angle projected into the w - v plane. The coordinates of the feed phase center as a function of the beam scan angle are then

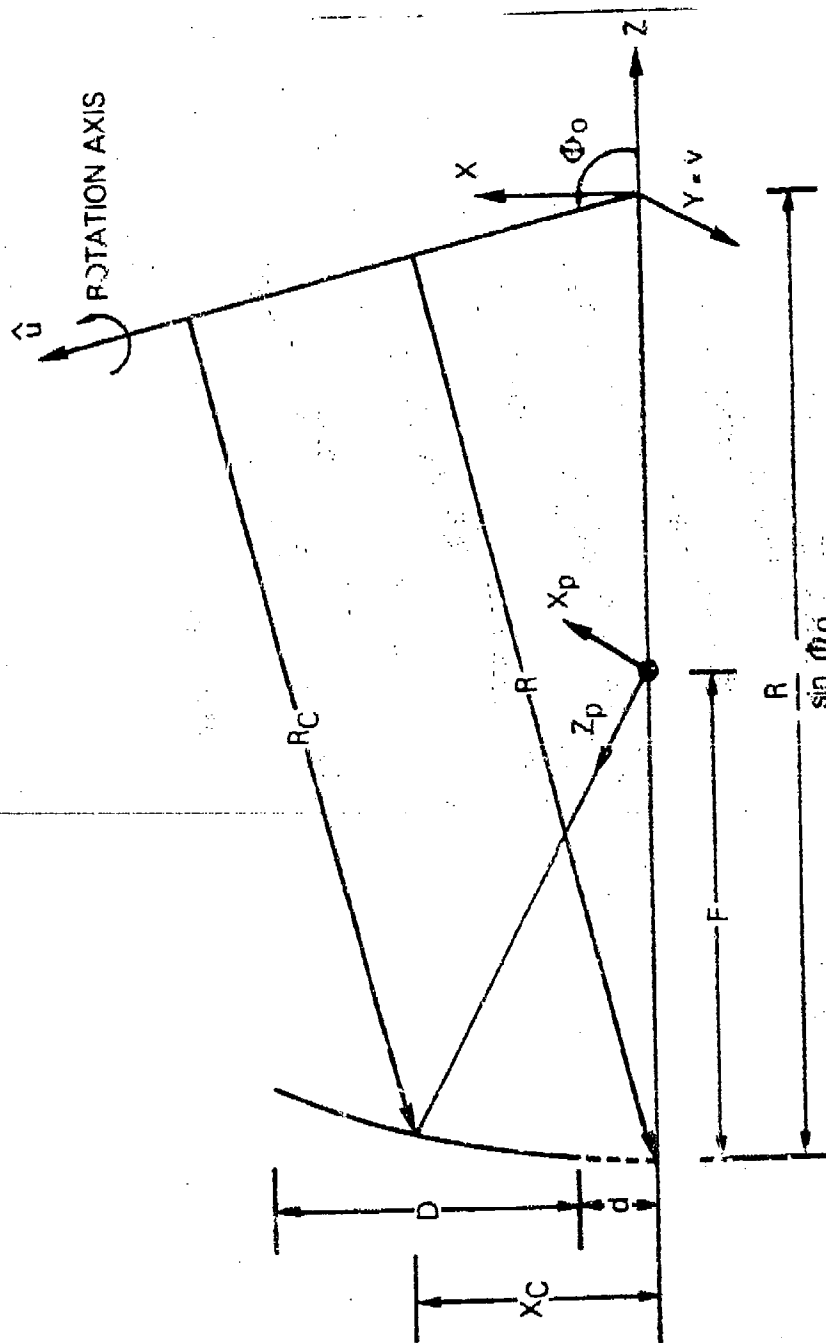


Figure 5-45. Feed Pointing Parameters for Offset MBTA

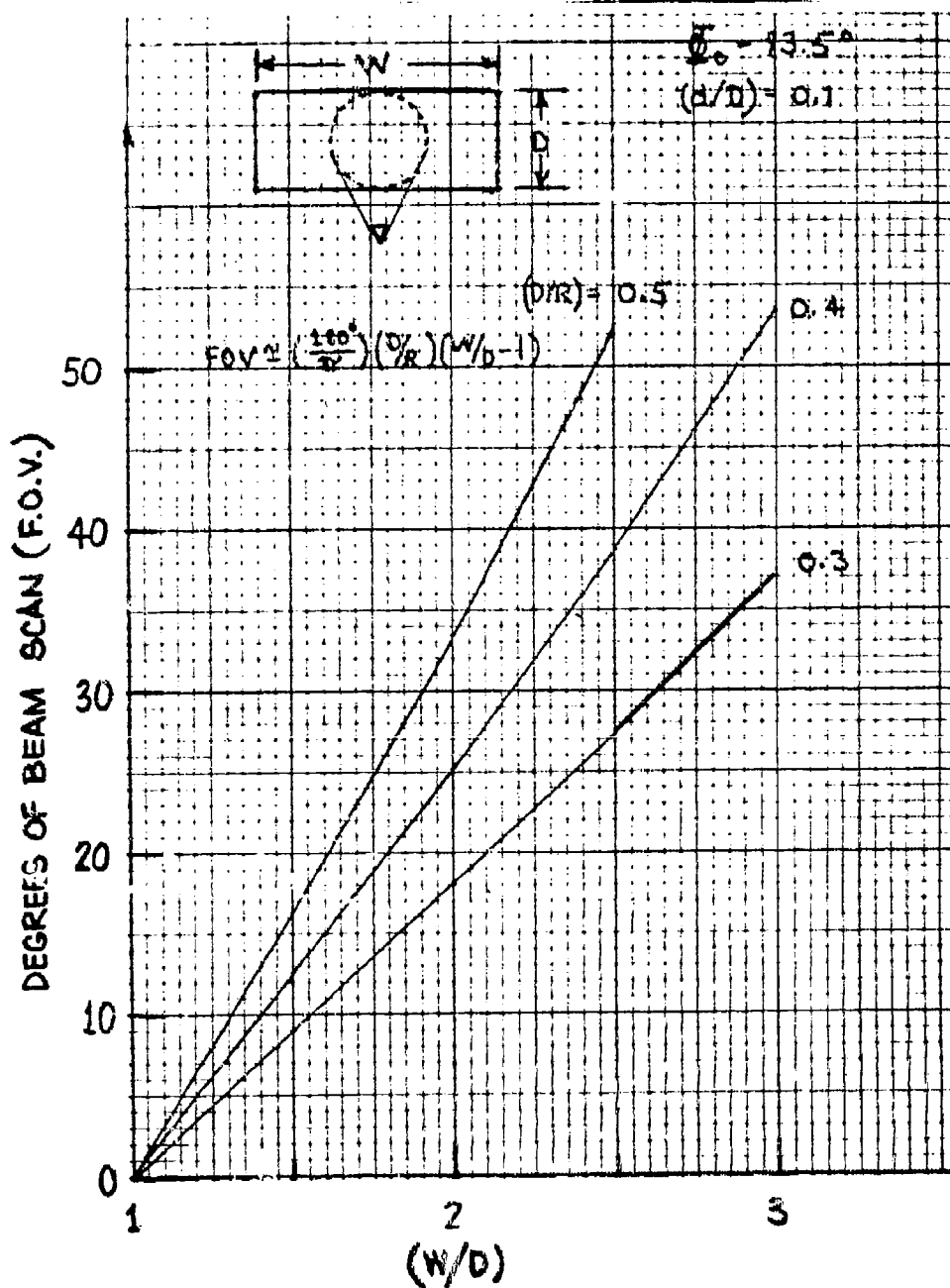


Figure 5-46. 10-Percent Offset MBTA Field of View vs (W/D)

$$w_f = -(R - F \sin \phi_0) \cos \theta_s \quad (5-103)$$

$$v_f = \pm(R - F \sin \phi_0) \sin \theta_s \quad (5-104)$$

Using the coordinate transformation in equation (5-45) and translating to an (x,y,z) system with origin at the focus yields

$$x_F = (R - F \sin \phi_0) \cos \phi_0 (\cos \theta_s - 1) \quad (5-105)$$

$$y_F = \pm(R - F \sin \phi_0) \sin \theta_s \quad (5-106)$$

$$z_F = \frac{(R - F \sin \phi_0)}{\sin \phi_0} \left[1 - \cos^2 \phi_0 - \sin^2 \phi_0 \cos \theta_s \right] \quad (5-107)$$

When normalized to the diameter, D , the feed phase center locations as a function of the spherical scan, θ_s , are

$$x_F = D \left(\frac{R}{D} \right) \left(1 - \frac{F}{R} \sin \phi_0 \right) \cos \phi_0 (\cos \theta_s - 1) \quad (5-108)$$

$$y_F = \pm D \left(\frac{R}{D} \right) \left(1 - \frac{F}{R} \sin \phi_0 \right) \sin \theta_s \quad (5-109)$$

$$z_F = D \left(\frac{R}{D} \right) \left(1 - \frac{F}{R} \sin \phi_0 \right) \left[\frac{1 - \cos^2 \phi_0 - \sin^2 \phi_0 \cos \theta_s}{\sin \phi_0} \right] \quad (5-110)$$

relative to an origin at the parabolic focus $(0,0,0)$.

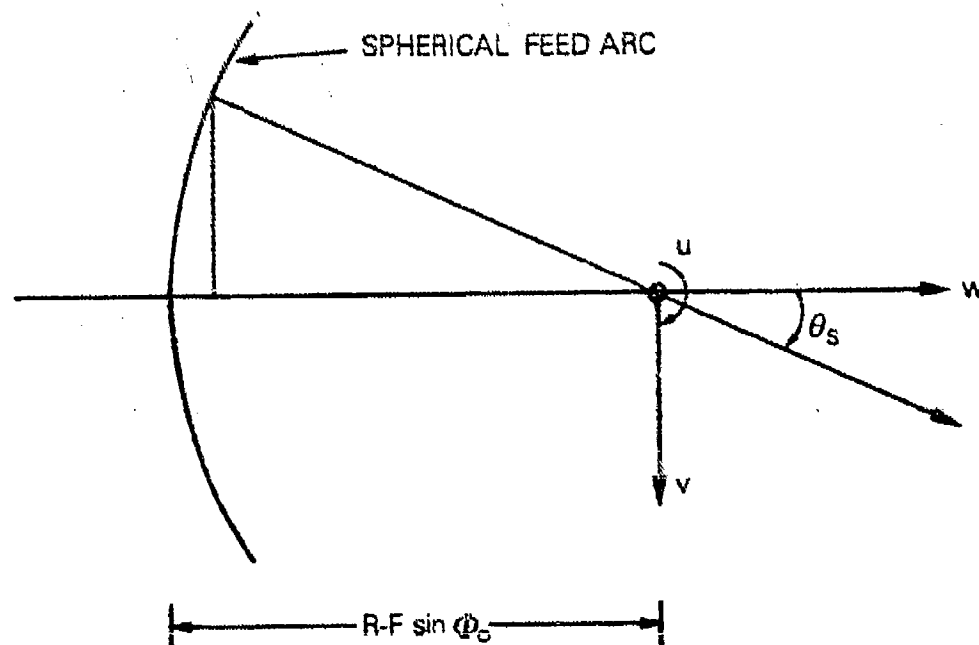


Figure 5-47. Scanned Beam Feed Position Geometry

The length of the projected feed arc for the offset
META is

$$L = 2\Delta v_F = 2(R - F \sin \phi_0) \sin \theta_s \quad (5-111)$$

$$L = 2\left(\frac{D}{D/R}\right)\left(1 - \frac{F}{R} \sin \phi_0\right) \sin \theta_s \quad (5-112)$$

The direction cosines defining the feed pointing axis and orientation as functions of scan are also required. The feed pointing axis, z_p , is shown in Figure 5-45. The projection of the z_p axis onto the v-w plane yields

$$u = \sin [\theta_{osf} + (\phi_0 - 90^\circ)] \quad (5-113)$$

$$v = \pm \sin \theta_s \cos [\theta_{osf} + (\phi_0 - 90^\circ)] \quad (5-114)$$

$$w = - \cos \theta_s \cos [\theta_{osf} + (\phi_0 - 90^\circ)] \quad (5-115)$$

The direction cosines for the feed pointing in the (x,y,z) coordinates with the origin at the parabolic focus are

$$\begin{aligned} \alpha_x = & \sin \theta_{osf} (\sin^2 \phi_0 + \cos^2 \phi_0 \cos \theta_s) \\ & + \cos \theta_{osf} \sin \phi_0 \cos \phi_0 (\cos \theta_s - 1) \end{aligned} \quad (5-116)$$

$$\alpha_y = - \sin \theta_s (\cos \theta_{osf} \sin \phi_0 + \sin \theta_{osf} \cos \phi_0) \quad (5-117)$$

$$\begin{aligned} \alpha_z = & \sin \theta_{osf} \sin \phi_0 \cos \phi_0 (1 - \cos \theta_s) \\ & - \cos \theta_{osf} (\cos^2 \phi_0 + \sin^2 \phi_0 \cos \theta_s) \end{aligned} \quad (5-118)$$

and

$$\sqrt{\alpha_x^2 + \alpha_y^2 + \alpha_z^2} = 1 \quad (5-119)$$

Program MBTA-10 calculates the feed phase center position relative to the initial focus given the desired scan angle. It also furnishes the direction cosines for the feed pointing.

5.13 PATTERNS AND POLARIZATION

The principal plane linearly polarized patterns for the baseline 27-ft-diameter MBTA are shown in Figures 5-48 and 5-49. In the geosynchronous plane ($\phi = 90^\circ$), the pattern is symmetrical in θ , first sidelobe levels are below 30 dB, and the maximum cross-polarization lobe for a corrugated feed horn is 33 dB. The half-power beamwidth is 0.36° . In the plane of the offset parabolic section ($\phi = 0^\circ$), the pattern is slightly asymmetrical due to asymmetrical amplitude and phase aperture distributions. A small amount of beam scan is noted when the feed is at the parabolic focus, and the half-power beamwidth is 0.34° . These patterns were calculated using a -10.6-dB feed taper over the feed illumination angle of 42.4° . Increasing the feed edge taper to -15 dB virtually eliminates feed spillover energy past the reflector with only a 0.2-dB gain loss. A 3λ circular aperture conical horn provides an identical pattern in the $\phi = 90^\circ$ plane and a slightly narrower pattern in the $\phi = 0^\circ$ plane. However, the maximum cross-polarization levels increase to 25 dB as a result of unequal E- and H-plane pattern amplitude functions from the conical horn aperture.

The large effective $F/D = 1.25$ of the baseline MBTA configuration means that circularly polarized beam squint effects are negligible. The circular cross-polarization response is essentially determined by the polarization characteristics of the feed system.^{16,17}

The wide-angle sidelobe characteristics of the baseline MBTA at X-band to $\pm 5^\circ$ are shown in Figures 5-50 and 5-51. The sidelobe envelopes are well below the $32 - 25 \log_{10} \theta$ criteria.^{18,19} The lack of a Cassegrain subreflector with its feed spillover contributions to the sidelobe envelope and feed or

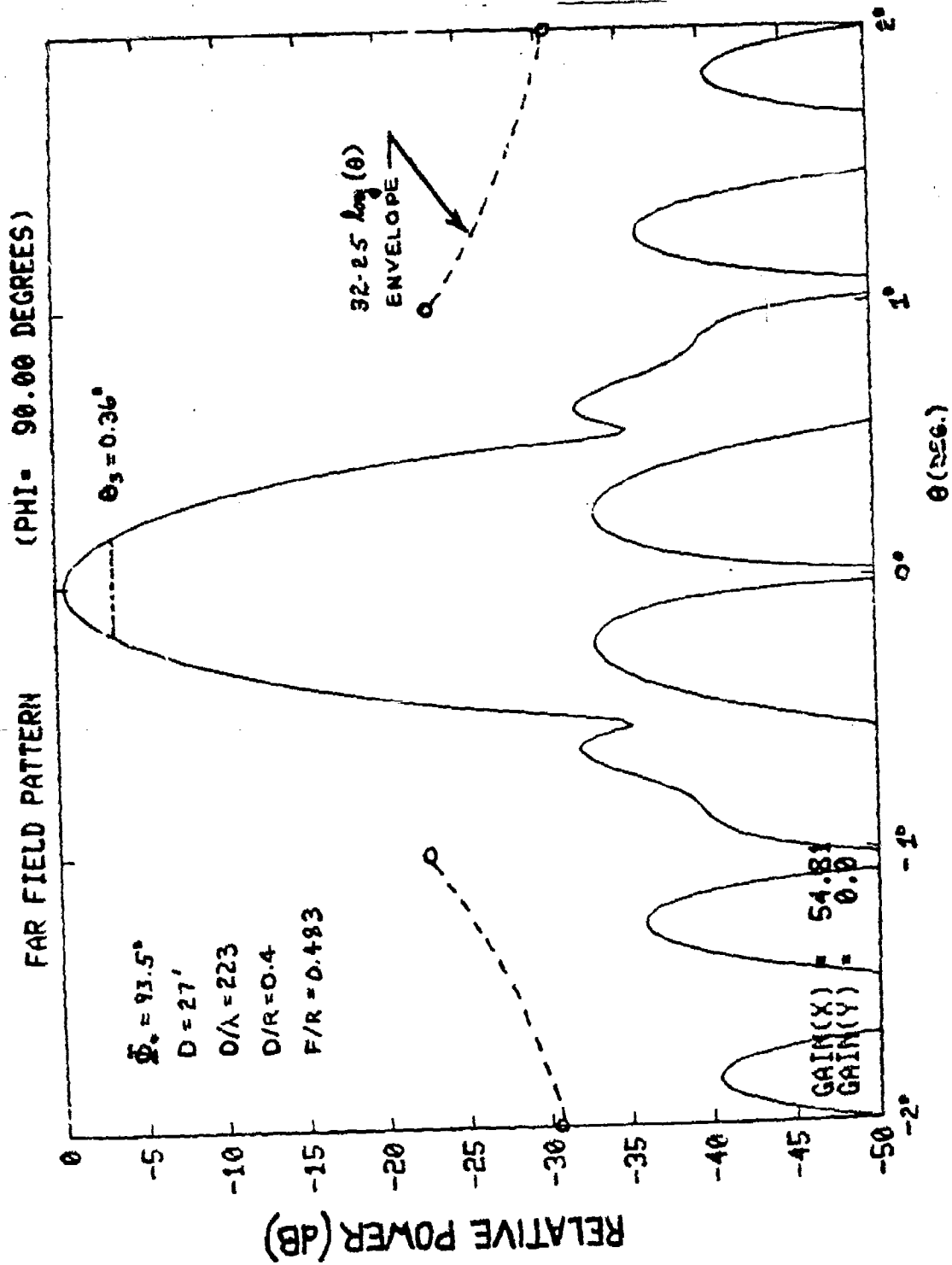


Figure 5-48. Baseline MBTA Pattern ($\phi = 90^\circ$)

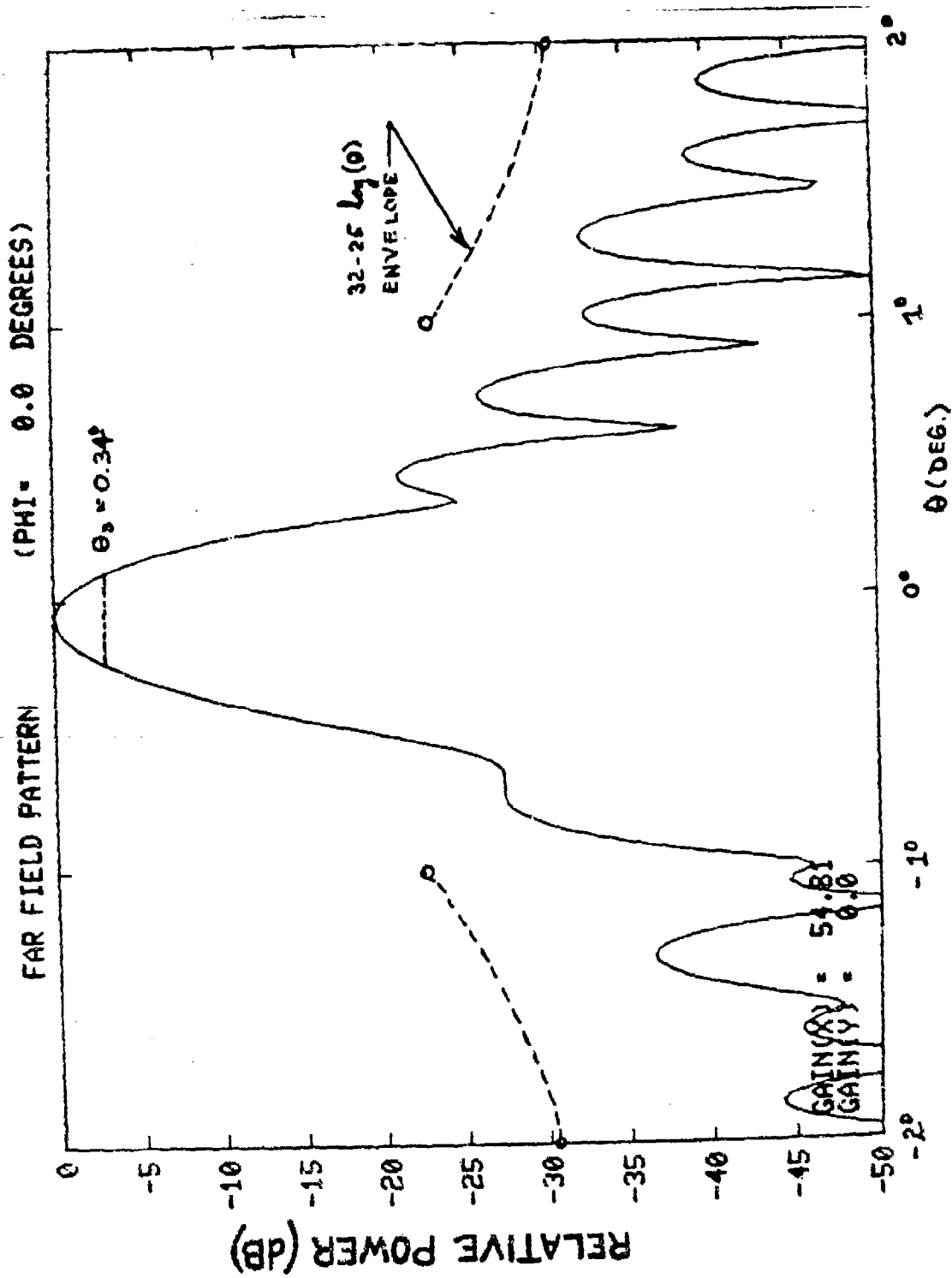


Figure 5-49. Baseline MBTA Pattern ($\phi = 0^\circ$)

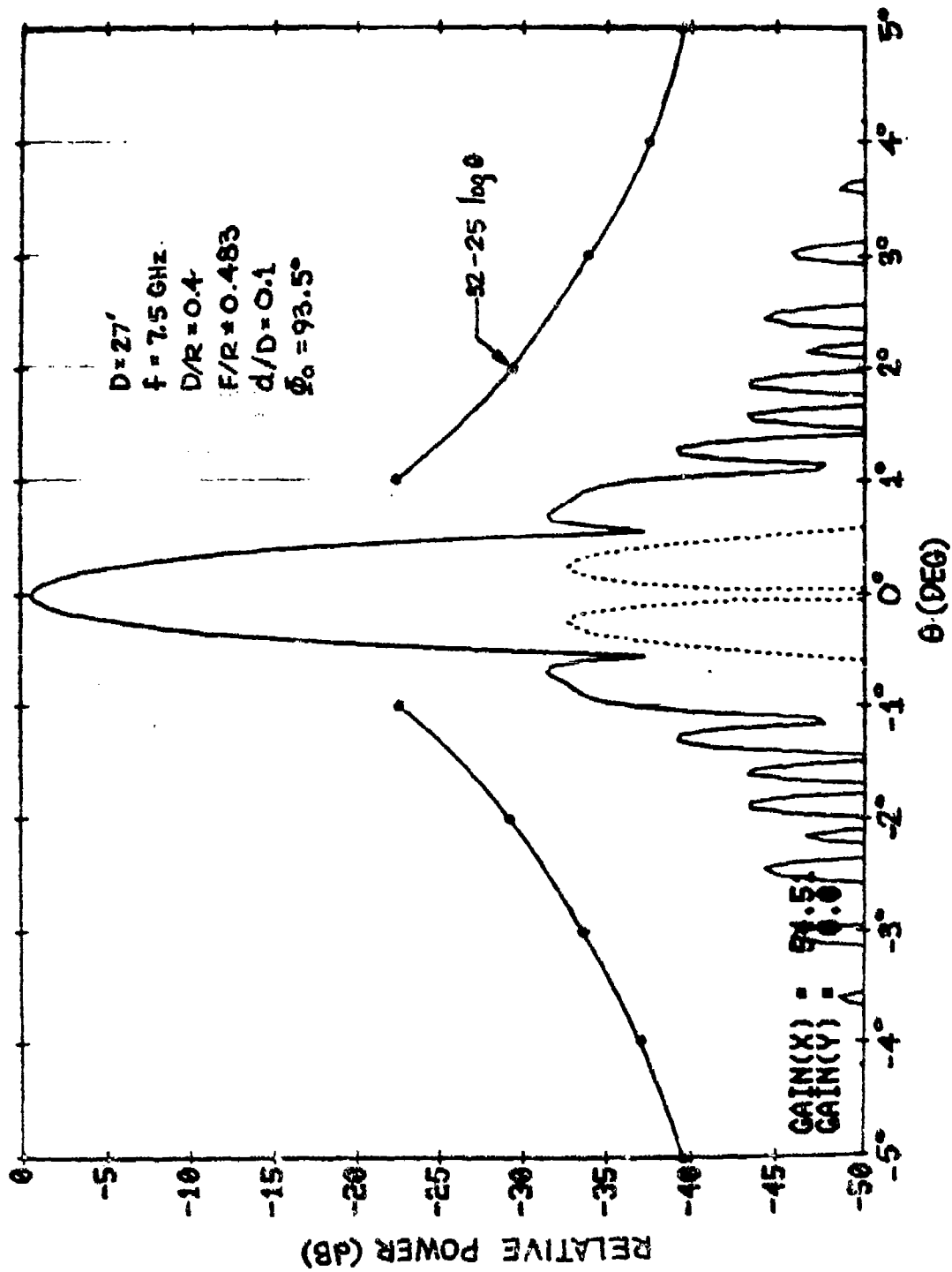


Figure 5-50. Baseline MBTA Receive Band Pattern at 7.5 GHz ($\phi = 90^\circ$)

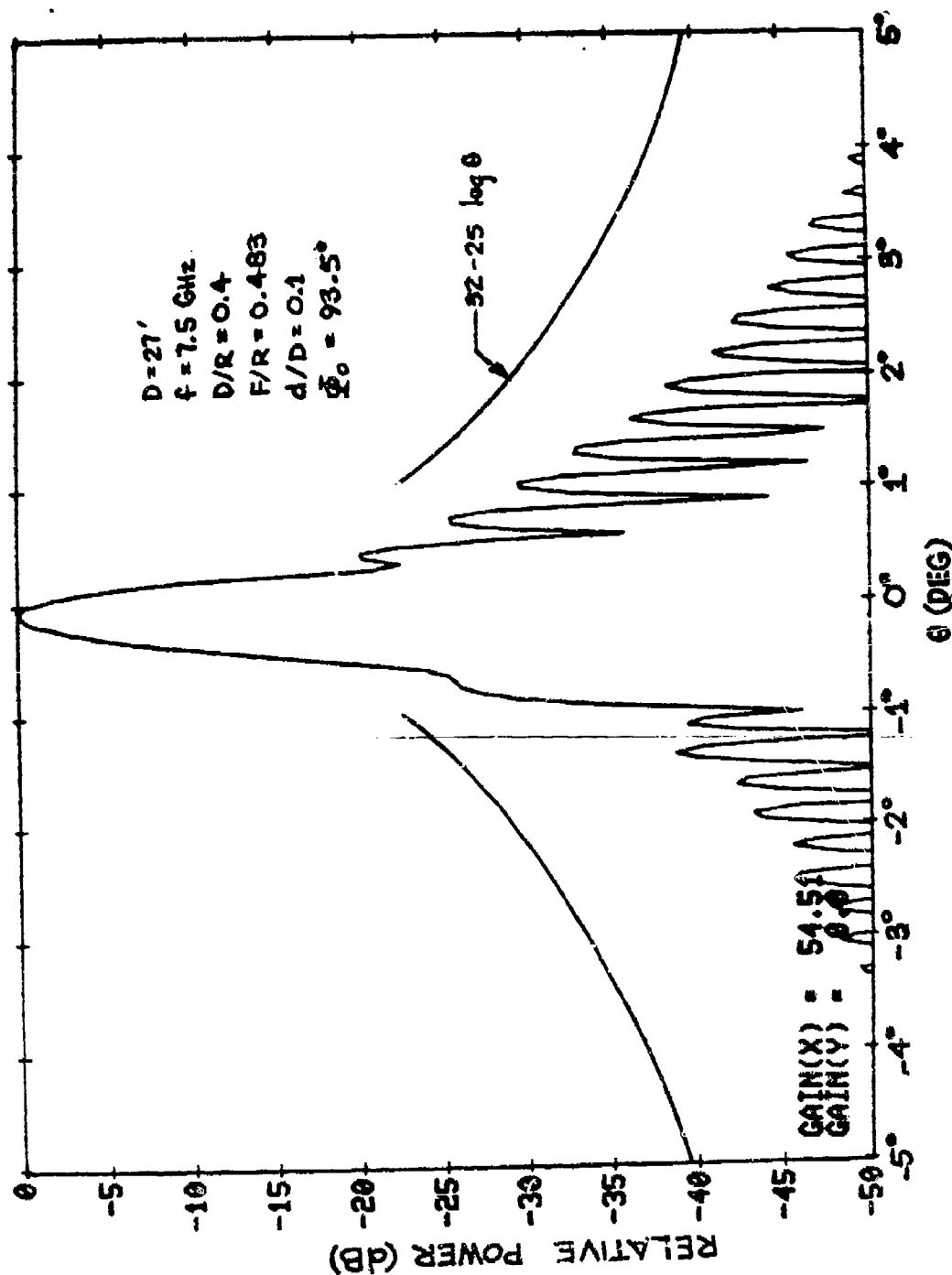


Figure 5-51. Baseline MBTA Receive Band Pattern at 7.5 GHz ($\phi = 0^\circ$)

subreflector/spar blockage provide the offset MBTA with exceptional wide-angle sidelobe envelopes. The principal plane patterns of the 27-ft-diameter MBTA ($D/R = 0.4$) geometry in the 4-, 12-, and 30-GHz receive bands are shown in Figures 5-52 through 5-57. The higher frequency band patterns indicate the effects of spherical aberration in the offset reflector. The $\phi = 90^\circ$ pattern broadens symmetrically, while the $\phi = 0^\circ$ pattern becomes more asymmetrical and the $-\theta$ scanning effect is more visible. A corrugated feed horn pattern was used to calculate these results.

The X-band patterns for a 48-ft-diameter MBTA with $D/R = 0.3$ are shown in Figures 5-58 and 5-59. A corrugated feed horn pattern was utilized for the pattern calculations. The maximum cross-polarization lobe is lower for the $D/R = 0.3$ geometry, since the reflector surface is flatter. Figure 5-60 shows the $D/R = 0.3$ offset geometry approximately to scale.

5.14 NOISE TEMPERATURE AND FEED SPILLOVER

The calculated and measured antenna noise temperatures for the offset front-fed MBTA are remarkably good. The antenna temperature measured on COMSAT Laboratories' 32- x 55-ft MBTA (elevation angle = 21.6°) was 23 K at 3.95 GHz.

Exceptional noise temperature characteristics are a result of the following:

- a. a corrugated feed horn with a rotationally symmetric (Gaussian) amplitude pattern which has virtually no sidelobes,
- b. the lack of aperture blockage (feed, subreflector, or spars) and forward feed spillover past a subreflector (Cassegrain geometries), and
- c. an oversize reflecting aperture relative to the required aperture area, which also reduces reflector spillover.

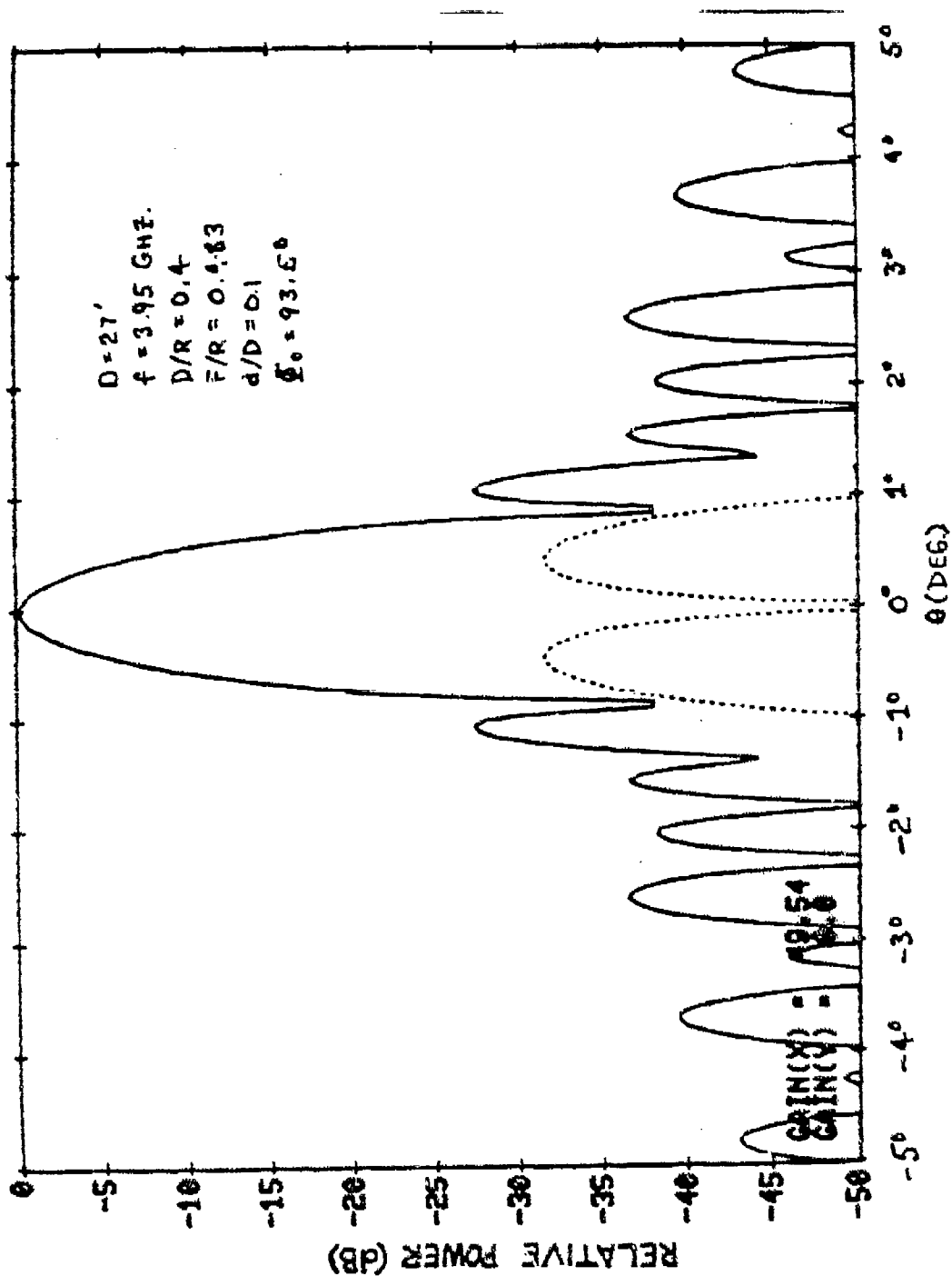
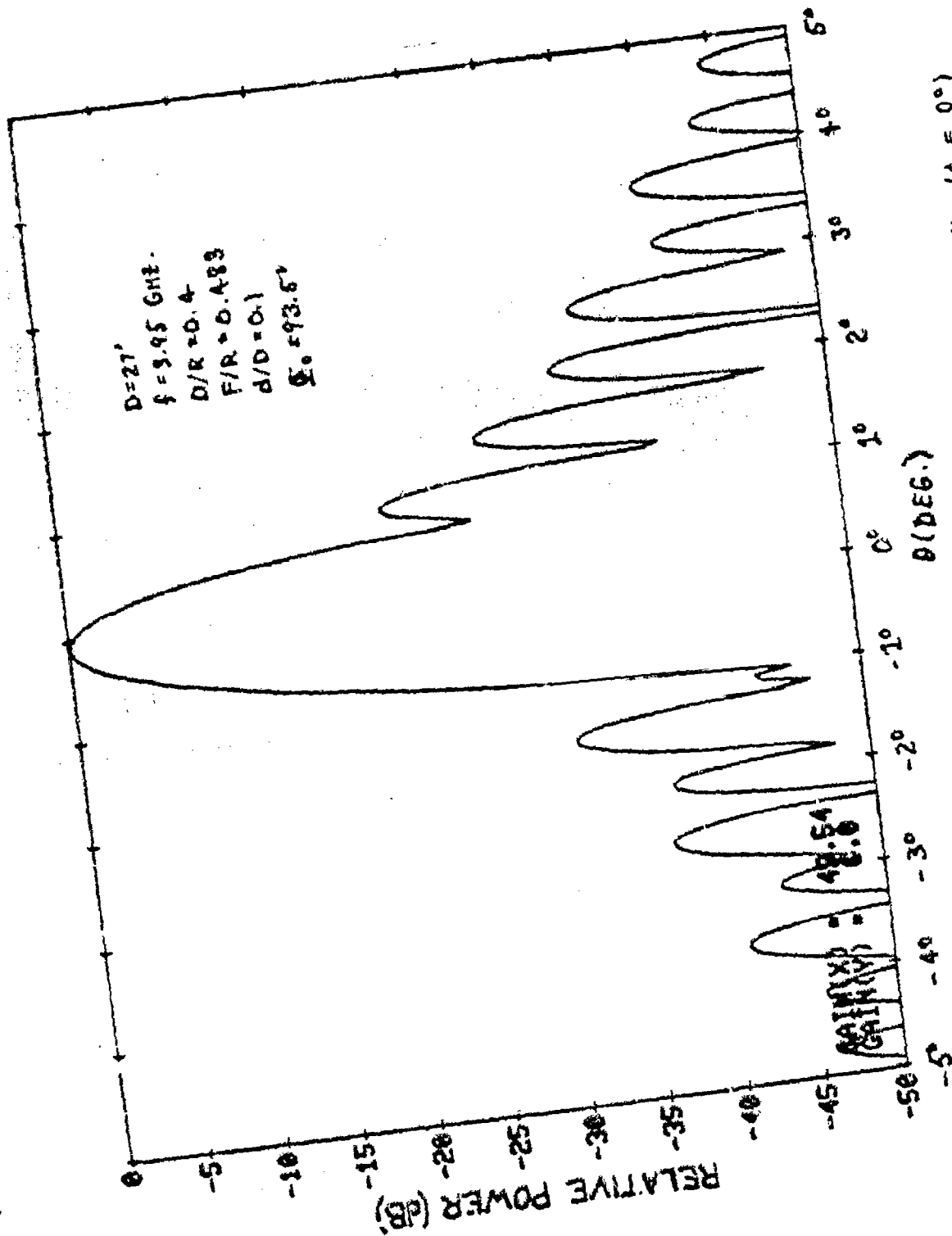


Figure 5-52. Baseline MBTA Receive Band Pattern at 3.95 GHz ($\phi = 90^\circ$)



Baseline MBTA Receive Band Pattern at 3.95 GHz ($\phi = 0^\circ$)

Figure 5-53.

Multiple Beam Torus
Antenna Study

COMSAT Labs

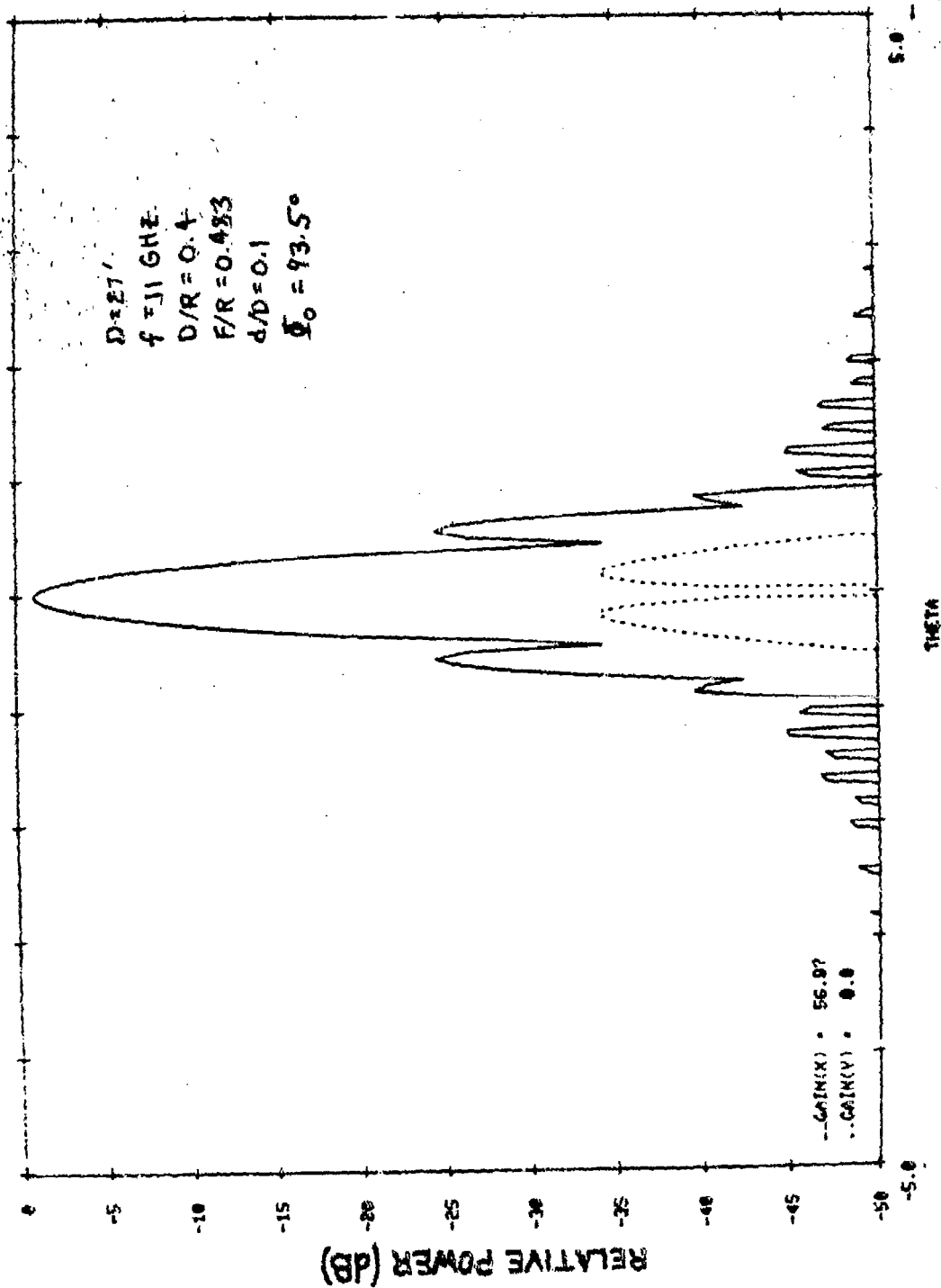
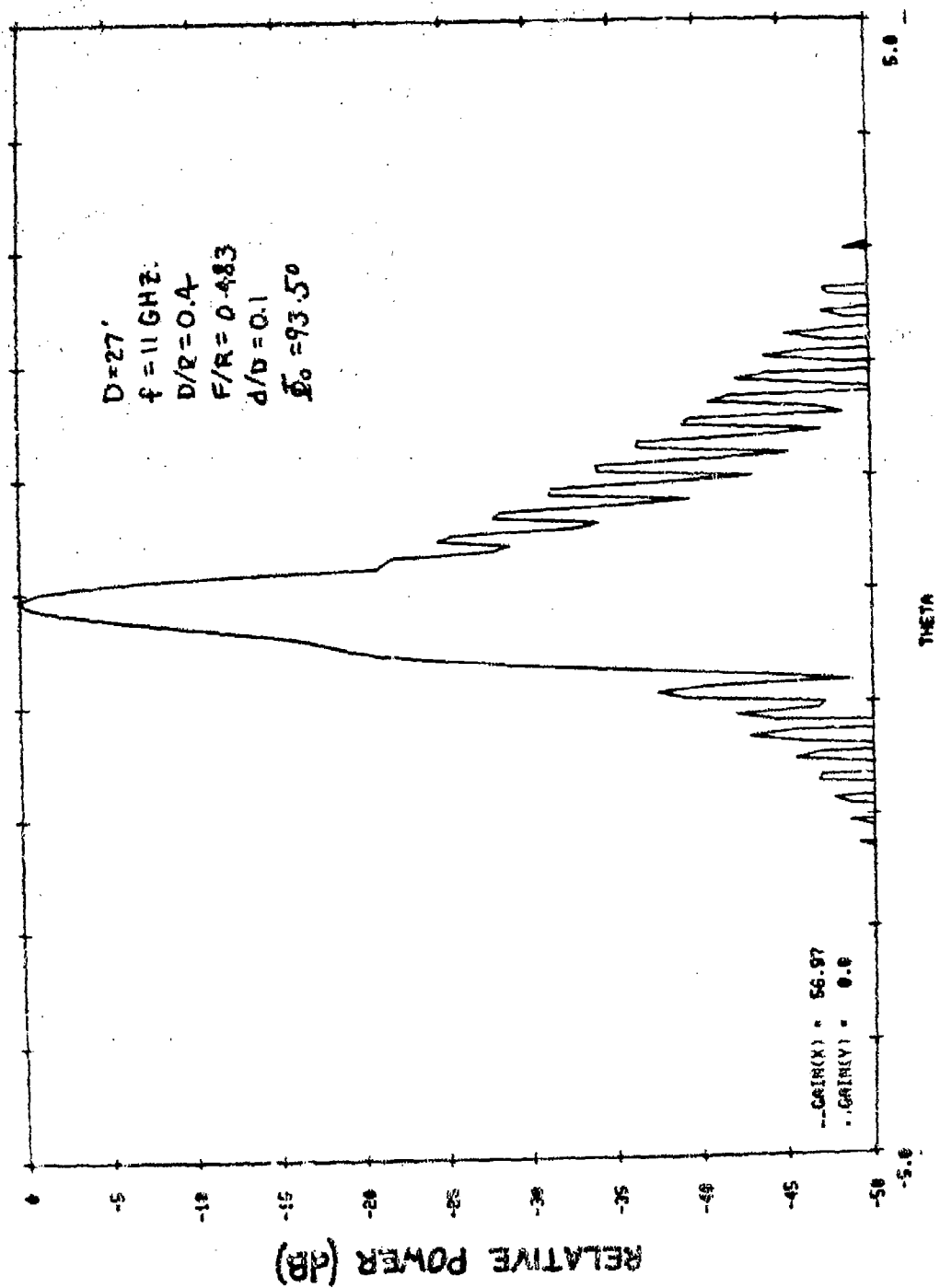


Figure 5-54. Baseline MBTA Receive Band Pattern at 11 GHz ($\phi = 90^\circ$)

Figure 5-55. Baseline MBTA Receive Band Pattern at 11 GHz ($\phi = 0^\circ$)

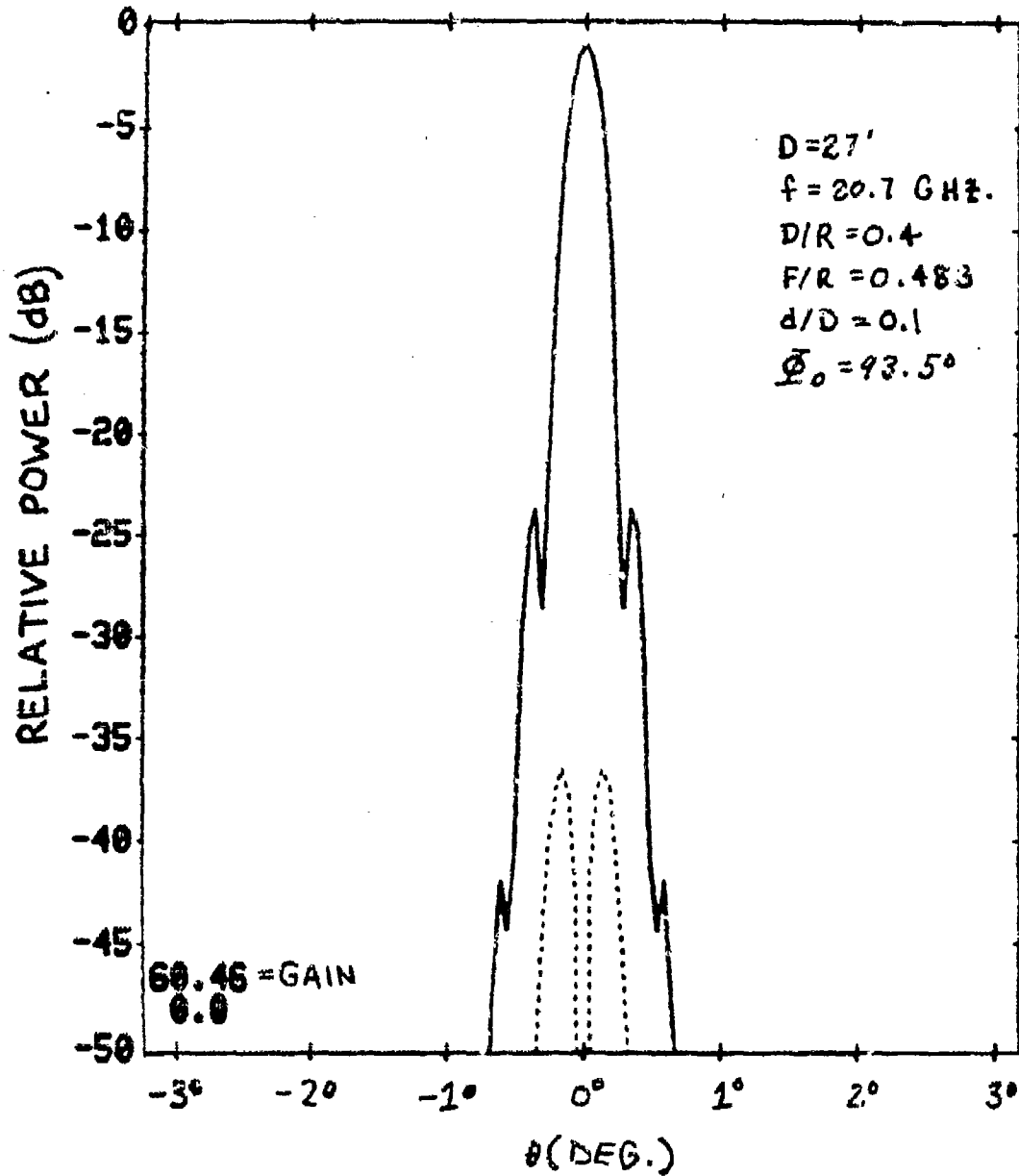


Figure 5-56. Baseline MBTA Receive Band Pattern at 20.7 GHz ($\phi = 90^\circ$)

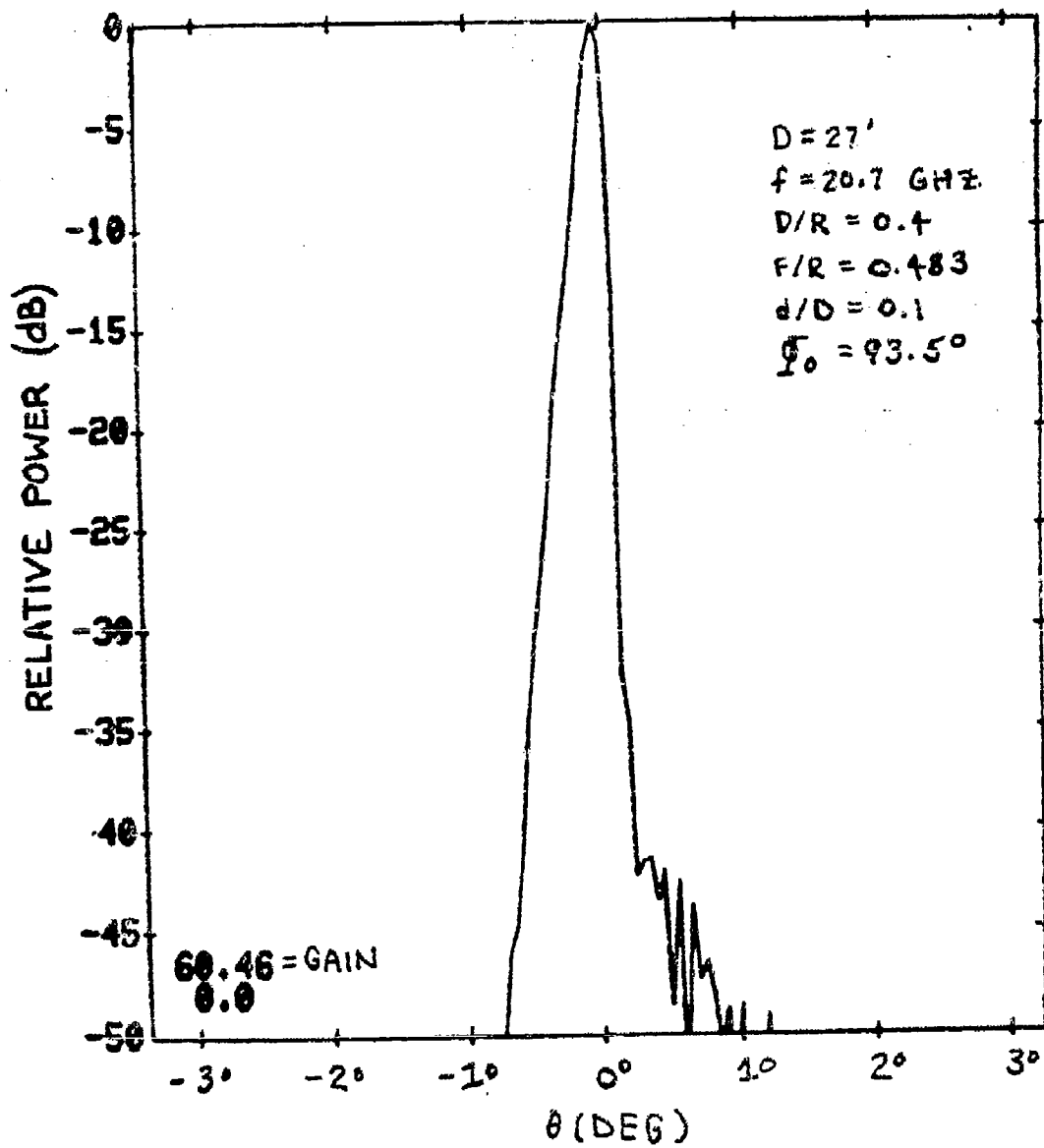


Figure 5-57. Baseline MBTA Receive Band Pattern
at 20.7 GHz ($\phi = 0^\circ$)

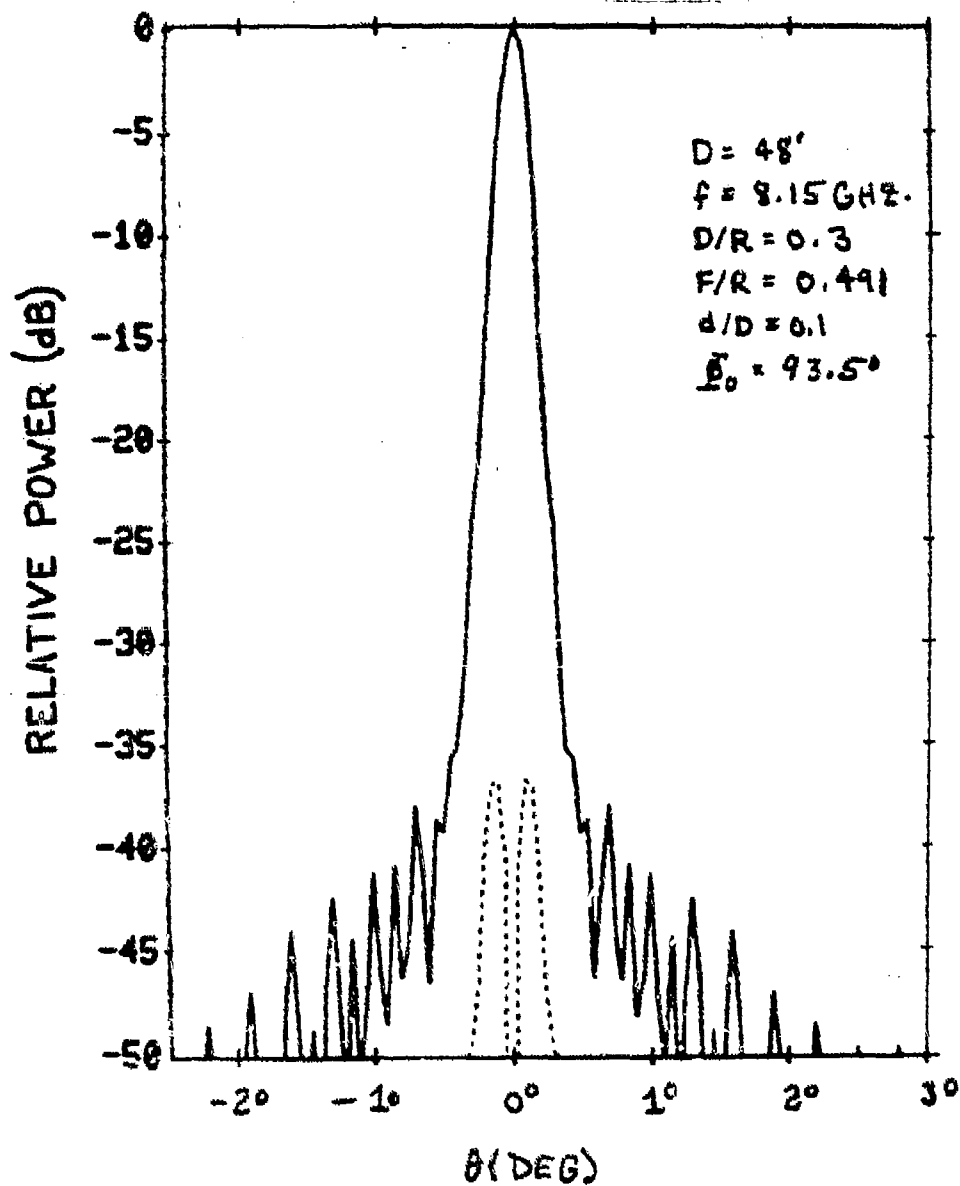


Figure 5-58. 48-ft-Diameter MBTA ($D/R = 0.3$)
Pattern at 8.15 GHz ($\theta = 90.2^\circ$)

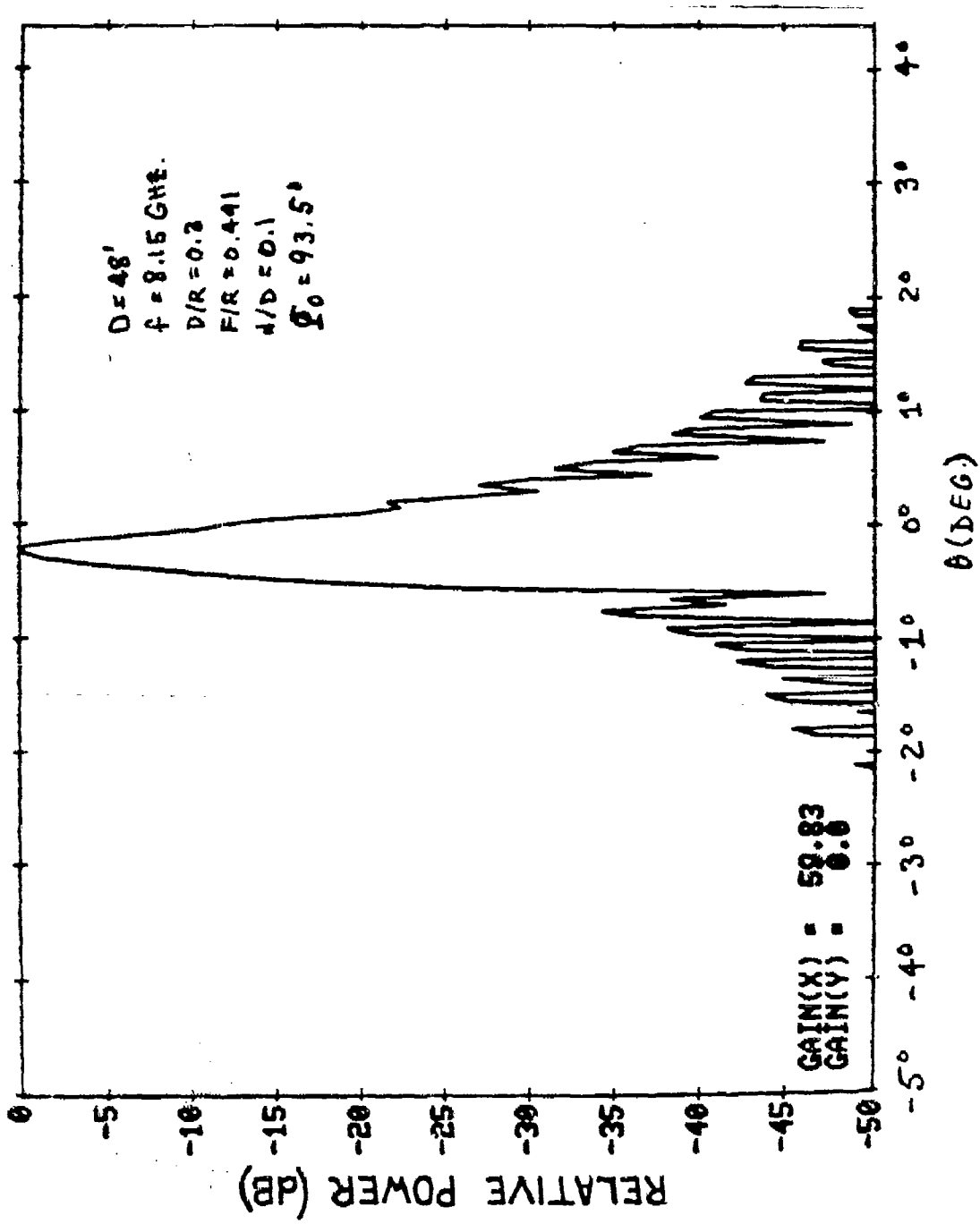


Figure 5-59. 48-ft-Diameter MBTA ($D/R = 0.3$) Pattern at
8.15 GHz ($\phi = 0^\circ$)

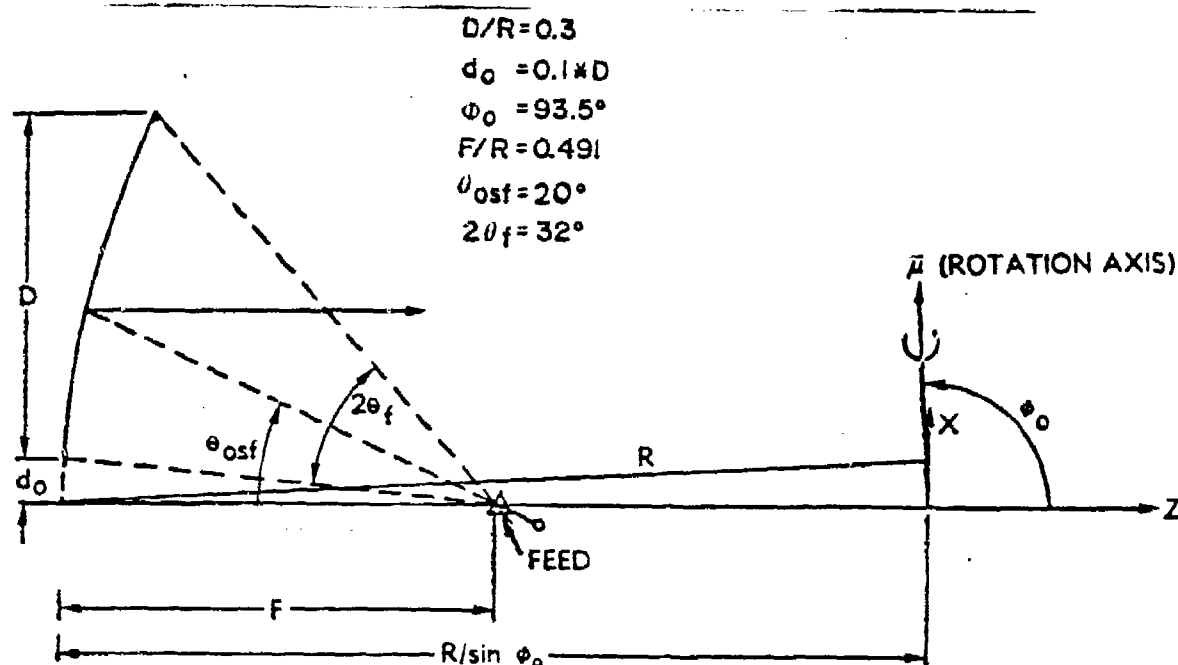


Figure 5-60. Offset MBTA $D/R = 0.3$ Geometry

The corrugated feed horn patterns minimize feed spillover energy past the reflector. In addition, the corrugated horn has exceptionally low backscatter patterns as a result of the highly tapered feed horn amplitude distribution. Electromagnetic fields are zero at the edges of the aperture. Hence, exterior currents, which would contribute to a backscatter pattern, are not induced on the outside of the horn.

The percentage of corrugated feed horn energy beyond a specified amplitude level is

$$\text{spillover} = \frac{\int_{\theta_0}^{180^\circ} \int_0^{360^\circ} P(\theta) \sin \theta \, d\theta \, d\phi}{\int_0^{180^\circ} \int_0^{360^\circ} P(\theta) \sin \theta \, d\theta \, d\phi} \quad (5-120)$$

where θ_0 is one-half the feed illumination angle.

With a rotationally symmetric feed amplitude pattern, the feed spillover beyond a specified illumination half-angle is

$$\text{spillover} = \frac{\int_{\theta_0}^{180^\circ} P(\theta) \sin \theta \, d\theta}{\int_0^{180^\circ} P(\theta) \sin \theta \, d\theta} \quad (5-121)$$

Figure 5-61 shows the spillover characteristics of corrugated feed horns with beamwidths applicable to the offset MBTA geometries. A -10-dB edge taper over the $2\theta_f = 24.4^\circ$ feed illumination angle of the baseline $D = 27$ ft, $D/R = 0.4$ geometry gives less than 0.57 dB of spillover. Increasing the edge taper to -15 dB reduces the spillover to 0.18 dB.

The lack of aperture blockage and forward feed spillover past a subreflector results in excellent wide-angle sidelobes for the MBTA. Aperture blockage raises the average sidelobe level and is a major source of wide-angle scatter in large-aperture antenna systems. Forward feed spillover in Cassegrain geometries partially couples to a warm earth and generally gives rise to a significant sidelobe contribution along the geostationary arc at an angle off the beam axis that corresponds to the feed spillover angle past the subreflector. The gain (in dBi) of this sidelobe contribution is the feed system gain at the specified angle if the feed spillover contribution is significantly larger than the sidelobe contribution of the reflector aperture illumination.

Figure 5-62 shows the aperture illuminated areas on the MBTA for beams at the center and edge of the field of view. For the majority of beam positions, most of the feed "spillover" past the circular illumination area is collimated by the reflector and appears in the main beam.

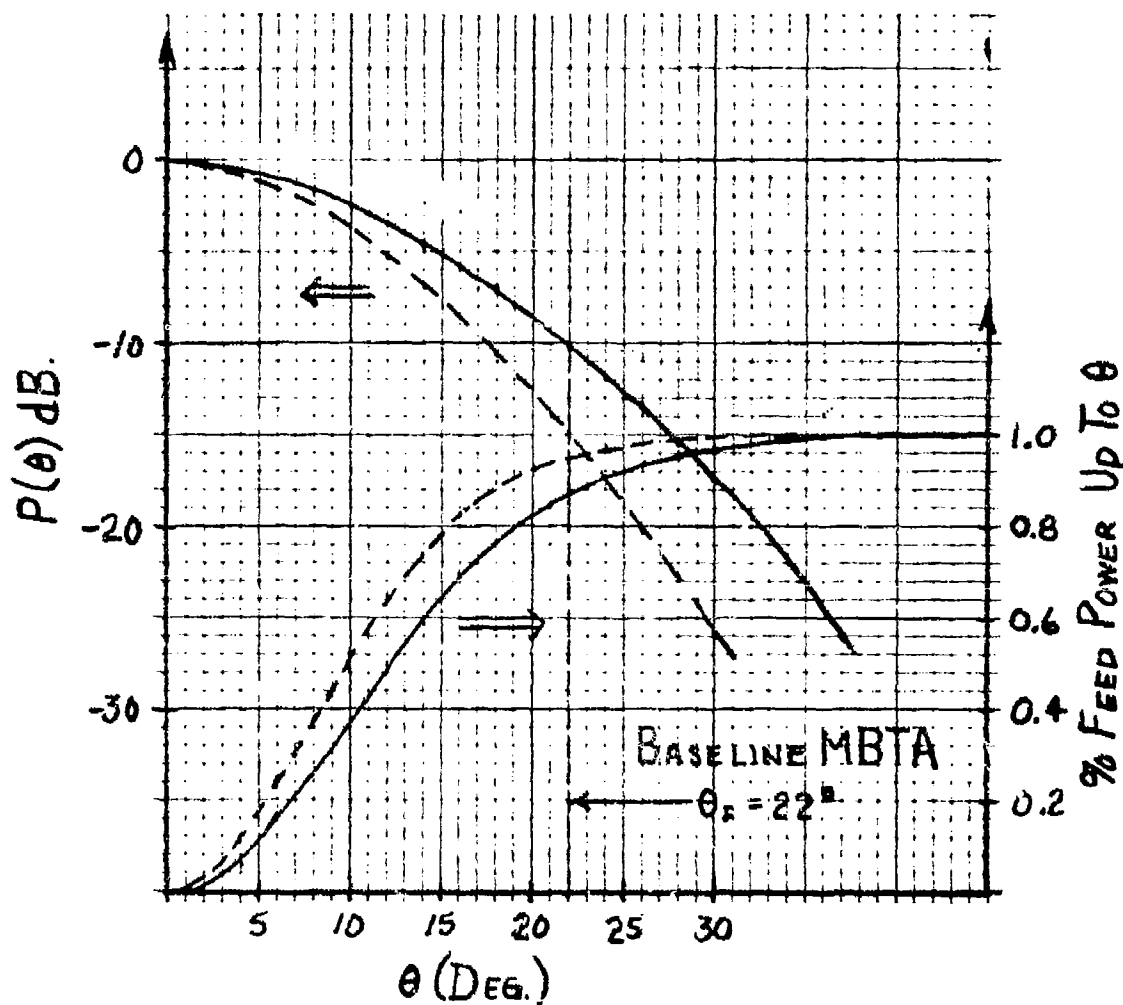


Figure 5-61. Spillover Characteristics of Corrugated Feed Horn for Baseline MBTA

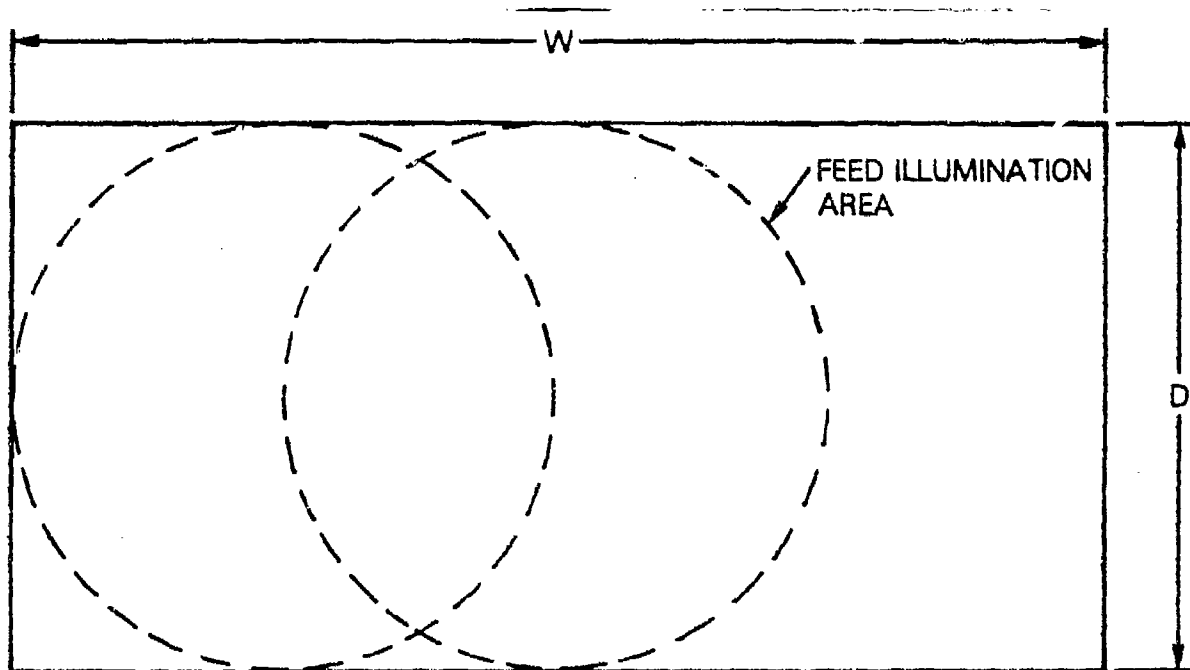


Figure 5-62. Extended MBTA Aperture Area
Decreases Feed Spillover

The calculated antenna temperature characteristics of the offset MBTA at X-band are shown in Figure 5-63 as a function of the local elevation angle. This curve, which is applicable to both the $D = 27$ ft and $D = 48$ ft MBTA geometries, includes 0.1-dB feed system losses. Additional losses would add

$$T_{\text{FEED LOSS}} (K) \approx \text{loss (dB)} \left(\frac{7 K}{0.1 \text{ dB}} \right) \quad (5-122)$$

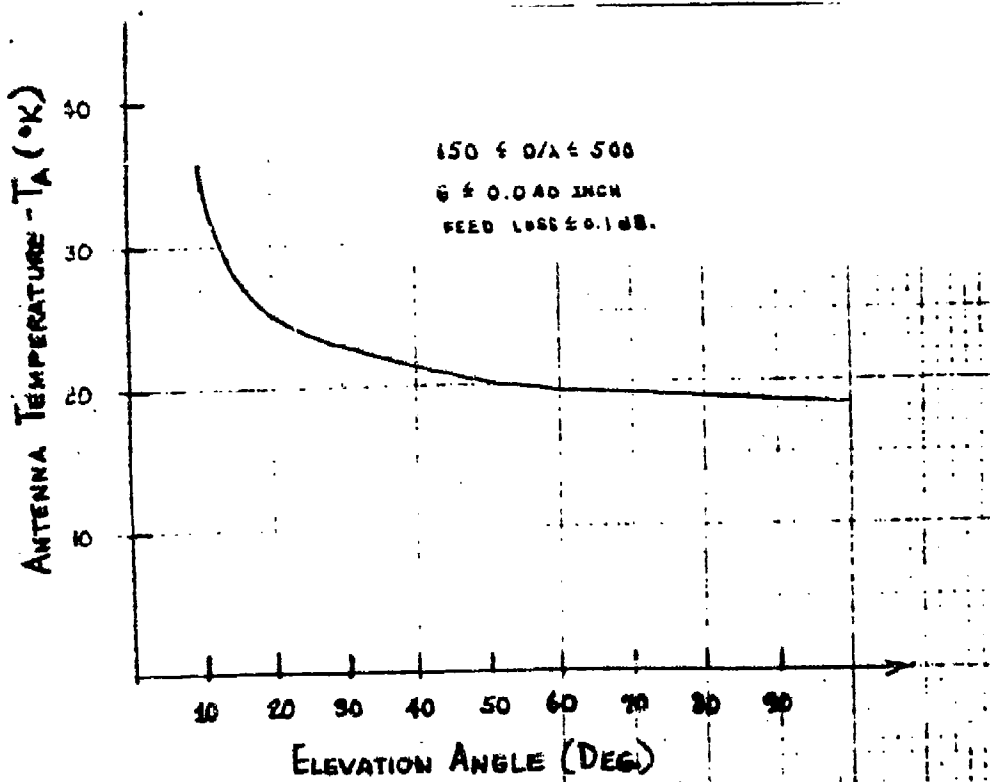


Figure 5-63. MBTA Antenna Temperature at X-Band

5.15

ABERRATION-CORRECTING SUBREFLECTORS

Aberration-correcting subreflectors²⁰ have been investigated at COMSAT Laboratories as a means of obtaining better aperture illumination efficiencies in large-aperture ($D/\lambda \geq 300$) offset MBTA antennas. The correcting subreflector concept, shown in Figure 5-64, involves the design of a second reflecting surface between the aperture plane of the MBTA and a designated feed position so that the path length from any point in the aperture to the feed position is identical. To realize a reasonably shaped

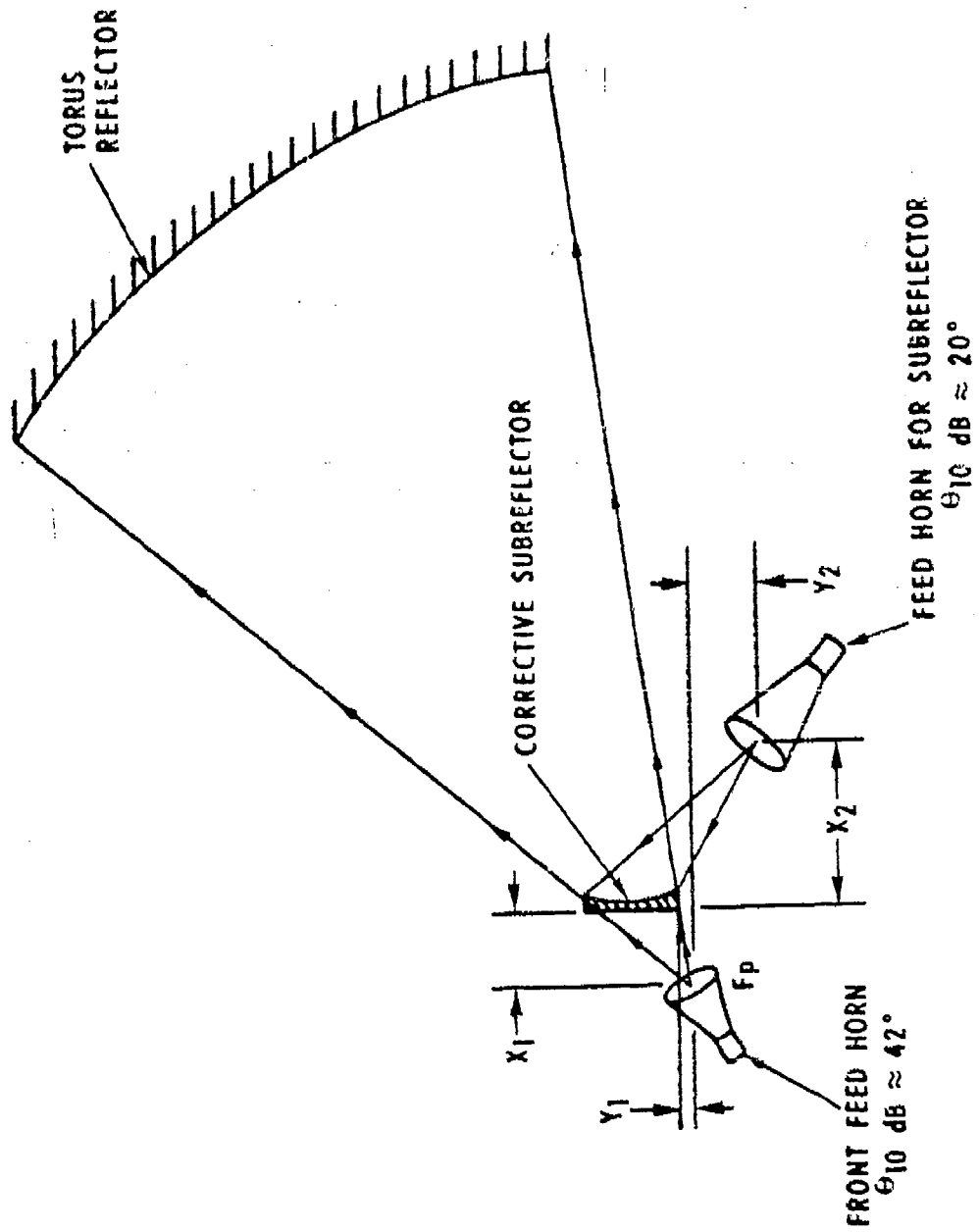


Figure 5-64. MBTA with Phase Corrective Subreflector

subreflector design, it was found necessary to displace the parabolic and spherical foci of the MBTA. Hence, because the corrected MBTA reflector has very poor efficiency when utilized with a focal point feed, all frequency bands (ranges of D/λ) that utilize the corrected MBTA configuration must operate in conjunction with a correcting subreflector.

In principle, a correcting subreflector could improve the aperture illumination efficiency associated with the smaller radius of curvature MBTA design ($D/R = 0.5$) and permit the use of smaller aperture dimension ratios (W/D) for a specified field of view. The correcting subreflector surface is lossless and a simple feed horn is used.

There are several disadvantages associated with the use of an aberration-correcting subreflector. The first is the mechanical complexity associated with the feed/subreflector system. The feed and subreflector must be carefully aligned and must maintain their alignment while both travel on different radii of curvature to scan the beam. For larger aperture X-band antennas, the subreflector diameter would typically be 5-10 ft and the precision subreflector surface required would have to be protected.

Use of the aberration-correcting subreflector results in a considerable increase in the minimum beam spacing along the geosynchronous arc. Figure 5-65 shows that the diameter of the subreflector limits the minimum beam spacing rather than the diameter of the feed horn aperture. Figure 5-66 is a photograph of the correcting subreflector that was designed and tested on a 10-ft scale model torus at COMSAT Laboratories. The aberration-correcting torus demonstrated aperture illumination efficiencies of $\eta = 72$ percent for $D/\lambda \leq 430$. The 10-in. correcting subreflector diameter for the 10-ft scale model would correspond to 4 feet for a 48-ft-diameter MBTA.

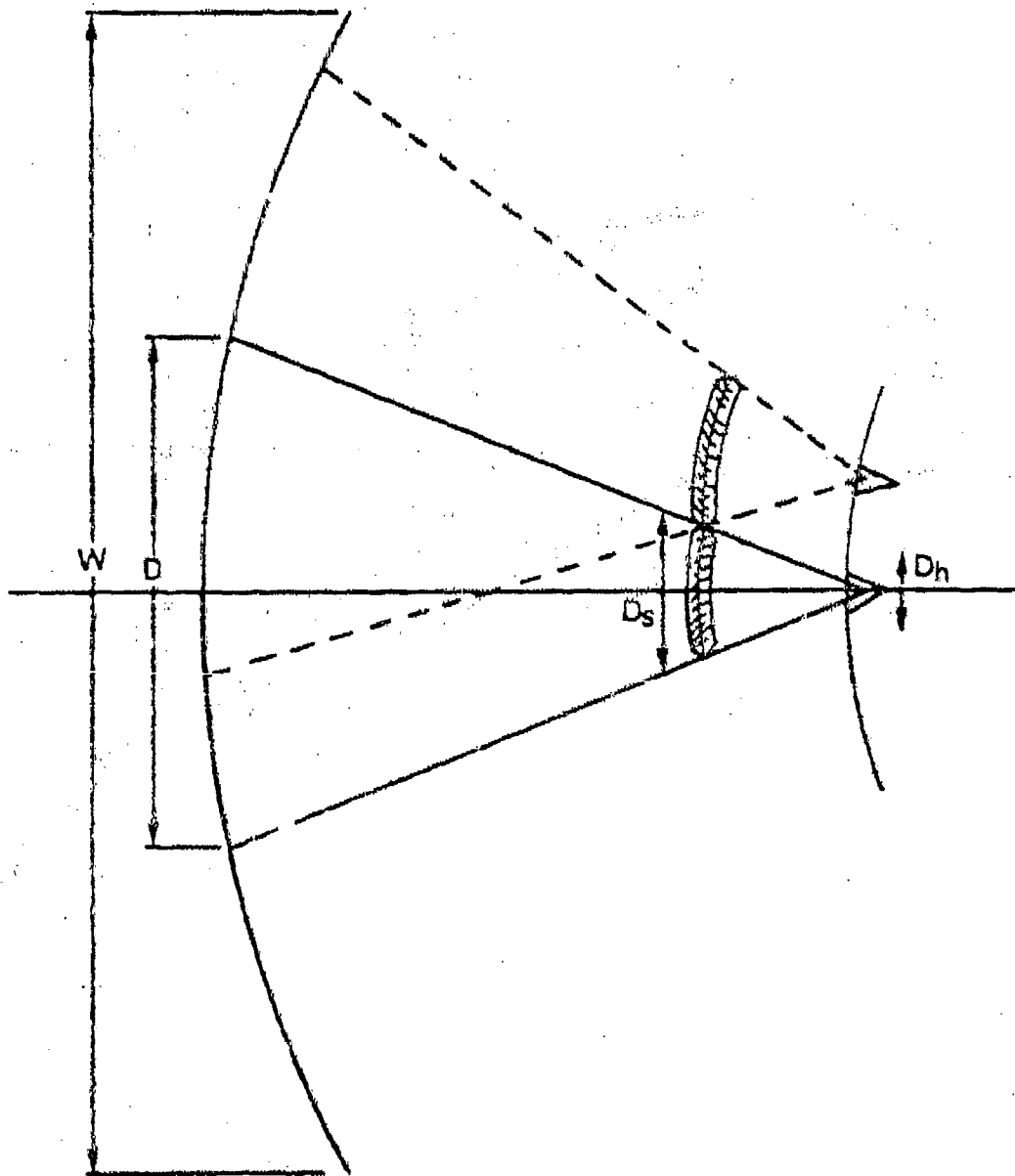


Figure 5-85. Correcting Subreflector Diameter in Geo-
synchronous Plane Limits Minimum Beam Spacing

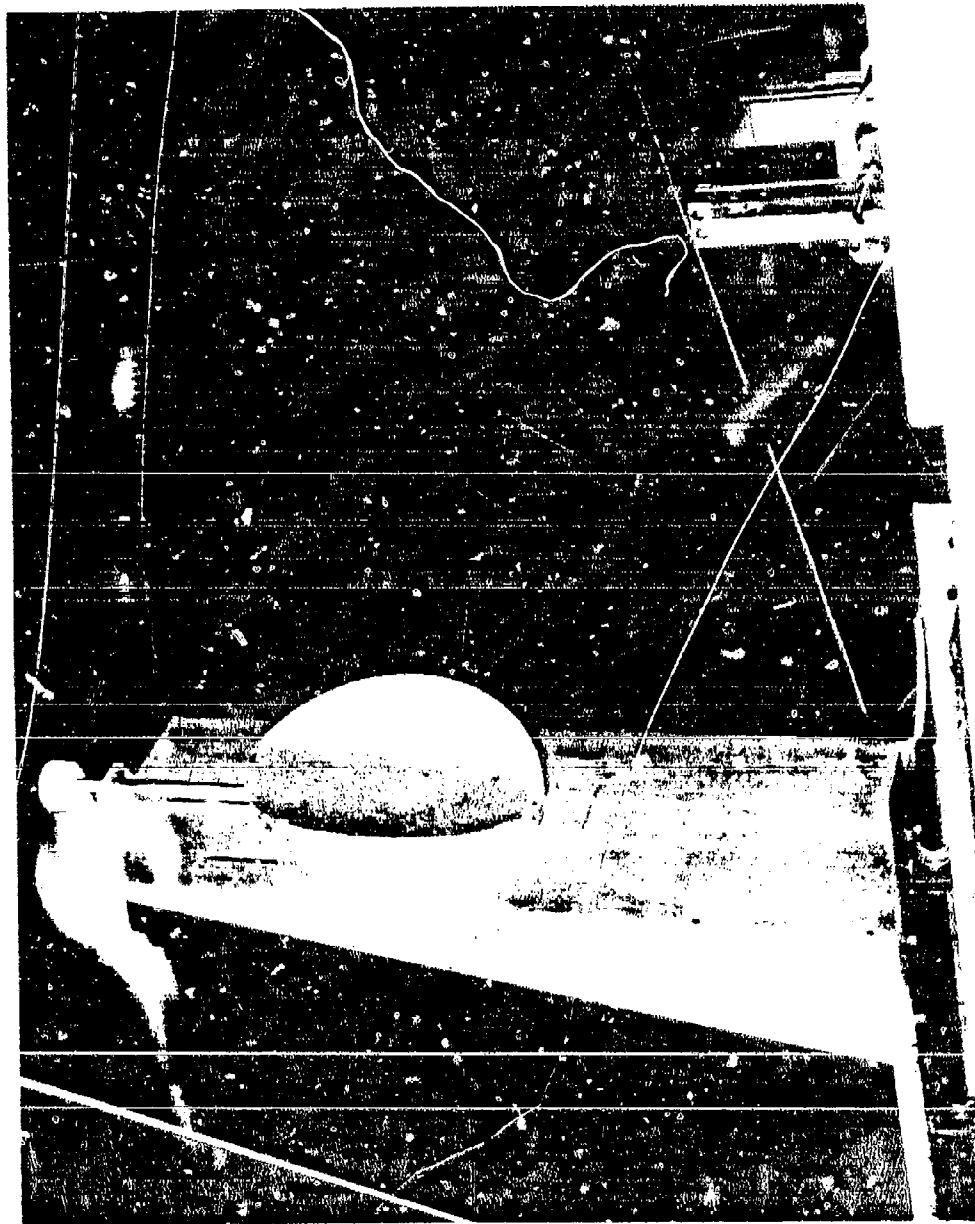


Figure 5-66. Phase-Corrective Subreflector Designed and
Tested at COMSAT Laboratories

5.16 ABERRATION-CORRECTING FEEDS

As a second method of offsetting the spherical aberration associated with large-aperture MBTAs, COMSAT Laboratories has developed a unique aberration-correcting feed system concept.²¹ The primary feed illumination phase pattern is designed to compensate for the spherical aberration phase errors^{22,23} of the reflector system. The feed system required to correct for spherical aberration effects has the characteristics shown in Figure 5-67. The amplitude pattern is rotationally symmetric. The phase patterns, which are uniform in the plane of the parabolic section, have a phase characteristic in orthogonal directions which is the inverse of the phase error introduced by the spherical aberration of the reflector.

A simple 3-element array implementation of an aberration-correcting feed system is shown in Figure 5-68. If the element pattern factors associated with the central and outer elements are respectively $\cos^{n1}(x_1\theta)$ and $\cos^{n2}(x_2\theta)$, the feed array voltage becomes

$$E(\theta, \phi) = \cos^{n1}(x_1\theta) + 2a \cos^{n2}(x_2\theta) e^{j\delta} \cos\left(2\pi \frac{d}{\lambda} \sin \theta \sin \phi\right) \quad (5-123)$$

The greatest amount of phase variation in the $\phi = 90^\circ$ plane is obtained for a given outer element amplitude weight, a , by setting

$$\delta = \pm 90^\circ \quad (5-124)$$

The phase pattern in the non-arrayed plane is then

$$\psi(\theta, 0^\circ) = \tan^{-1} \left[\frac{2a \cos^{n2}(x_2\theta)}{\cos^{n1}(x_1\theta)} \right] \quad (5-125)$$

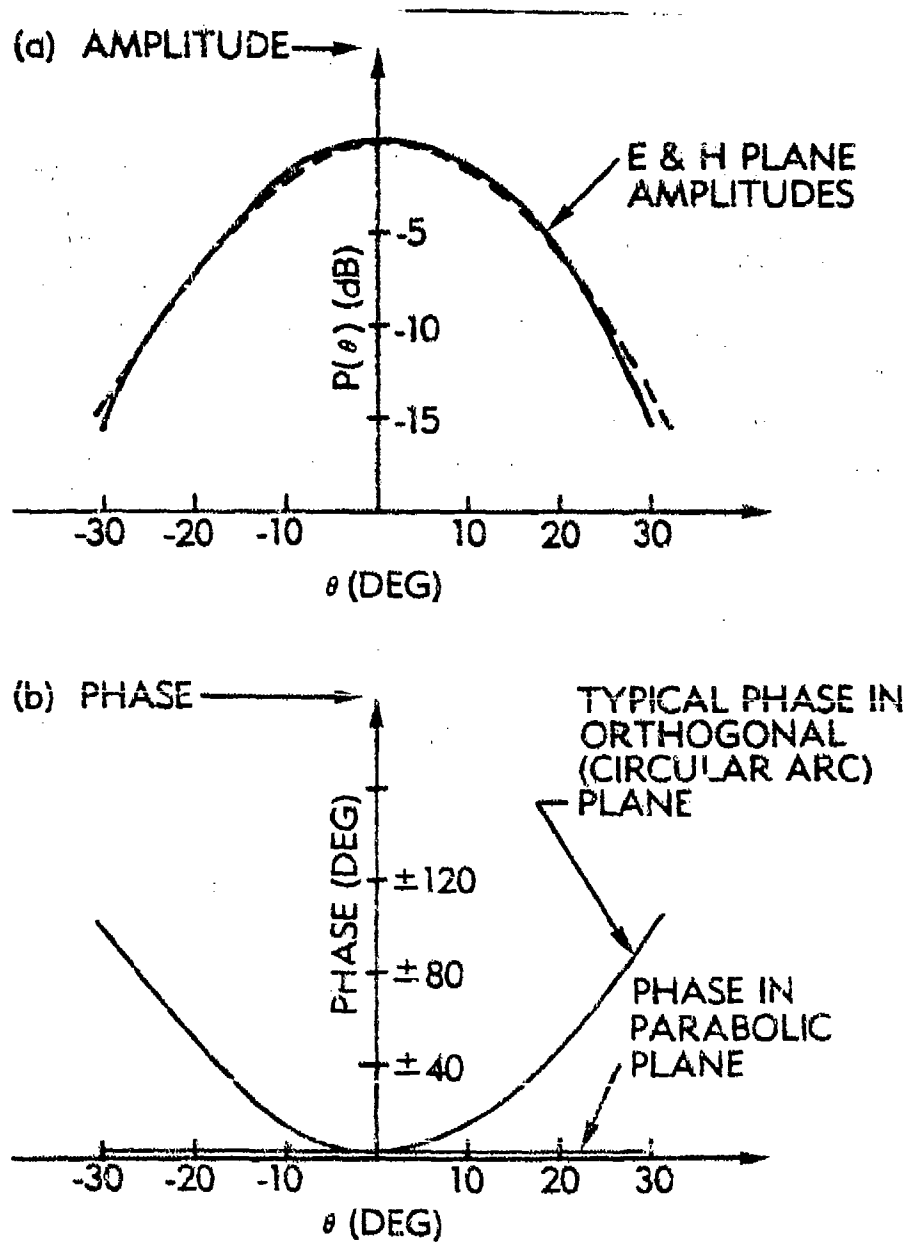


Figure 5-67. Primary Pattern Characteristics of Aberration-Correcting Feed System

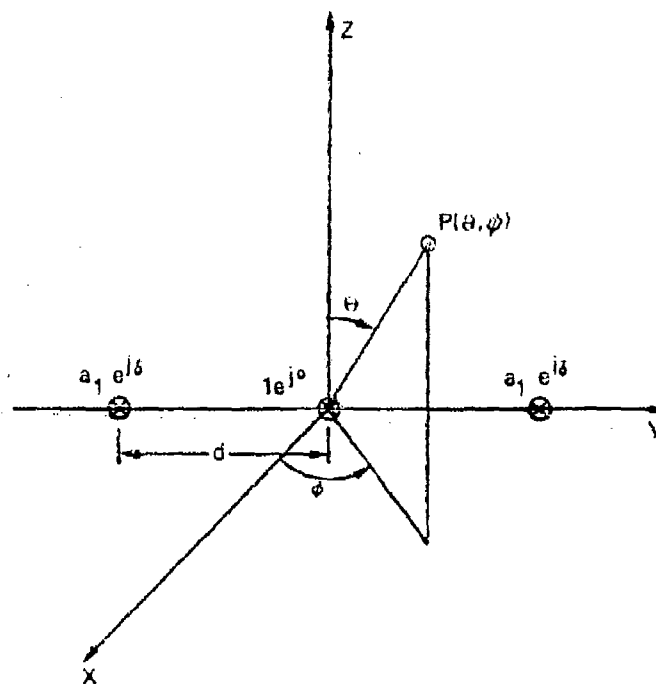


Figure 5-68. 3-Element Aberration-Correcting
Feed Array

A uniform phase (independent of θ) requires identical
element patterns

$$\cos^{n_1}(x_1\theta) = \cos^{n_2}(x_2\theta) \quad (5-126)$$

The phase pattern in the arrayed plane then becomes

$$\psi(\theta, 90^\circ) = \tan^{-1} \left[2a \cos \left(2\pi \frac{d}{\lambda} \sin \theta \right) \right] \quad (5-127)$$

The amplitude of this phase distribution is determined primarily by a , the relative voltage weight of the two outer array elements; the spatial distribution is determined primarily by d/λ , the feed element diameters. Figure 5-69 shows the amplitude and phase patterns of a 3-element array. There is generally a tradeoff between the desired amplitude and phase patterns. In terms of transmission, the outer feed elements can be assumed to create "mini-beams" in the geosynchronous arc plane which are phased to narrow the beam provided by the central feed element.

Figure 5-70 shows 5- and 7-element array feeds that provide additional degrees of freedom in realizing aberration-correcting feed arrays. The corrected and uncorrected principal plane patterns of a symmetrical MBTA geometry ($D/\lambda = 1000$, $D/R = 0.5$) are shown in Figure 5-71. A 5-element array feed improves the directivity by 0.8 dB, and the overall aperture illumination efficiency, η , increases from 60 to 72 percent. The corrected and uncorrected patterns in the geosynchronous plane for an off-set MBTA ($D/\lambda = 820$, $D/R = 0.4$, and 10-percent offset) are compared in Figure 5-72. The directivity improves by 1.3 dB with a 4-element aberration-correcting feed.

Further work is necessary to fully evaluate the capabilities of aberration-correcting feed systems in the MBTA. The improvement in beam directivity must be weighed against increased feed system complexity and losses. One major advantage of the correcting feed system is that it is used with MBTA geometries designed for focal point feeds. Hence, lower frequency bands can utilize a single focal point feed, while higher frequency bands associated with increased spherical aberration can utilize an aberration-correcting feed array. Of course, the minimum beam spacing increases with the effective diameter of the aberration-correcting feed system.

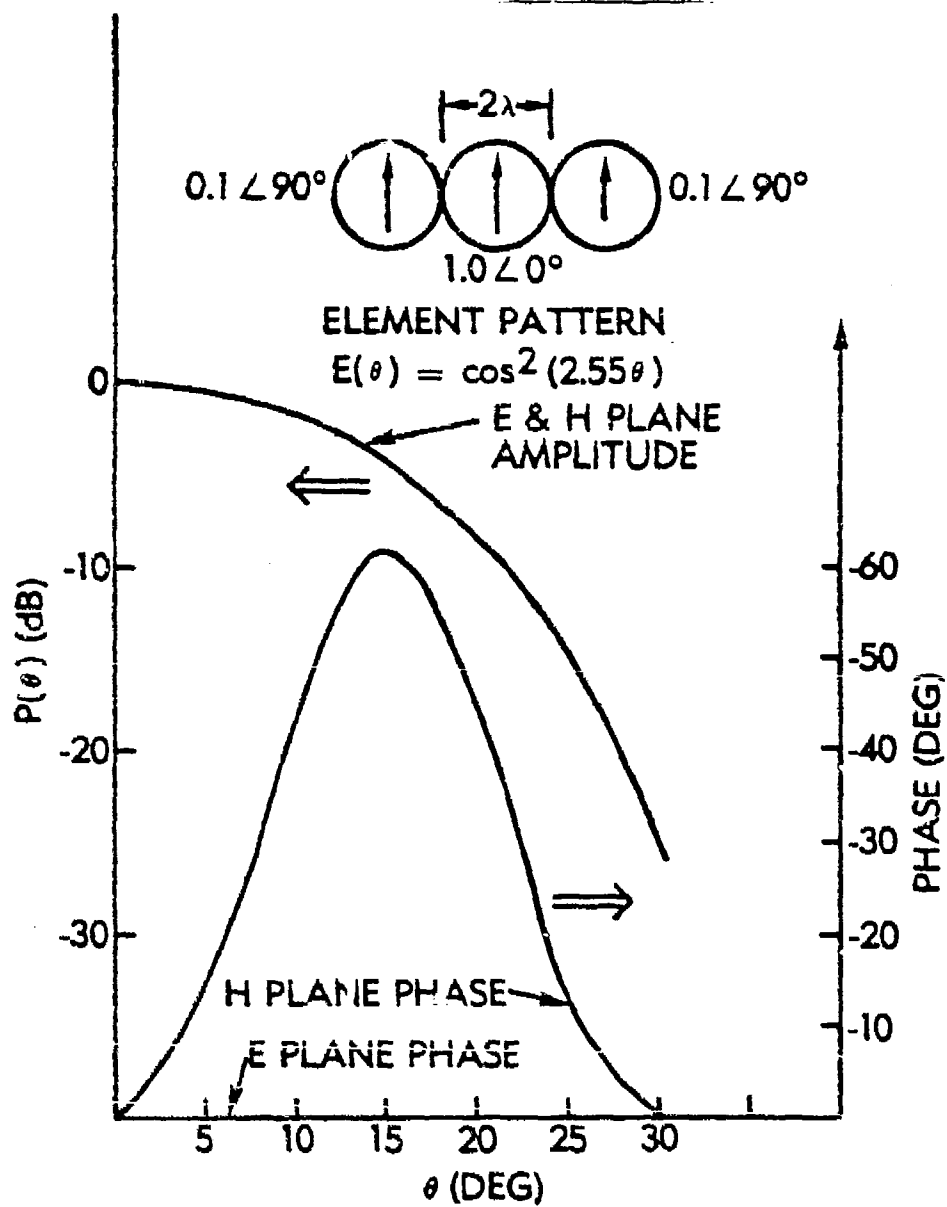


Figure 5-69. Primary Pattern Characteristics of 3-Element Aberration-Correcting Feed

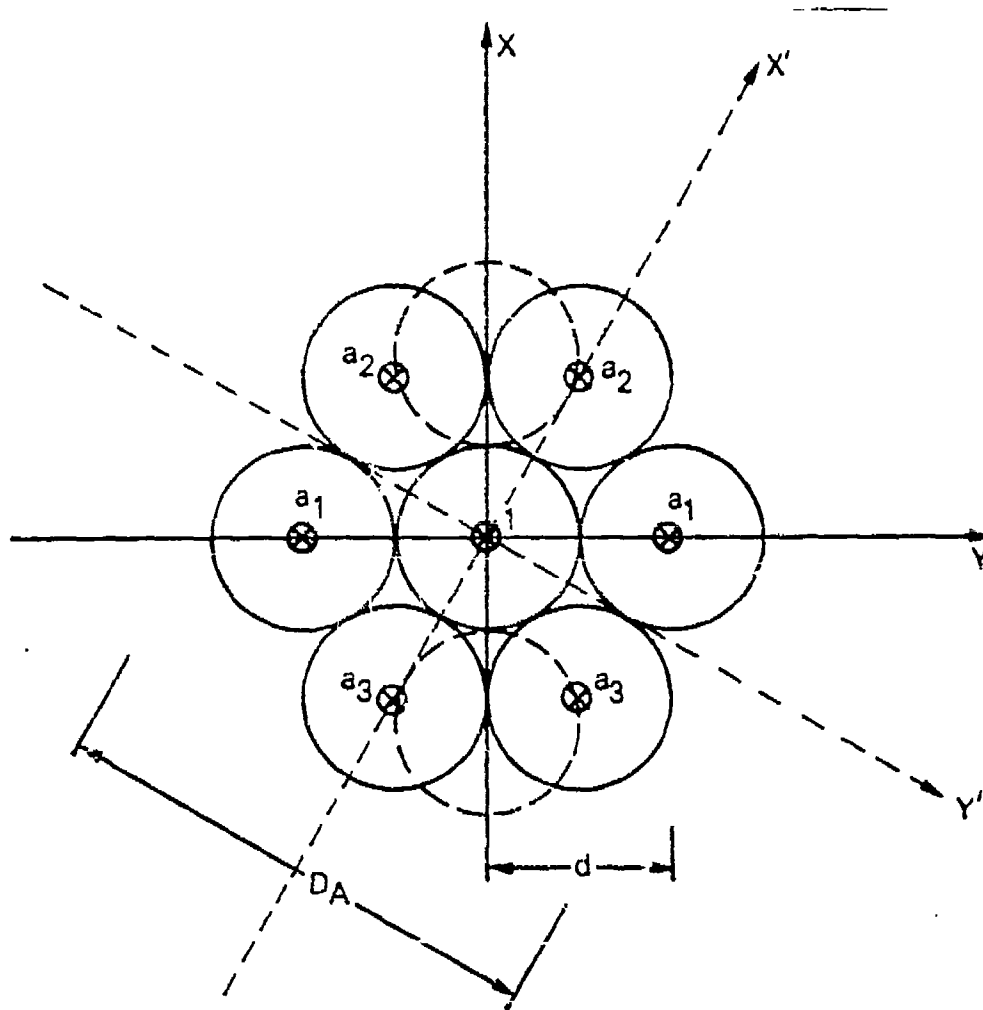


Figure 5-70. 7- (or 5-) Element Aberration-Correcting Feed Array

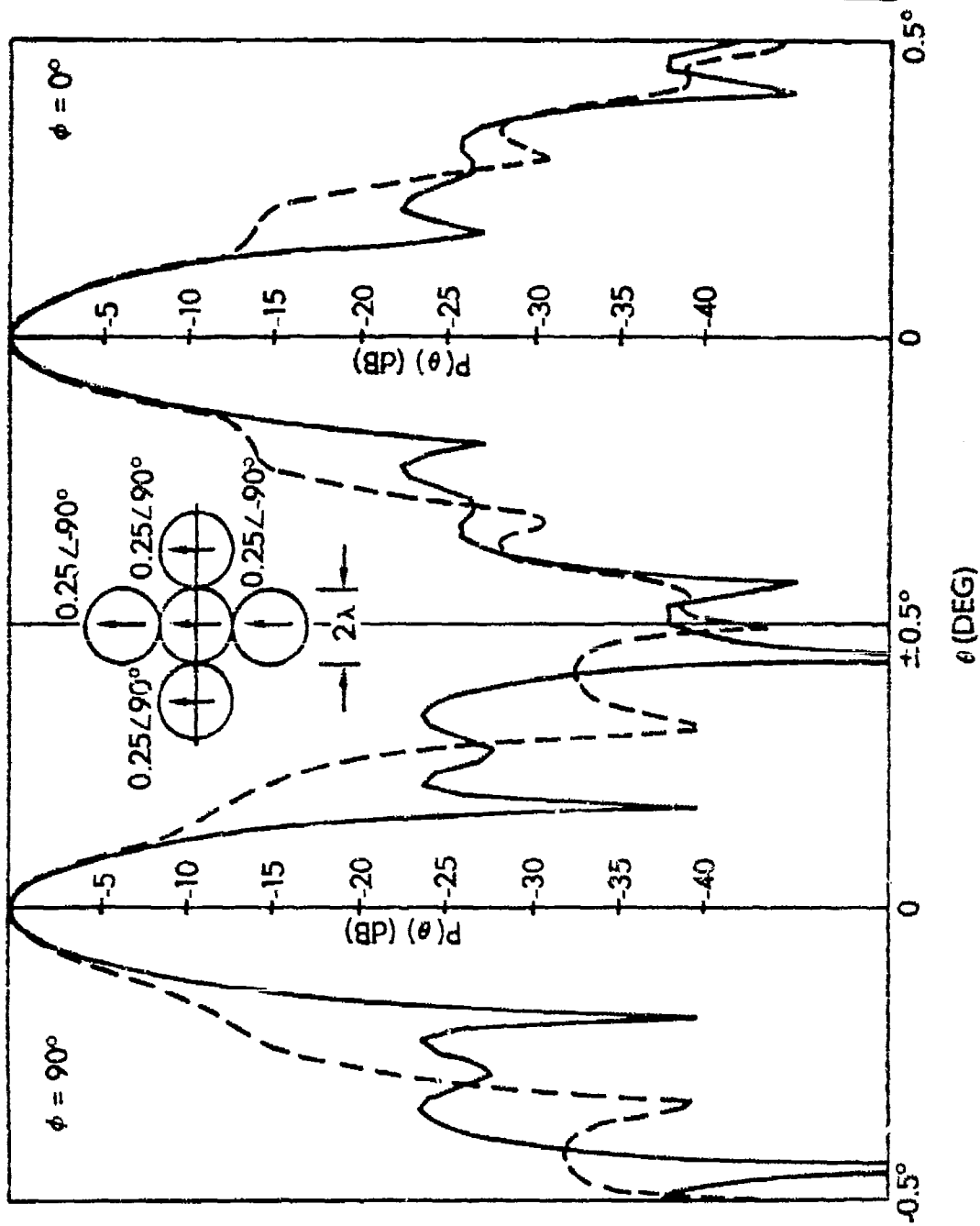


Figure 5-71. Symmetrical MBTA Patterns ($D/R = 0.4$, $D/\lambda = 1000$) with 5-Element Aberration-Correcting Feed

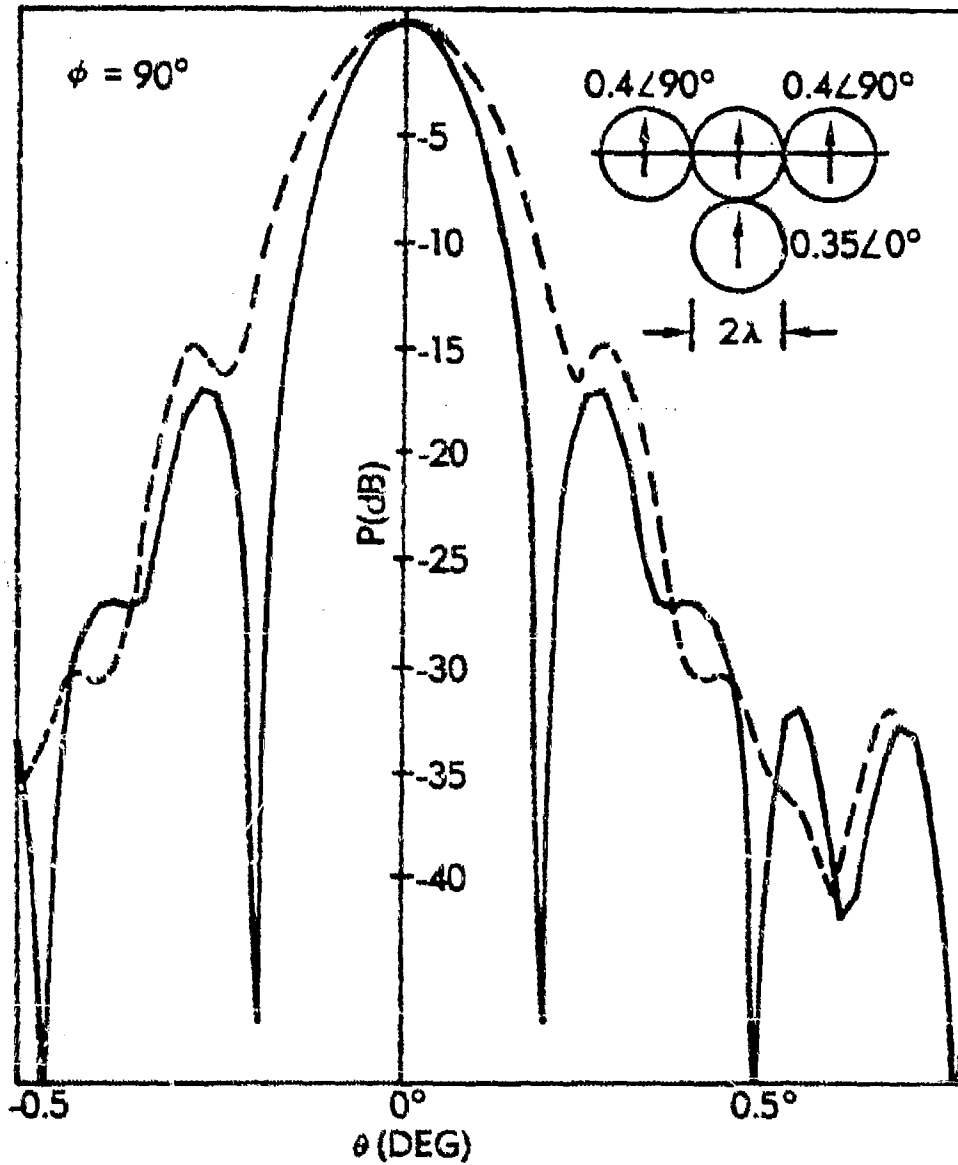


Figure 5-72. Offset MBTA Patterns ($D/R = 0.4$,
 $D/\lambda = 820$) with 4-Element Aberration-
Correcting Feed

6. MECHANICAL AND STRUCTURAL CHARACTERISTICS OF THE UNCORRECTED FRONT-FED MBTA

6.1 WORLDWIDE DEPLOYMENT CONSIDERATIONS

The decision to restrict detailed mechanical and structural analysis to the case of 54-dB gain at 7.25 GHz resulted in the selection of the 27-ft aperture as the basic MBTA to be considered. Fixing electrical performance parameters such as ϕ_0 , FOV, D/R, F/R, and D/ λ yields an overall mechanical description of the reflector as summarized in the specifications table. The projected aperture dimensions, W x D, are 60 x 27 ft (18 x 8 m), with the generating parabola vertex offset from the bottom edge of the reflector by 3 ft (0.9 m). The aperture width/diameter (W/D) parameter is related to the electrical parameters FOV and D/R as follows:

$$\frac{W}{D} = \left[\frac{\sin(\text{FOV})}{D/R} + 1 \right] = \left[\frac{\text{FOV}_{\text{RAD}}}{D/R} + 1 \right] \quad (6-1)$$

The amount of offset, d, of the bottom edge of the parabola from the feed center is based on mechanical criteria of feed rail support and expected building roof dimensions as well as the amount of parabolic plane beam scan required. This distance enables the construction of an enclosed feed structure without aperture area blockage.

The use of one reflector geometry for worldwide deployment by DSCS was possible once a single angle of generation,

$$\phi_0 = 93.5^\circ$$

was found to satisfy electrical performance criteria at all locations. The range of latitudes and differential longitudes to which the torus geometry is applicable varies from 0° to 75°, corresponding to locations with elevation angles greater than 5°.

Mechanical description of the single reflector/backup structure begins with the generating parabola definition,

$$x'' = \frac{z''^2}{4F} \quad (6-2)$$

where the focal length, F , is defined on the basis of parameters D , D/R , and F/R . Figure 6-1 shows the rotation of the generating parabola into the local coordinates system x, y, z according to the transformation

$$\begin{bmatrix} x \\ y \\ z \end{bmatrix} = \begin{bmatrix} \cos \alpha & 0 & \sin \alpha \\ 0 & 1 & 0 \\ -\sin \alpha & 0 & \cos \alpha \end{bmatrix} \begin{bmatrix} x'' \\ y'' \\ z'' \end{bmatrix} \quad (6-3)$$

where $\alpha = \phi_0 - 90^\circ$.

Figure 6-2 shows the derivation of the angle of circular rotation:

$$\beta = \text{FOV}^\circ + 2 \sin^{-1} \left[\frac{D}{2R_{\text{MID}}} \right] \quad (6-4)$$

where R_{MID} is the radius of curvature at reflector aperture height $d + D/2$. These two rotations define the parabolic torus surface in the local coordinate system. If a common backup structure is defined in the x, y, z system, as shown in Figure 6-3, it can be rotated with the reflector surface about angle β to form a universal structure with the same electrical performance regardless of location. The support structure becomes the means of translating the torus into its global coordinates.

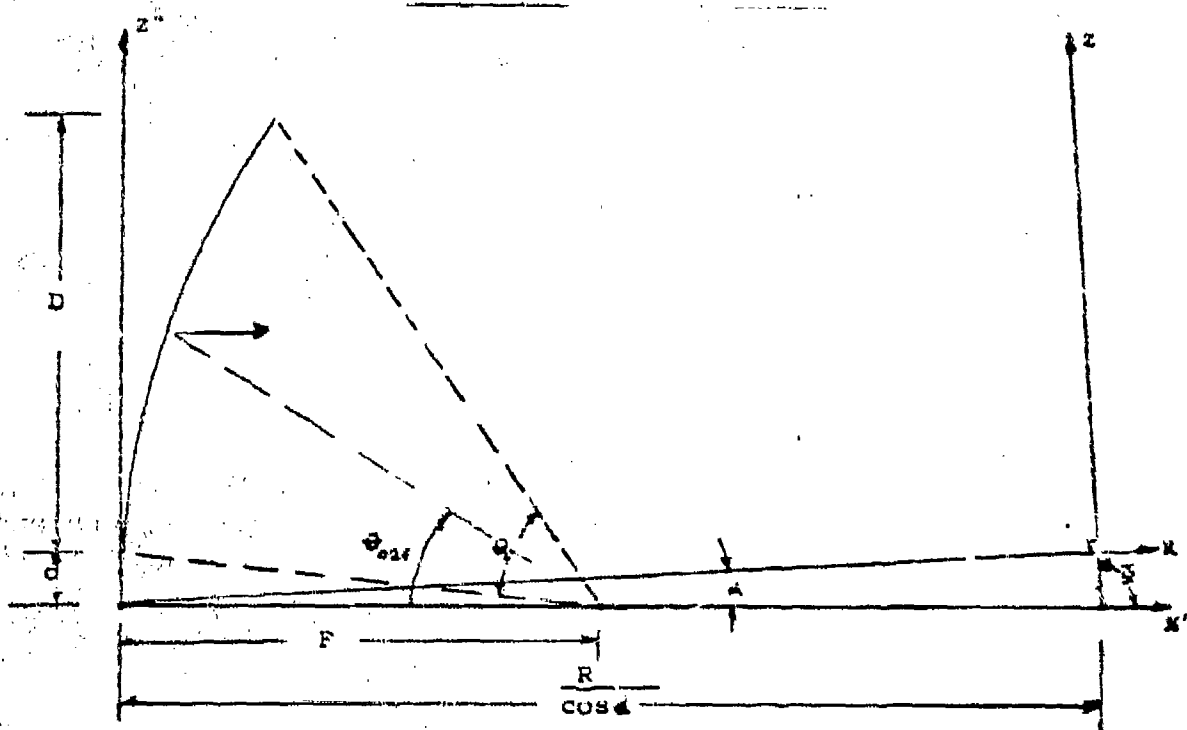


Figure 6-1. Offset Feed Configuration

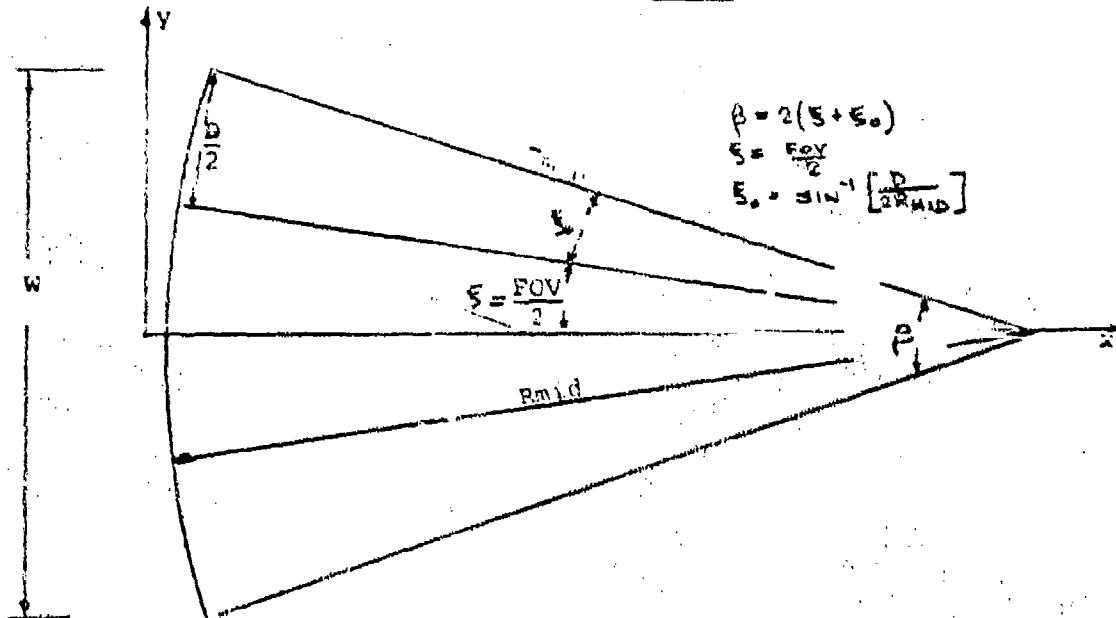


Figure 6-2. Circular Angle of Generation

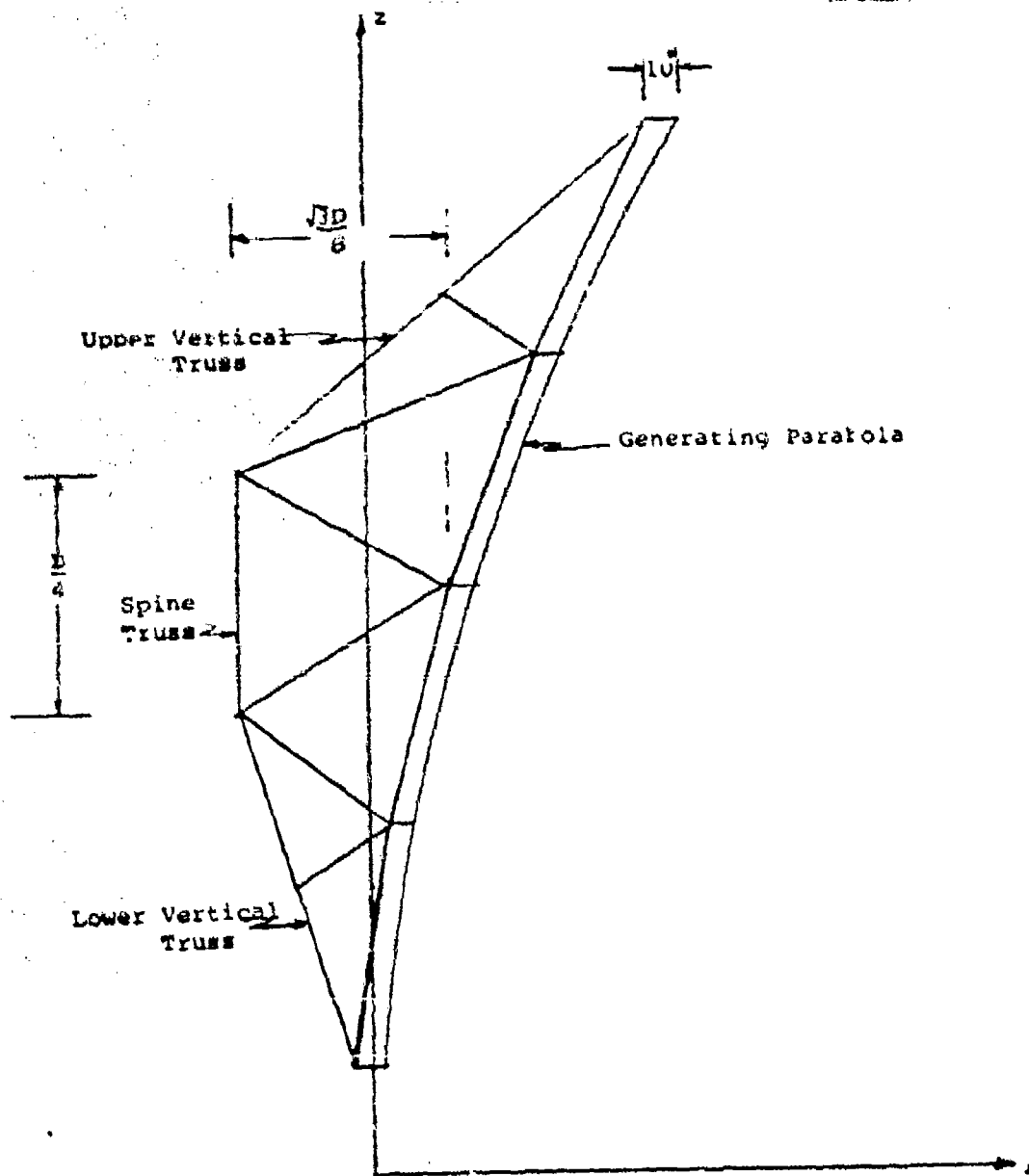


Figure 6-3. Typical 4-Panel Generating Truss

The relationship between the antenna local coordinates and the position-dependent global coordinates is defined via three angles: the surface generation angle, α , the elevation angle in the aperture plane, ξ , and the torus azimuth angle in the aperture plane, Ω . Angles ξ and Ω , which are functions of latitude, differential longitude from the earth station to the subsatellite position, and the ratios of earth radius to satellite orbit distance, are defined as²⁴

$$\xi = \tan^{-1} \left[\frac{\cos \phi \cos \lambda - m}{\sin \psi} \right] \quad (6-5)$$

$$\Omega = \tan^{-1} \left[\frac{(\sin^2 \psi - \cos^2 \phi)^{1/2}}{\cos \phi} \frac{m - \cos \psi}{(1 + m^2 - 2m \cos \psi)^{1/2}} \right] \quad (6-6)$$

where

- m = earth radius/satellite + earth radius
- ϕ = ground station latitude
- λ = longitudinal separation of ground station from the subsatellite position
- $\psi = \cos^{-1} [\cos \phi \cos \lambda]$

The mounting coordinates are found by translating the local coordinates through the three angles, as shown in Figure 6-4. The transformation relationship between the x, y, z and global X, Y, Z systems is

$$\begin{bmatrix} X \\ Y \\ Z \end{bmatrix} = \begin{bmatrix} \cos \alpha \cos \xi \cos \Omega & \cos \alpha \cos \xi \sin \Omega & \cos \alpha \sin \xi \\ -\sin \alpha \cos \xi \cos \Omega & -\sin \alpha \cos \xi \sin \Omega & -\sin \alpha \sin \xi \\ \sin \alpha \sin \xi & 0 & \cos \alpha \cos \xi \end{bmatrix} \begin{bmatrix} x \\ y \\ z \end{bmatrix} \quad (6-7)$$

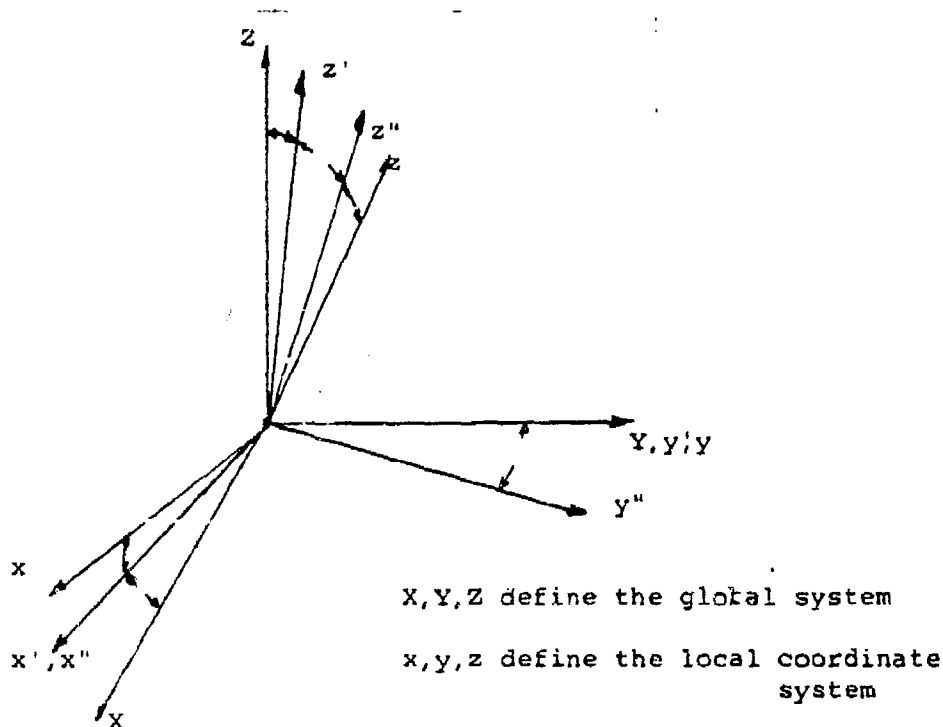


Figure 6-4. Coordinate System Rotation Angles

For the analysis five sites, listed in Table 6-1, have been chosen to represent the diversity resulting from worldwide deployment of the MBTA. These sites, which represent the potential spread of the differential longitude and latitude of existing DCA antennas, are chosen relative to a central satellite location at $333^{\circ}00'00''$ E longitude. The locations of COMSAT Labs (Fort Dietrick) and Sweden represent the majority of stations for θ between 20° and 60° latitude and 20° to 60° differential longitude. Iceland represents the case of extreme latitude, but the antenna mounting does not change radically from the previous case.

Table 6-1. Representative Sites for Worldwide
MBTA Deployment

Site	Longitude	Latitude	Differential Longitude
Mt. Margret	37°E	2°S	64°
Sweden	13°E	60°N	40°
Iceland	340°E	66°N	7°
Ascension Island	346°E	7°S	13°
COMSAT Laboratories	282.7°E	39.2°N	-50.3°

Mt. Margret and Ascension Island represent the two extreme siting locations. Only two DCA antenna sites appear to fall in the Ascension Island category of nearly horizontal aperture plane with the station at the subsatellite point. This case should not present any special mechanical problems, since its horizontal attitude precludes severe wind loading effects. The Mt. Margret location represents those earth stations at extreme differential longitude ($>60^\circ$) and low latitude ($<20^\circ$). Several DCA earth stations appear to fall in this category. This type of antenna attitude experiences the most severe environmental effects. If the same type of support structure is used for all antennas, it will provide the least stiffness for these locations due to the reflector's extreme height.

6.2 MECHANICAL CONSIDERATIONS

The electrical performance requirements are satisfied by a 27-ft reflector with $D/R = 0.4$. However, the mechanical problem is to maintain the stringent RF gain requirements, especially at higher frequencies. The relationship

$$G_L = 10 \log_{10} \exp \left[- \frac{4\pi\epsilon}{\lambda} \cos(\theta_{\text{osf}}) \right]^2 \quad (6-3)$$

defines the correspondence between gain degradation of the antenna (G_L) and the normal surface root-mean square (rms) deviation (ϵ), where λ is the beam wavelength, and θ_{osf} is the feed pointing angle.

The basic specifications require the design of one structure whose surface deformation is small enough under normal conditions to realize 54-dB gain at 7.25 GHz. A second iteration of the same structure was performed to further reduce surface errors to meet the more stringent requirements at 20 and 30 GHz. Figure 6-5 plots the curves of gain loss vs surface deviation in inches for the RF bands under consideration. The steep slope of the curves at higher frequencies emphasizes the performance limitations associated with surface tolerances above the 11/14-GHz bands. More gain loss must be allowed at these frequencies under the same environmental conditions. If the gain loss must be held to 0.5 dB under operational conditions at 20/30 GHz, a radome protective structure such as that shown in Figure 6-6 may be necessary.

For the baseline antenna, the maximum rms error considered was 0.040 in. (1 mm), allowing a maximum gain degradation of 0.5 dB at 8.4 GHz. The degraded performance specification was set at 0.060-in. (1.5-mm) deformation for 1-dB allowable gain loss in the 7/8-GHz band. The effect of restricting surface deformation to 0.020 in. (0.5 mm) was investigated for higher frequency antenna performance. In this case, the gain loss is restricted to 0.75 dB at 20 GHz and 1.5 dB at 30 GHz. Design iterations were performed to identify the required structural characteristics for achieving 0.040- and 0.020-in. surface tolerances.

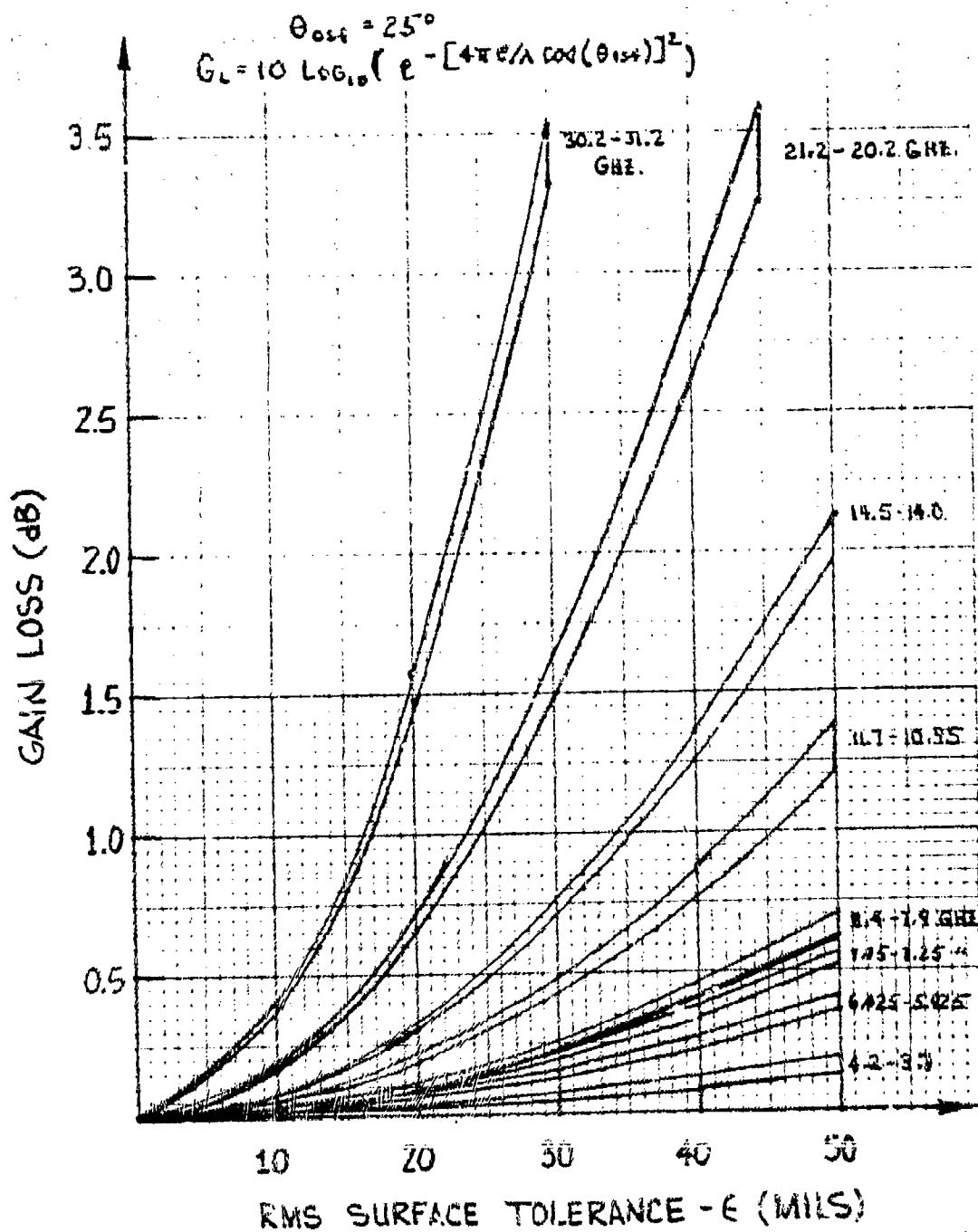


Figure 6-5. Gain Loss of MBTA vs rms Surface Tolerance, ε

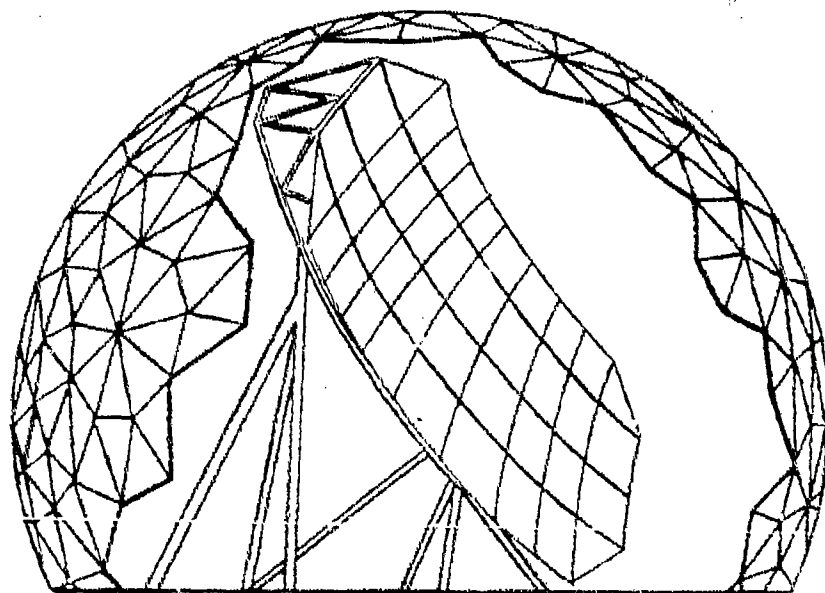


Figure 6-6. MBTA with Radome Environmental Protection

The feed transport mechanism considered for the study is based on a design that has been built and tested at COMSAT Labs.²⁵ Although the transport shown in Figures 6-7 and 6-8 utilizes a front rail support upon the wall of the building, a bottom rail support may be used so that the transport will have an independent support and foundation.

The narrow width of the transport allows two adjacent feeds to be separated by approximately 2° . Additionally, the universality of the transport design permits it to operate at any azimuth angle in the aperture plane. The self-contained drive and support features of this transport allow any feed to be mounted with a wide variation in allowable center of gravity and feed weight.

The two orthogonal drives are capable of tracking both spacecraft diurnal motions and spacecraft station variations using an open-loop control system driven by a minicomputer.

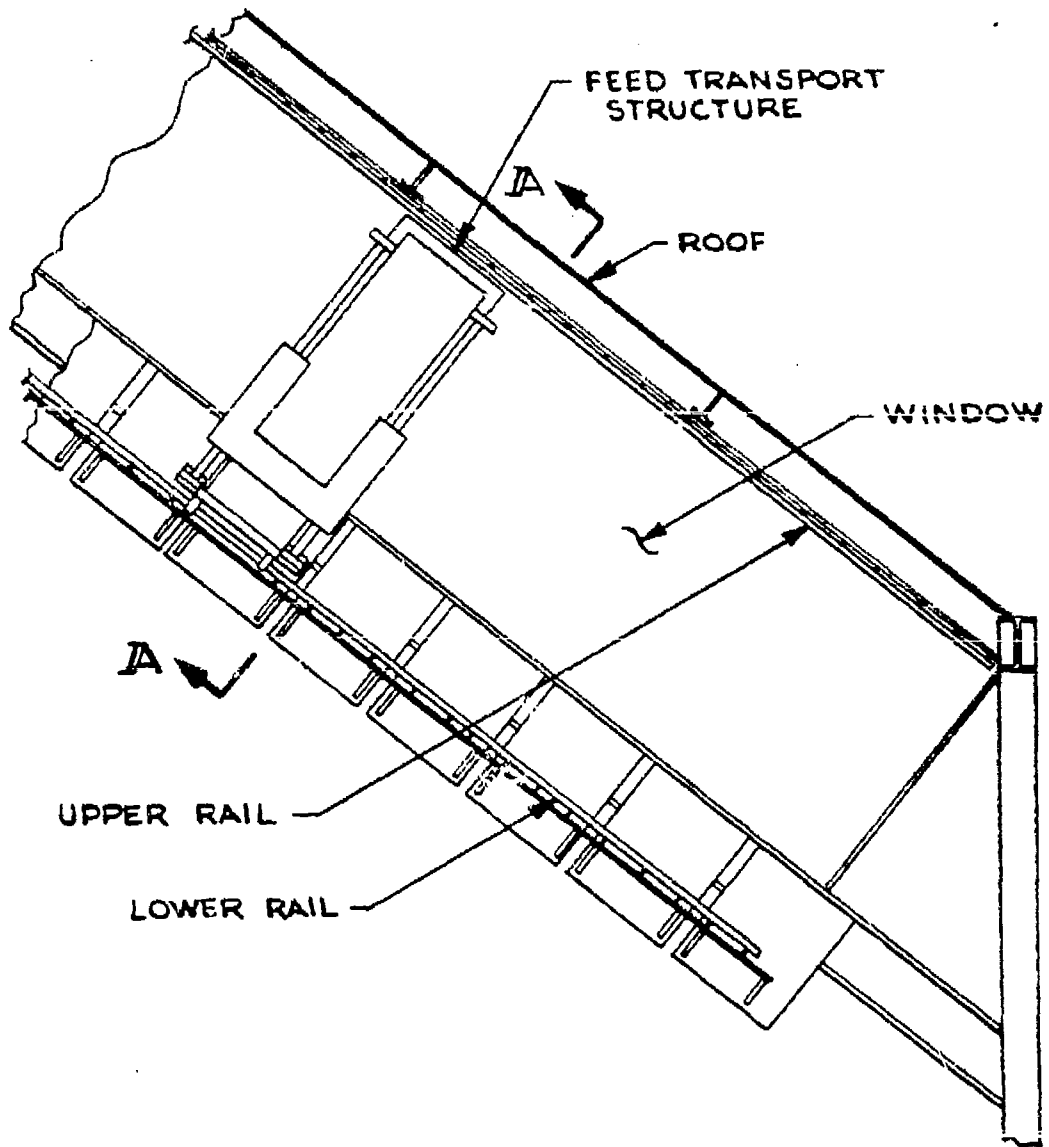


Figure 6-7. Existing Feed Transport Mechanism Support

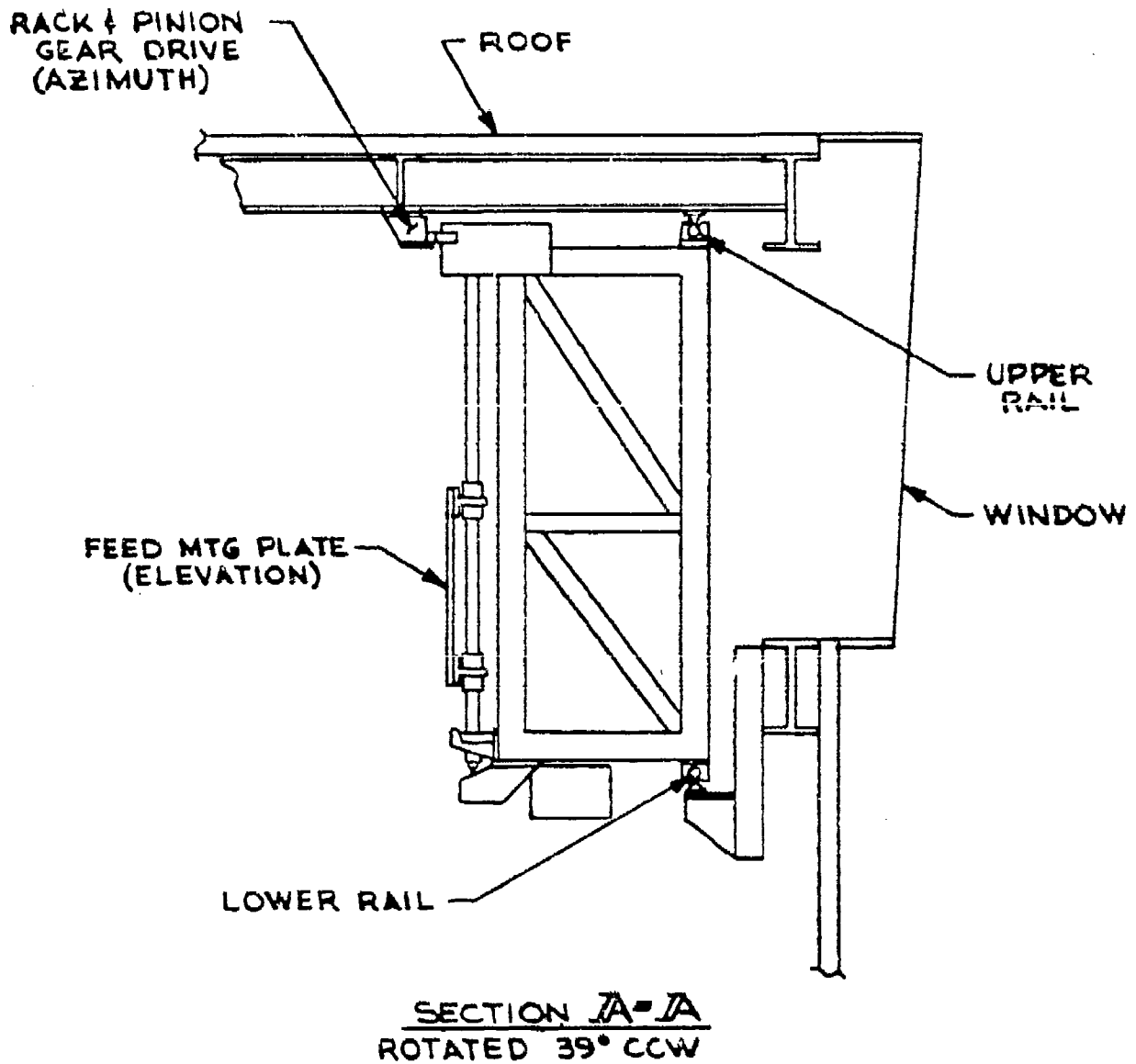


Figure 6-8. Orthogonal View of Feed Transport Mechanism Support

can be reduced by minimizing the number of parabolic panels. However, other considerations including handling, storage, and shipping become important, especially as the aperture diameter size increases. Figure 6-10 shows the configuration that is considered optimum based on a tradeoff study. For a reflector in the 27-ft-aperture-diameter range, a configuration of four parabolic and eight circular sections appears to be advantageous in terms of weight and complexity.

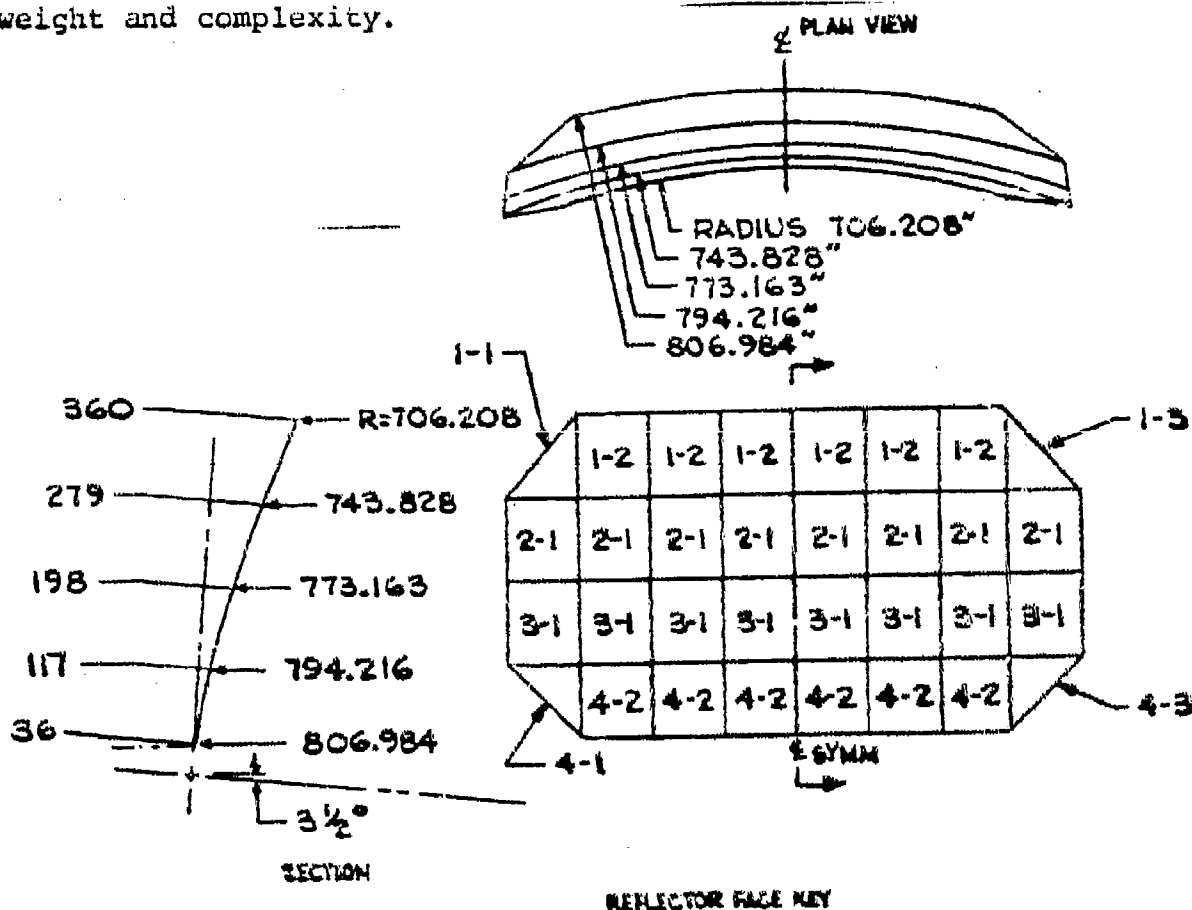


Figure 6-10. 27-ft MBTA Reflector Panel Configuration

The backup structure for this panel configuration requires a support at each panel corner, adequate stiffness, modularity, reasonable weight, simply erectable connections, and

universal applicability. Figure 6-3 shows the primary vertical members. A triangular spine truss is rotated about the axis of revolution, and a vertical truss is built around the spine at each circular panel section. The vertical members are stabilized by secondary horizontal trusses also following the curvature of the axis of revolution. Additional diagonal bracing is added during structural analysis to obtain the required structural stiffness and mechanical performance. Figure 6-11, which shows a typical backup truss, indicates the location of diagonal members and vertical and horizontal trusses. The reflector surface would be tied into the backup truss through adjustable support mechanisms to enable the maintenance of proper panel alignment and contour and thermal stress relief between the aluminum panels and steel members.

A 3-point pickup support enables perfect alignment of the elevation and tilt angles of the reflector during erection. However, for a structure of 60 x 27 ft or more, the stiffness of only three supports would be inadequate to maintain performance even at lower frequencies. Consequently, a minimum of four support points has been adopted. The configuration shown in Figure 6-12 has the required stiffness for the 27-ft reflector at most locations under all specified conditions. For earth stations for which a more extreme positioning or tighter rms tolerance is required, a support of six or more points might be necessary (Figure 6-13).

The feed transport building is assumed to be a pre-engineered environmental enclosure for a cost-effective structure. To ensure that environmental effects do not result in beam deformation, the feed mechanism support is assumed to be independent of the enclosure's foundation. The minimum building size of 12 ft on a side accommodates other mechanical and electrical equipment and provides work room around the transport mechanism.

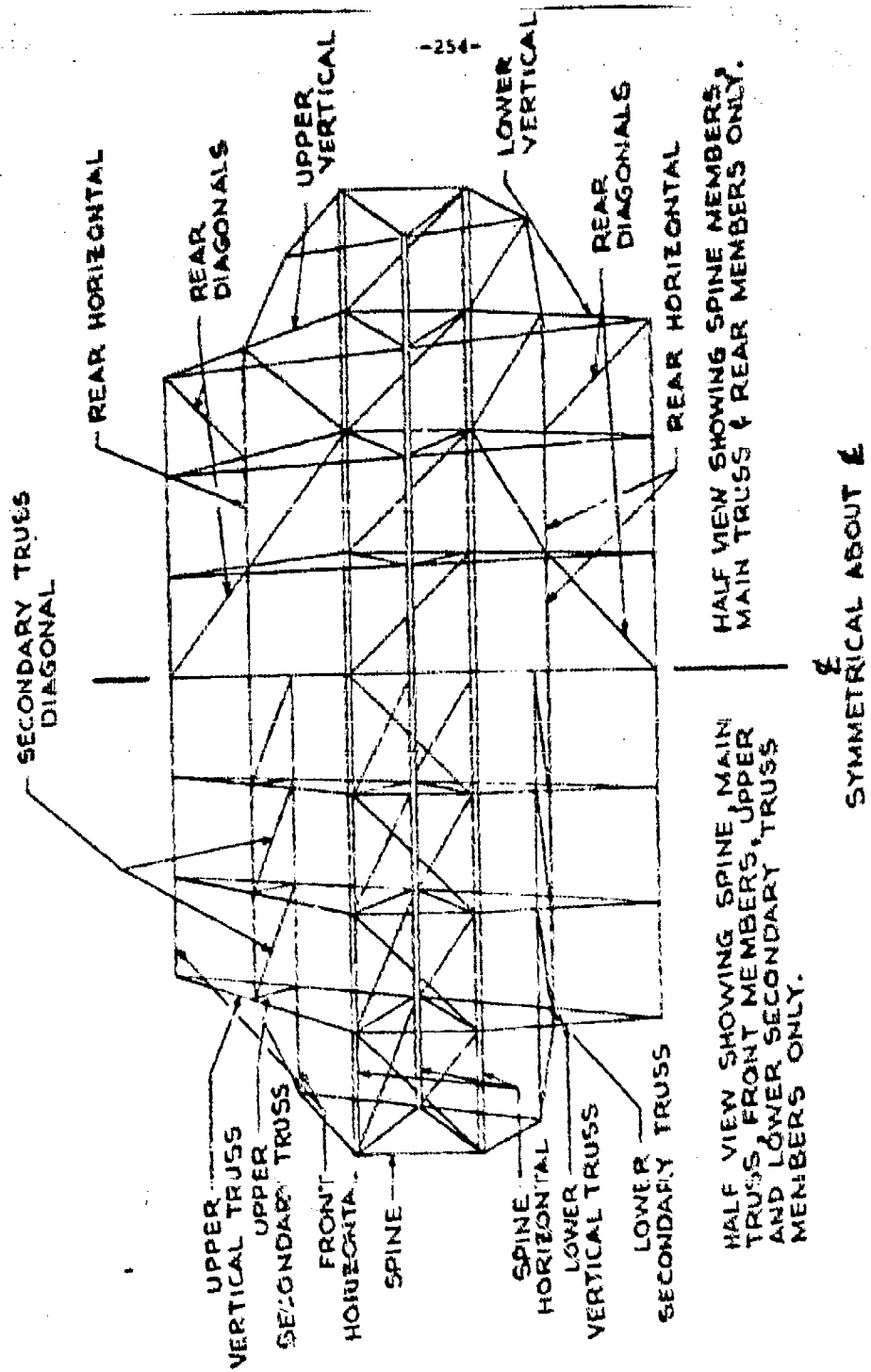


Figure 6-11. Detail of Backup Truss Members

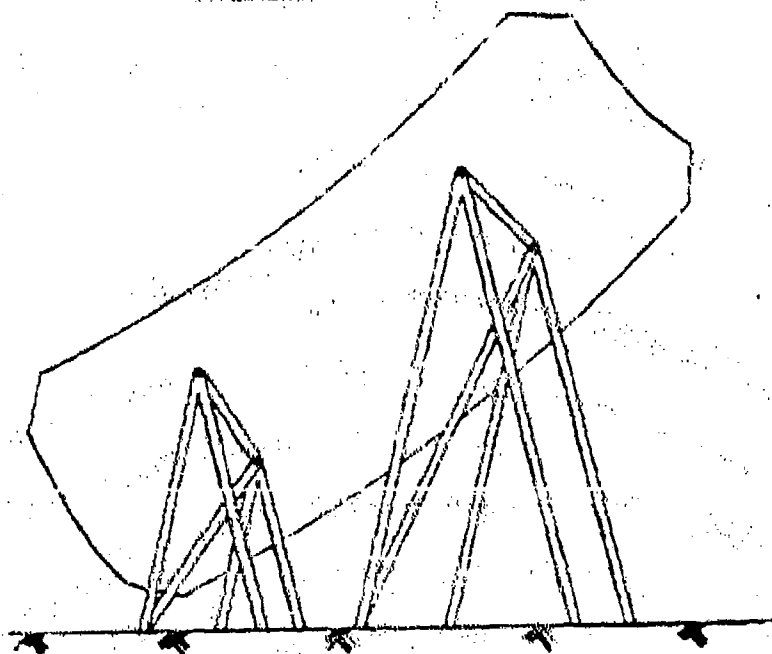


Figure 6-12. 4-Point Pickup Support Structure

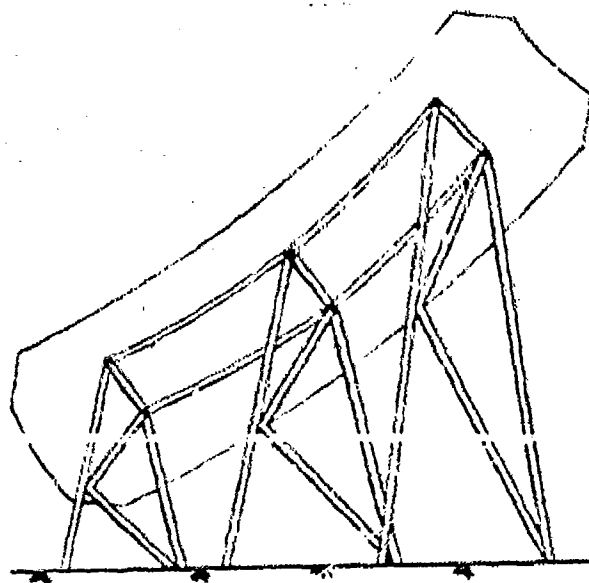


Figure 6-13. 6-Point Pickup Support Structure

6.4 APPLIED LOADS ANALYSIS

To design a universally applicable torus antenna, the basic system specifications have been used to define the required loading conditions for all members and the necessary RF performance of the final structure under those conditions. The basic forces applied to the MBTA structural model to test its performance are wind, gravity, and temperature variations. Of these three, wind loading is by far the most severe design condition.

6.4.1 GRAVITY

The deflection of the structure under its own weight is calculated alone and in combination with the other forces. Since gravity is a static load, its effects can be offset by applying a corrective deflection at each of the panel support points during erection.

6.4.2 WIND

The operational, degraded operational, and survival wind loads are defined in the specifications as 45, 60, and 125 mph, respectively. Wind forces are applied to the structure by calculating the wind pressure on the reflector panels according to the relationship²⁶

$$P = qC_DV^2 \quad (6-9)$$

where

- V = wind velocity in mph
- C_D = discharge coefficient = 1.4
- q = dynamic air pressure = 0.00256

The net force applied to each joint of the backup structure is the wind pressure times the projected panel surface area in the direction of the load. Both front and side wind forces are calculated to determine the worst-case conditions for design. The global X and Y axes are used to define front and side wind directions. Figure 6-14 demonstrates the variation in projected wind surface area with change in station location.

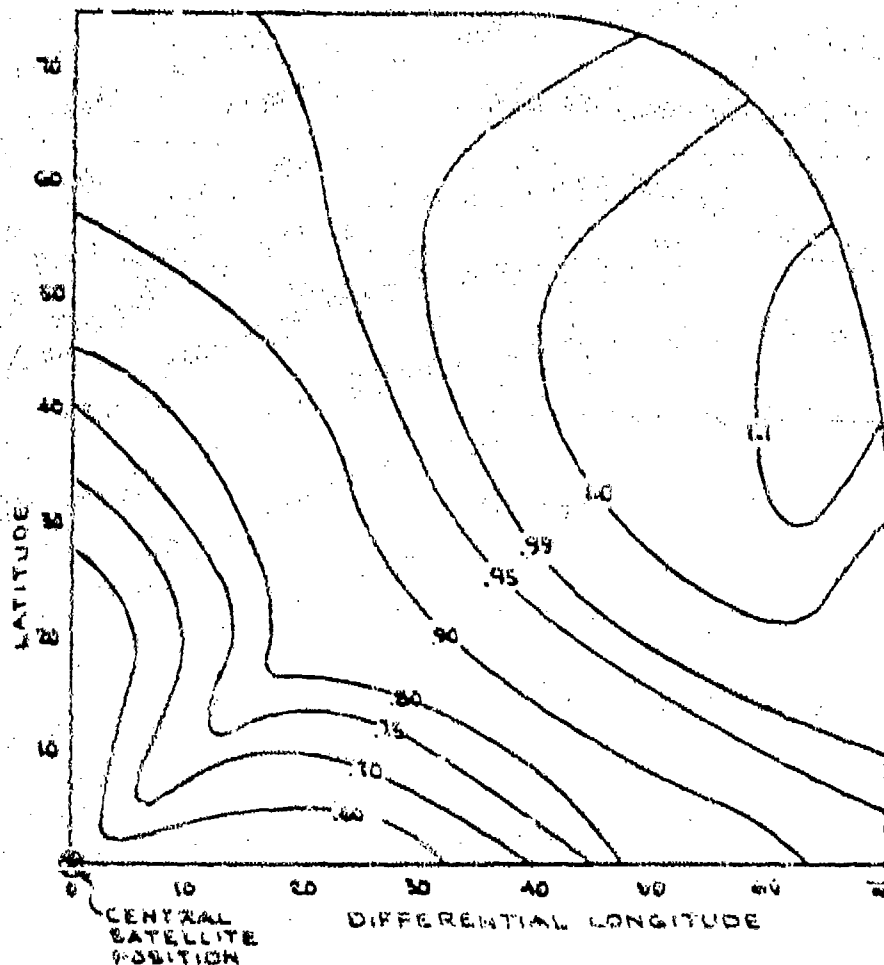


Figure 6-14. Normalized Projected Area $[A/(W \times D)]$

6.4.3 TEMPERATURE

Structural deflections due to a 10°F (5.5°C) differential temperature between the front surface (reflector joints) and the backup and support structures are calculated. This loading condition represents the case in which solar reflection warms up the exposed reflector surface faster than the sheltered structural members, for example, in the early morning.

6.5 ALLOWABLE DEFORMATION AND TILT ERROR BUDGET

6.5.1 SURFACE rms

Manufacturing tolerances, rigging adjustments, and deflections due to gravity, wind, and thermal loads are sources of surface deformation. For a first design iteration the total allowable rms error budget, ϵ_T , is split equally among the three separate categories, manufacturing (ϵ_m), erection (ϵ_r), and environment (ϵ_e), since their effects are uncorrelated²⁷:

$$\epsilon_T = \sum_{i=1}^n [\epsilon_i^2]^{1/2} = [\epsilon_m^2 + \epsilon_r^2 + \epsilon_e^2]^{1/2} \quad (6-10)$$

The total environmental rms error is the sum of the deflections of the panel surface (ϵ_p) and the backup/support structures (ϵ_s) due to wind, thermal, and gravity forces:

$$\epsilon_e = [\epsilon_p^2 + \epsilon_s^2]^{1/2} \quad (6-11)$$

Manufacturing and rigging rms errors are considered as a total for the whole system.

The basic MBTA required gain of 54 dB at 7.25 GHz calls for a minimum operational rms surface tolerance of 0.040 in. (1 mm), including 0.023-in. (0.58-mm) deformation due to each of the manufacturing, erection, and environmental effects. If these effects are kept equal, the deflection due to wind, temperature, and gravity is limited to 0.016 in. (0.41 mm) each for the panels and support structure. Ideally the deflection of the structure under its own weight is corrected during erection, and the distortions due to differential temperature are relatively small. Consequently, the majority of the environmental errors can be budgeted to the wind load deformations.

6.5.2 POINTING ERROR

The possible sources of pointing error are wind, gravity, and thermal deflections of the support structure; alignment errors during erection of the antenna; and displacements of the feed. Deflection of the feed structure itself can be eliminated by separating the foundation and supports of the feed mechanism and the feed tower. Thus, the feed travel is not subjected to displacement due to wind loads on the building walls or thermal distortions in its controlled environment. Adjustments of the feed can be used to compensate for the lateral displacement of the reflector structure and reduce the pointing error. Hence, displacements due to overall MBTA pointing error are subtracted from the total displacement at each point to obtain the uncorrected rms surface error.

6.5

STRUCTURAL MODEL

The RF transmission data define the generating parabolic toroidal surface²⁵:

$$z^4 - 8Fz^2 - 16F^2(x^2 + y^2) + 16(FR)^2 = 0 \quad (6-12)$$

where x , y , and z are calculated via transformation equation (6-3). The four basic parts of the torus antenna are the reflector surface panels, the backup truss, the support structure, and the concrete foundation. Since the backup, support, and foundation are dependent on the panel size, and number and type of corner supports, design iterations were first performed on a typical reflector surface panel to optimize its parameters.

6.6.1 PANELS

Panel optimization involved finding a practical design of minimum cost and weight. The factors influencing the design were material type, fabrication, assembly techniques, transportability, and erection ease. It was decided to limit the design to established fabrication techniques, easily available materials, and common overall size and weight. The maximum panel dimension was chosen as 9 ft to accommodate shipping size limitations. Aluminum was used as the basic surface material due to its good strength-to-weight ratio, availability, good RF characteristics, relatively low cost, and the large number of fabrication houses familiar with its use in curved panels. For ease of erection it was decided to limit backup structure connections to simple supports at each corner point.

For large panels, the advantages in terms of cost were as follows:

- a. few manufacturing mandrels,
- b. less joints for simpler erection procedures,
- c. greater alignment control, and
- d. a simpler backup structure.

For smaller panels the advantages were as follows:

- a. light weight for ease of shipping and handling,
- b. greater stiffness for each panel,
- c. ease of manufacture, and
- d. lower cost per unit area.

In addition, the following panel material configuration tradeoffs were considered:

- a. solid aluminum plate,
- b. thin aluminum plate backed with corrugated aluminum sheet,
- c. thin aluminum plate with aluminum stiffeners, or
- d. aluminum honeycomb with aluminum face skins.

To determine the optimum plate size and configuration, the maximum rms deviation is defined as

$$c_{rms}^2 = \frac{\delta_{max}^2}{3}$$

(6-13)

where δ_{\max} is the maximum allowable panel deflection. From the error budget, δ_{\max} is 0.014 in. (0.089 cm) and 0.028 in. (0.176 cm), respectively, for 20- and 40-mil overall rms tolerances in 45-mph winds.

For simplicity, the plates are assumed to be flat for the initial sizing. This is a conservative assumption since curved plates have greater rigidity than flat The deflection of corner-supported square plates is defined as²⁹

$$\delta_{\max} = \alpha \frac{qa^4}{D} \quad (6-14)$$

where

- α = function of edge stiffness = 0.0249
- q = uniform wind load = 0.050 lb/in² (0.034 N/cm²)
- a = side dimension
- D = plate stiffness = $Eh^3/[12(1 - \nu^2)]$
- E = 10^7 psi (7×10^6 N/cm²), the aluminum modulus of elasticity
- ν = Poisson's ratio = 0.3
- h = plate equivalent thickness

The resultant equivalent plate thickness required for various rms surface tolerances is shown in Figure 6-15. This figure indicates that the minimum total weight is 22.5 psf (1089 N/cm²) for a solid aluminum 8-ft square plate configuration vs 8.9 psf (427 N/m²) for a 4-ft plate. The equivalent plate thickness for corrugated honeycomb or beam-stiffened thin plates is

$$h_{\text{equiv}} = \sqrt[3]{12I} \quad (6-15)$$

where I is the section area moment of inertia per unit length.

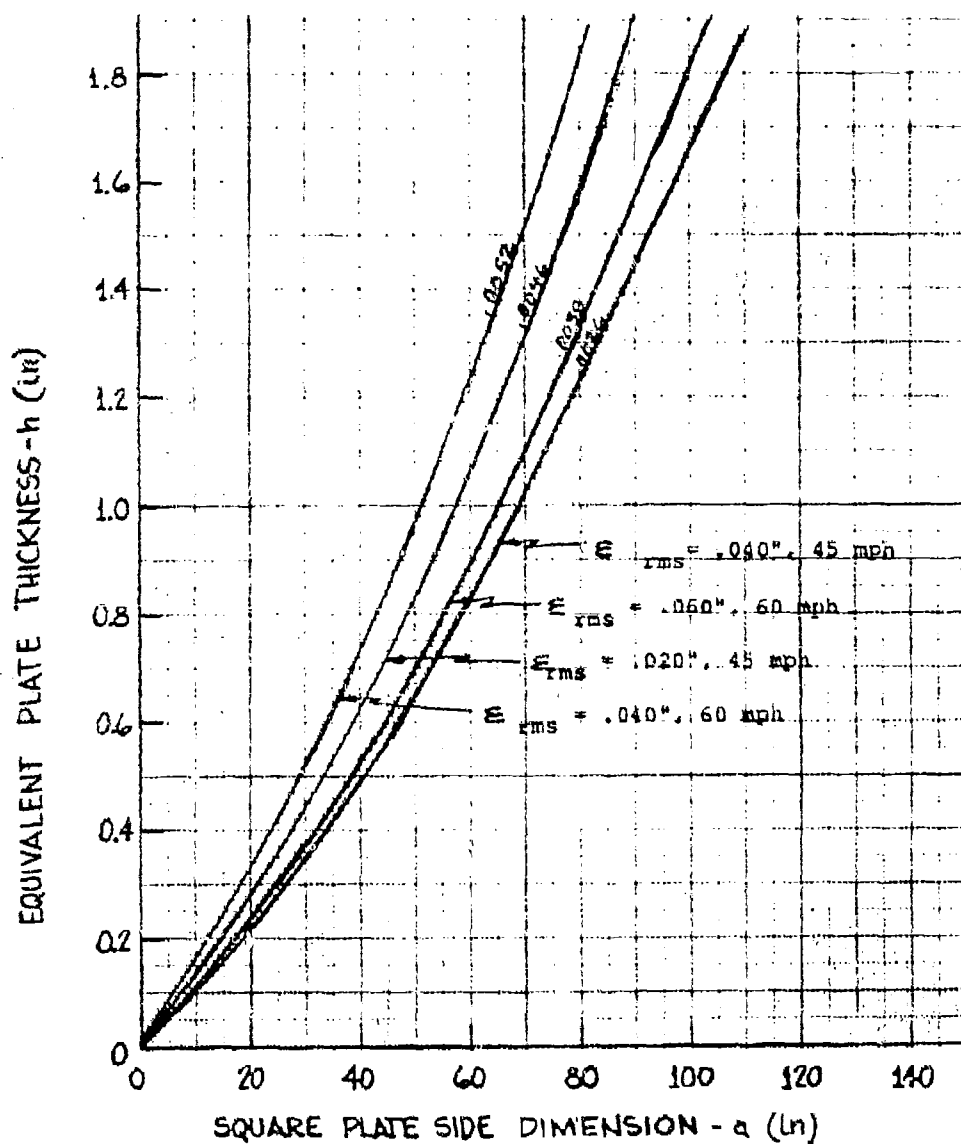


Figure 6-15. Equivalent Plate Thickness

Figure 6-15 indicates the critical relationship of panel size to surface tolerance. Since the 60-mph curve dominates in both cases, the recommended maximum panel sizes appear to be 8 and 6 ft for the 40- and 20-mil cases, respectively. Some examples of equivalent stiffened plates are shown in Figure 6-16. For a typical 8-ft square plate, the section moment of inertia required to meet the 60-mph surface tolerance criteria at 60 mph would be 0.42 in³/in. (2.7 cm³/cm).

Regardless of configuration, the thinnest aluminum face sheet used was 0.060 in. (0.152 cm) to protect the reflector surface from permanent deformation due to the impact of hailstones or other moderate size particles.^{27, 30} Based on a maximum panel dimension of 9 ft (2.7 m), several reflector configurations were analyzed (Figure 6-17). To reduce wind deflections on the struc-

the four corner panels were shaped to eliminate unnecessary area. The configuration of three parabolic panel sections would require irregularly shaped corner panels to accomplish the area reduction without gain loss. Simple triangular corner panels can be used with four parabolic panel sections to minimize area reduction.

6.6.2 BACKUP STRUCTURE

Based on the results of the panel optimization, a stiff, lightweight, universal support was needed for the reflector. To add commonality to both the backup structure and the reflector, the main structural frame is a basic vertical truss structure tied to the panels at each corner point. The generating truss is rotated about the axis of revolution of the reflector. Additional stiffness is obtained by tying each vertical frame together via horizontal trusses and diagonal bracing. Given the latitude and

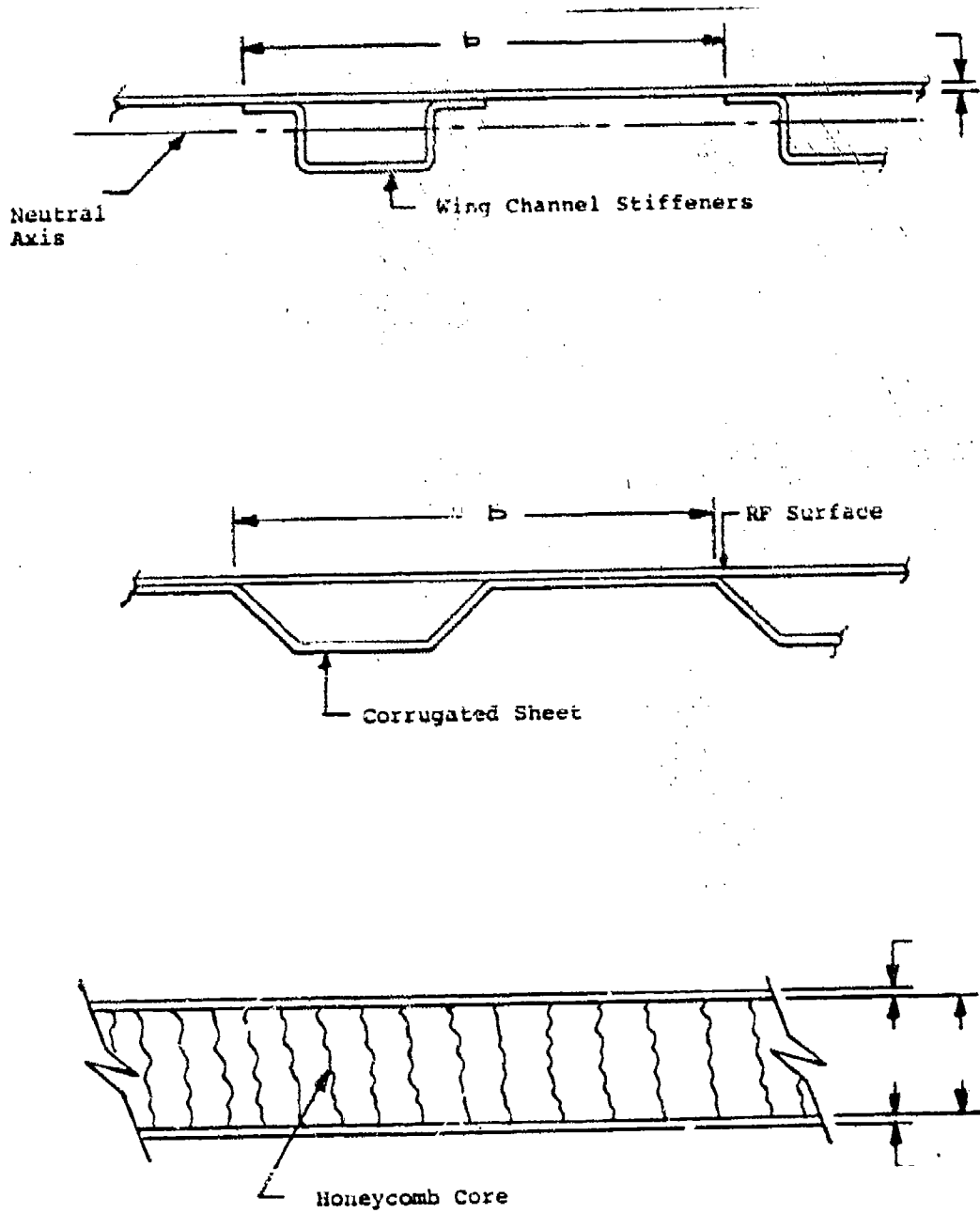


Figure 6-16. Reflector Panel Cross Section

Multiple Beam Torus
Antenna Study

COMSAT Labs

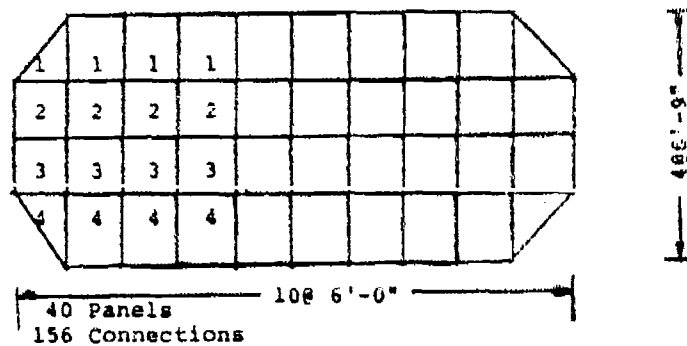
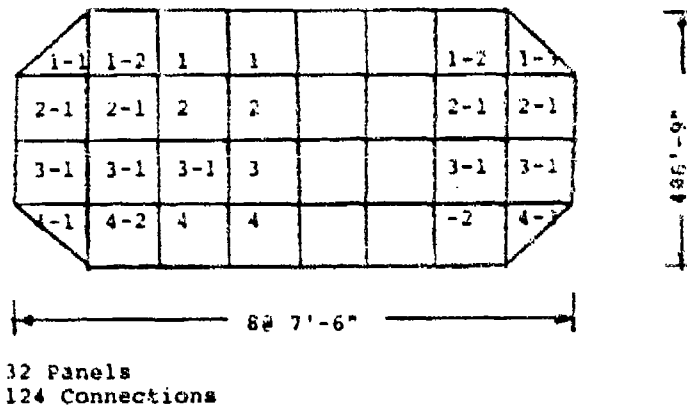
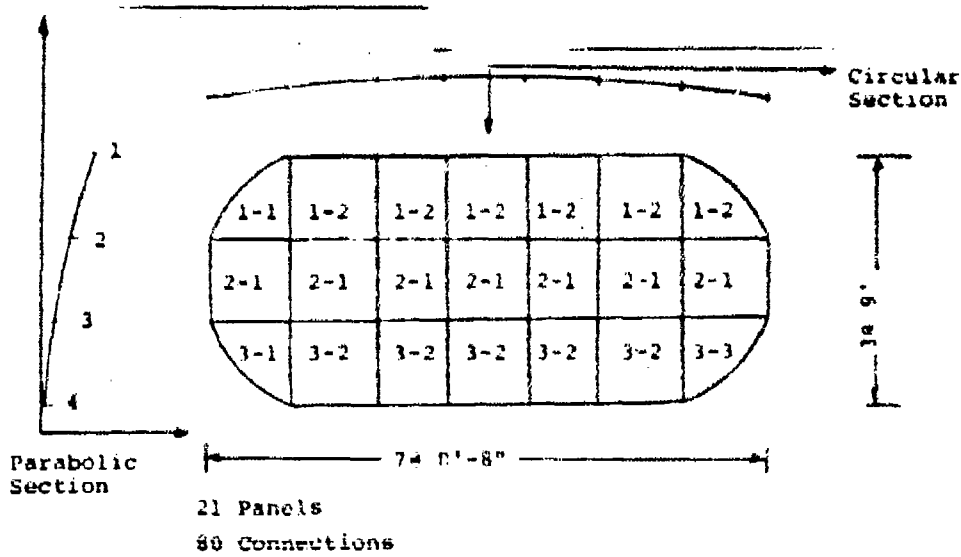


Figure 6-17. Panel Configurations

longitude at the desired earth station location, the backup structure and reflector panels are then rotated into the global coordinate system via transformation equation (6-7). Some typical configurations considered for the generating vertical truss are shown in Figure 6-18.

After panel analysis design iterations, it was decided to use a 4 x 8 panel reflector surface as the baseline configuration. The panel layout shown in Figure 6-19 was chosen for design iterations. The nine vertical trusses required for this configuration are supported by the main spine truss generated as a curve about the axis of rotation of the reflector.

All members in this analysis are A36 structural steel in commonly available sizes. Ideally the reflector surface panels are attached to the truss at each corner by rods with adjustment mechanisms to make alignment corrections during erection.

A 4-point attachment to the support structure was used for the initial design iterations. A detailed view of the backup structure reduced from a NASTRAN plot for the 27-ft MBTA is shown in Figure 6-20.

6.5.3 SUPPORT POINTS

The type of support members is determined by the required stiffness of the torus structure in its operational position. The structural stiffness in turn is a function of the number and spacing of pickup and foundation points, the unbraced length of the steel members, and their relative configuration. Thus, each location requires a unique support structure to accommodate its antenna positioning.

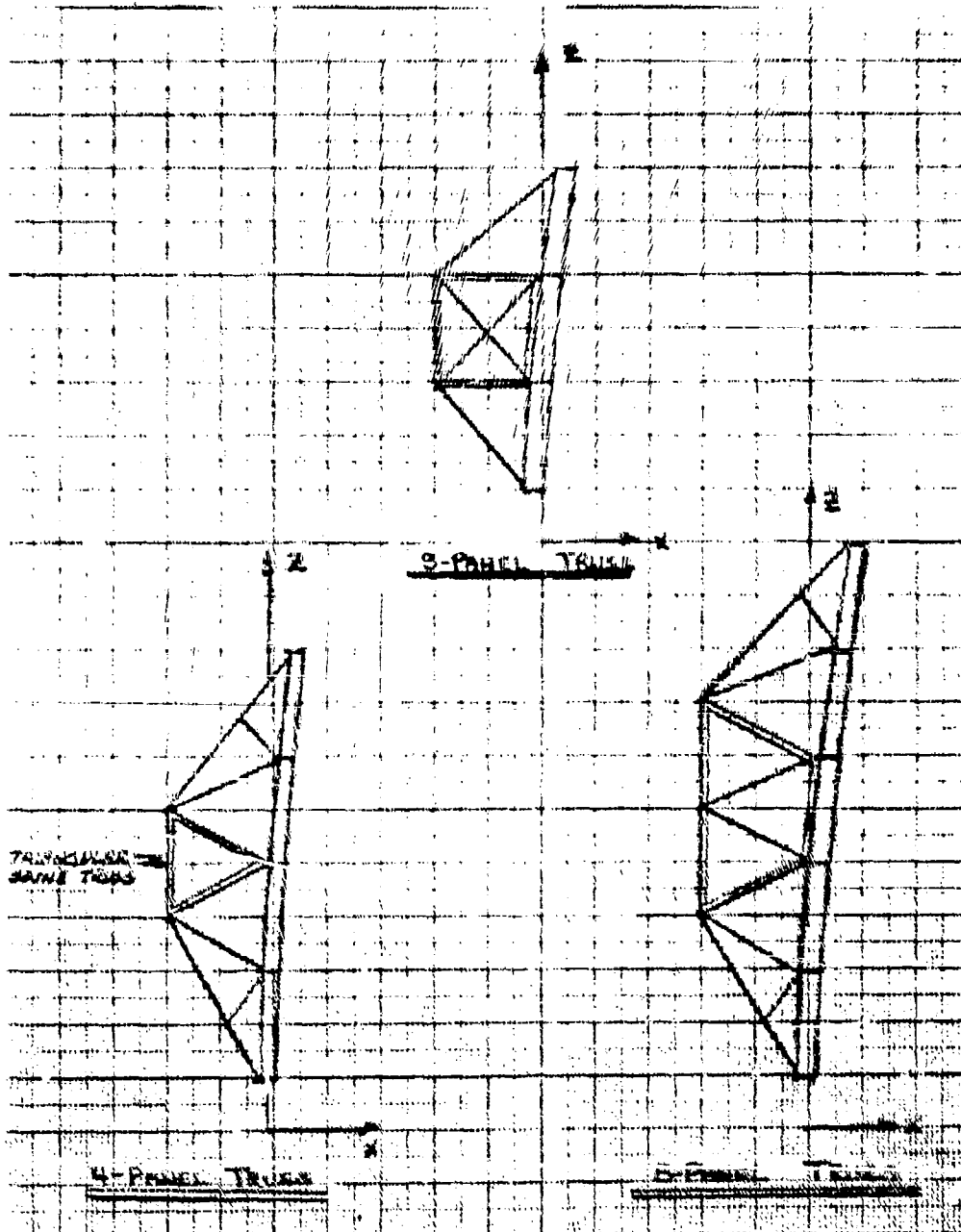


Figure 6-18. Vertical Truss Configurations

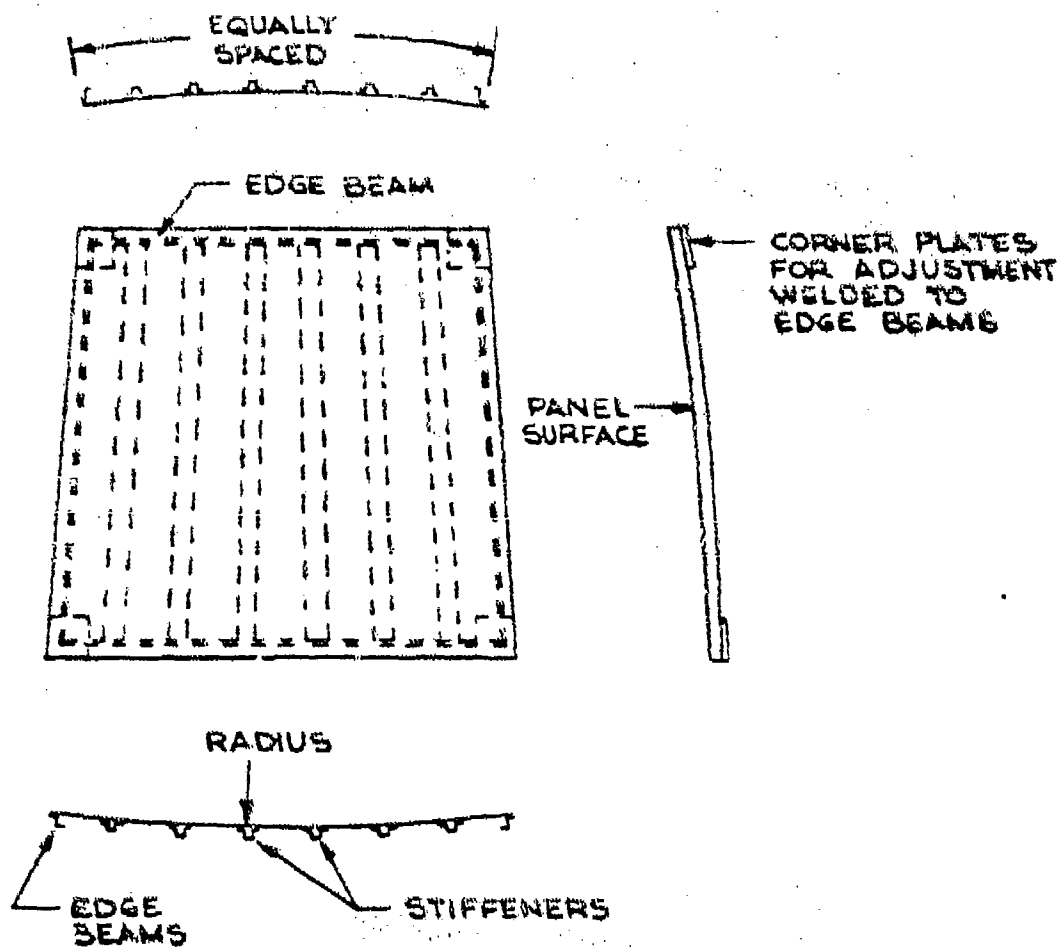


Figure 6-19. Typical Panel Layout

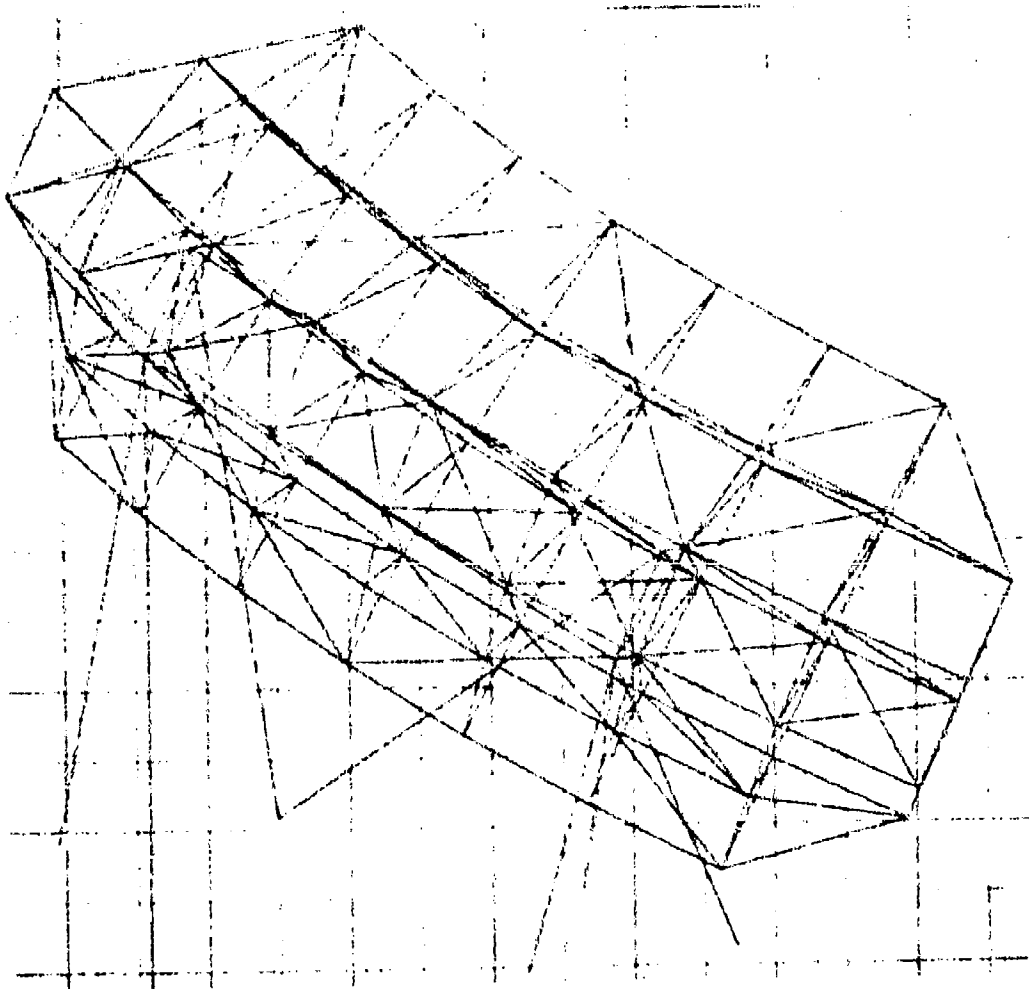


Figure 6-20. NASTRAN Plot of Backup Structure

The simple 7-member steel support structure shown in Figure 6-21 was used for design iterations of the basic MBTA antenna. It uses a lower tripod as the main static load carrying member. The dynamic wind load is transmitted through the V and A frames to ground. The V frame can also serve as a pivot mechanism for correcting the tilt of the antenna during erection. This particular support system is not a self-standing structure; the backup structure member assembly must be included to achieve overall stability.¹¹

Figure 6-11 shows a stable and less flexible support structure. This configuration might be necessary at sites where the most severe wind load overturning moments occur, or where, because of the extreme length of the V and A frame members and the required antenna size or extreme site location, the 6-member design is unconservative.

Figure 6-22 shows the stiffness requirements of the same reflector translated to different locations. The projected area times maximum reflector height is normalized to its surface area times the aperture height to give a measure of the relative wind loading deformation problem. It can be seen that the dynamic deflections at the Mt. Margret location are potentially six times as severe as those at the Ascension Island location.

6.7 STRUCTURAL LAYOUT

The MBTA-11 program, developed at COMSAT Labs, establishes the precise geometrical coordinates of antenna panels, backup, support structures, and feeds based on optimum RF parameters and site location. The main part of the program lays out the panel and panel support geometry, front and side wind loads,

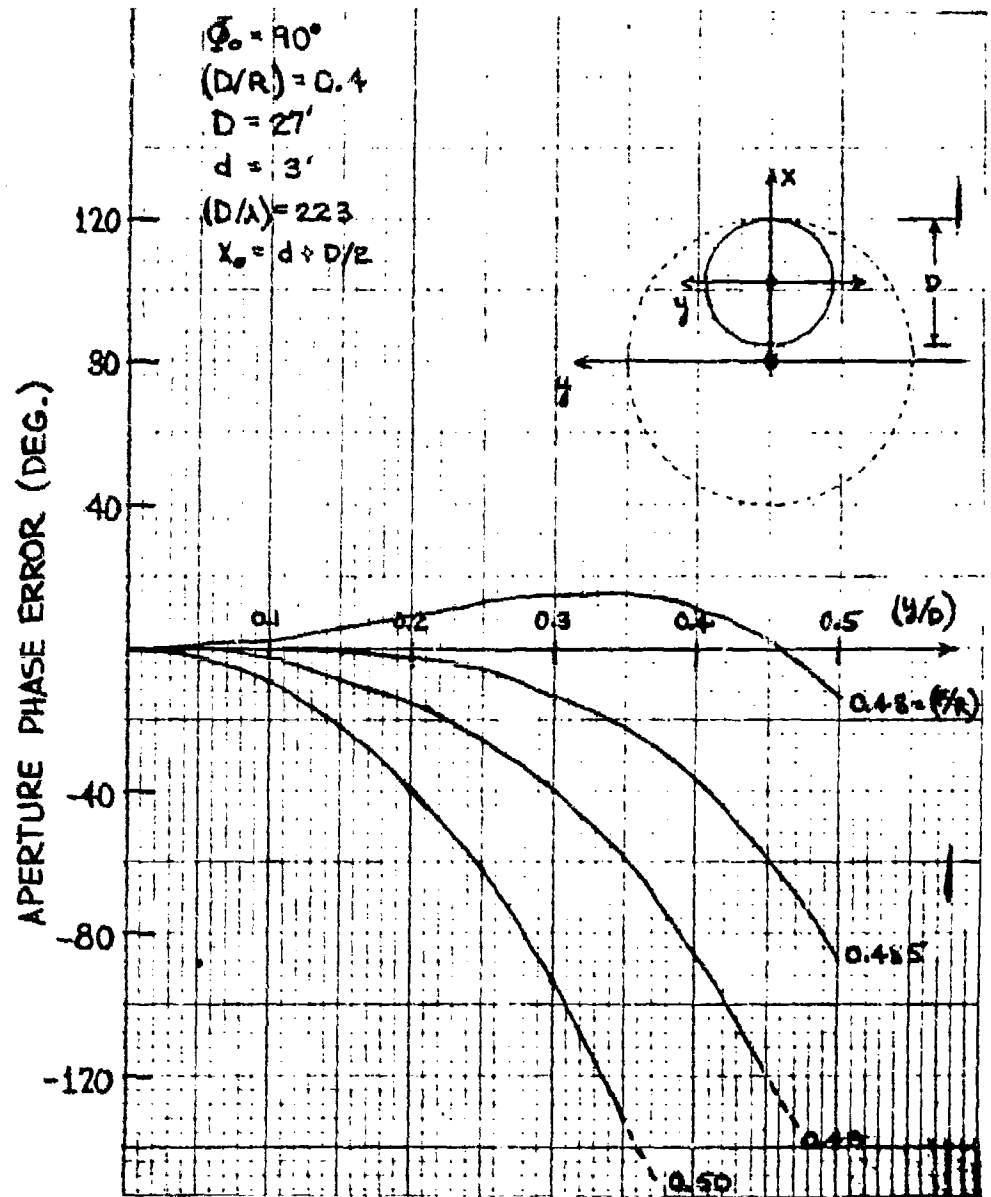


Figure 5-25. Offset (11%) MBTA ($D/R = 0.4$) Aperture Plane Phase Errors

(minimum weighted phase error) is expected for $0.48 \leq F/R \leq 0.485$. In Figure 5-26, which shows the calculated gain of an offset MBTA with a specified feed amplitude taper, the middle curve ($D/R = 0.4$) indicates a maximum gain at $F/R = 0.483$. The generating axis angle, ϕ_0 , is slightly different for the antenna geometries ($\phi_0 = 90 \rightarrow 93.5^\circ$) compared in these two figures. The conclusion, which will also be demonstrated later, is that small changes in ϕ_0 do not markedly affect the aperture plane phase error distribution.

Figure 5-27 shows the center of aperture plane phase errors when the offset distance, d , is increased to 6 ft ($d/D = 22$ percent). A comparison of Figures 5-25 and 5-27 indicates that the F/R optimization is quite sensitive to the offset distance. Figure 5-28 shows the center of aperture plane phase errors for the $D/R = 0.3$ geometry. Comparison with Figure 5-25 again demonstrates that the feed positioning (F/R) can be optimized on the basis of a relatively simple aperture phase error expression.

The full aperture plane phase errors for the baseline MBTA configuration are shown in Figure 5-29. The phase error distribution is symmetrical in y , but the offset configuration gives rise to an asymmetrical distribution in x (except at the center of the aperture, since the feed is at the focus of the parabolic section). The effective radius of the curvature is changing as a function of x [equation (5-69)] over the aperture. The path lengths to positions on the top portion of the aperture are shorter than those to the bottom portion of the aperture. Hence, the parabolic plane pattern tends to be scanned somewhat in the $(-\theta)$ direction.

The aperture plane phase errors can be directly scaled by D/λ . As the frequency increases the edge of aperture phase errors increase in magnitude until voltage contributions from the edge of the aperture actually cause a decrease in peak gain.

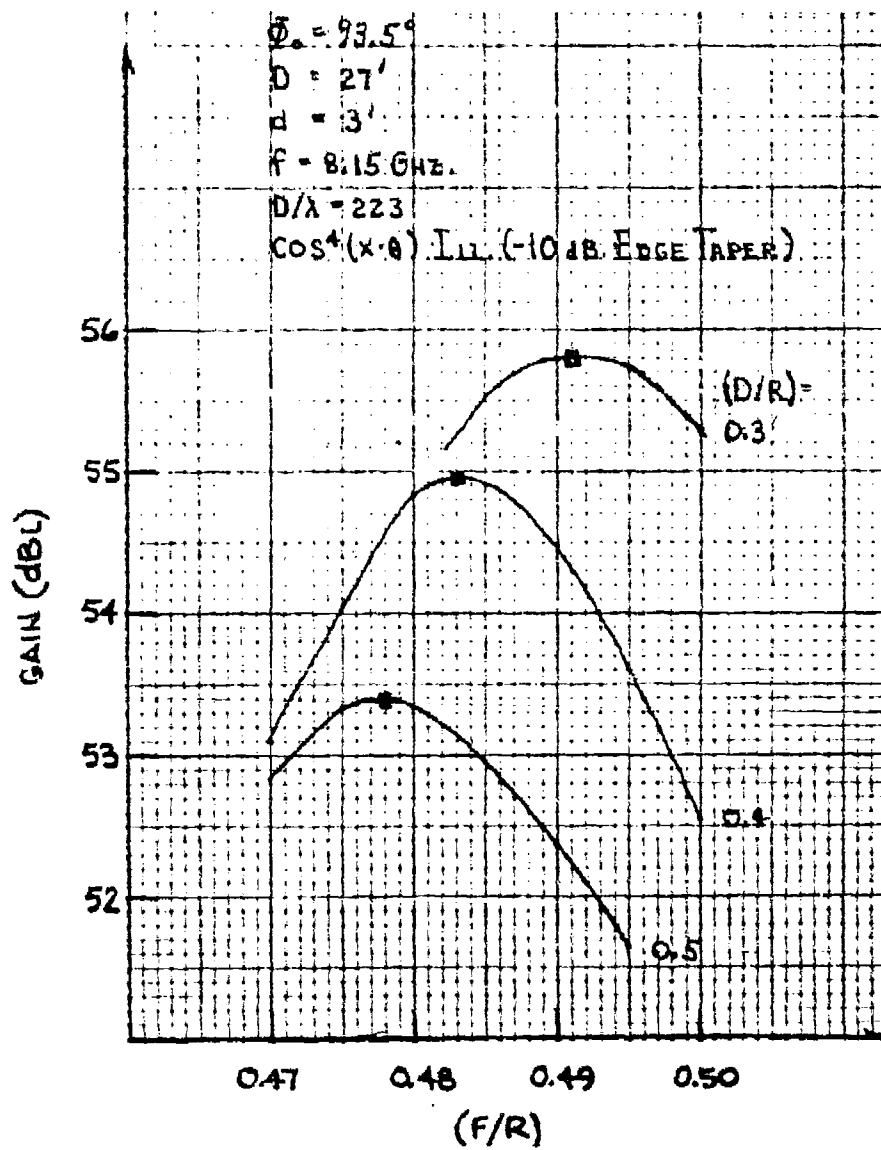


Figure 5-26. Offset (118) MBTA Aperture
Illumination Gain vs (F/R)

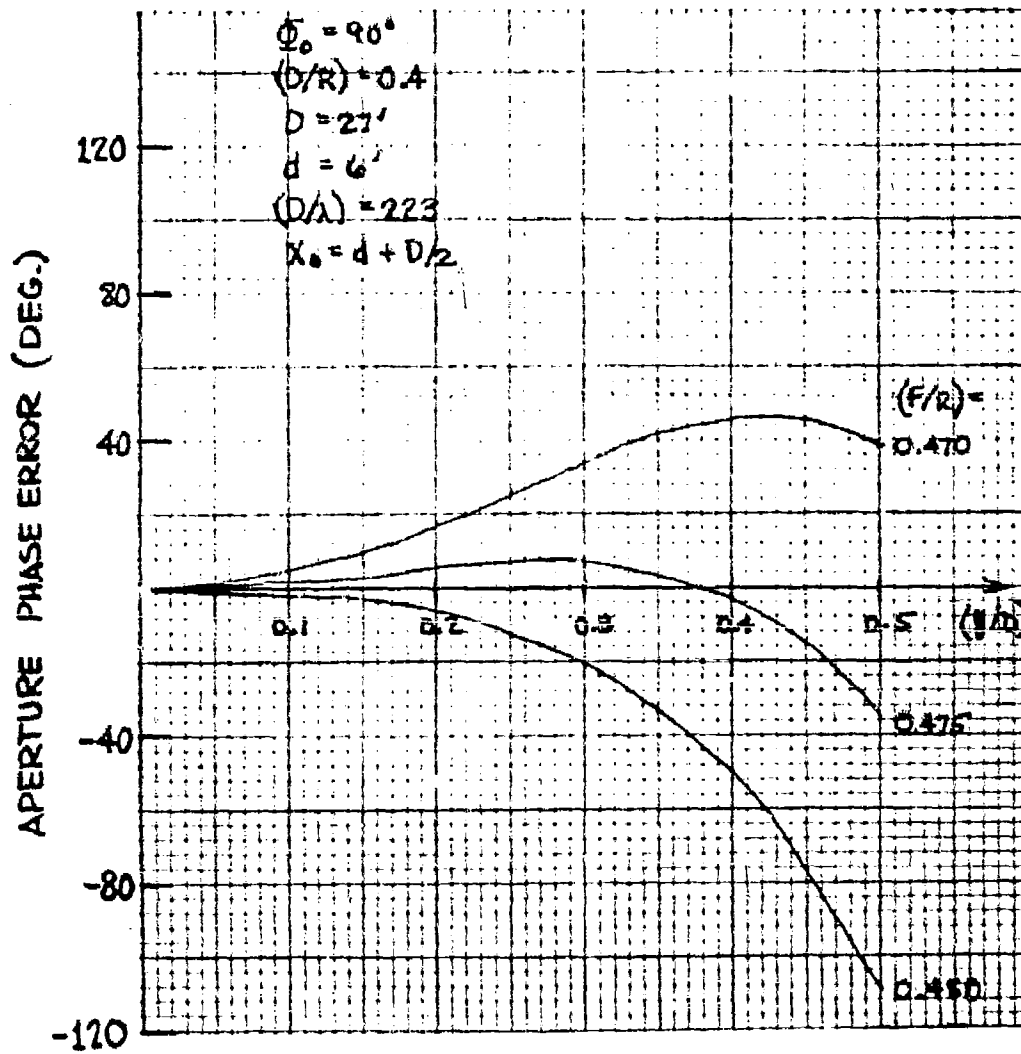


Figure 5-27. Offset (22%) MFTA (D/R = 0.4) Aperture Plane Phase Errors

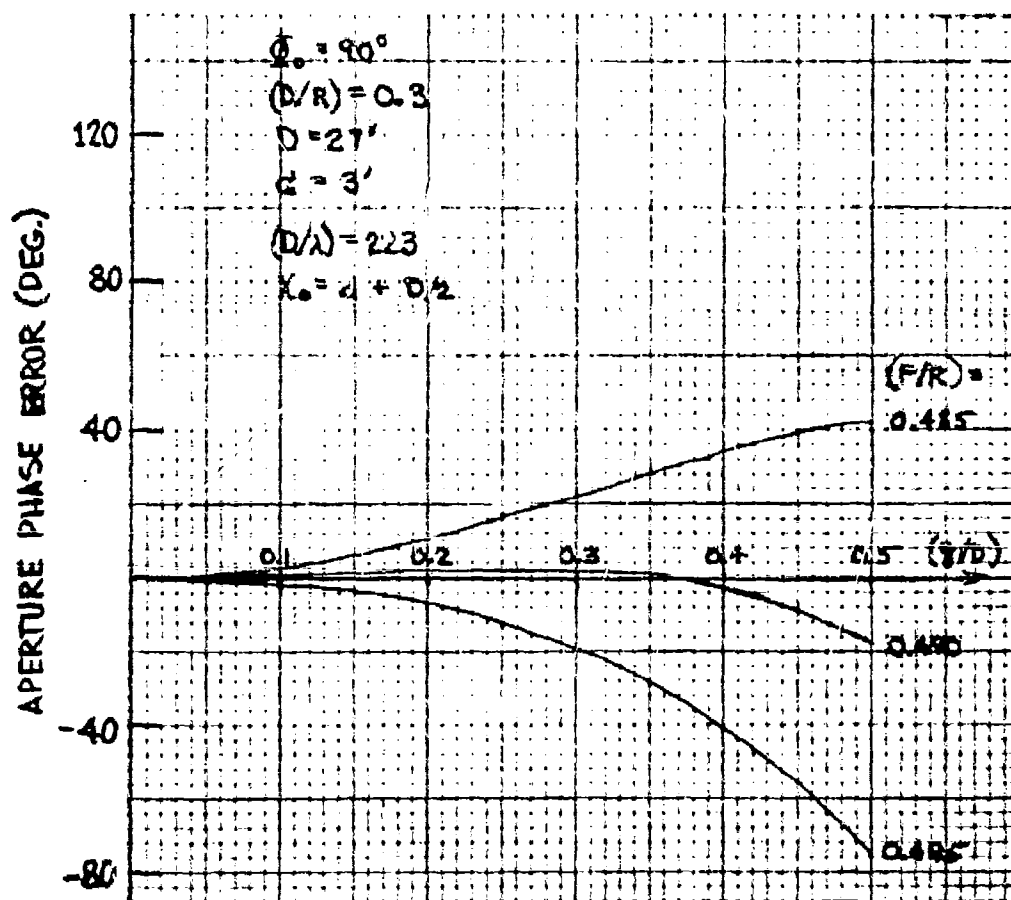


Figure 5-28. Offset (11%) MBTA ($D/R = 0.3$) Aperture Plane Phase Errors

APERTURE PHASE ERROR

$\phi_0 = 90^\circ$ $F/R = 0.483$
 $D = 21'$ $D/R = 0.4$
 $d = 3'$
 $D/\lambda = 223$

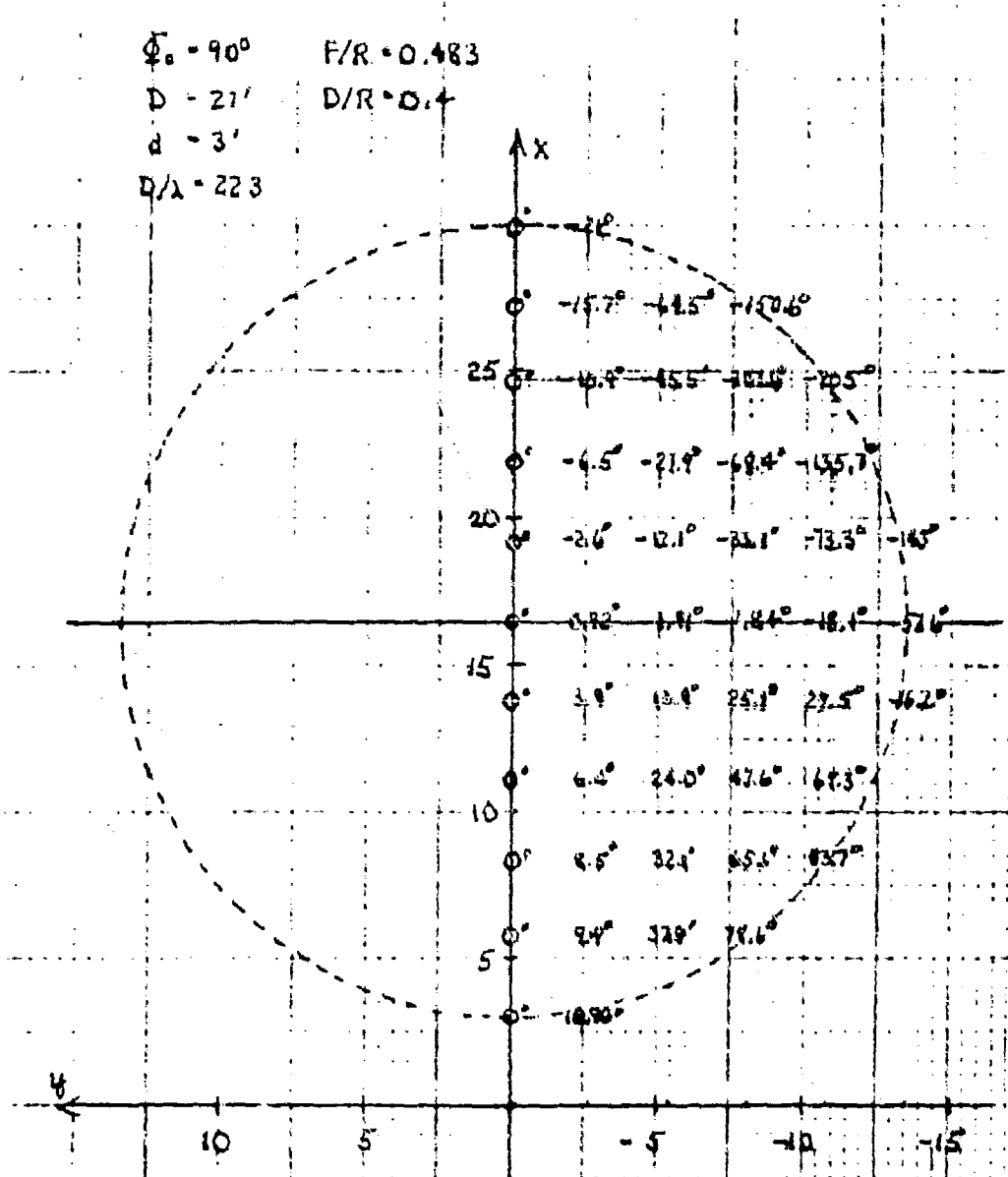


Figure 5-29. Offset (11%) MBTA (D/R = 0.4) Aperture Plane Phase Errors with Optimum Focusing

Maximum gain is then achieved by illuminating only an inner portion of the physical aperture, D. Figure 5-30 shows the calculated gain of the baseline offset MBTA geometry at 30 GHz as a function of the -10-dB feed beamwidth. Maximum gain occurs when the -10-dB feed illumination angle is $2 \times 13^\circ = 26^\circ$. If the full physical aperture is illuminated with a feed illumination angle of $2 \times 21^\circ = 42^\circ$, the peak gain is reduced by 0.9 dB.

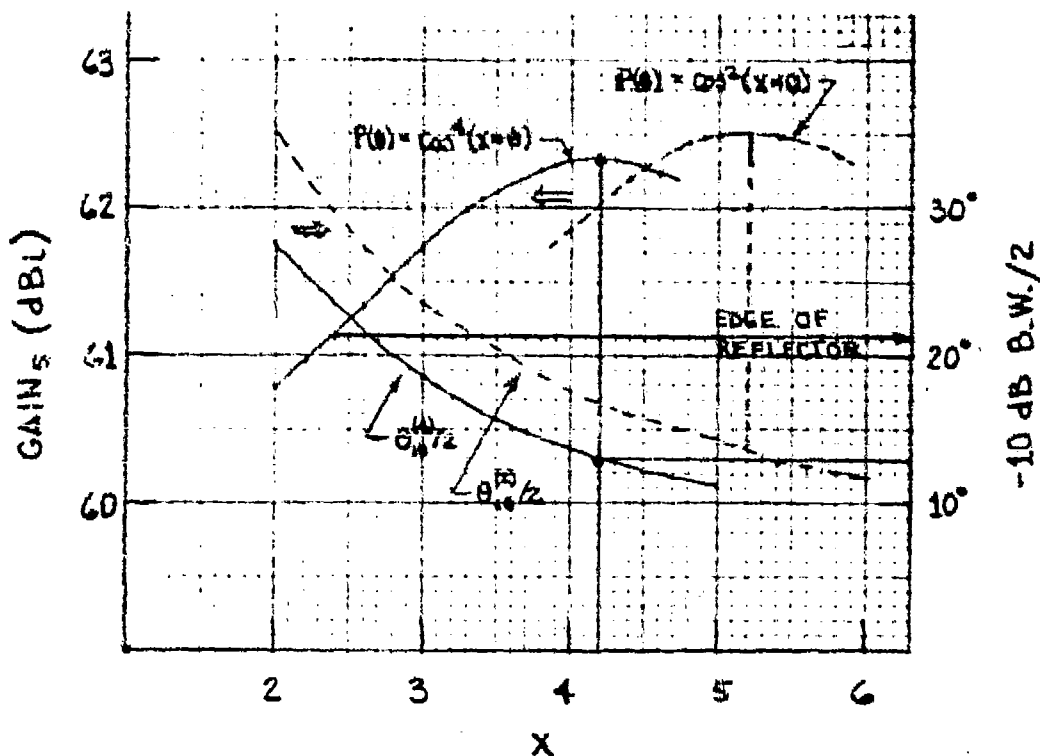


Figure 5-30. Gain vs Feed Illumination Angle at 30 GHz (baseline MBTA)

The full aperture plane phase error distribution for a $D/R = 0.5$ offset geometry is shown in Figure 5-31. Peak gain occurs when the -10-dB feed illumination angle projects to the

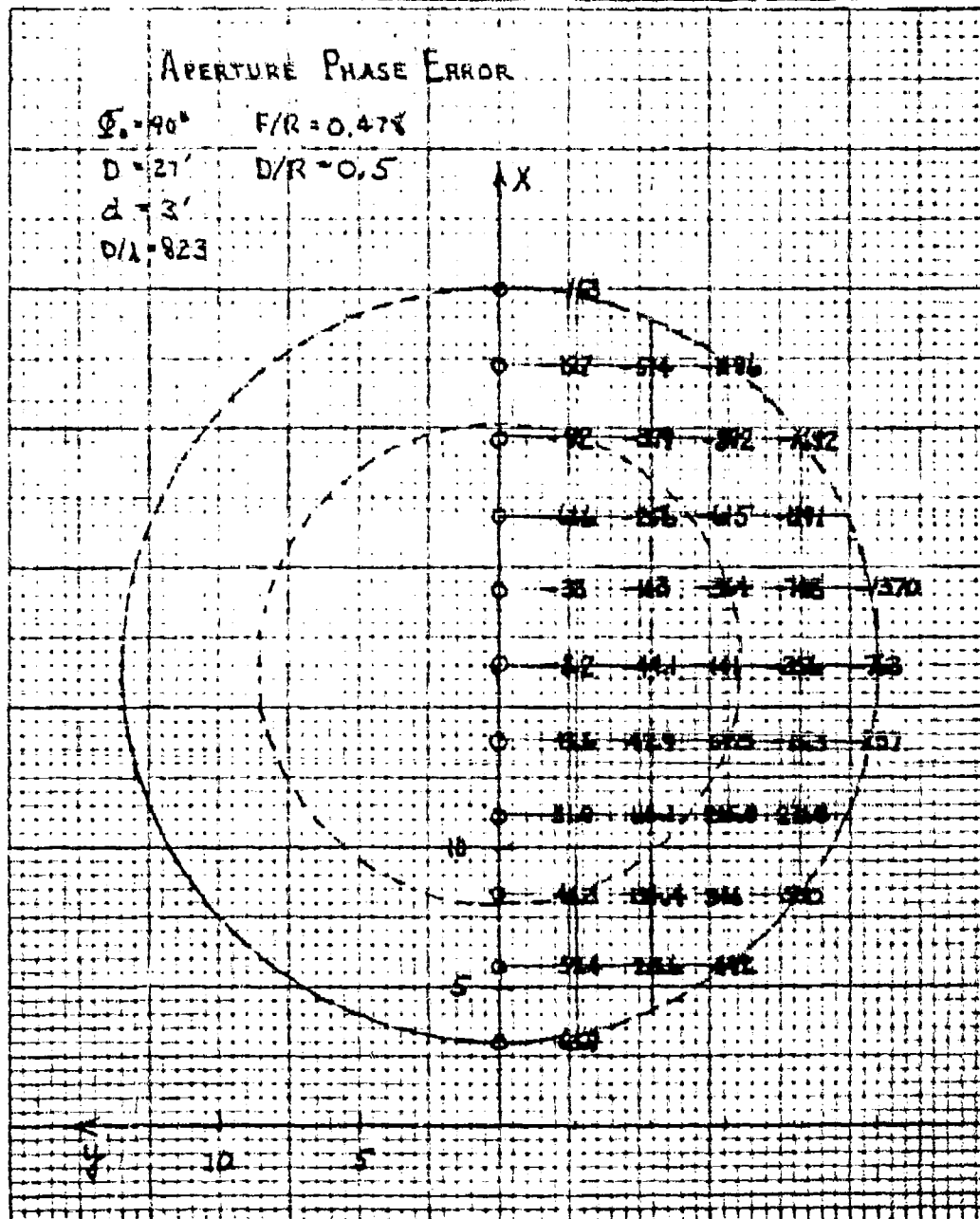


Figure 5-31. Offset (11%) MBTA ($D/R = 0.5$) Aperture Plane Phase Errors with Optimum Focusing

dashed circular aperture shown in the figure. The average edge of aperture phase error on the dashed optimum aperture is $\approx 120^\circ$. The peak gain versus the -10 -dB beamwidth is plotted in Figure 5-32. If the full aperture is illuminated, the peak gain is reduced by 1.4 dB.

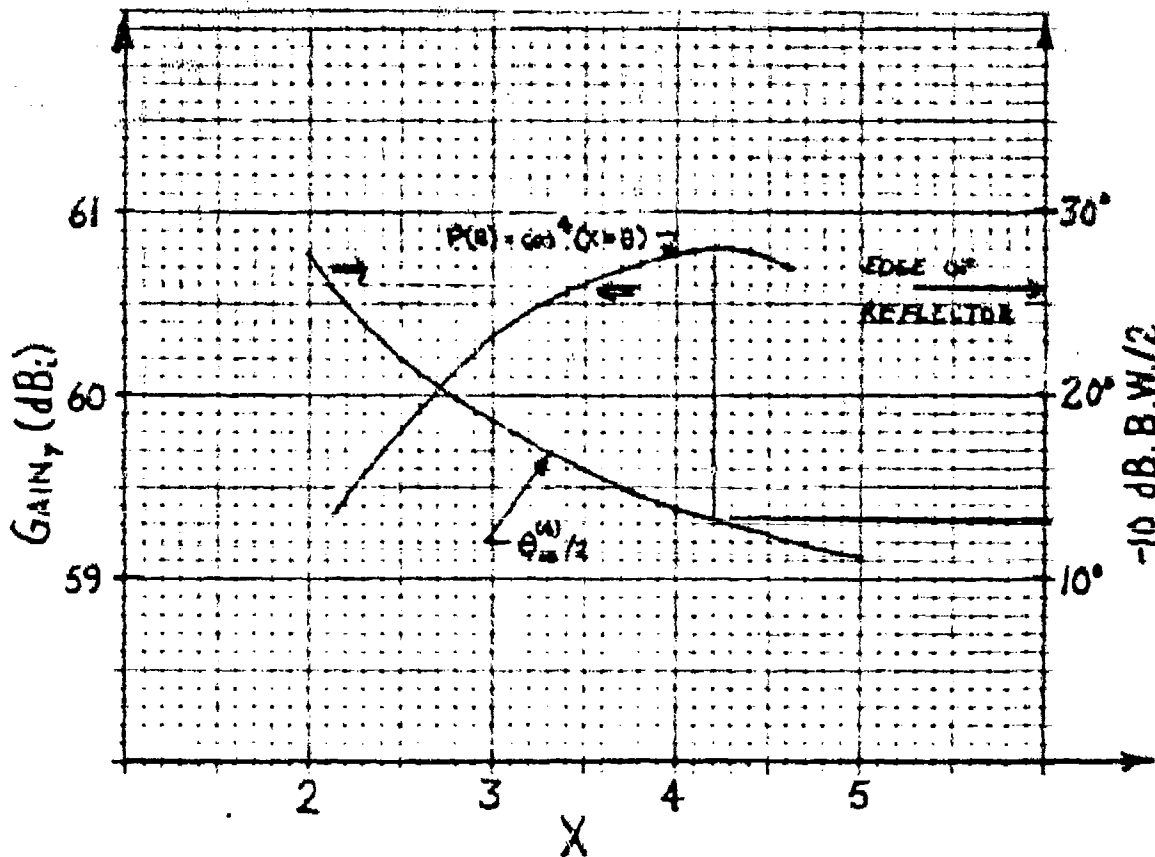


Figure 5-32. Gain vs Feed Illumination Angle at 30 GHz
(D/R = 0.5 geometry)

The aperture plane phase error expression for an MBTA with a general ϕ_0 angle is derived by using the geometry shown in

Figure 5-33. The description of the central path length ray ϵ_0 is identical to the previous results derived for the special case of $\phi_0 = 90^\circ$ [equation (5-66)]. The equation of the rotated parabolic section is

$$v^2 + w^2 - R^2(u) = 0 \quad (5-81)$$

or

$$y^2 + \left[-\cos \phi_0 x + \sin \phi_0 \left(z - \frac{R}{\sin \phi_0 - F} \right) \right]^2 = R^2(u) \quad (5-82)$$

and

$$R(u) = w \quad (5-83)$$

(when $v = y = 0$) is obtained from the equation for the parabolic section:

$$x^2 - 4F(z + F) = 0 \quad (5-84)$$

or

$$(\sin \phi_0 u - \cos \phi_0 w)^2 - 4F(\cos \phi_0 u + \sin \phi_0 w + F) = 0 \quad (5-85)$$

as the general equation of the M/TA rotated surface.

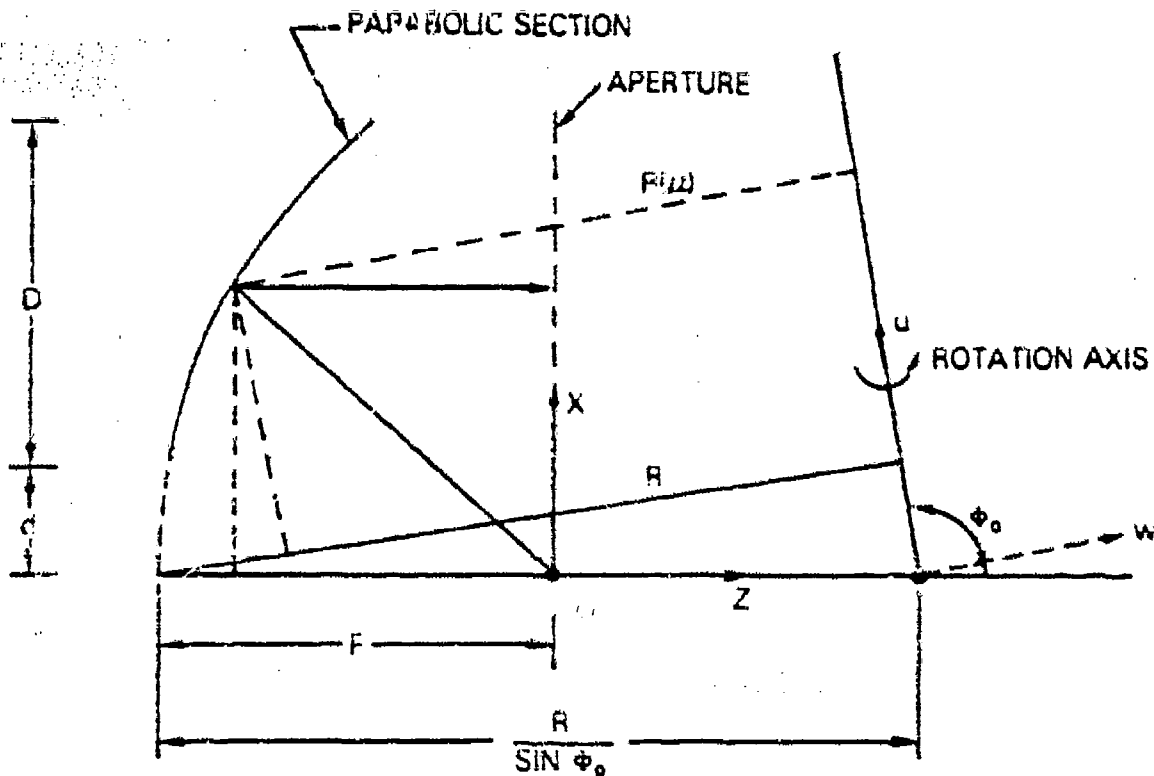


Figure 5-33. Geometry for General ϕ_0 Reflector Surface

The general aperture plane phase error expression for arbitrary ϕ_0 and feed position (x_F, y_F, z_F) relative to the parabolic focus referenced to the phase at $(x_c, 0, 0)$ in the aperture is

$$\begin{aligned} \psi(x, y, 0) = & 360^\circ \left(\frac{D}{\lambda} \right) \left\{ \sqrt{\left(\frac{x - x_F}{D} \right)^2 + \left(\frac{y - y_F}{D} \right)^2 + \left(\frac{z - z_F}{D} \right)^2} + \left| \frac{z}{D} \right| \right. \\ & - \sqrt{\left(\frac{x_c - x_F}{D} \right)^2 + \left[\frac{(x_c/D)^2}{4F/R \times R/D} - \frac{F/R}{R/D} - \frac{z_F}{D} \right]^2} \\ & \left. - \left[\frac{F/R}{R/D} - \frac{(x_c/D)^2}{4F/R \times R/D} \right] \right\} \end{aligned} \quad (5-86)$$

where z is found from the reflector surface equation $f(x, y, z) = 0$.

5.9 PARABOLIC PLANE SCANNED BEAM FEED POSITIONS AND SCAN GAIN LOSS

The aperture plane phase error expressions derived in the previous subsection can be utilized to determine to a first order the feed positions $(x_{f_s}, 0, z_{f_s})$ required to scan the parabolic plane pattern. The sum of the phase errors at the top and bottom of the aperture plane in the $y = 0$ (parabolic) plane is equated to zero:

$$\text{Err}(x_{f_s}, z_{f_s}) = \psi(x = d + D, 0, 0) + \psi(x = d, 0, 0) = 0 \quad (5-87)$$

A family of (x_{f_s}, z_{f_s}) feed positions which satisfy this equation is obtained. Each set is associated with an absolute phase error difference across the aperture plane that corresponds to the scanned beam location. If the aperture phase errors at the top and bottom of the aperture are $\Delta\psi$ and $-\Delta\psi$, respectively, the scanned beam position is

$$\theta_s = \tan^{-1} \left(\frac{\Delta\psi}{180^\circ \times D/\lambda} \right) \quad (5-88)$$

Since the expression for $\Delta\psi$ is directly proportional to D/λ , the scanned beam location is independent of frequency.

For small scan angles,

$$\Delta\psi \text{ (deg)} = \theta_s \text{ (deg)} \times \frac{D}{\lambda} \quad (5-89)$$

Program MBTA-9 calculates the scanned beam feed positions and associated scan angle.

Figure 5-34 shows the locus of scanned beam feed positions calculated by using equation (5-87) and the corresponding parabolic plane scan angle for the baseline MBTA geometry. The calculated scan beam feed positions were then verified using COMSAT's GAP program. The full aperture integration (GAP) includes the effects of feed amplitude weighting. The peak gain as a function of parabolic plane beam scan is shown in Figure 5-35 for the baseline MBTA. Note that the scan gain loss characteristic is not symmetrical as a result of differential feed amplitude weighting effects.

The space taper amplitude varies differentially with scan. The maximum loss at $\pm 2.5^\circ$ is 2 dB at $D/\lambda = 223$.

5.10 SPHERICAL GENERATING CURVE MBTA

For applications which require a considerable amount of scan (or beamwidths of scan) in a plane perpendicular to the geosynchronous arc, the use of a spherical generating curve for the MBTA may prove useful. The reflector system can then be designed to have a constant gain for a specified out-of-plane scan requirement. This constant gain will be lower than the gain achieved with the parabolic generating curve when there is no scan. In addition, it requires the reflector diameter to be increased to provide a full aperture illumination with the maximum scan angles. The geometry of an offset MBTA using a spherical generating section with a generating axis angle, $\phi_0 = 90^\circ$ is shown in Figure 5-36.

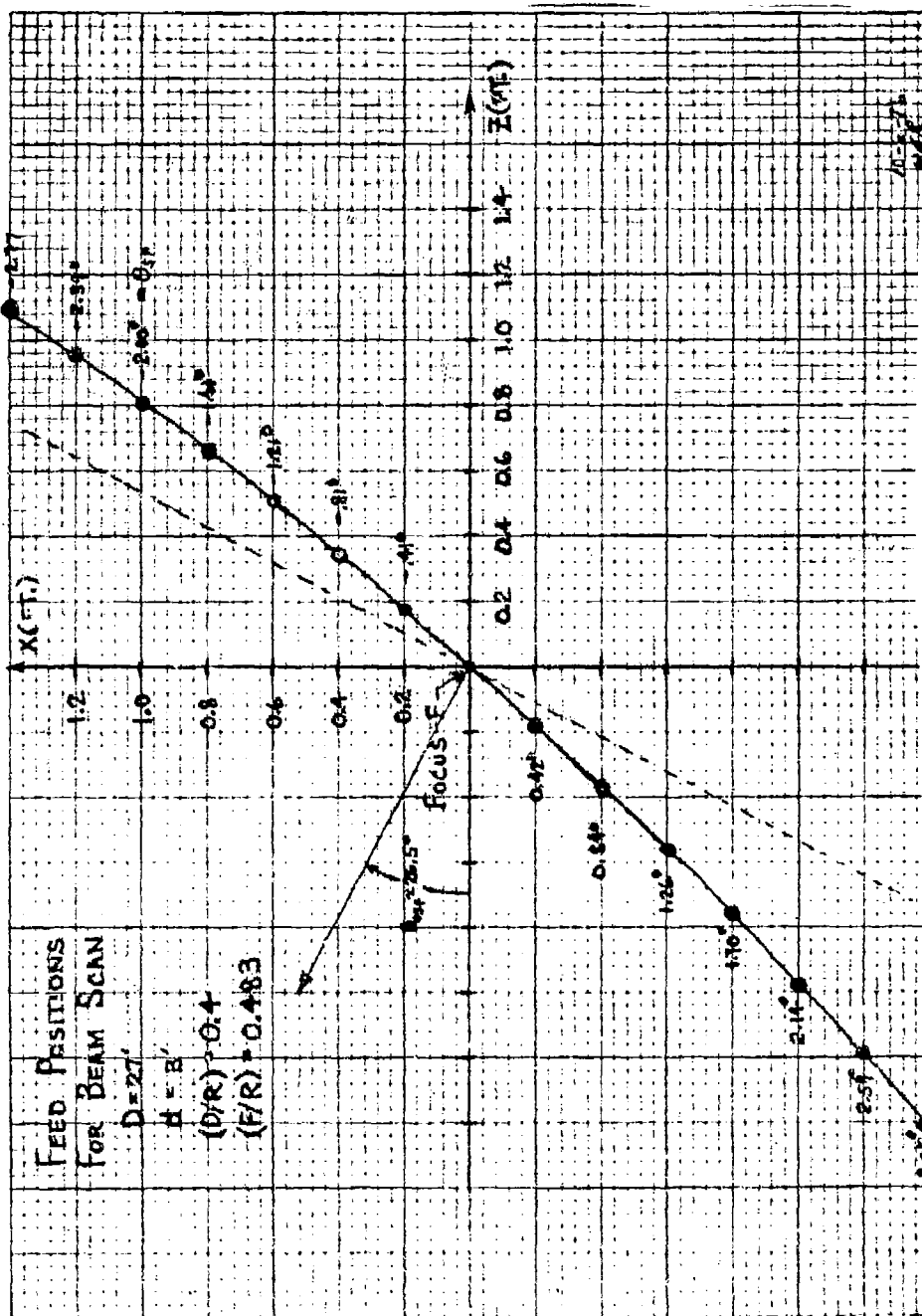


Figure 5-34. Scanned Beam Feed Positions for Baseline MBTA

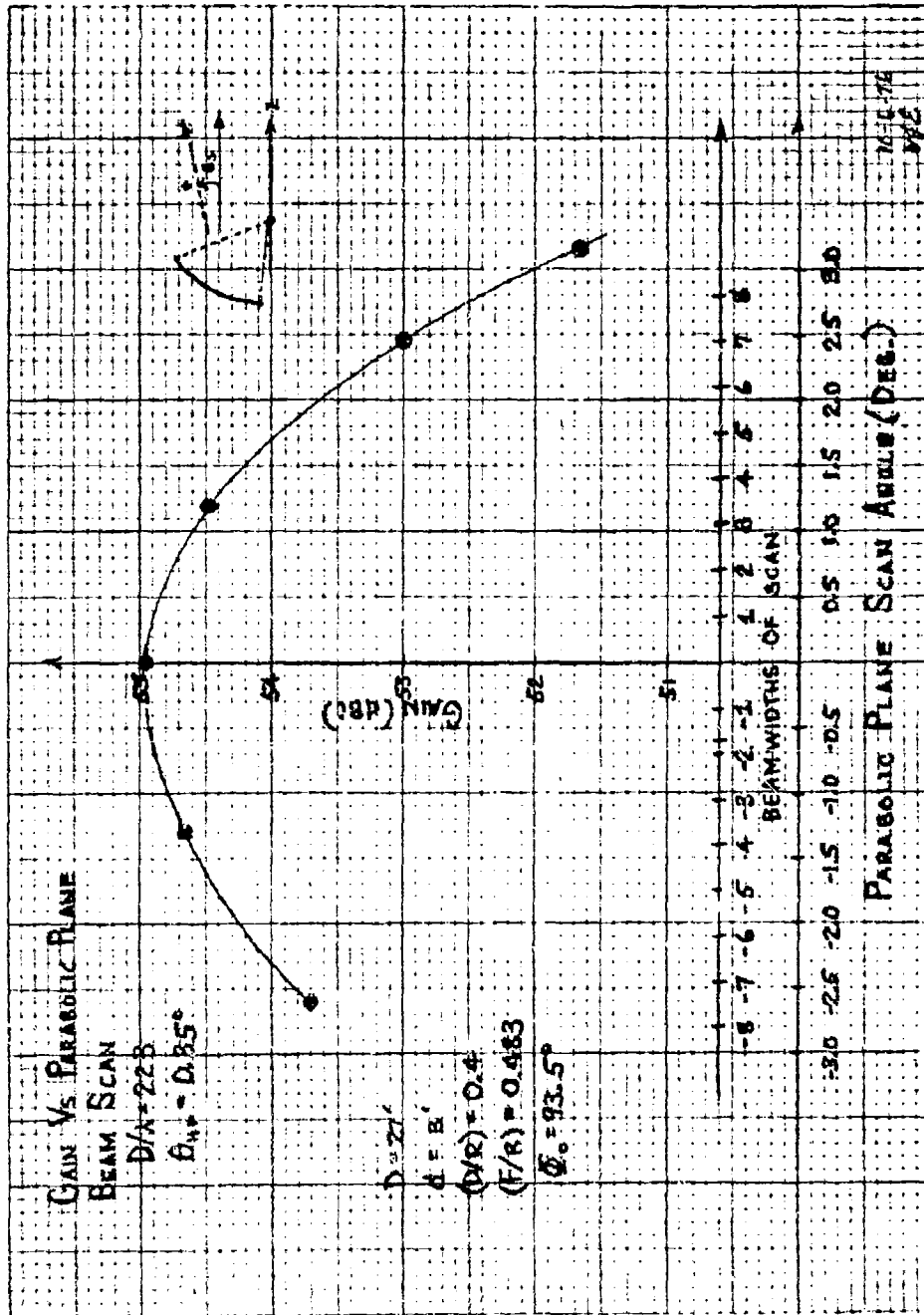


Figure 5-35. Parabolic Plane Beam Scan Loss for Baseline MBTA at 8.15 GHz

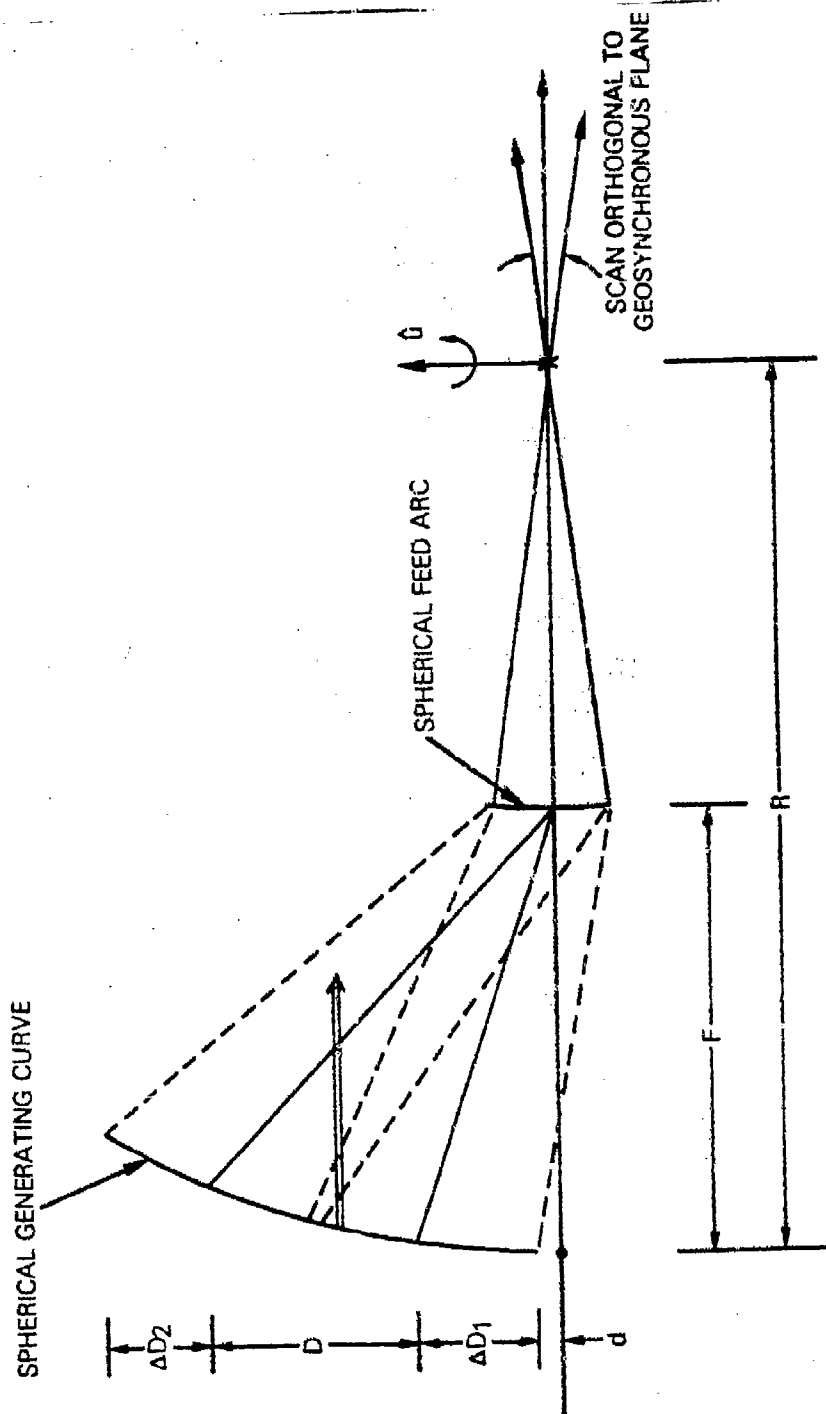


Figure 5-36. MBTA with Spherical Generating Curve

The equation of the spherical cross section in the $y = 0$ plane is

$$x^2 + [z - (R - F)]^2 = R^2 \quad (5-90)$$

or

$$z = (R - F) - \sqrt{R^2 - x^2} \quad (5-91)$$

The radius of curvature about the rotation axis, \hat{u} , is

$$R(x) = \sqrt{R^2 - x^2} \quad (5-92)$$

The general rotated plane curve is described by

$$z = (R - F) - \sqrt{R^2 - x^2 - y^2} \quad (5-93)$$

The path length for a ray from a general feed position (x_F, y_F, z_F) relative to F into the aperture plane $(x, y, 0)$ is

$$\begin{aligned} \ell(x, y, 0) = & \sqrt{(x - x_F)^2 + (y - y_F)^2 + \left[(R - F) - \sqrt{R^2 - x^2 - y^2} - z_F \right]^2} \\ & + \sqrt{R^2 - x^2 - y^2} - (R - F) \end{aligned} \quad (5-94)$$

and the aperture plane phase error expression is

$$\psi(x, y, 0) = 360^\circ \left(\frac{D}{\lambda} \right) \left[\frac{\ell(x, y, 0) - \ell(x_0, 0, 0)}{D} \right] \quad (5-95)$$

The aperture plane phase errors in the $y = 0$ plane, are plotted in Figures 5-37 and 5-38 for two geometries that are similar to those considered for the MBTA baseline configuration.

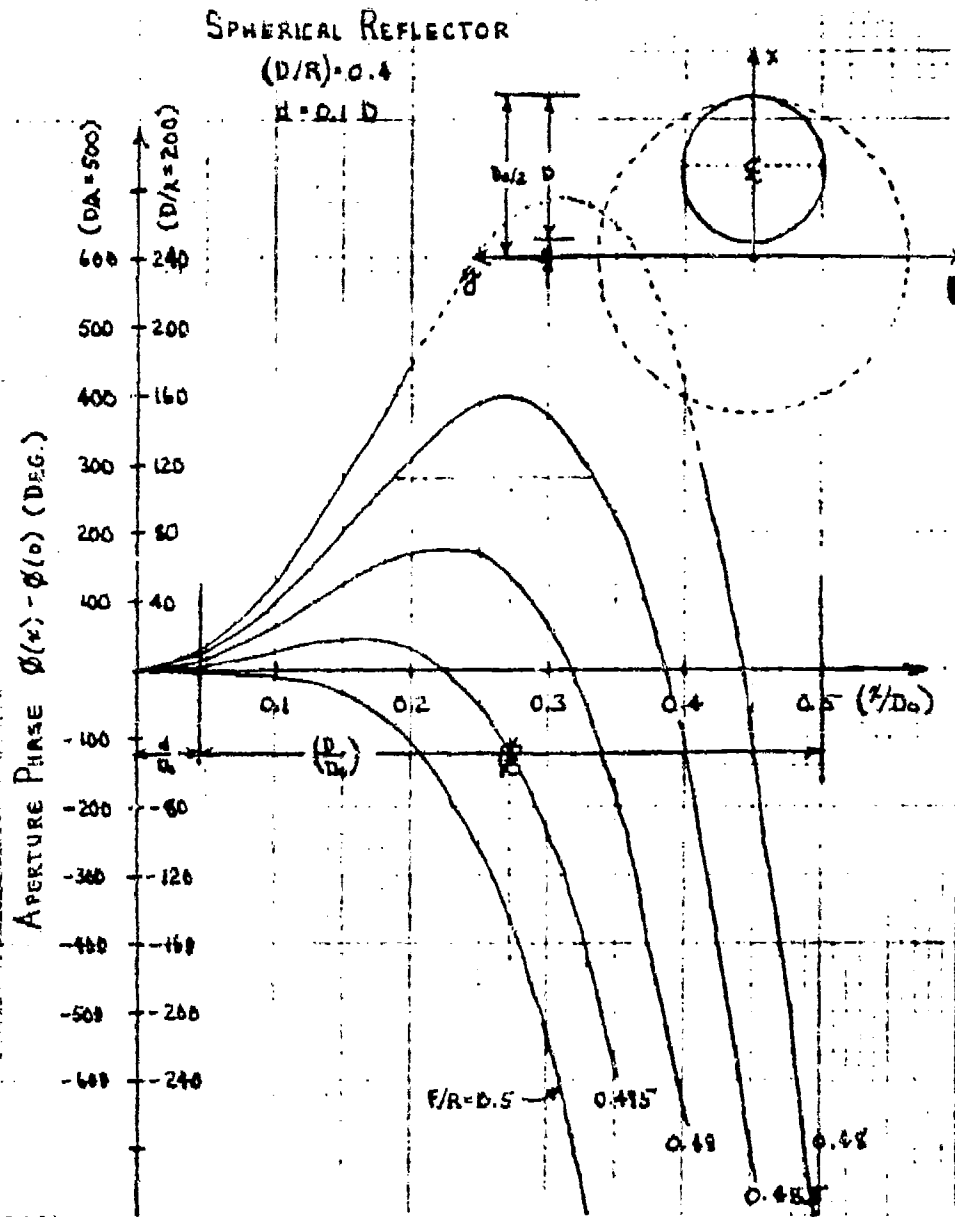


Figure 5-37. Aperture Plane Phase Error vs Feed Focusing with Spherical Generating Curve (D/R = 0.4)

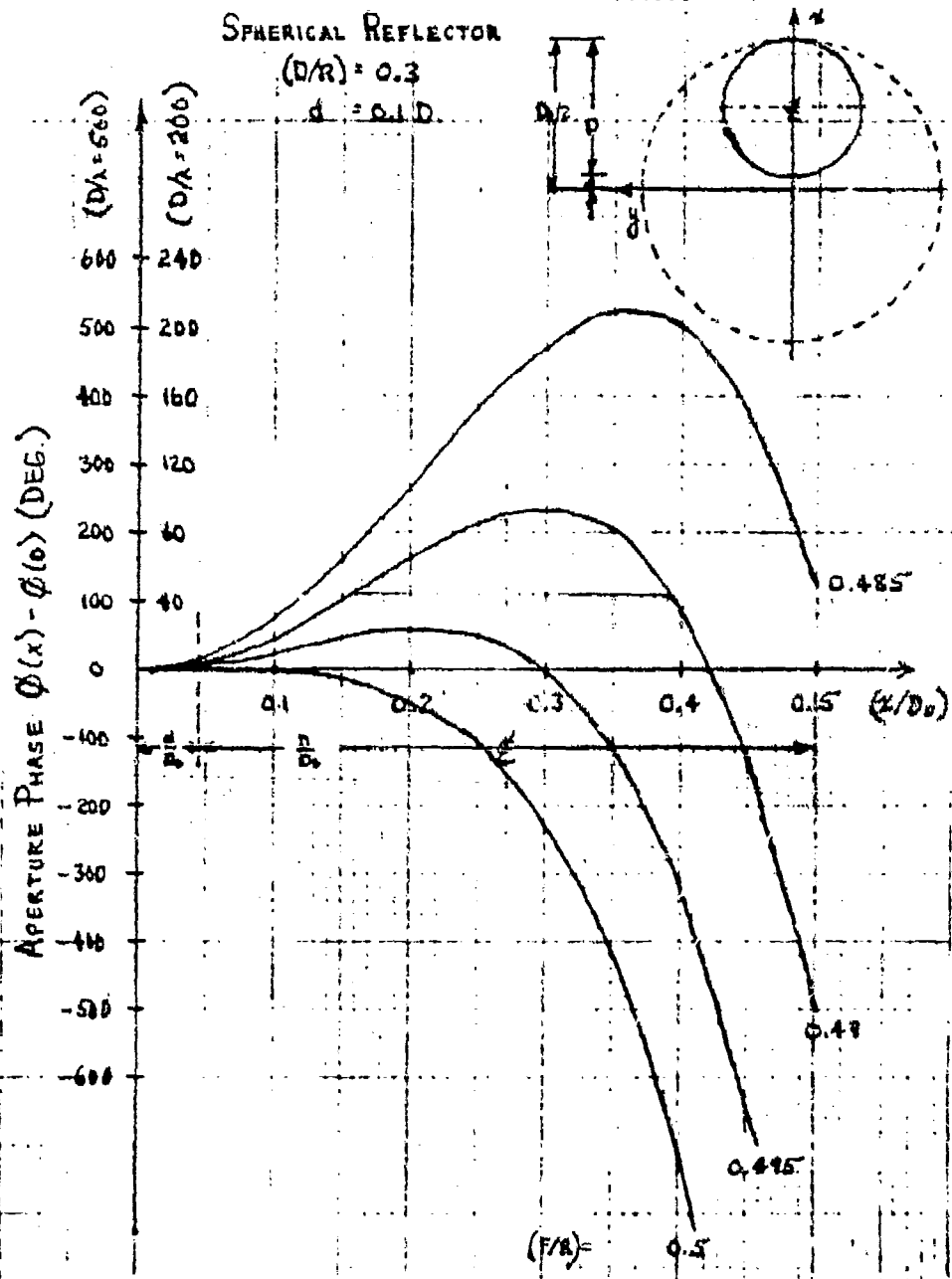


Figure 5-38. Aperture Plane Phase Error vs Feed Focusing with Spherical Generating Curve (D/R = 0.3)

5.11 ILLUMINATION GAIN OF FRONT-FED MBTA

The illumination gain of the front-fed offset reflector MBTA, excluding feed system or reflector rms surface tolerance losses, is summarized in Figure 5-39. The gain for a 10-percent offset ($d/D = 0.1$) and a 93.5° generating axis angle is shown as a function of D/λ for fixed D/R values. Gain increases as the radius of curvature increases. Because of edge-of-aperture phase errors, the tradeoff between peak gain and feed illumination taper is slower for the MBTA than for a conventional parabola. The aperture illumination gain versus feed edge taper is shown in Figure 5-40 for the baseline MBTA geometry. A feed edge taper of -15 dB virtually eliminates feed spillover past the reflector with little impact on peak gain.

The aperture illumination gain versus errors in the feed offset angle, θ_{osf} , is shown in Figure 5-41 for the baseline antenna. Variation of θ_{osf} produced no changes in the beam pointing direction. A $\pm 2^\circ$ variation about the calculated θ_{osf} angle is required before a decrease in gain is noted.

The illumination gain of the baseline 27-ft-diameter MBTA as a function of frequency from 3.7 to 31 GHz is shown in Figure 5-42. An 11-percent offset is utilized to ensure that the aperture plane is unblocked by the feed (or feed house) at the extreme parabolic plane scan position. The horn diameter must be used in conjunction with Figure 5-34 to determine the minimum offset distance. In addition, an allowance for the roof of the

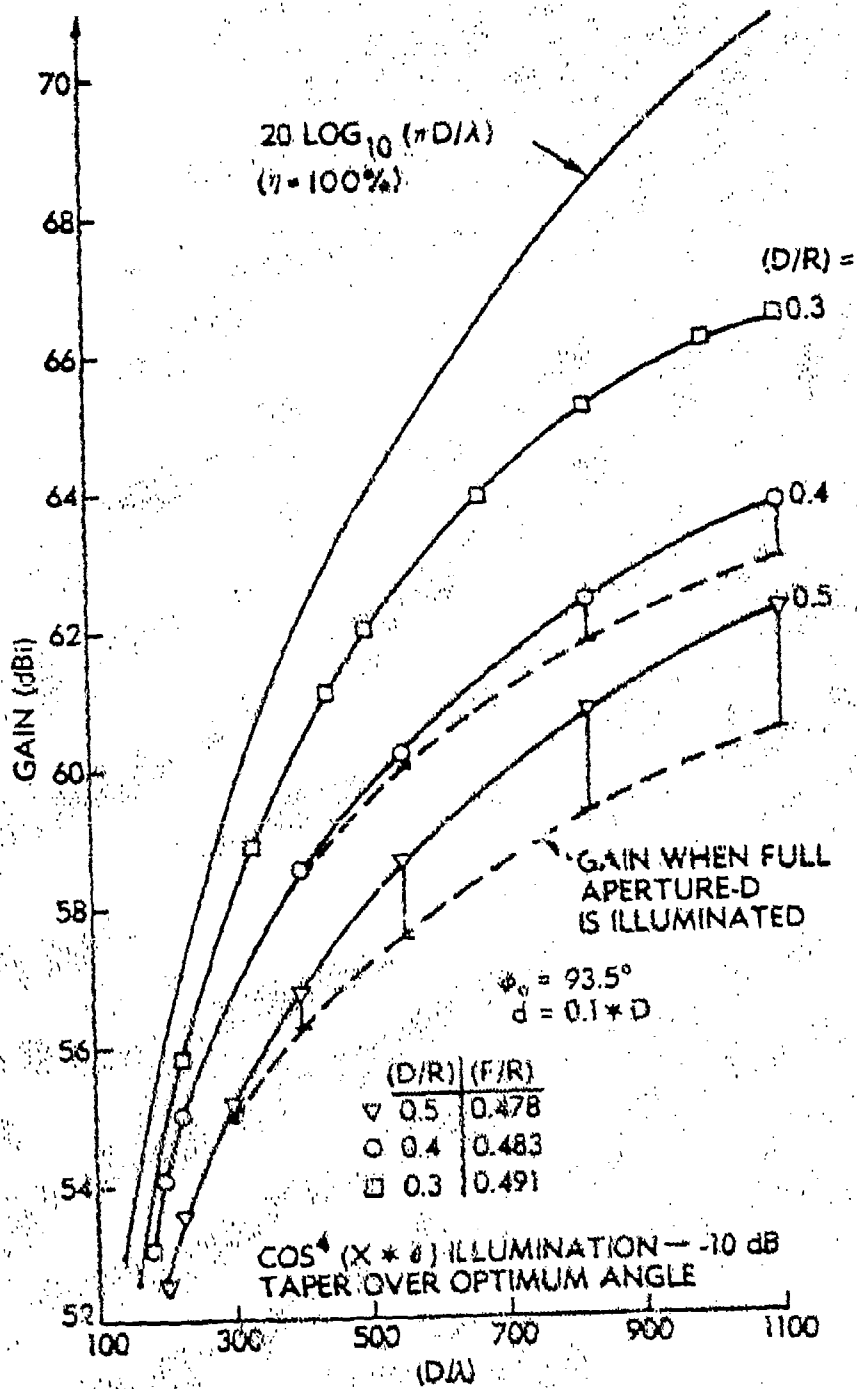
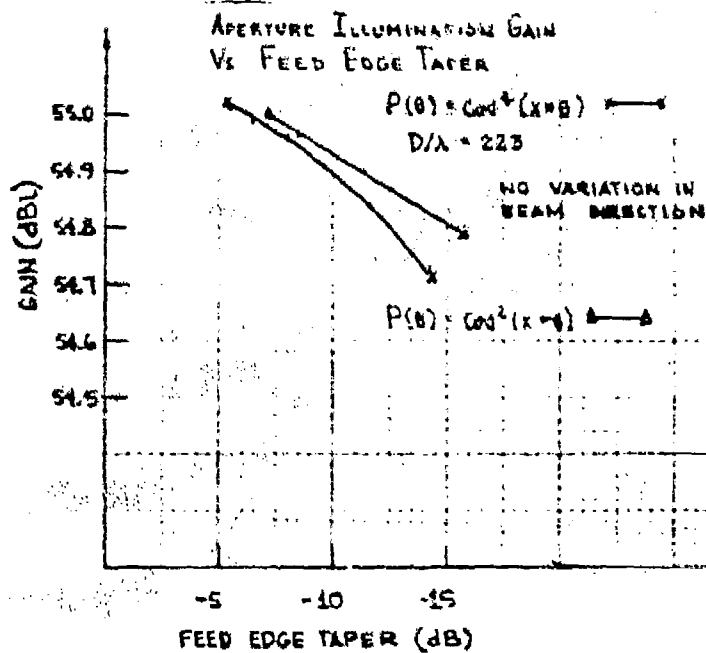
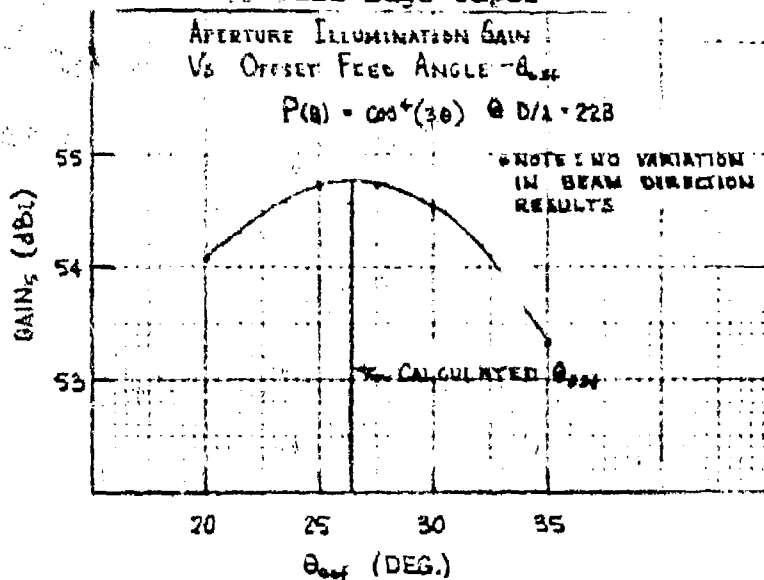


Figure 5-39. MBTA Illumination Gain vs D/λ

Figure 5-40. Aperture Illumination Gain
vs Feed Edge TaperFigure 5-41. Aperture Illumination Gain
vs Feed Offset Angle

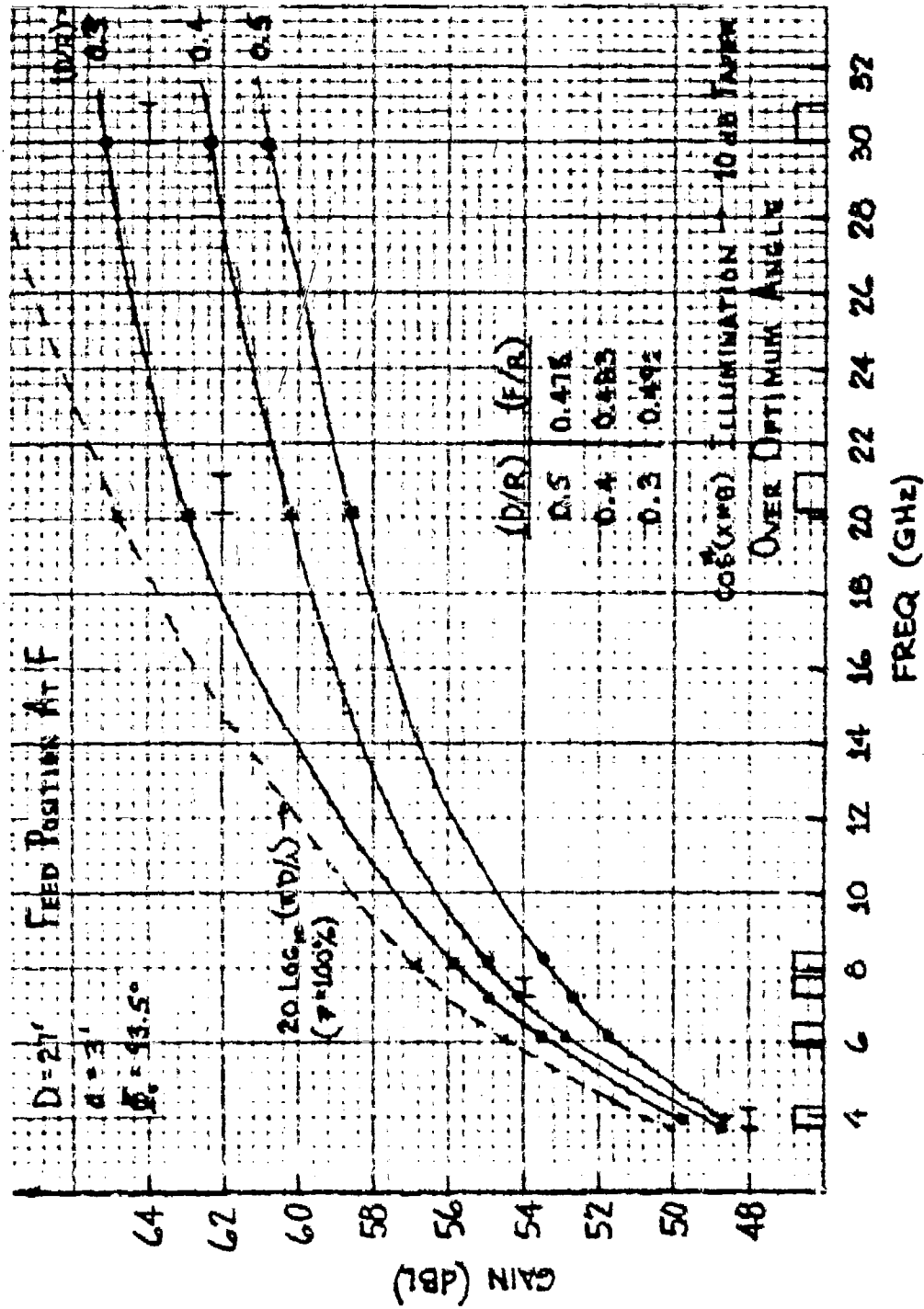


Figure 5-42. Aperture Illumination Gain (D = 27 ft) vs Frequency

room housing the feed/rail structure must be included. The $D/R = 0.4$ geometry provides an optimum 54-dB X-band gain solution for a 20° - 40° field of view. [The solution is optimum in the sense of minimizing the overall reflector area and ratio of reflector aperture dimensions (W/D) and ultimately cost.]

The relative projected aperture area of the MBTA is

$$\text{area} = WD \quad (5-96)$$

if the corner panels are not rounded. Since

$$\text{FOV} = \left(\frac{\pi}{180^\circ} \right) \left(\frac{D}{R} \right) \left(\frac{W}{D} - 1 \right) \quad (5-97)$$

then

$$\frac{\text{area}}{D^2} = \frac{(\pi/180^\circ)}{(D/R)} \text{FOV} + 1 \quad (5-98)$$

The projected aperture area¹⁵ of the MBTA as a function of D/R for fixed field of view requirements is shown in Figure 5-43. Contours of equal projected aperture areas can be placed on the illumination gain curves for a fixed field of view requirement, as shown in Figure 5-44. The relationship between D/λ and D/R , given a fixed area and field of view, is

$$\frac{D}{\lambda} = \sqrt{\frac{(\text{area}/\lambda^2)}{[(\pi/180^\circ)/(D/R)] \text{FOV}_0 + 1}} \quad (5-99)$$

These curves are quite helpful in arriving at a first-order optimum MBTA solution. Given a specified gain and field of view at a design frequency, the contours of equal projected aperture area identify the optimum D/R geometry.

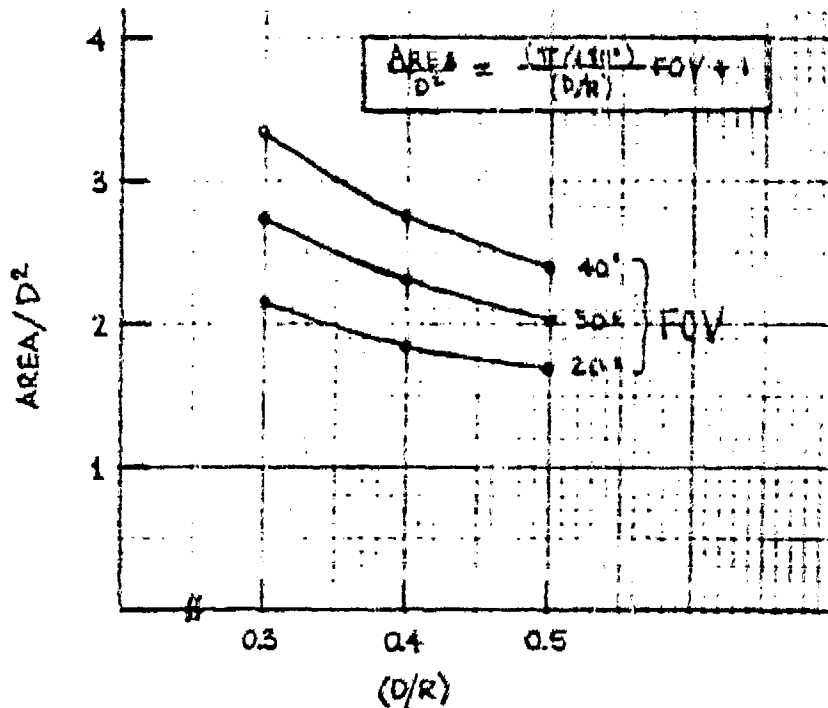


Figure 5-43. Projected Aperture Area of MBTA

5.12 OFFSET MBTA FIELD OF VIEW AND SCANNED
FEED PARAMETERS

The relationship between the MBTA field of view and the ratio of aperture plane dimensions for the offset geometry is

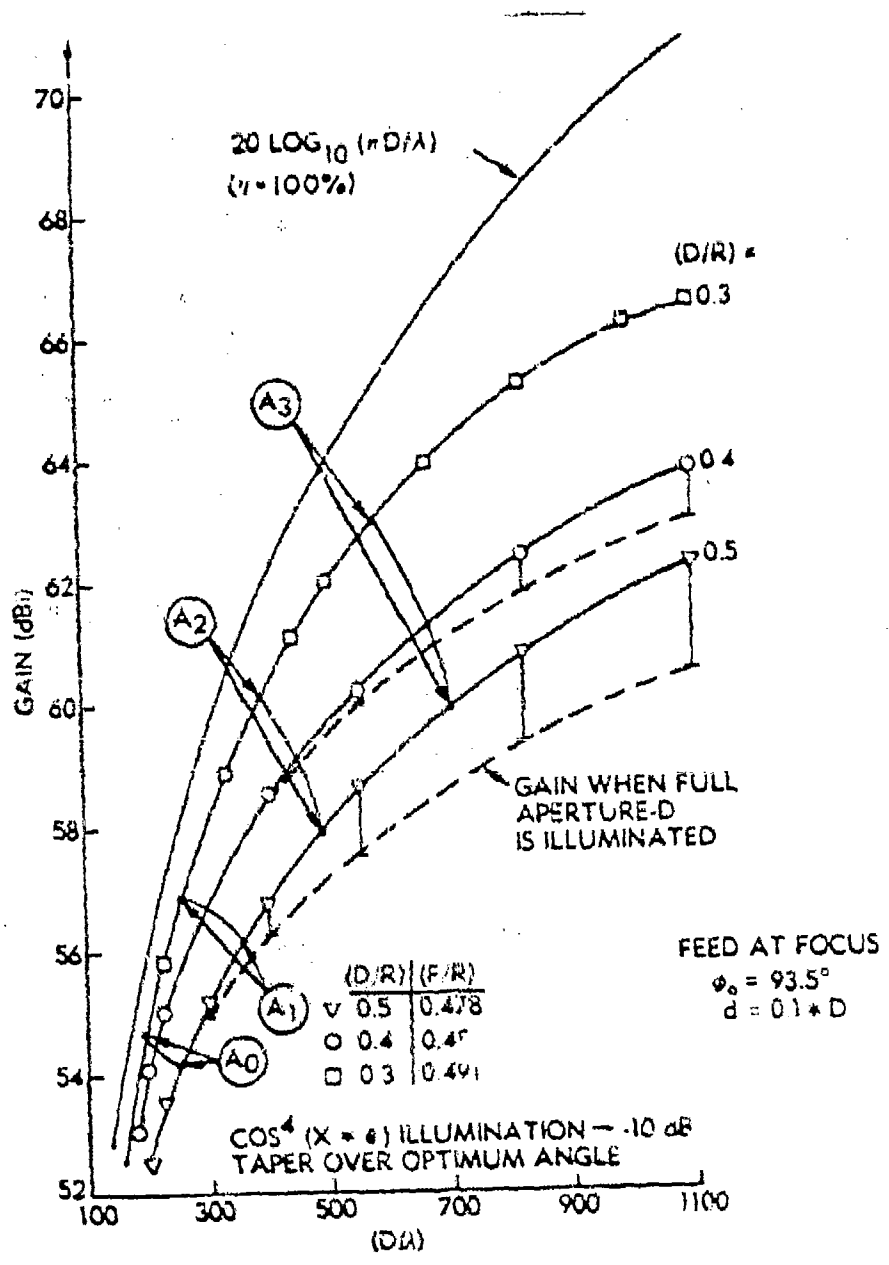


Figure 5-44. Illumination Gain with Equal Projected Area Contours

$$\text{FOV} = 2 \left[\sin^{-1} \left(\frac{W}{2D} \frac{D}{R} \frac{R}{R_c} \right) - \sin^{-1} \left(\frac{D}{2R} \frac{R}{R_c} \right) \right] \quad (5-100)$$

$$\text{FOV} = \left(\frac{180^\circ}{\pi} \right) \left(\frac{D}{R} \right) \left(\frac{W}{D} - 1 \right) \left(\frac{R}{R_c} \right) \quad (5-101)$$

where the ratio of the radius at the center of the aperture plane, R_c , to the radius, R , shown in Figure 5-45 is

$$\frac{R_c}{R} = 1 + \cos \phi_0 \left(\frac{D}{R} \right) \left(\frac{x_c}{D} \right) - \sin \phi_0 \frac{(D/R)^2 \left(\frac{x_c}{D} \right)^2}{4(F/R)} \quad (5-102)$$

The field of view versus W/D for the 10-percent offset geometry is shown in Figure 5-46. Comparison of the field of view in this figure with that for a symmetrical MBTA (Figure 5-5) indicates that the shorter radius of curvature at the center of the aperture for an offset geometry increases the field of view for a fixed W/D ratio. Program MBTA-2 calculates the field of view versus reflector parameters.

The locus of feed phase center positions as a function of spherical scan is derived from the geometry in Figure 5-47. The feed arc is defined in the v - w plane as the feed revolves around the rotation axis, \hat{u} . The scanned beam locus does not lie in the v - w plane, but the maximum angular deviation out of this plane is $2(\phi_0 - 90^\circ)$ for a full $\pm 180^\circ$ field of view. The beam scan angle, θ_s , is assumed to be the beam angle projected into the w - v plane. The coordinates of the feed phase center as a function of the beam scan angle are then

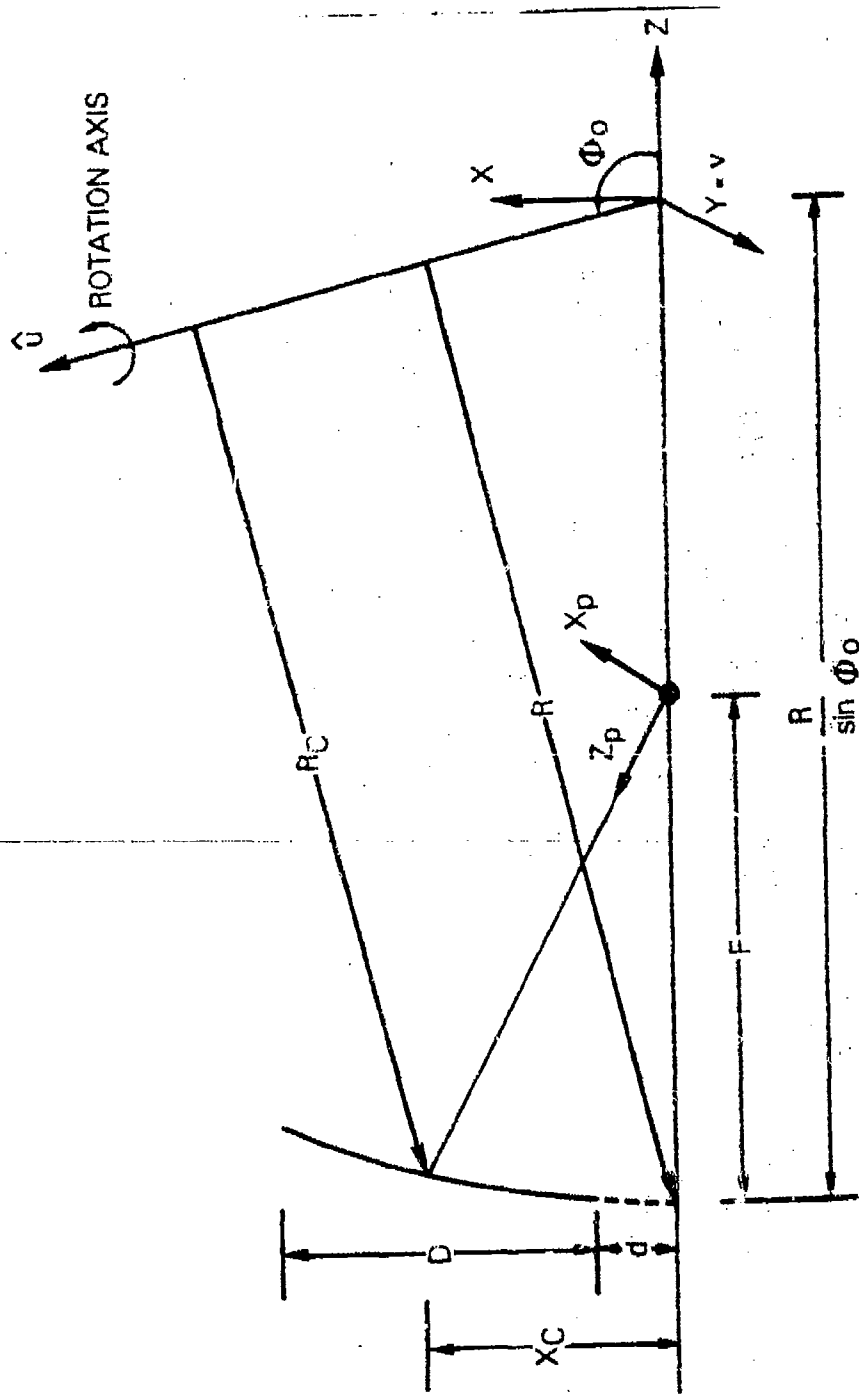


Figure 5-45. Feed Pointing Parameters for Offset MBTA

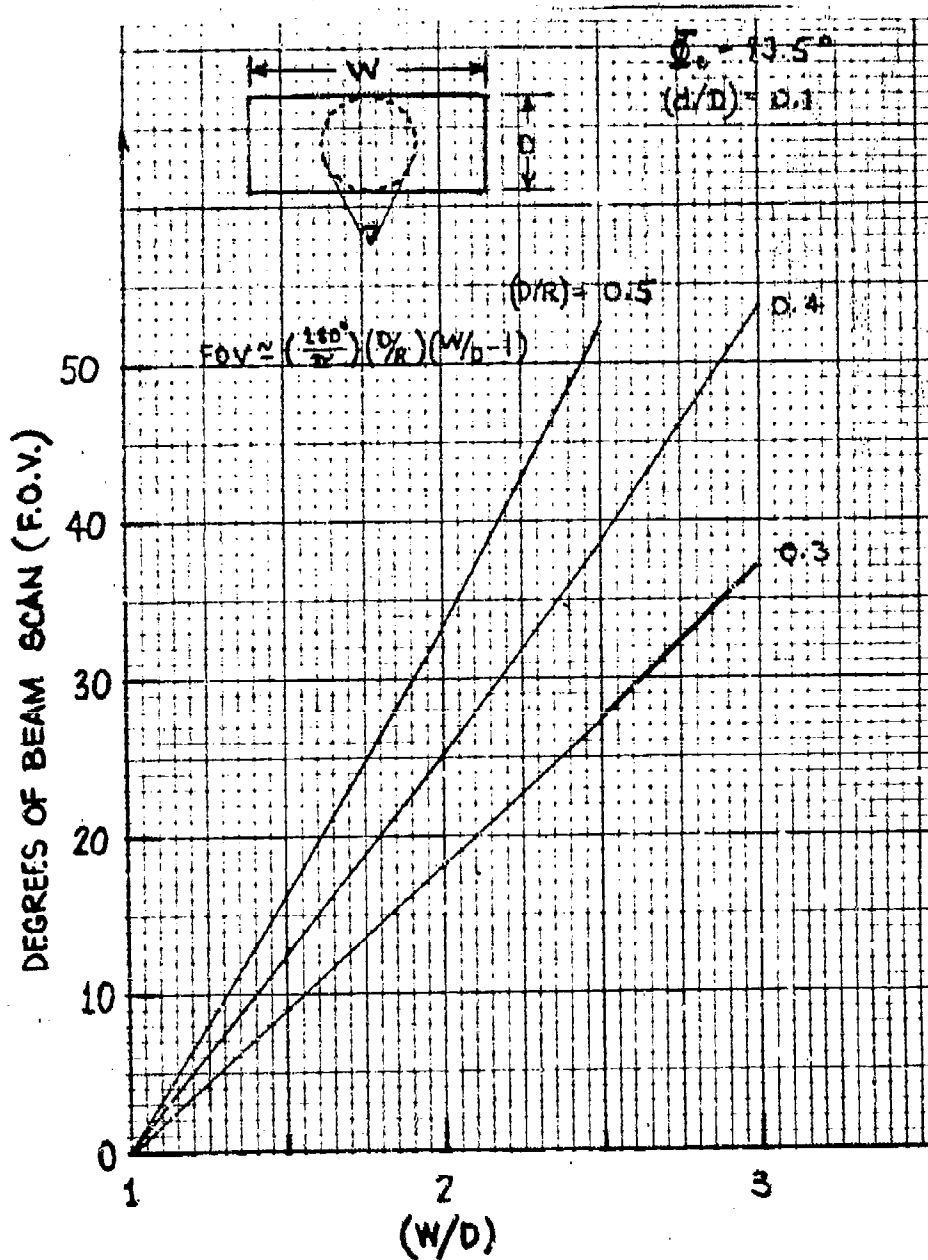


Figure 5-46. 10-Percent Offset MBTA Field of View vs (W/D)

$$w_f = -(R - F \sin \phi_0) \cos \theta_s \quad (5-103)$$

$$v_f = \pm(R - F \sin \phi_0) \sin \theta_s \quad (5-104)$$

Using the coordinate transformation in equation (5-45) and translating to an (x,y,z) system with origin at the focus yields

$$x_F = (R - F \sin \phi_0) \cos \phi_0 (\cos \theta_s - 1) \quad (5-105)$$

$$y_F = \pm(R - F \sin \phi_0) \sin \theta_s \quad (5-106)$$

$$z_F = \frac{(R - F \sin \phi_0)}{\sin \phi_0} \left[1 - \cos^2 \phi_0 - \sin^2 \phi_0 \cos \theta_s \right] \quad (5-107)$$

When normalized to the diameter, D , the feed phase center locations as a function of the spherical scan, θ_s , are

$$x_F = D \left(\frac{R}{D} \right) \left(1 - \frac{F}{R} \sin \phi_0 \right) \cos \phi_0 (\cos \theta_s - 1) \quad (5-108)$$

$$y_F = \pm D \left(\frac{R}{D} \right) \left(1 - \frac{F}{R} \sin \phi_0 \right) \sin \theta_s \quad (5-109)$$

$$z_F = D \left(\frac{R}{D} \right) \left(1 - \frac{F}{R} \sin \phi_0 \right) \left[\frac{1 - \cos^2 \phi_0 - \sin^2 \phi_0 \cos \theta_s}{\sin \phi_0} \right] \quad (5-110)$$

relative to an origin at the parabolic focus $(0,0,0)$.

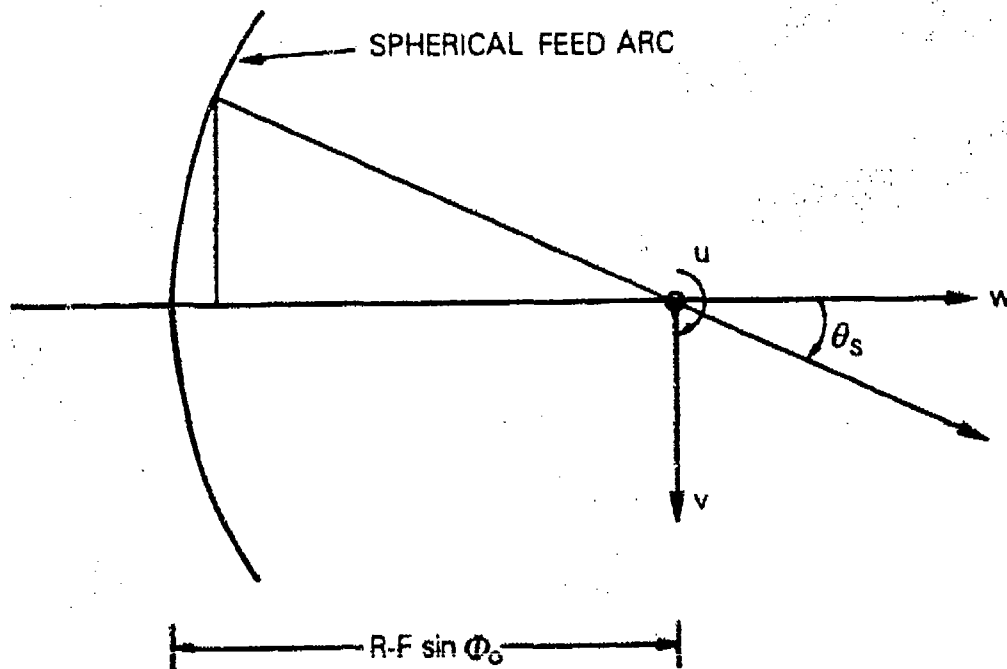


Figure 5-47. Scanned Beam Feed Position Geometry

The length of the projected feed arc for the offset
META is

$$l = 2\Delta v_f = 2(R - F \sin \phi_0) \sin \theta_s \quad (5-111)$$

$$l = 2 \left(\frac{D}{D/R} \right) \left(1 - \frac{F}{R} \sin \phi_0 \right) \sin \theta_s \quad (5-112)$$

The direction cosines defining the feed pointing axis and orientation as functions of scan are also required. The feed pointing axis, z_p , is shown in Figure 5-45. The projection of the z_p axis onto the v-w plane yields

$$u = \sin [\theta_{osf} + (\phi_0 - 90^\circ)] \quad (5-113)$$

$$v = \pm \sin \theta_s \cos [\theta_{osf} + (\phi_0 - 90^\circ)] \quad (5-114)$$

$$w = - \cos \theta_s \cos [\theta_{osf} + (\phi_0 - 90^\circ)] \quad (5-115)$$

The direction cosines for the feed pointing in the (x,y,z) coordinates with the origin at the parabolic focus are

$$\begin{aligned} \alpha_x = & \sin \theta_{osf} (\sin^2 \phi_0 + \cos^2 \phi_0 \cos \theta_s) \\ & + \cos \theta_{osf} \sin \phi_0 \cos \phi_0 (\cos \theta_s - 1) \end{aligned} \quad (5-116)$$

$$\alpha_y = - \sin \theta_s (\cos \theta_{osf} \sin \phi_0 + \sin \theta_{osf} \cos \phi_0) \quad (5-117)$$

$$\begin{aligned} \alpha_z = & \sin \theta_{osf} \sin \phi_0 \cos \phi_0 (1 - \cos \theta_s) \\ & - \cos \theta_{osf} (\cos^2 \phi_0 + \sin^2 \phi_0 \cos \theta_s) \end{aligned} \quad (5-118)$$

and

$$\sqrt{\alpha_x^2 + \alpha_y^2 + \alpha_z^2} = 1 \quad (5-119)$$

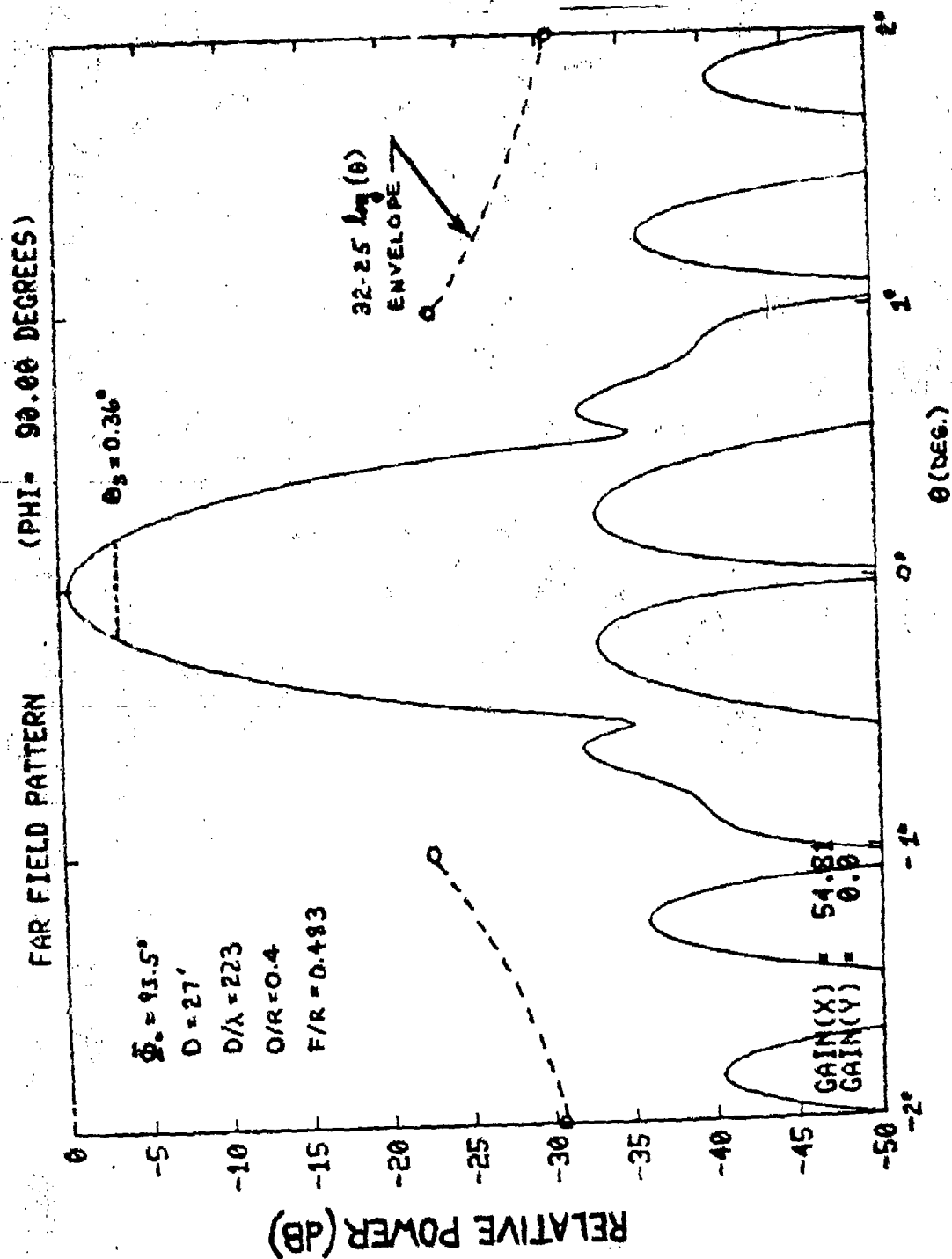
Program MBTA-10 calculates the feed phase center position relative to the initial focus given the desired scan angle. It also furnishes the direction cosines for the feed pointing.

5.13 PATTERNS AND POLARIZATION

The principal plane linearly polarized patterns for the baseline 27-ft-diameter MBTA are shown in Figures 5-48 and 5-49. In the geosynchronous plane ($\phi = 90^\circ$), the pattern is symmetrical in θ , first sidelobe levels are below 30 dB, and the maximum cross-polarization lobe for a corrugated feed horn is 33 dB. The half-power beamwidth is 0.36° . In the plane of the offset parabolic section ($\phi = 0^\circ$), the pattern is slightly asymmetrical due to asymmetrical amplitude and phase aperture distributions. A small amount of beam scan is noted when the feed is at the parabolic focus, and the half-power beamwidth is 0.34° . These patterns were calculated using a -10.6-dB feed taper over the feed illumination angle of 42.4° . Increasing the feed edge taper to -15 dB virtually eliminates feed spillover energy past the reflector with only a 0.2-dB gain loss. A 3λ circular aperture conical horn provides an identical pattern in the $\phi = 90^\circ$ plane and a slightly narrower pattern in the $\phi = 0^\circ$ plane. However, the maximum cross-polarization levels increase to 25 dB as a result of unequal E- and H-plane pattern amplitude functions from the conical horn aperture.

The large effective $F/D = 1.25$ of the baseline MBTA configuration means that circularly polarized beam squint effects are negligible. The circular cross-polarization response is essentially determined by the polarization characteristics of the feed system.^{16,17}

The wide-angle sidelobe characteristics of the baseline MBTA at X-band to $\pm 5^\circ$ are shown in Figures 5-50 and 5-51. The sidelobe envelopes are well below the $32 - 25 \log_{10} \theta$ criteria.^{18,19} The lack of a Cassegrain subreflector with its feed spillover contributions to the sidelobe envelope and feed or

Figure 5-48. Baseline MBTA Pattern ($\phi = 90^\circ$)

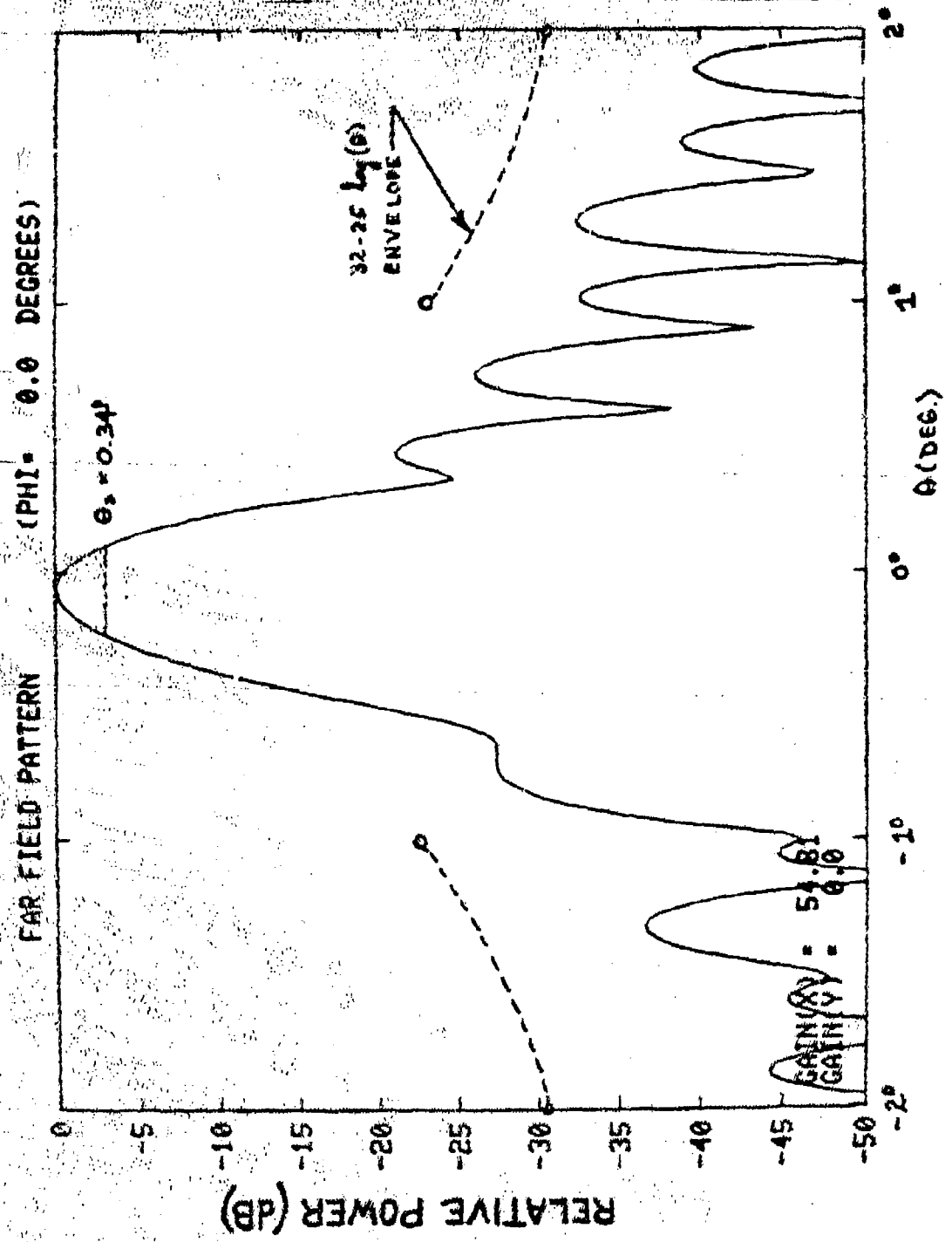


Figure 5-49. Baseline MBTA Pattern ($\phi = 0^\circ$)

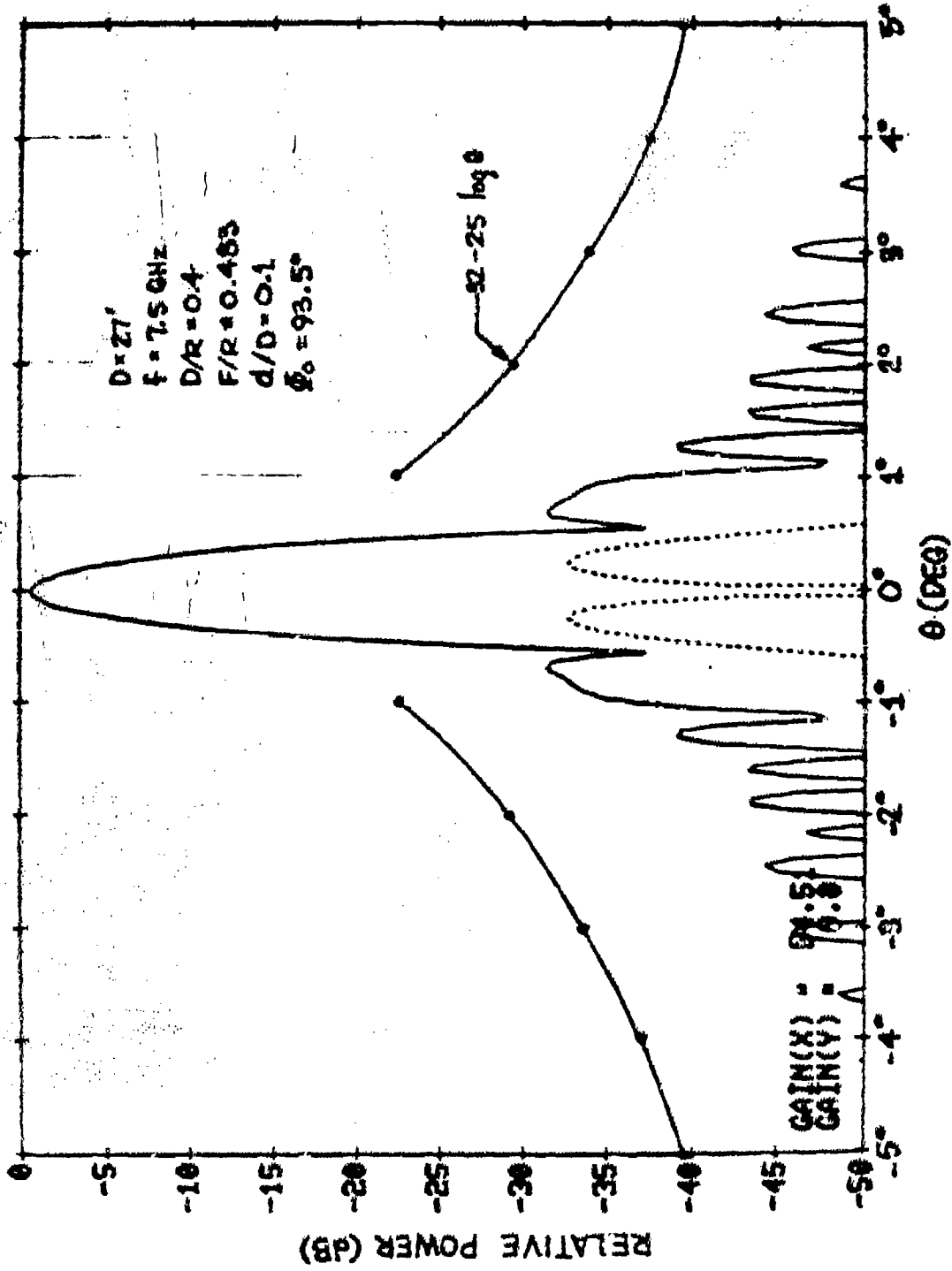


Figure 5-50. Baseline MBTA Receive Band Pattern at 7.5 GHz ($\phi = 90^\circ$)

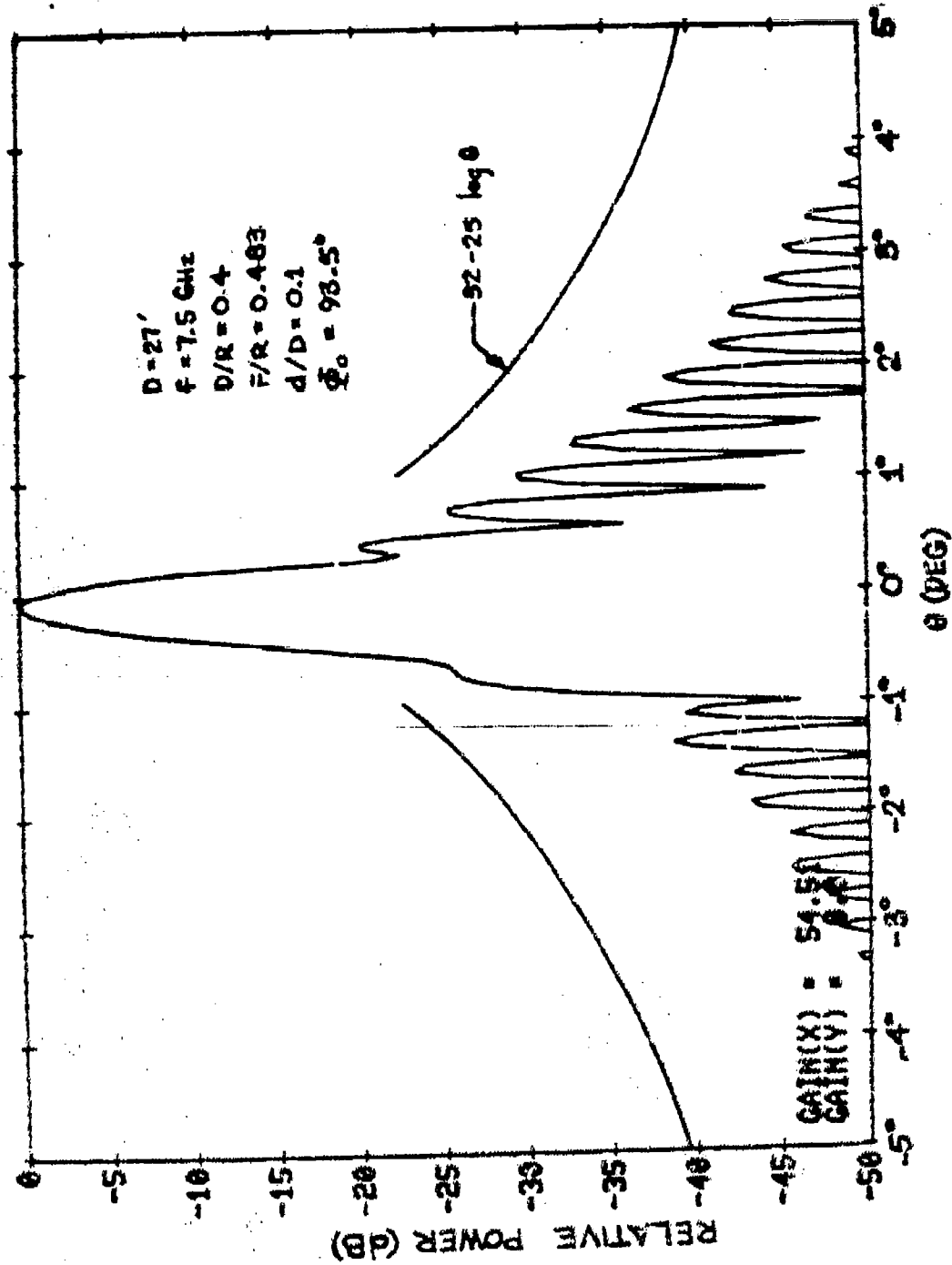


Figure 5-51. Baseline MBTA Receive Band Pattern at 7.5 GHz ($\phi = 0^\circ$)

subreflector/spar blockage provide the offset MBTA with exceptional wide-angle sidelobe envelopes. The principal plane patterns of the 27-ft-diameter MBTA ($D/R = 0.4$) geometry in the 4-, 12-, and 30-GHz receive bands are shown in Figures 5-52 through 5-57. The higher frequency band patterns indicate the effects of spherical aberration in the offset reflector. The $\phi = 90^\circ$ pattern broadens symmetrically, while the $\phi = 0^\circ$ pattern becomes more asymmetrical and the $-\theta$ scanning effect is more visible. A corrugated feed horn pattern was used to calculate these results.

The X-band patterns for a 48-ft-diameter MBTA with $D/R = 0.3$ are shown in Figures 5-58 and 5-59. A corrugated feed horn pattern was utilized for the pattern calculations. The maximum cross-polarization lobe is lower for the $D/R = 0.3$ geometry, since the reflector surface is flatter. Figure 5-60 shows the $D/R = 0.3$ offset geometry approximately to scale.

5.14 NOISE TEMPERATURE AND FEED SPILLOVER

The calculated and measured antenna noise temperatures for the offset front-fed MBTA are remarkably good. The antenna temperature measured on COMSAT Laboratories' 32- x 55-ft MBTA (elevation angle = 21.6°) was 23 K at 3.95 GHz.

Exceptional noise temperature characteristics are a result of the following:

- a. a corrugated feed horn with a rotationally symmetric (Gaussian) amplitude pattern which has virtually no sidelobes,
- b. the lack of aperture blockage (feed, subreflector, or spars) and forward feed spillover past a subreflector (Cassegrain geometries), and
- c. an oversize reflecting aperture relative to the required aperture area, which also reduces reflector spillover.

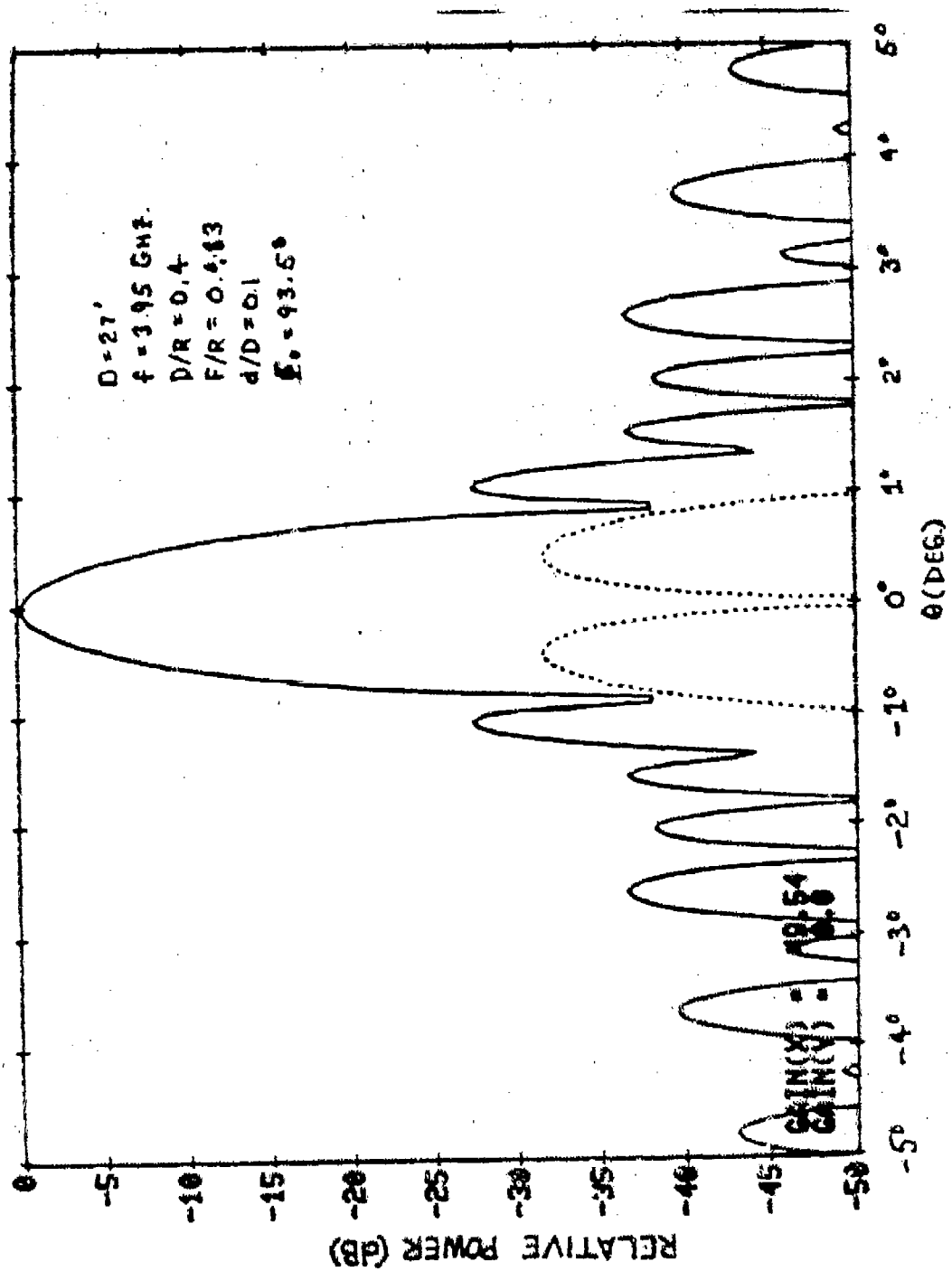


Figure 5-52. Baseline MBTA Receive Band Pattern at 3.95 GHz ($\phi = 90^\circ$)

COMBAT Labs

Multiple Beam Torus
Antenna Study

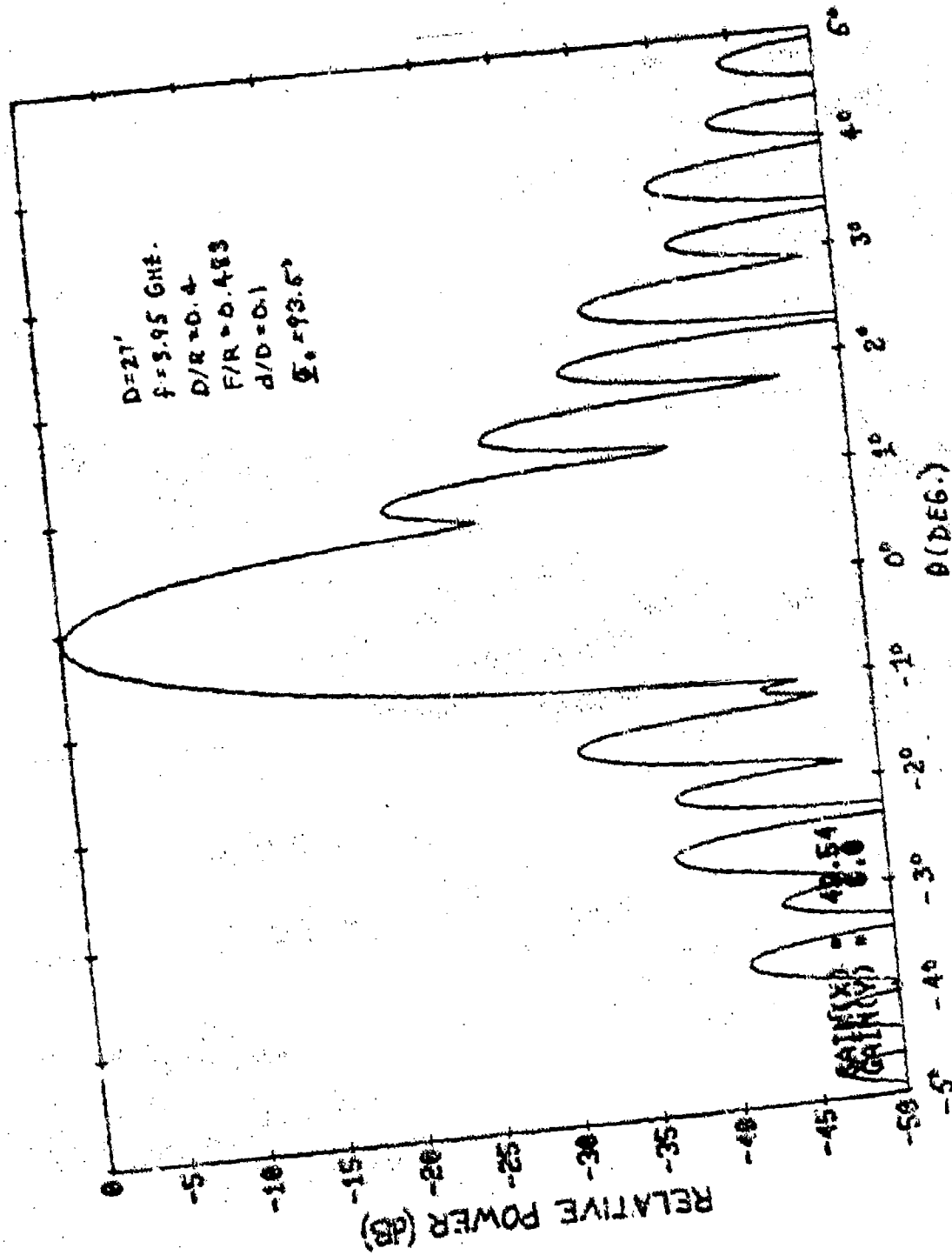


Figure 5-53. Baseline MTA Receive Band Pattern at 3.95 GHz ($\phi = 0^\circ$)

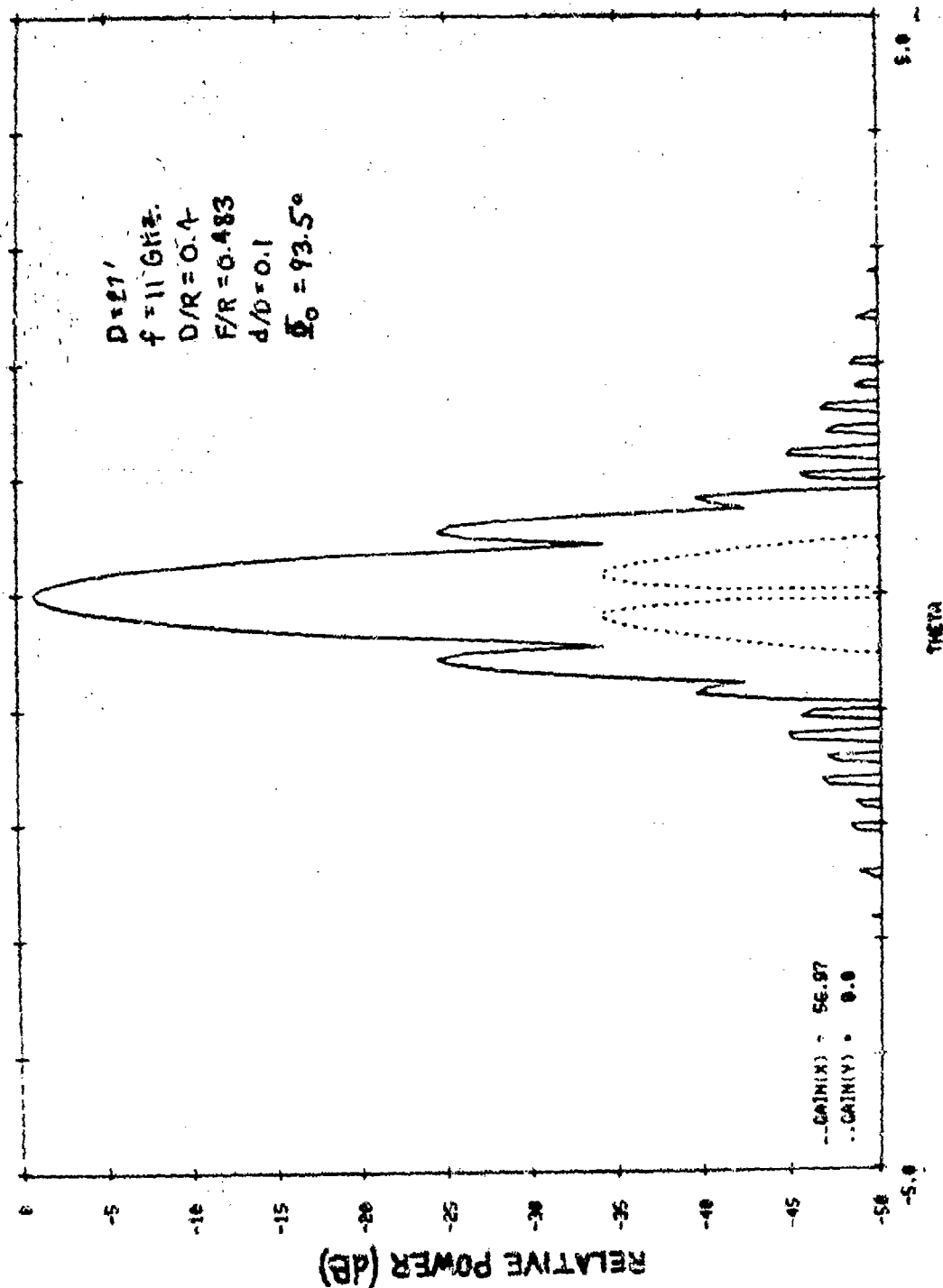


Figure 5-54. Baseline MBTA Receive Band Pattern at 11 GHz ($\phi = 90^\circ$)

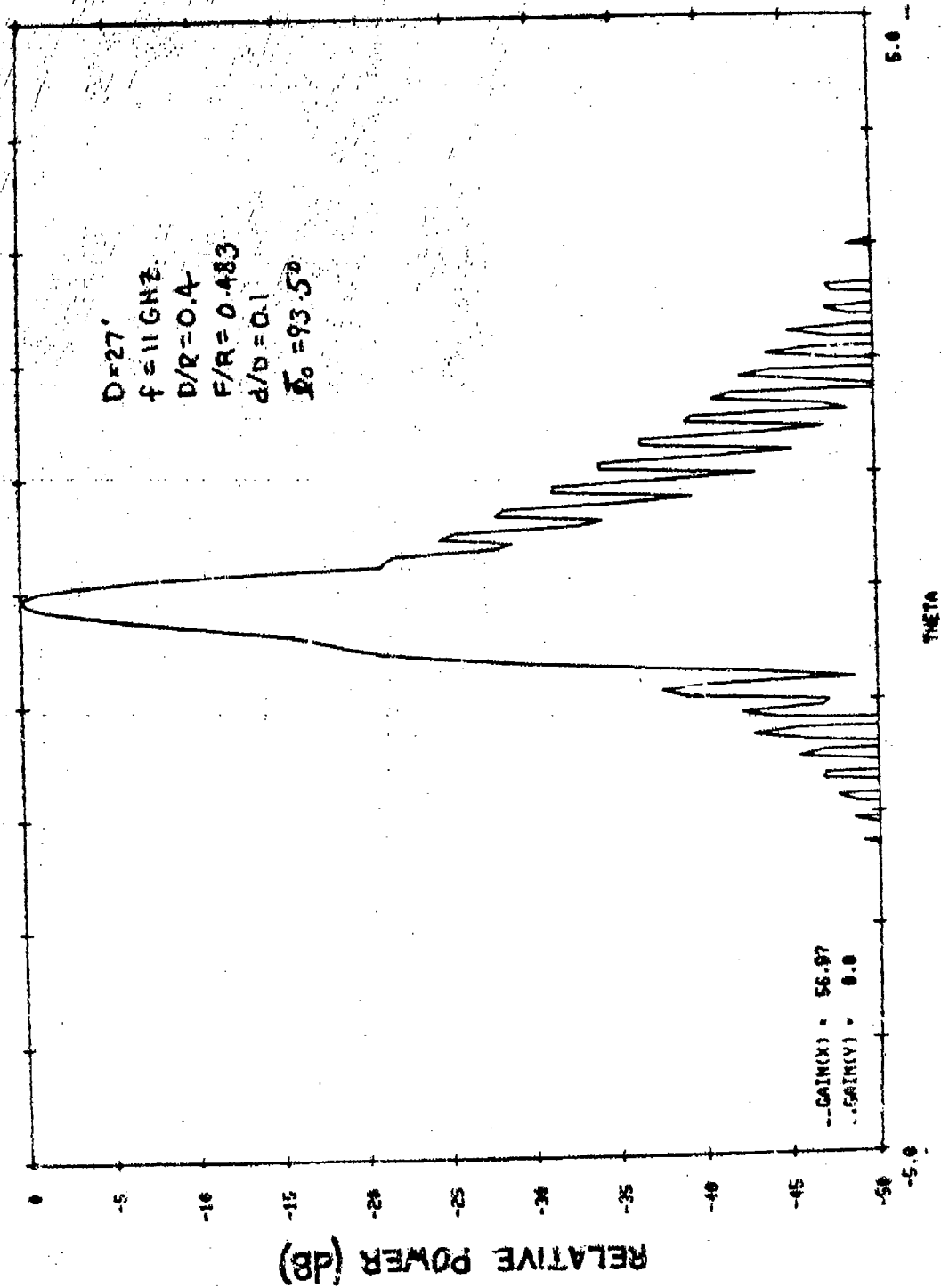


Figure 5-55. Baseline MBTA Receive Band Pattern at 11 GHz ($\phi = 0^\circ$)

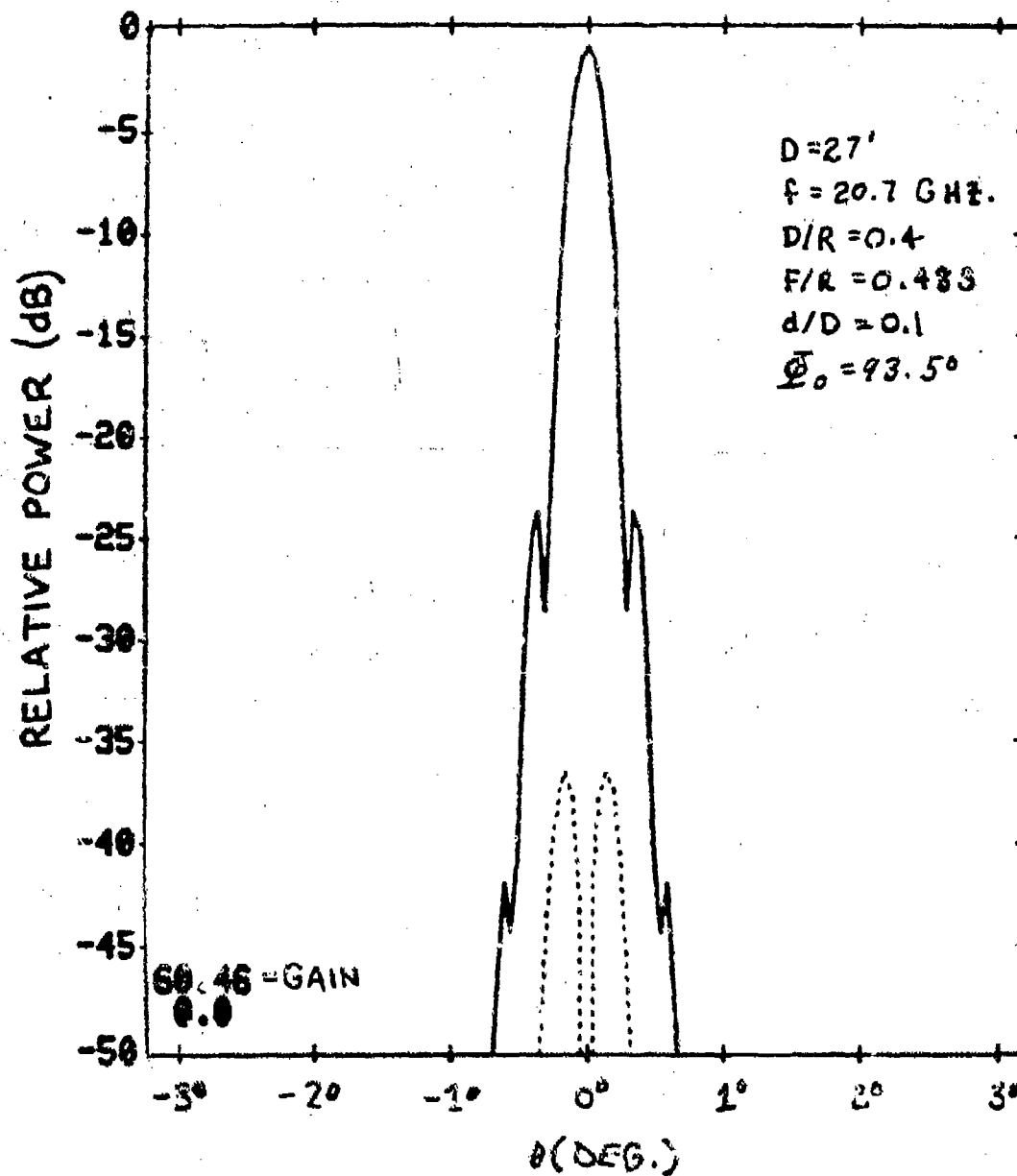


Figure 5-50. Baseline MBTA Receive Band Pattern
at 20.7 GHz ($\phi = 90^\circ$)

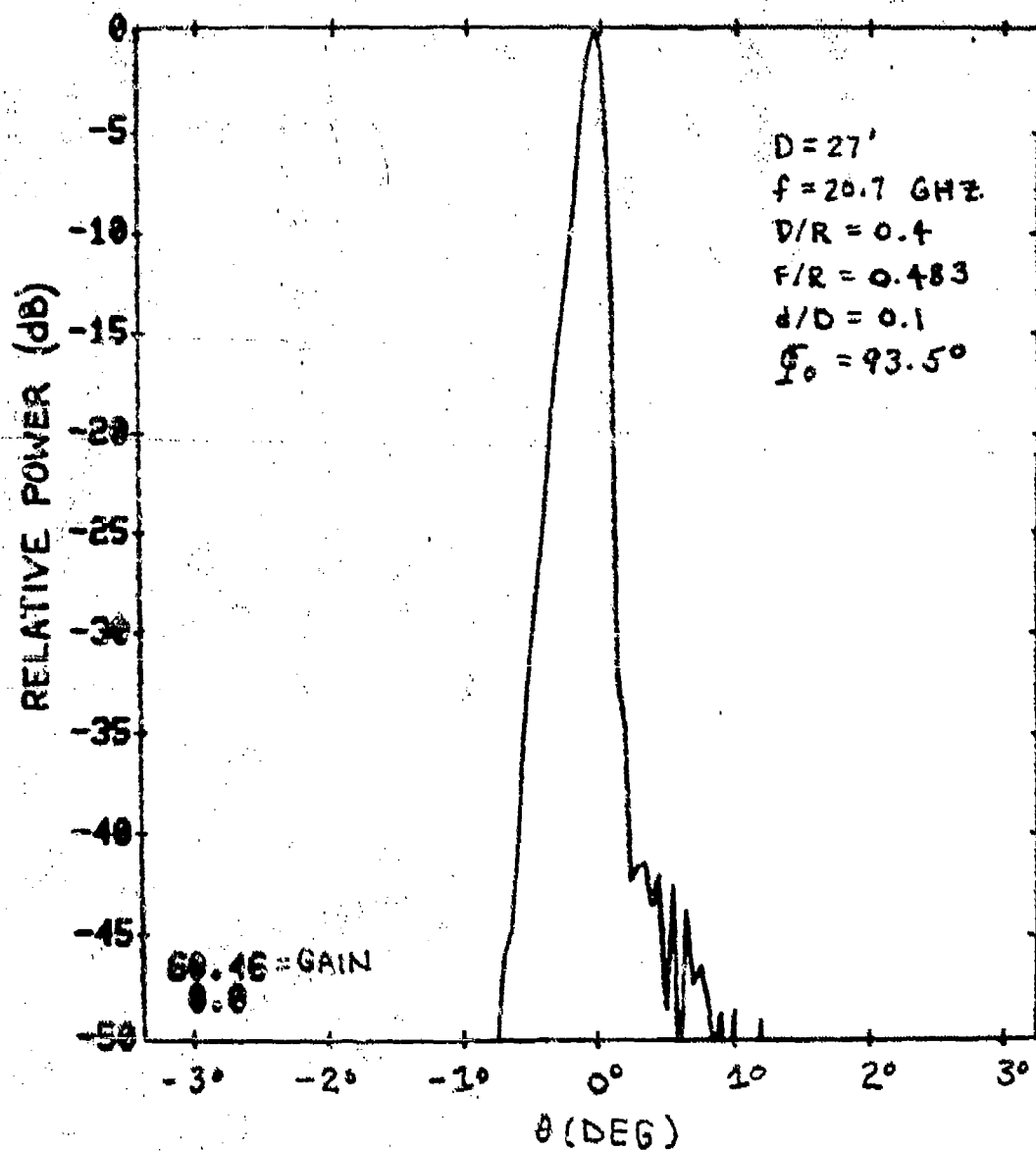


Figure 5-57. Baseline MBTA Receive Band Pattern
at 20.7 GHz ($\phi = 0^\circ$)

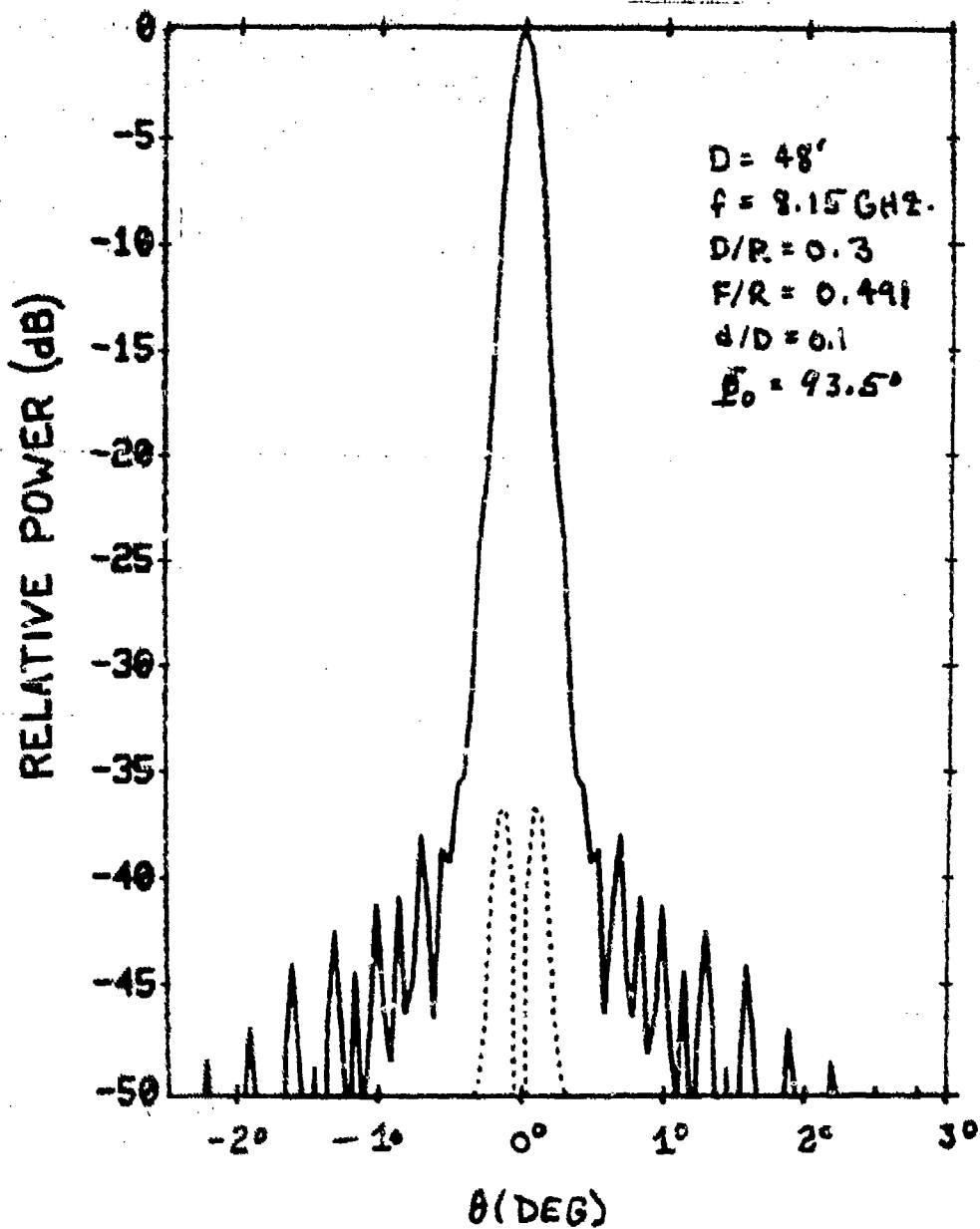


Figure 5-58. 48-ft-Diameter MBTA ($D/R = 0.3$)
Pattern at 8.15 GHz ($\theta = 90.2^\circ$)

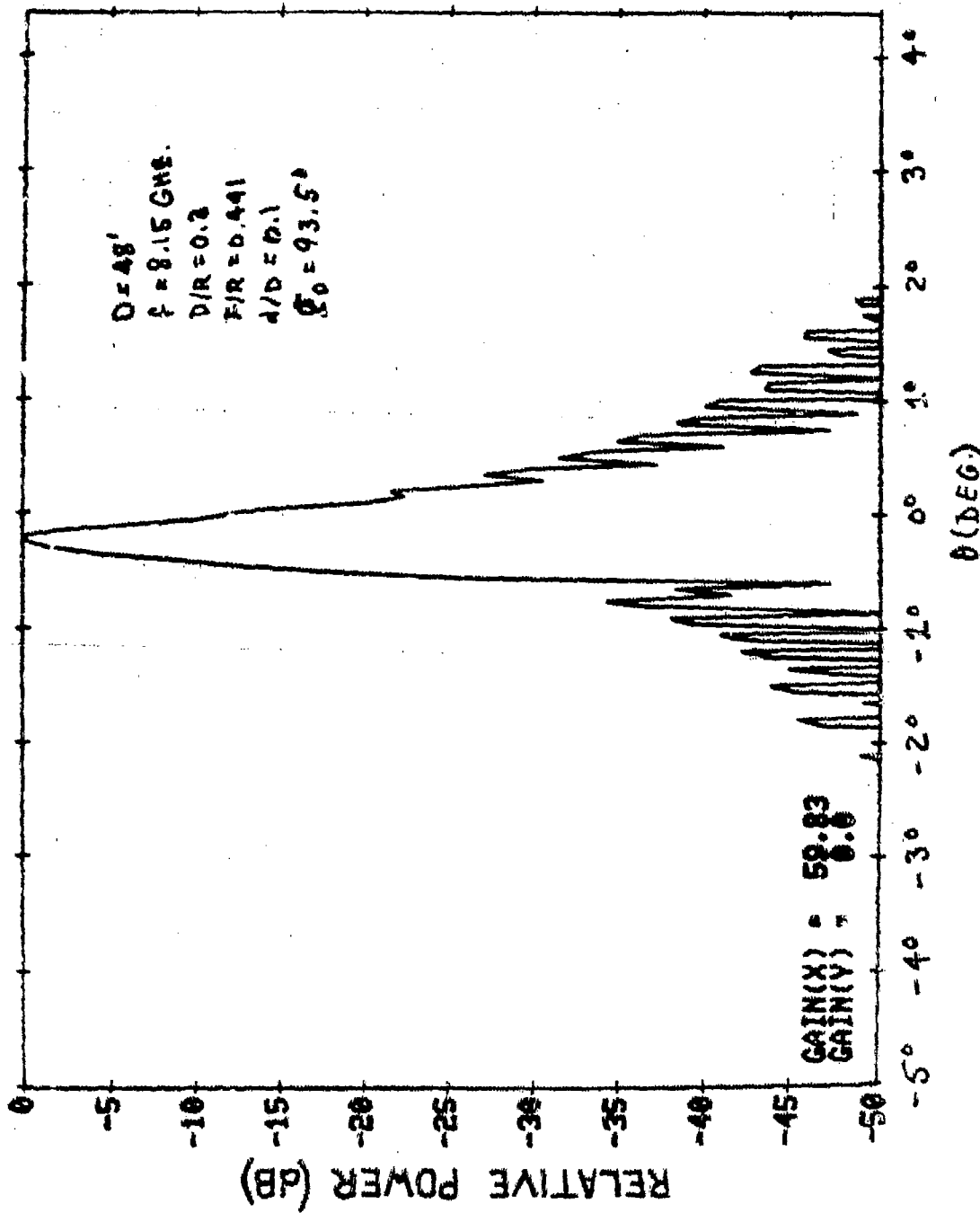


Figure 5-59. 48-ft-Diameter MBTA ($D/R = 0.3$) Pattern at
8.15 GHz ($\phi = 0^\circ$)

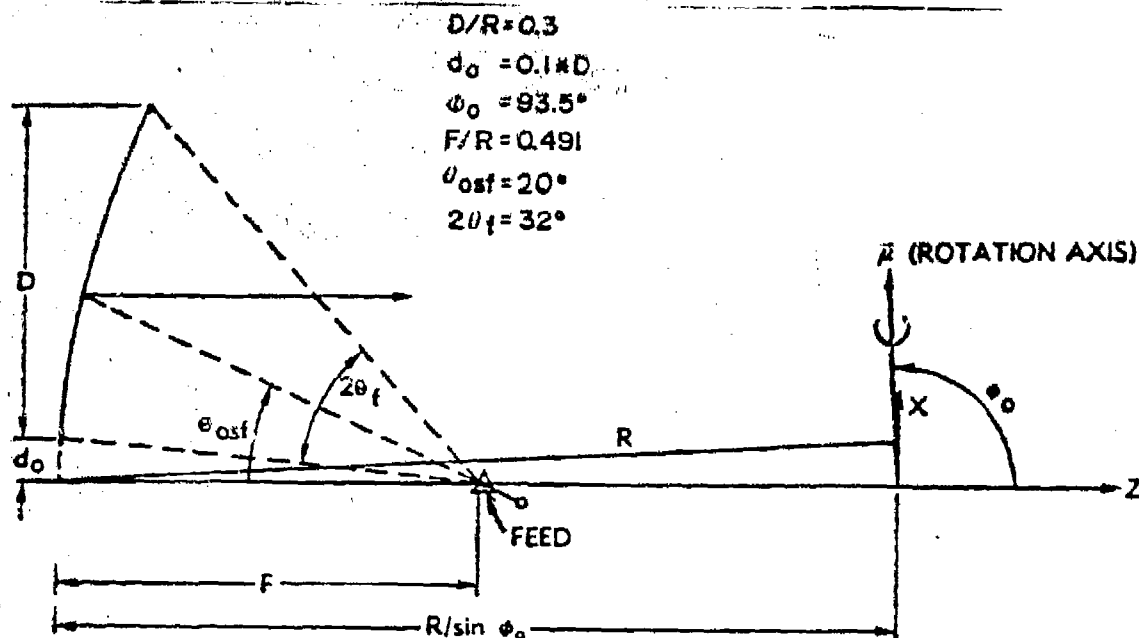


Figure 5-60. Offset MBTA $D/R = 0.3$ Geometry

The corrugated feed horn patterns minimize feed spillover energy past the reflector. In addition, the corrugated horn has exceptionally low backscatter patterns as a result of the highly tapered feed horn amplitude distribution. Electromagnetic fields are zero at the edges of the aperture. Hence, exterior currents, which would contribute to a backscatter pattern, are not induced on the outside of the horn.

The percentage of corrugated feed horn energy beyond a specified amplitude level is

$$\text{spillover} = \frac{\int_{\theta_0}^{180^\circ} \int_0^{360^\circ} P(\theta) \sin \theta \, d\theta \, d\phi}{\int_0^{180^\circ} \int_0^{360^\circ} P(\theta) \sin \theta \, d\theta \, d\phi} \quad (5-120)$$

where θ_0 is one-half the feed illumination angle.

With a rotationally symmetric feed amplitude pattern, the feed spillover beyond a specified illumination half-angle is

$$\text{spillover} = \frac{\int_{\theta_0}^{180^\circ} P(\theta) \sin \theta \, d\theta}{\int_0^{180^\circ} P(\theta) \sin \theta \, d\theta} \quad (5-121)$$

Figure 5-61 shows the spillover characteristics of corrugated feed horns with beamwidths applicable to the offset MBTA geometries. A -10-dB edge taper over the $2\theta_f = 24.4^\circ$ feed illumination angle of the baseline $D = 27$ ft, $D/R = 0.4$ geometry gives less than 0.57 dB of spillover. Increasing the edge taper to -15 dB reduces the spillover to 0.18 dB.

The lack of aperture blockage and forward feed spillover past a subreflector results in excellent wide-angle sidelobes for the MBTA. Aperture blockage raises the average sidelobe level and is a major source of wide-angle scatter in large-aperture antenna systems. Forward feed spillover in Cassegrain geometries partially couples to a warm earth and generally gives rise to a significant sidelobe contribution along the geostationary arc at an angle off the beam axis that corresponds to the feed spillover angle past the subreflector. The gain (in dBi) of this sidelobe contribution is the feed system gain at the specified angle if the feed spillover contribution is significantly larger than the sidelobe contribution of the reflector aperture illumination.

Figure 5-62 shows the aperture illuminated areas on the MBTA for beams at the center and edge of the field of view. For the majority of beam positions, most of the feed "spillover" past the circular illumination area is collimated by the reflector and appears in the main beam.

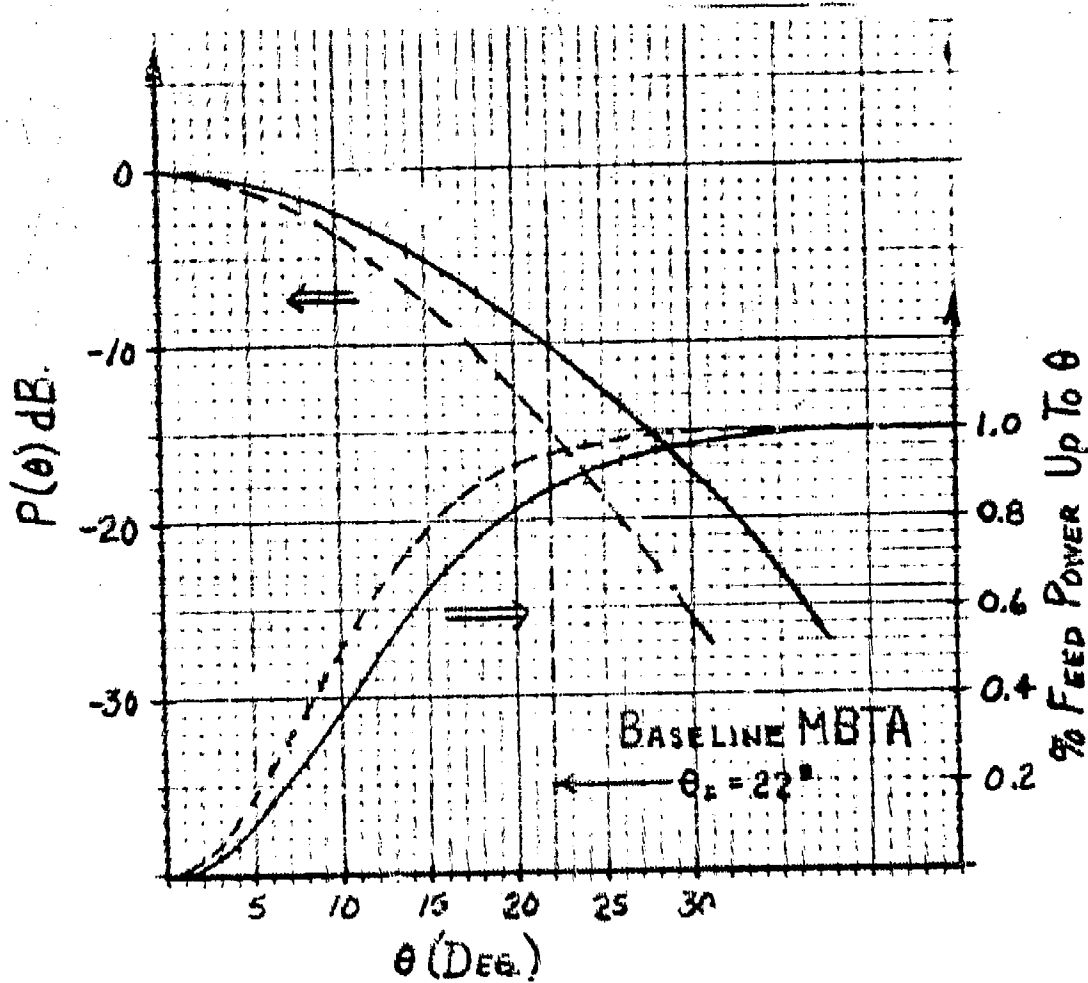


Figure 5-61. Spillover Characteristics of Corrugated Feed Horn for Baseline MBTA

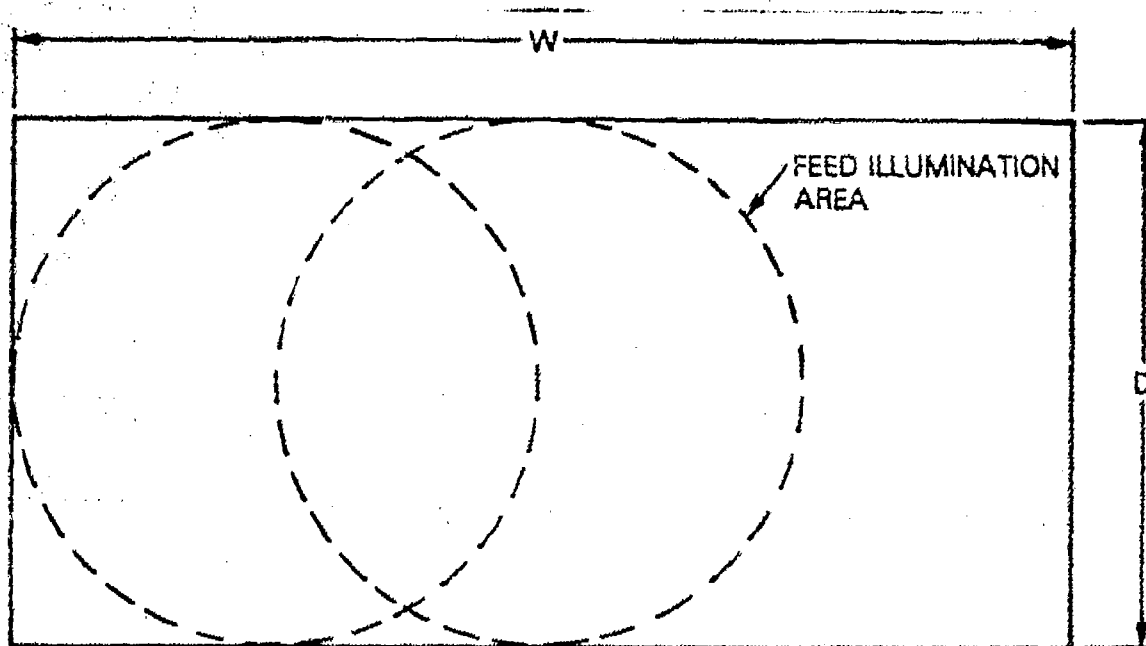


Figure 5-62. Extended MBTA Aperture Area
Decreases Feed Spillover

The calculated antenna temperature characteristics of the offset MBTA at X-band are shown in Figure 5-63 as a function of the local elevation angle. This curve, which is applicable to both the $D = 27$ ft and $D = 48$ ft MBTA geometries, includes 0.1-dB feed system losses. Additional losses would add

$$T_{\text{FEED LOSS}} (K) = \text{loss (dB)} \left(\frac{7 K}{0.1 \text{ dB}} \right) \quad (5-122)$$

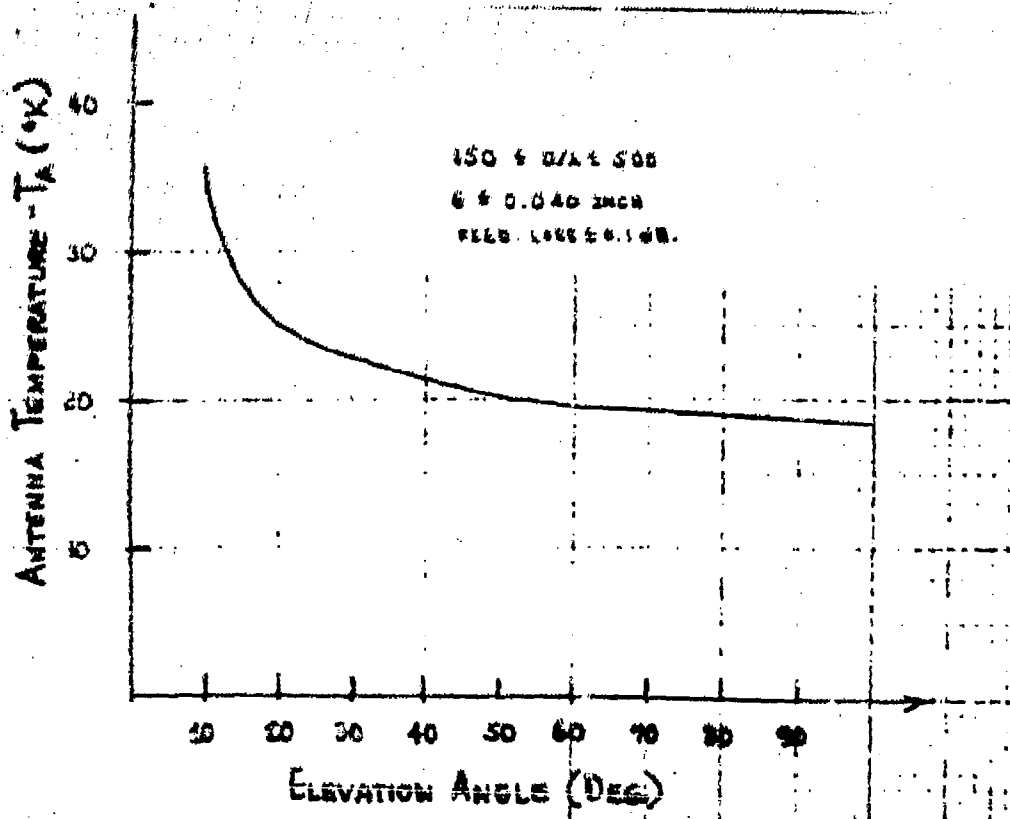


Figure 5-63. MBTA Antenna Temperature at X-Band

5.15

ABERRATION-CORRECTING SUBREFLECTORS

Aberration-correcting subreflectors²⁰ have been investigated at COMSAT Laboratories as a means of obtaining better aperture illumination efficiencies in large-aperture ($D/\lambda \geq 300$) offset MBTA antennas. The correcting subreflector concept, shown in Figure 5-64, involves the design of a second reflecting surface between the aperture plane of the MBTA and a designated feed position so that the path length from any point in the aperture to the feed position is identical. To realize a reasonably shaped

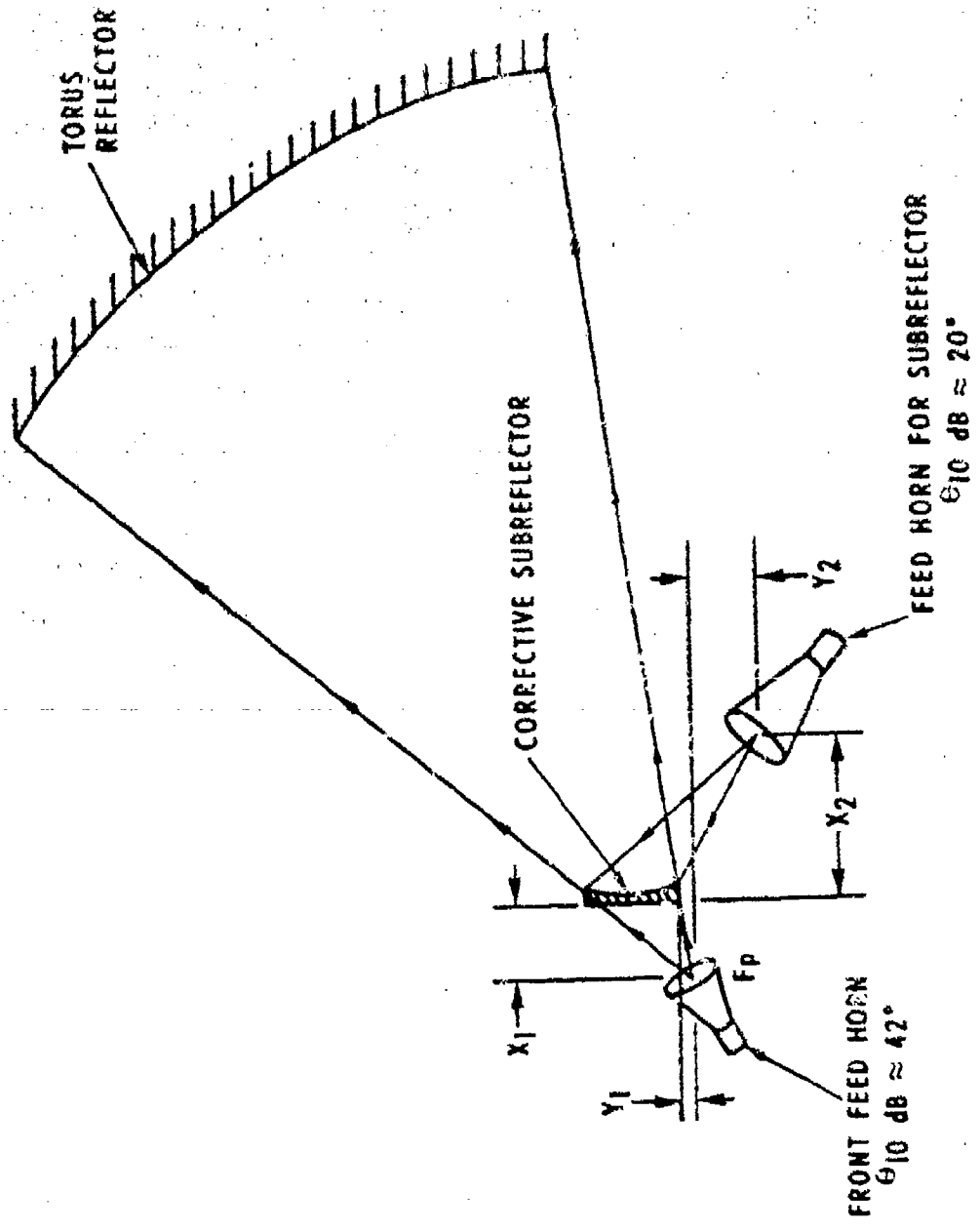


Figure 5-64. MBTA with Phase Corrective Subreflector

subreflector design, it was found necessary to displace the parabolic and spherical foci of the MBTA. Hence, because the corrected MBTA reflector has very poor efficiency when utilized with a focal point feed, all frequency bands (ranges of D/λ) that utilize the corrected MBTA configuration must operate in conjunction with a correcting subreflector.

In principle, a correcting subreflector could improve the aperture illumination efficiency associated with the smaller radius of curvature MBTA design ($D/R = 0.5$) and permit the use of smaller aperture dimension ratios (W/D) for a specified field of view. The correcting subreflector surface is lossless and a simple feed horn is used.

There are several disadvantages associated with the use of an aberration-correcting subreflector. The first is the mechanical complexity associated with the feed/subreflector system. The feed and subreflector must be carefully aligned and must maintain their alignment while both travel on different radii of curvature to scan the beam. For larger aperture X-band antennas, the subreflector diameter would typically be 5-10 ft and the precision subreflector surface required would have to be protected.

Use of the aberration-correcting subreflector results in a considerable increase in the minimum beam spacing along the geosynchronous arc. Figure 5-65 shows that the diameter of the subreflector limits the minimum beam spacing rather than the diameter of the feed horn aperture. Figure 5-66 is a photograph of the correcting subreflector that was designed and tested on a 10-ft scale model torus at COMSAT Laboratories. The aberration-correcting torus demonstrated aperture illumination efficiencies of $\eta = 72$ percent for $D/\lambda \leq 430$. The 10-in. correcting subreflector diameter for the 10-ft scale model would correspond to 4 feet for a 48-ft-diameter MBTA.

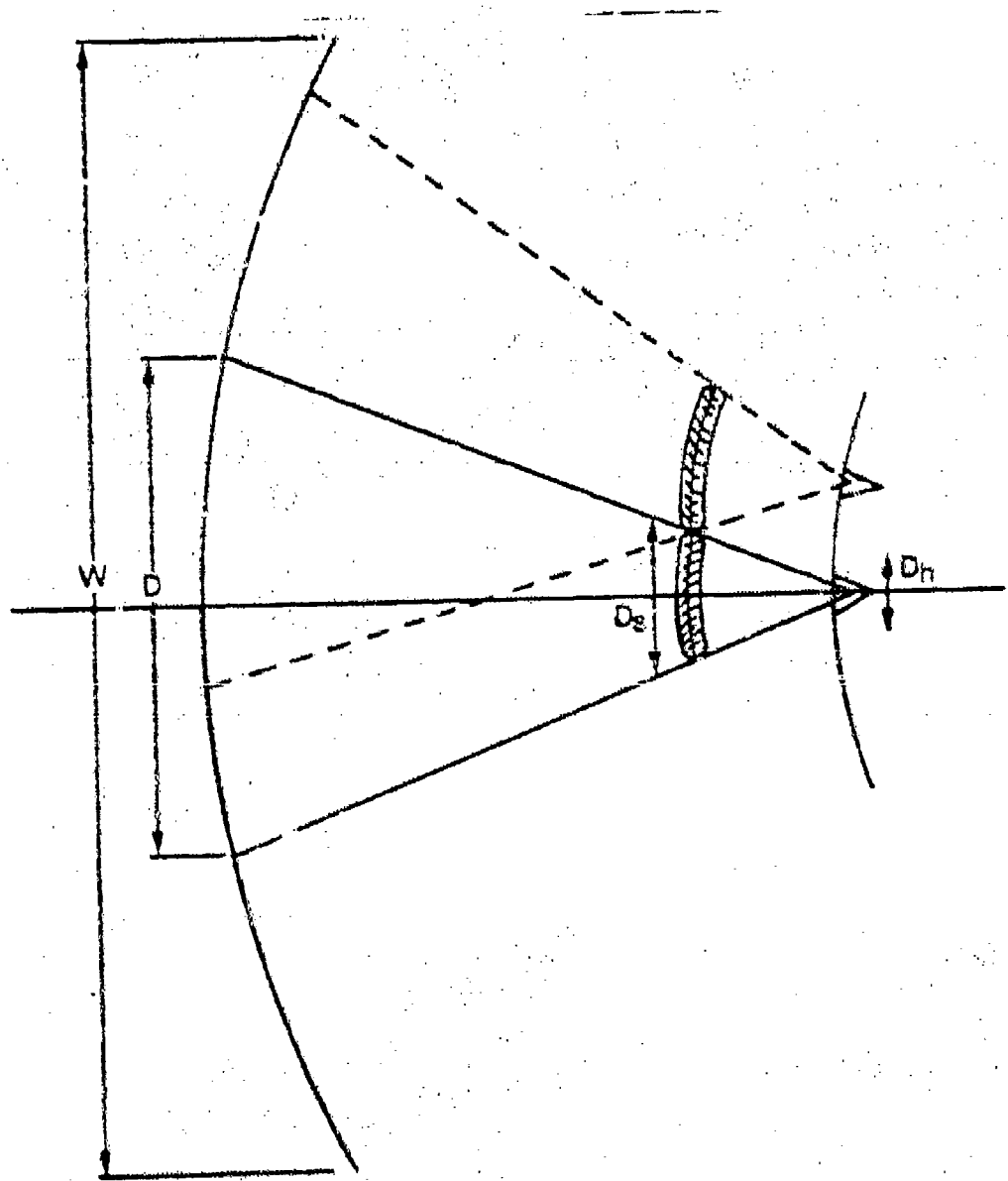


Figure S-65. Correcting Subreflector Diameter in Geo-
synchronous Plane Limits Minimum Beam Spacing

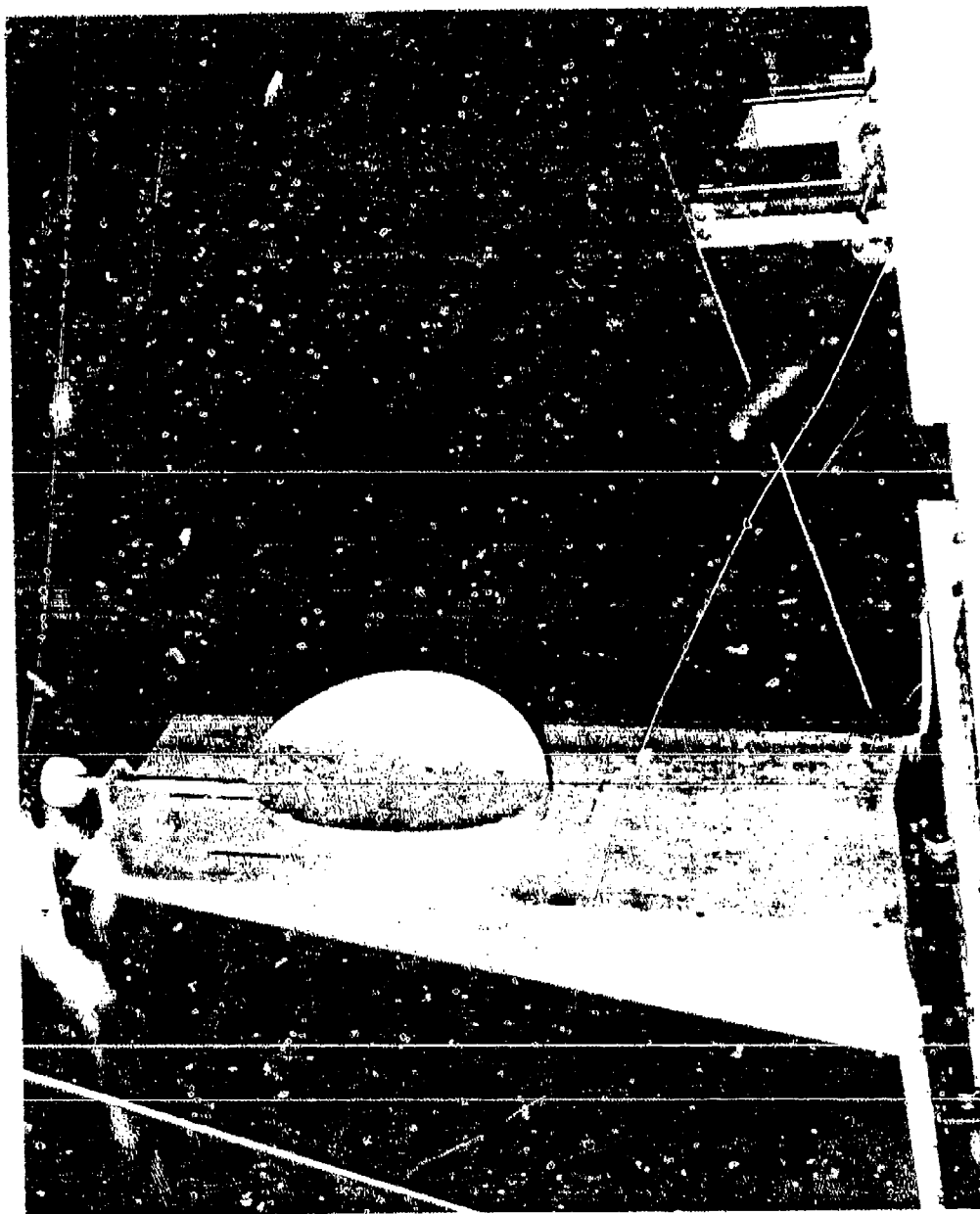


Figure 5-66. Phase-Corrective Subreflector Designed and Tested at COMSAT Laboratories

5.16 ABERRATION-CORRECTING FEEDS

As a second method of offsetting the spherical aberration associated with large-aperture MBTAs, COMSAT Laboratories has developed a unique aberration-correcting feed system concept.²¹ The primary feed illumination phase pattern is designed to compensate for the spherical aberration phase errors^{22, 23} of the reflector system. The feed system required to correct for spherical aberration effects has the characteristics shown in Figure 5-67. The amplitude pattern is rotationally symmetric. The phase patterns, which are uniform in the plane of the parabolic section, have a phase characteristic in orthogonal directions which is the inverse of the phase error introduced by the spherical aberration of the reflector.

A simple 3-element array implementation of an aberration-correcting feed system is shown in Figure 5-68. If the element pattern factors associated with the central and outer elements are respectively $\cos^{n1}(x_1\theta)$ and $\cos^{n2}(x_2\theta)$, the feed array voltage becomes

$$E(\theta, \phi) = \cos^{n1}(x_1\theta) + 2a \cos^{n2}(x_2\theta) e^{j\theta} \cos\left(2\pi \frac{d}{\lambda} \sin\theta \sin\phi\right) \quad (5-123)$$

The greatest amount of phase variation in the $\phi = 90^\circ$ plane is obtained for a given outer element amplitude weight, a , by setting

$$\theta = \pm 90^\circ \quad (5-124)$$

The phase pattern in the non-arrayed plane is then

$$\psi(\theta, 0^\circ) = \tan^{-1} \left[\frac{2a \cos^{n2}(x_2\theta)}{\cos^{n1}(x_1\theta)} \right] \quad (5-125)$$

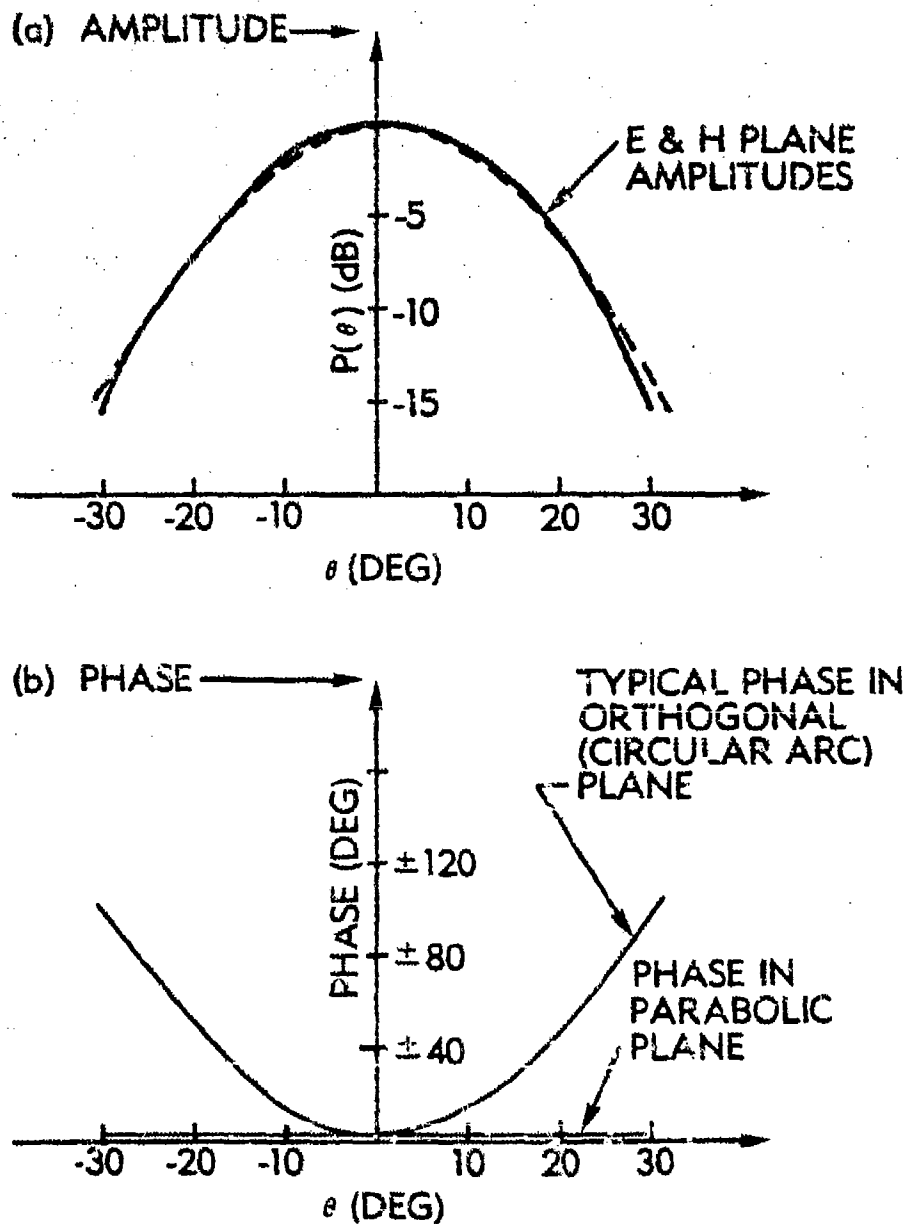


Figure 5-67. Primary Pattern Characteristics of Aberration-Correcting Feed System

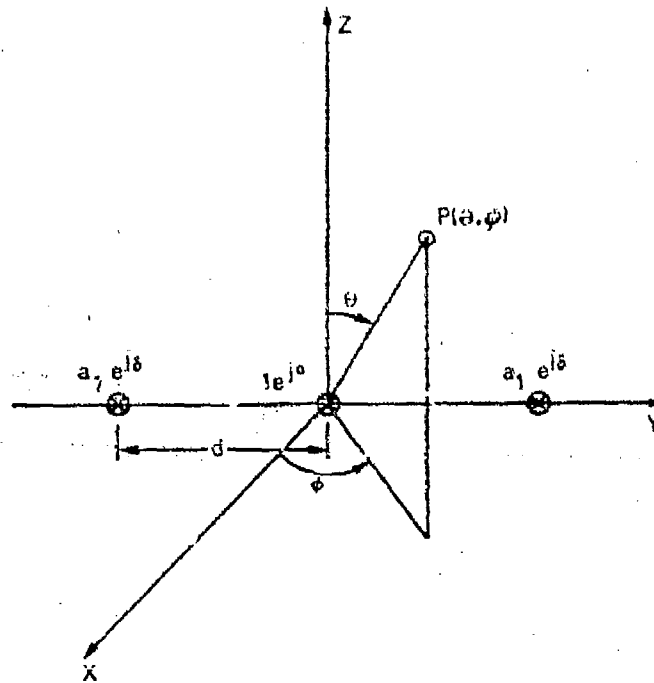


Figure 5-68. 3-Element Aberration-Correcting Feed Array

A uniform phase (independent of θ) requires identical element patterns

$$\cos^{n_1} (x_1 \theta) = \cos^{n_2} (x_2 \theta) \quad (5-126)$$

The phase pattern in the arrayed plane then becomes

$$\psi(\theta, 90^\circ) = \tan^{-1} \left[2a \cos \left(2\pi \frac{d}{\lambda} \sin \theta \right) \right] \quad (5-127)$$

The amplitude of this phase distribution is determined primarily by a, the relative voltage weight of the two outer array elements; the spatial distribution is determined primarily by d/λ , the feed element diameters. Figure 5-69 shows the amplitude and phase patterns of a 3-element array. There is generally a tradeoff between the desired amplitude and phase patterns. In terms of transmission, the outer feed elements can be assumed to create "mini-beams" in the geosynchronous arc plane which are phased to narrow the beam provided by the central feed element.

Figure 5-70 shows 5- and 7-element array feeds that provide additional degrees of freedom in realizing aberration-correcting feed arrays. The corrected and uncorrected principal plane patterns of a symmetrical MBTA geometry ($D/\lambda = 1000$, $D/R = 0.5$) are shown in Figure 5-71. A 5-element array feed improves the directivity by 0.8 dB, and the overall aperture illumination efficiency, η , increases from 60 to 72 percent. The corrected and uncorrected patterns in the geosynchronous plane for an offset MBTA ($D/\lambda = 820$, $D/R = 0.4$, and 10-percent offset) are compared in Figure 5-72. The directivity improves by 1.3 dB with a 4-element aberration-correcting feed.

Further work is necessary to fully evaluate the capabilities of aberration-correcting feed systems in the MBTA. The improvement in beam directivity must be weighed against increased feed system complexity and losses. One major advantage of the correcting feed system is that it is used with MBTA geometries designed for focal point feeds. Hence, lower frequency bands can utilize a single focal point feed, while higher frequency bands associated with increased spherical aberration can utilize an aberration-correcting feed array. Of course, the minimum beam spacing increases with the effective diameter of the aberration-correcting feed system.

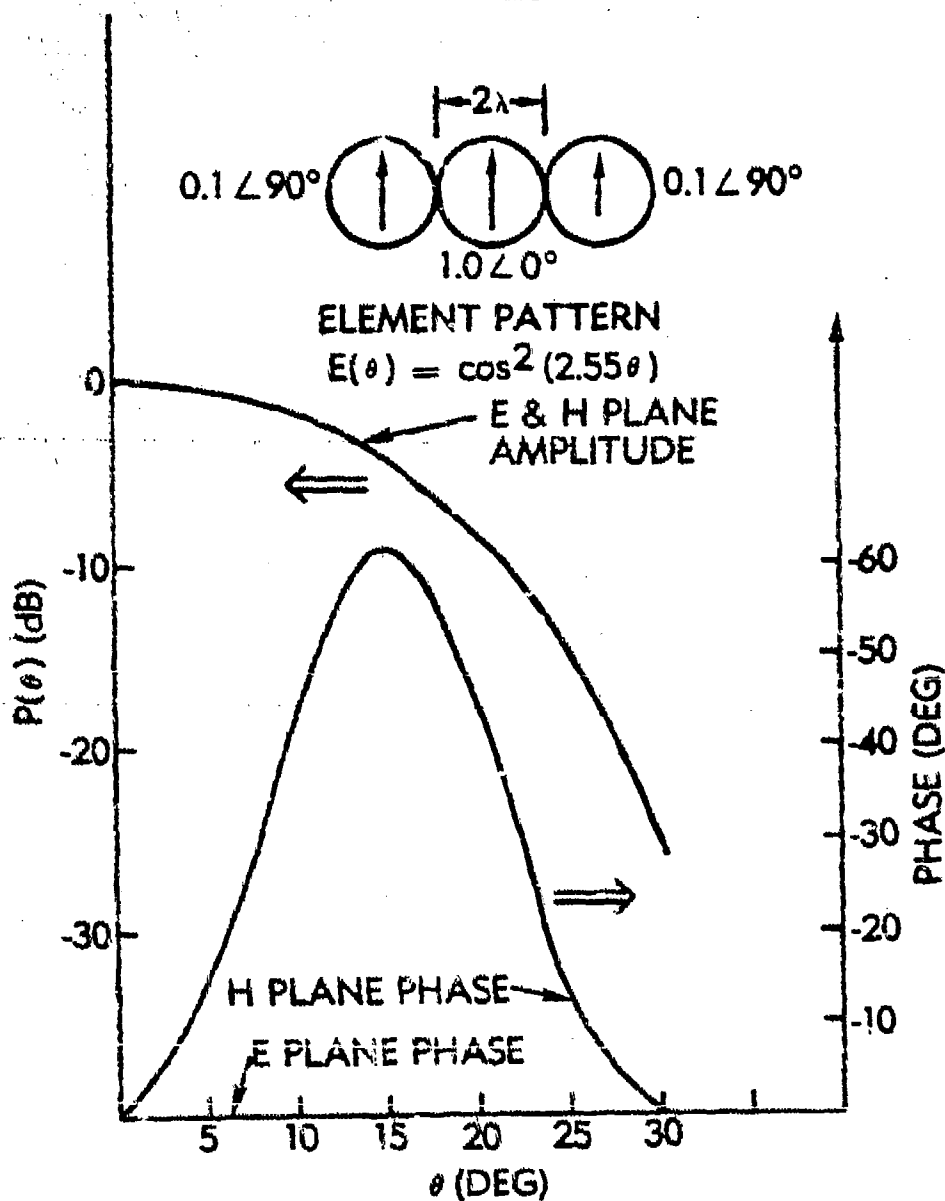


Figure 5-69. Primary Pattern Characteristics of 3-Element Aberration-Correcting Feed

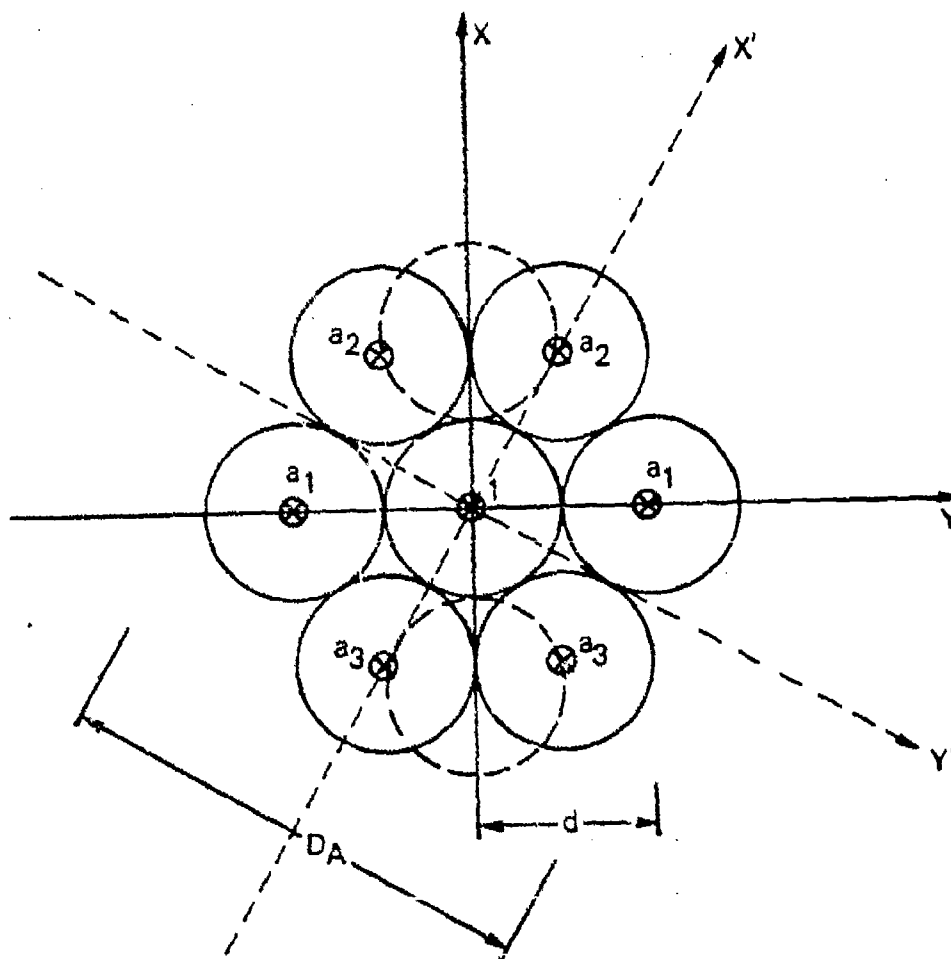


Figure 5-70. 7- (or 5-) Element Aberration-
Correcting Feed Array

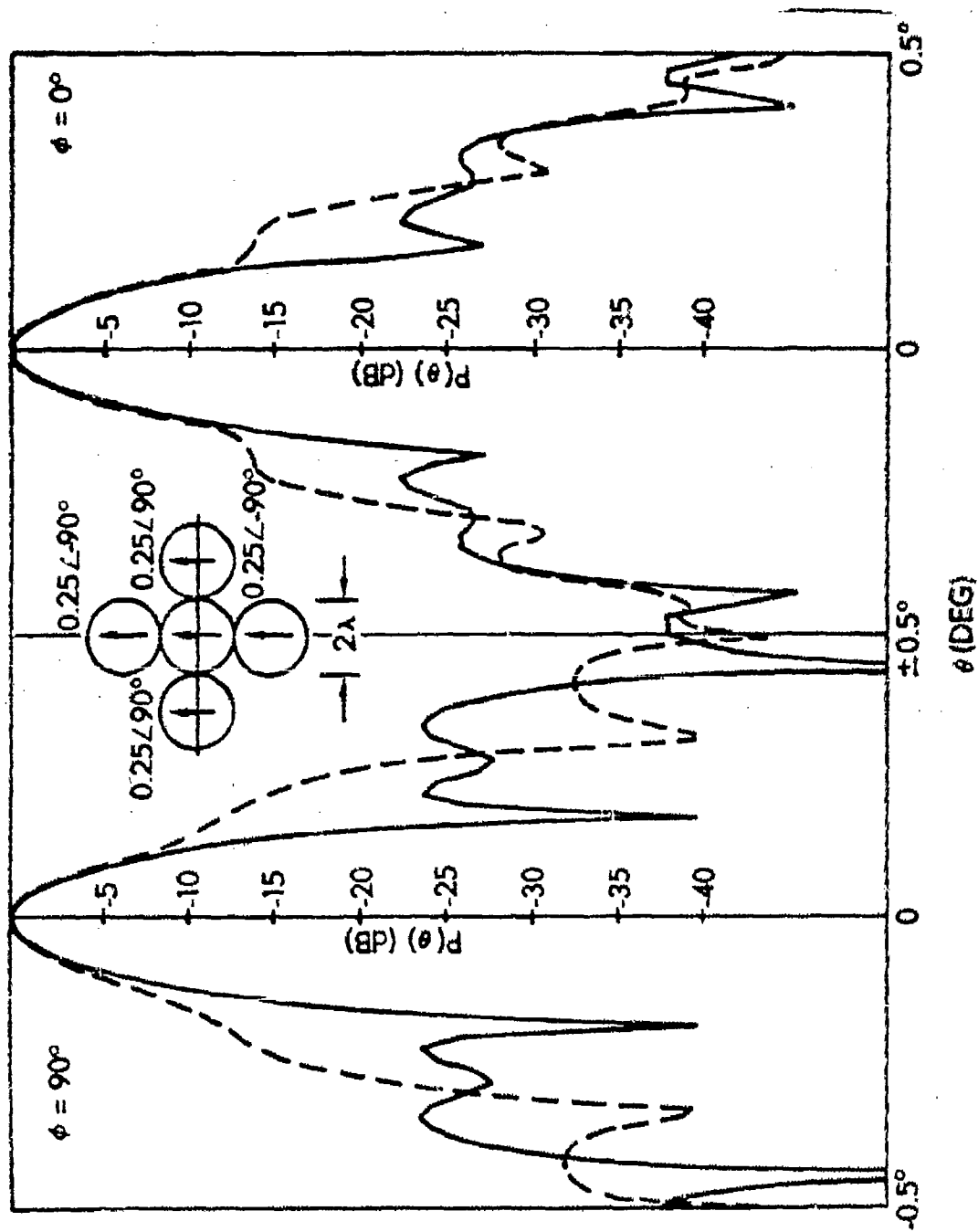


Figure 5-71. Symmetrical MBTA Patterns ($D/R = 0.4$, $D/\lambda = 1000$) with 5-Element Aberration-Correcting Feed

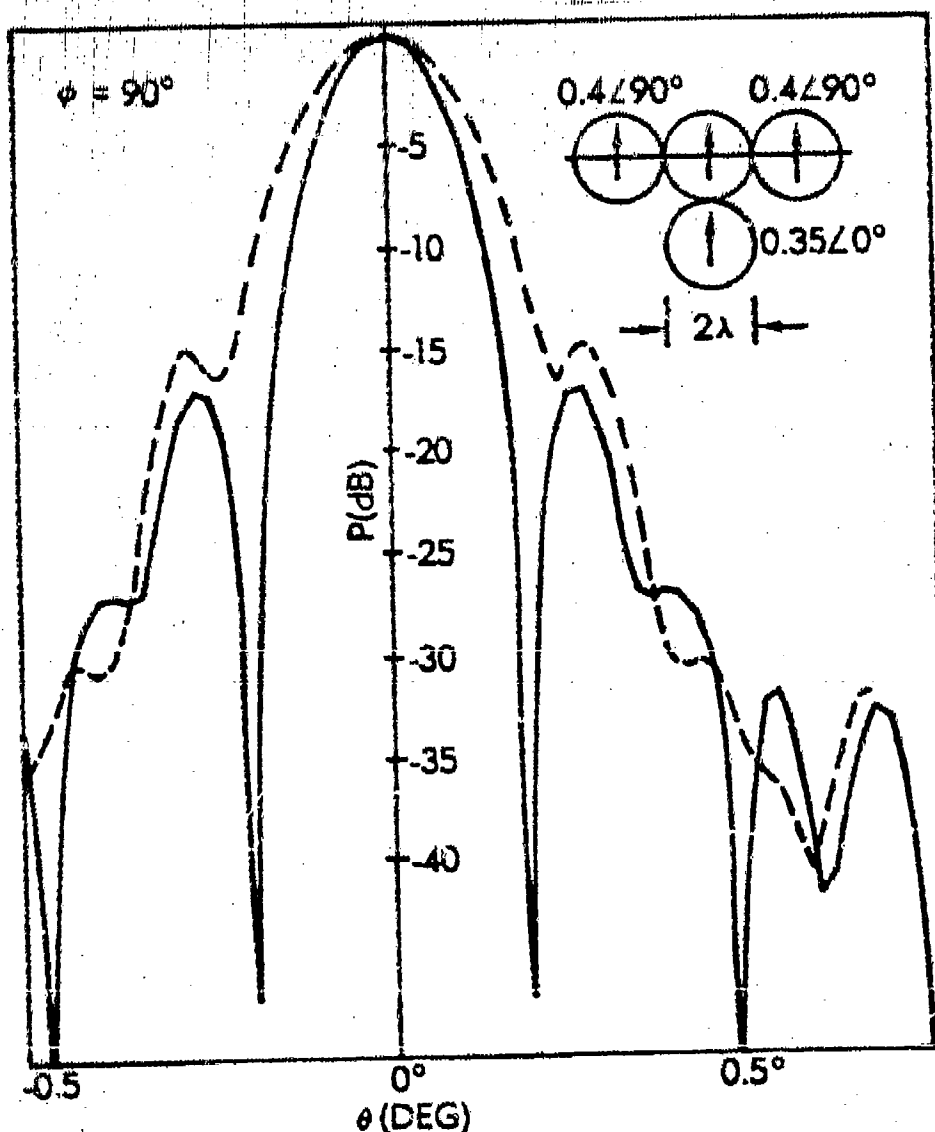


Figure 5-72. Offset MBTA Patterns ($D/R = 0.4$,
 $D/\lambda = 820$) with 4-Element Aberration-
Correcting Feed

6. MECHANICAL AND STRUCTURAL CHARACTERISTICS OF THE UNCORRECTED FRONT-FED MBTA

6.1 WORLDWIDE DEPLOYMENT CONSIDERATIONS

The decision to restrict detailed mechanical and structural analysis to the case of 54-dB gain at 7.25 GHz resulted in the selection of the 27-ft aperture as the basic MBTA to be considered. Fixing electrical performance parameters such as ϕ_0 , FOV, D/R, F/R, and D/ λ yields an overall mechanical description of the reflector as summarized in the specifications table. The projected aperture dimensions, W x D, are 60 x 27 ft (19 x 8 m), with the generating parabola vertex offset from the bottom edge of the reflector by 3 ft (0.9 m). The aperture width/diameter (W/D) parameter is related to the electrical parameters FOV and D/R as follows:

$$\frac{W}{D} = \left[\frac{\sin(\text{FOV})}{D/R} + 1 \right] = \left[\frac{\text{FOV}_{\text{RAD}}}{D/R} + 1 \right] \quad (6-1)$$

The amount of offset, d, of the bottom edge of the parabola from the feed center is based on mechanical criteria of feed rail support and expected building roof dimensions as well as the amount of parabolic plane beam scan required. This distance enables the construction of an enclosed feed structure without aperture area blockage.

The use of one reflector geometry for worldwide deployment by DSCS was possible once a single angle of generation,

$$\phi_0 = 93.5^\circ$$

was found to satisfy electrical performance criteria at all locations. The range of latitudes and differential longitudes to which the torus geometry is applicable varies from 0° to 75°, corresponding to locations with elevation angles greater than 5°.

Mechanical description of the single reflector/backup structure begins with the generating parabola definition,

$$x^* = \frac{z^{*2}}{4F} \quad (6-2)$$

where the focal length, F , is defined on the basis of parameters D , D/R , and F/R . Figure 6-1 shows the rotation of the generating parabola into the local coordinates system x, y, z according to the transformation

$$\begin{bmatrix} x \\ y \\ z \end{bmatrix} = \begin{bmatrix} \cos \alpha & 0 & \sin \alpha \\ 0 & 1 & 0 \\ -\sin \alpha & 0 & \cos \alpha \end{bmatrix} \begin{bmatrix} x^* \\ y^* \\ z^* \end{bmatrix} \quad (6-3)$$

where $\alpha = \phi_0 - 90^\circ$.

Figure 6-2 shows the derivation of the angle of circular rotation:

$$\beta = \text{FOV}^\circ + 2 \sin^{-1} \left[\frac{D}{2R_{MID}} \right] \quad (6-4)$$

where R_{MID} is the radius of curvature at reflector aperture height $d + D/2$. These two rotations define the parabolic torus surface in the local coordinate system. If a common backup structure is defined in the x, y, z system, as shown in Figure 6-3, it can be rotated with the reflector surface about angle β to form a universal structure with the same electrical performance regardless of location. The support structure becomes the means of translating the torus into its global coordinates.

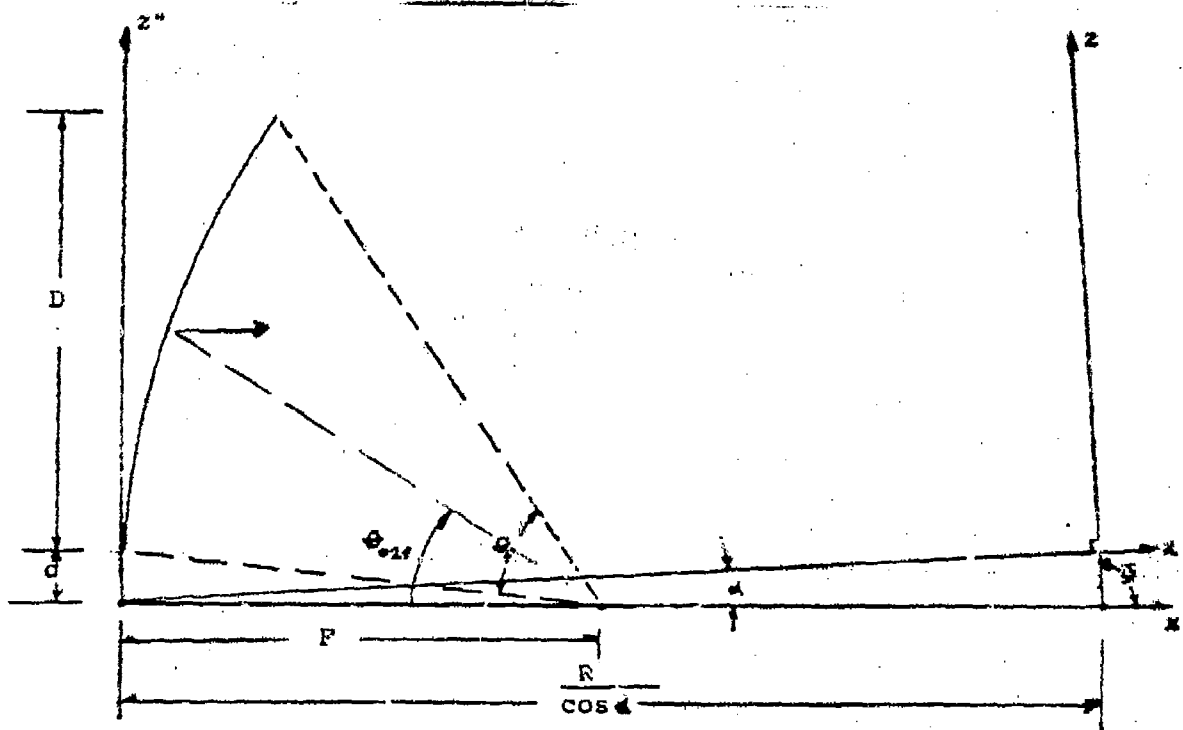


Figure 6-1. Offset Feed Configuration

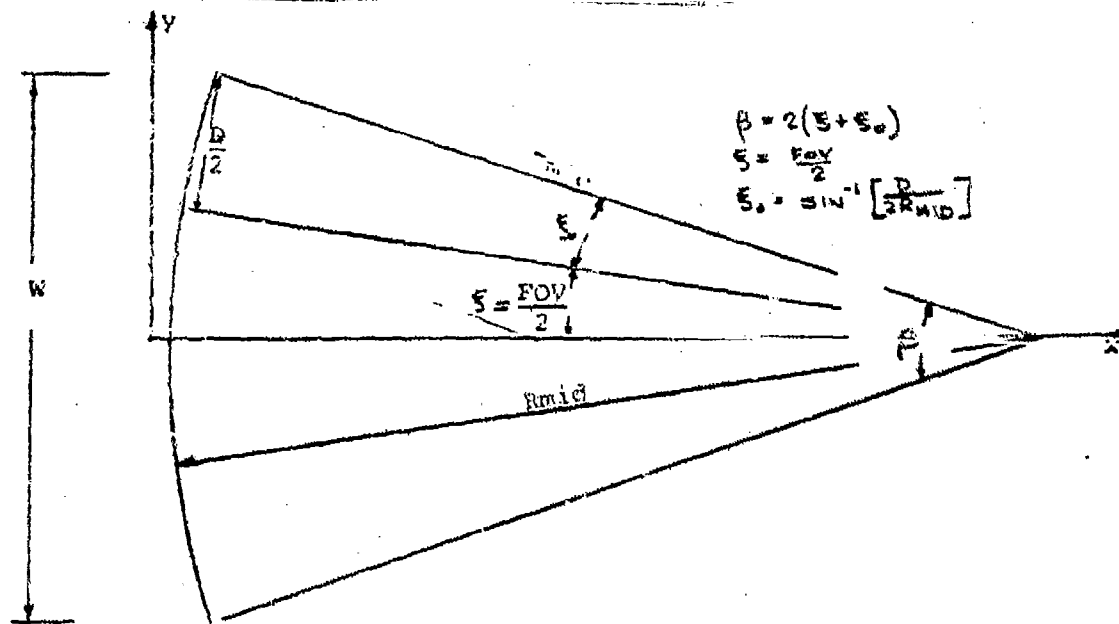


Figure 6-2. Circular Angle of Generation

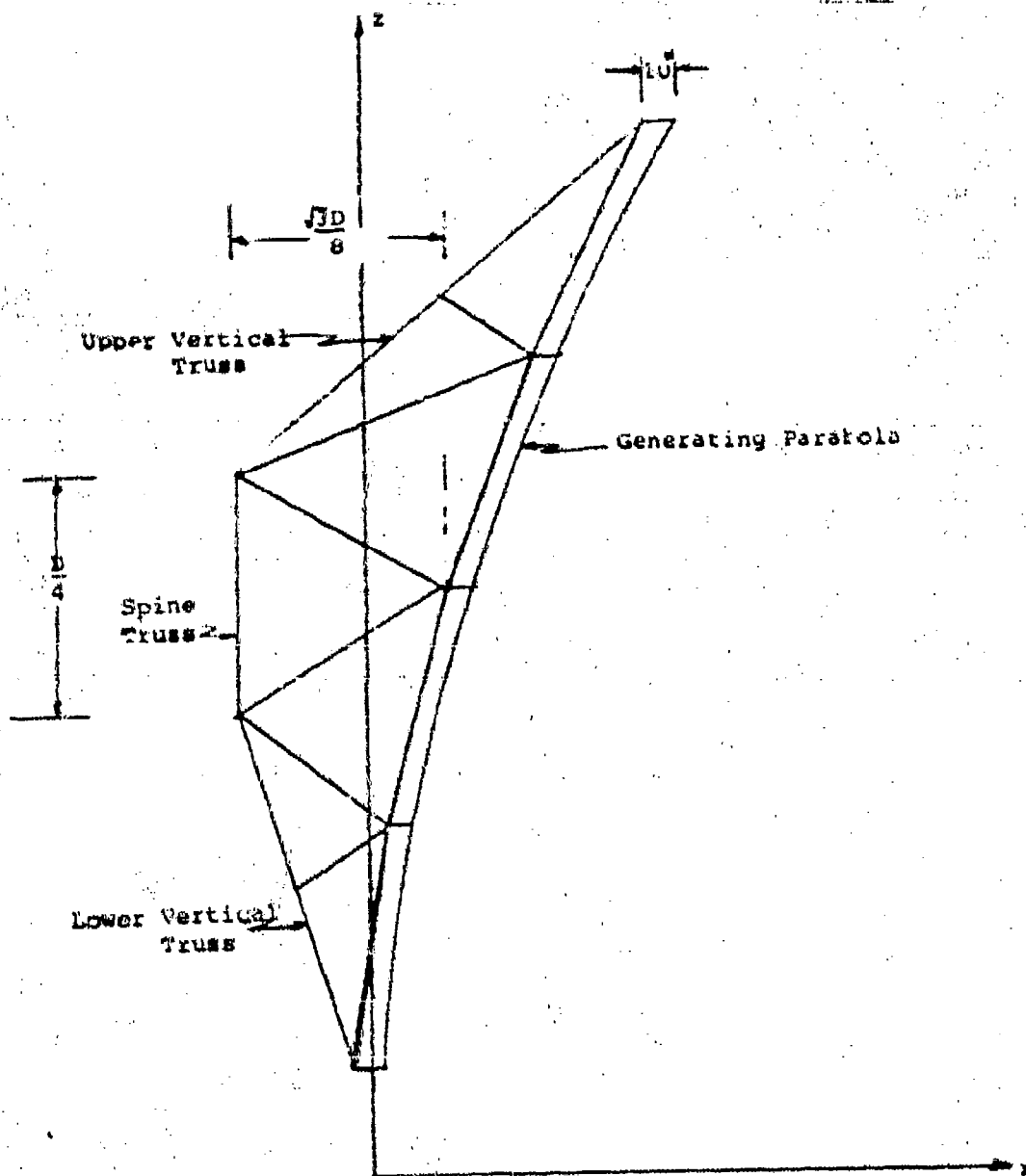


Figure 6-3. Typical 4-Panel Generating Truss

The relationship between the antenna local coordinates and the position-dependent global coordinates is defined via three angles: the surface generation angle, α , the elevation angle in the aperture plane, ξ , and the torus azimuth angle in the aperture plane, Ω . Angles ξ and Ω , which are functions of latitude, differential longitude from the earth station to the subsatellite position, and the ratios of earth radius to satellite orbit distance, are defined as²⁴

$$\xi = \tan^{-1} \left[\frac{\cos \phi \cos \lambda + m}{\sin \psi} \right] \quad (6-5)$$

$$\Omega = \tan^{-1} \left[\frac{(\sin^2 \psi - \cos^2 \phi)^{1/2}}{\cos \phi} \frac{m - \cos \psi}{(1 + m^2 - 2m \cos \psi)^{1/2}} \right] \quad (6-6)$$

where

- m = earth radius/satellite + earth radius
- ϕ = ground station latitude
- λ = longitudinal separation of ground station from the subsatellite position
- $\psi = \cos^{-1} (\cos \phi \cos \lambda)$

The mounting coordinates are found by translating the local coordinates through the three angles, as shown in Figure 6-4. The transformation relationship between the x, y, z and global X, Y, Z systems is

$$\begin{bmatrix} X \\ Y \\ Z \end{bmatrix} = \begin{bmatrix} \cos \alpha \cos \xi \cos \Omega & \cos \alpha \cos \xi \sin \Omega & \cos \alpha \sin \xi & 0 & 0 & 0 \\ \sin \alpha \cos \xi \cos \Omega & \sin \alpha \cos \xi \sin \Omega & \sin \alpha \sin \xi & 0 & 0 & 0 \\ 0 & 0 & 0 & \cos \psi & \sin \psi & 0 \\ 0 & 0 & 0 & -\sin \psi & \cos \psi & 0 \\ 0 & 0 & 0 & 0 & 0 & 1 \end{bmatrix} \begin{bmatrix} x \\ y \\ z \\ \rho \\ \theta \\ \phi \end{bmatrix} \quad (6-7)$$

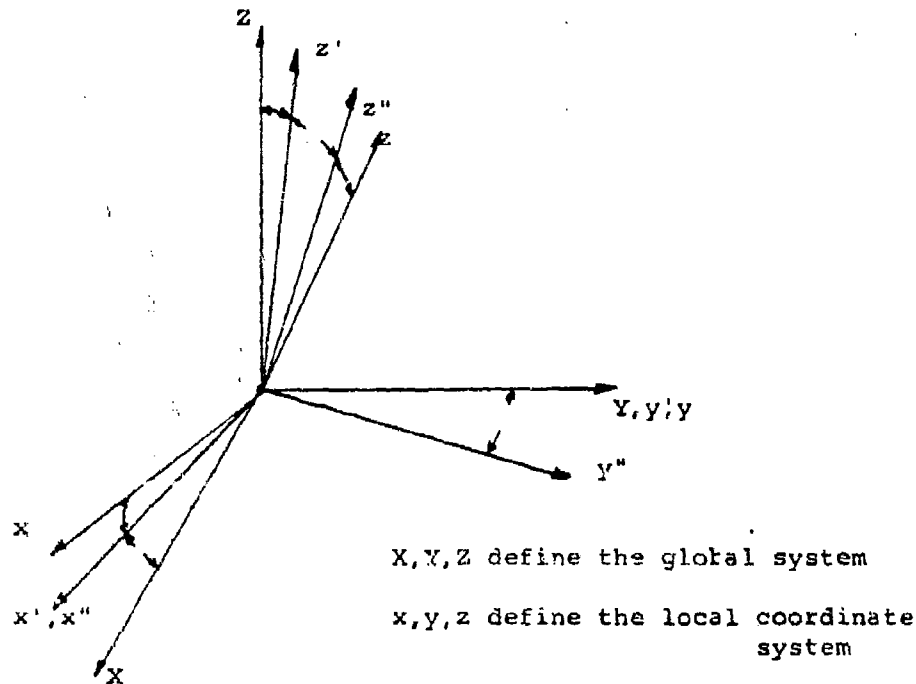


Figure 6-4. Coordinate System Rotation Angles

For the analysis five sites, listed in Table 6-1, have been chosen to represent the diversity resulting from worldwide deployment of the MBTA. These sites, which represent the potential spread of the differential longitude and latitude of existing DCA antennas, are chosen relative to a central satellite location at $333^{\circ}00'00''\text{E}$ longitude. The locations of COMSAT Labs (Fort Dietrick) and Sweden represent the majority of stations lying between 20° and 60° latitude and 20° to 60° differential longitude. Iceland represents the case of extreme latitude, but the antenna mounting does not change radically from the previous case.

Table 6-1. Representative Sites for Worldwide
MBTA Deployment

Site	Longitude	Latitude	Differential Longitude
Mt. Margret	37°E	2°S	64°
Sweden	13°E	60°N	40°
Iceland	340°E	66°N	7°
Ascension Island	346°E	7°S	13°
COMSAT Laboratories	282.7°E	39.2°N	-50.3°

Mt. Margret and Ascension Island represent the two extreme siting locations. Only two DCA antenna sites appear to fall in the Ascension Island category of nearly horizontal aperture plane with the station at the subsatellite point. This case should not present any special mechanical problems, since its horizontal attitude precludes severe wind loading effects. The Mt. Margret location represents those earth stations at extreme differential longitude ($>60^\circ$) and low latitude ($<20^\circ$). Several DCA earth stations appear to fall in this category. This type of antenna attitude experiences the most severe environmental effects. If the same type of support structure is used for all antennas, it will provide the least stiffness for these locations due to the reflector's extreme height.

6.2 MECHANICAL CONSIDERATIONS

The electrical performance requirements are satisfied by a 27-ft reflector with $D/R = 0.4$. However, the mechanical problem is to maintain the stringent RF gain requirements, especially at higher frequencies. The relationship

$$G_L = 10 \log_{10} \exp \left[- \frac{4\pi\epsilon}{\lambda} \cos (\theta_{\text{off}}) \right]^2 \quad (6-8)$$

defines the correspondence between gain degradation of the antenna (G_L) and the normal surface root-mean square (rms) deviation (ϵ), where λ is the beam wavelength, and θ_{off} is the feed pointing angle.

The basic specifications require the design of one structure whose surface deformation is small enough under normal conditions to realize 54-dB gain at 7.25 GHz. A second iteration of the same structure was performed to further reduce surface errors to meet the more stringent requirements at 20 and 30 GHz. Figure 6-5 plots the curves of gain loss vs surface deviation in inches for the RF bands under consideration. The steep slope of the curves at higher frequencies emphasizes the performance limitations associated with surface tolerances above the 11/14-GHz bands. More gain loss must be allowed at these frequencies under the same environmental conditions. If the gain loss must be held to 0.5 dB under operational conditions at 20/30 GHz, a radome protective structure such as that shown in Figure 6-6 may be necessary.

For the baseline antenna, the maximum rms error considered was 0.040 in. (1 mm), allowing a maximum gain degradation of 0.5 dB at 8.4 GHz. The degraded performance specification was set at 0.060-in. (1.5-mm) deformation for 1-dB allowable gain loss in the 7/8-GHz band. The effect of restricting surface deformation to 0.020 in. (0.5 mm) was investigated for higher frequency antenna performance. In this case, the gain loss is restricted to 0.75 dB at 20 GHz and 1.5 dB at 30 GHz. Design iterations were performed to identify the required structural characteristics for achieving 0.040- and 0.020-in. surface tolerances.

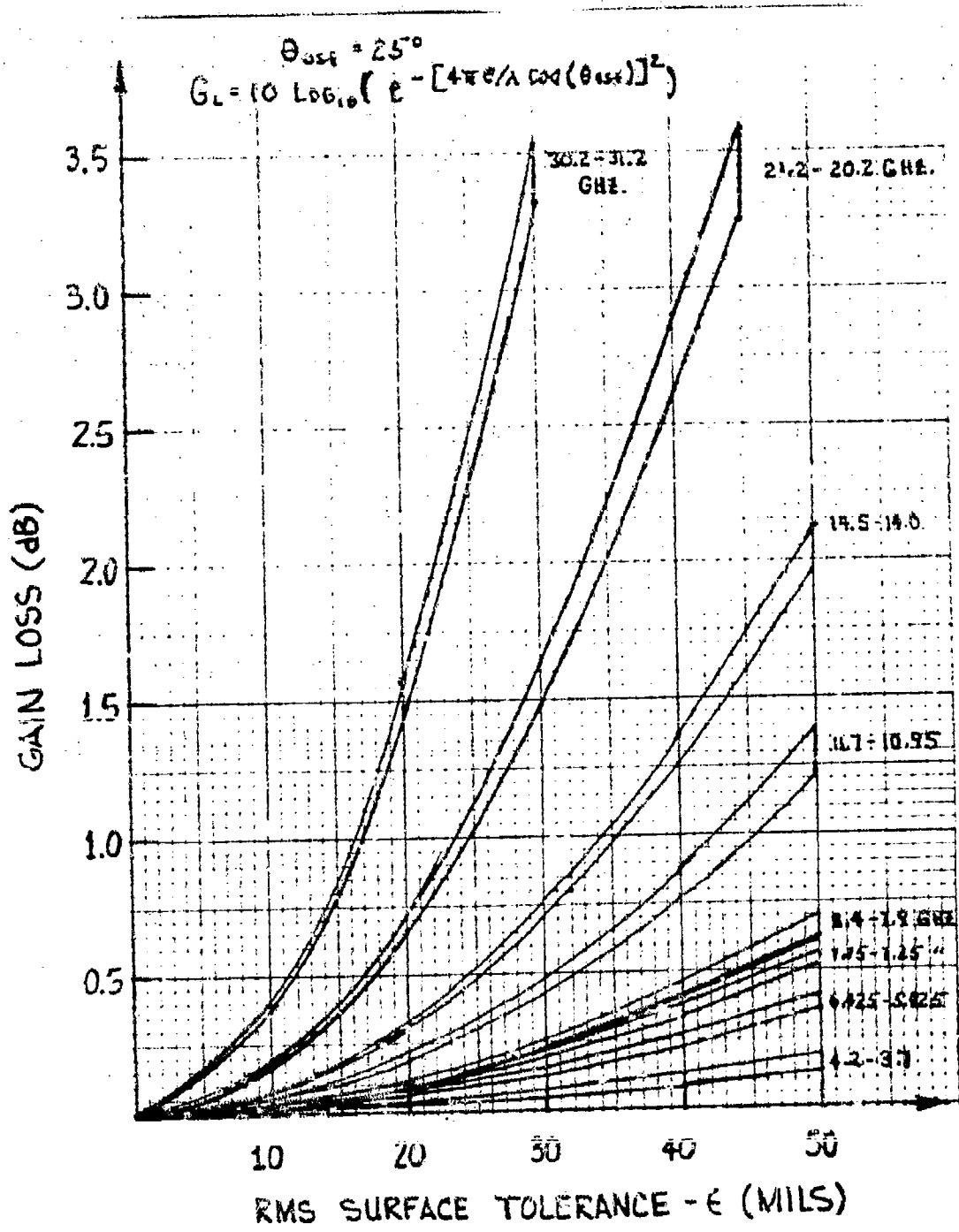


Figure 6-5. Gain Loss of MBTA vs rms Surface Tolerance, ε

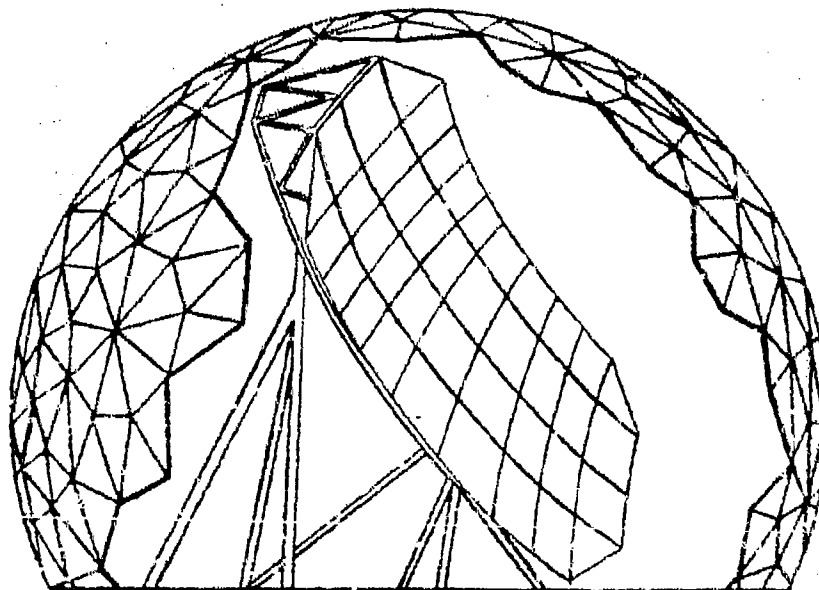


Figure 6-6. MBTA with Radome Environmental Protection

The feed transport mechanism considered for the study is based on a design that has been built and tested at COMSAT Labs.²⁵ Although the transport shown in Figures 6-7 and 6-3 utilizes a front rail support upon the wall of the building, a bottom rail support may be used so that the transport will have an independent support and foundation.

The narrow width of the transport allows two adjacent feeds to be separated by approximately 2° . Additionally, the universality of the transport design permits it to operate at any azimuth angle in the aperture plane. The self-contained drive and support features of this transport allow any feed to be mounted with a wide variation in allowable center of gravity and feed weight.

The two orthogonal drives are capable of tracking both spacecraft diurnal motions and spacecraft station variations using an open-loop control system driven by a minicomputer.

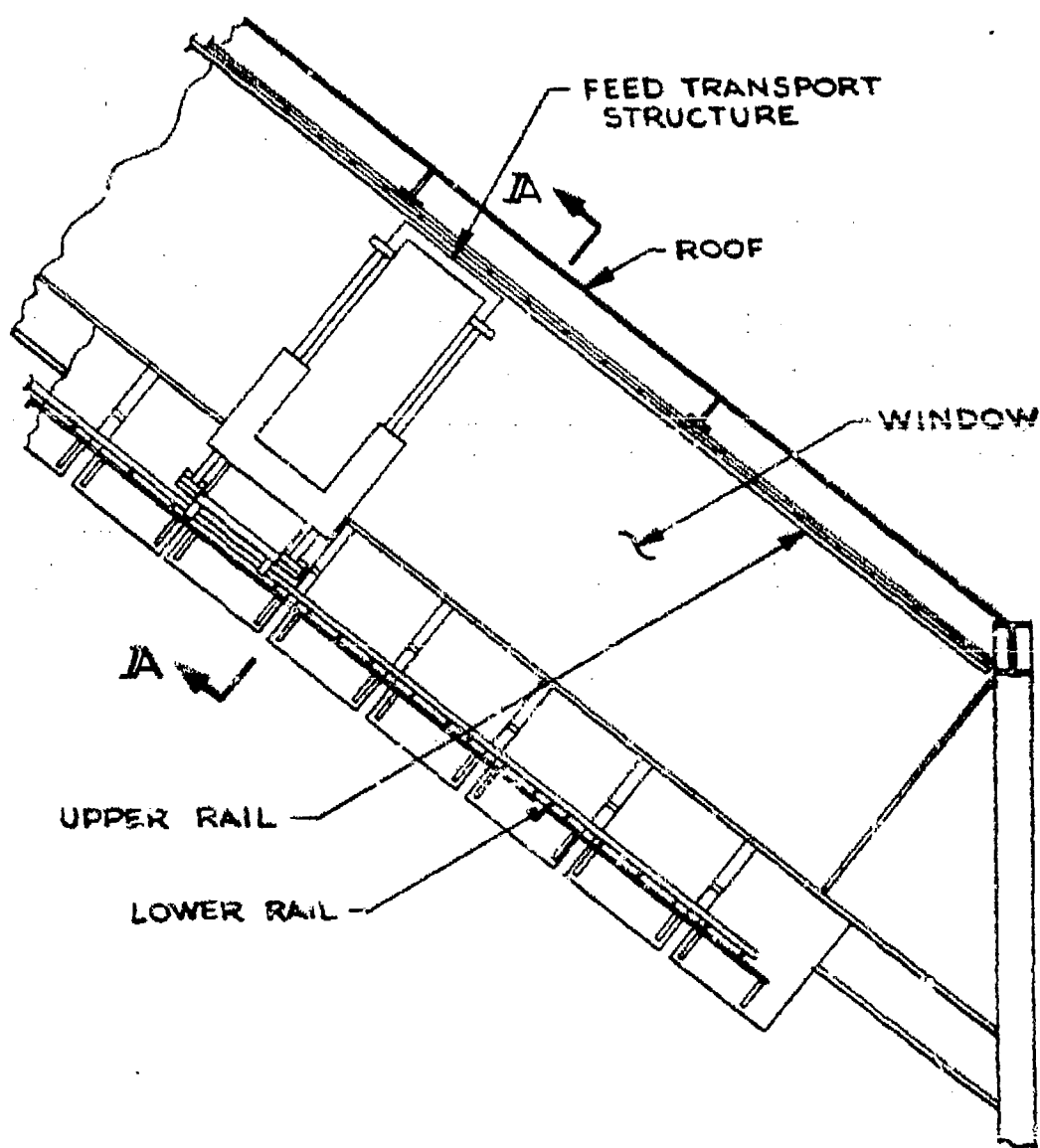


Figure 6-7. Existing Feed Transport Mechanism Support

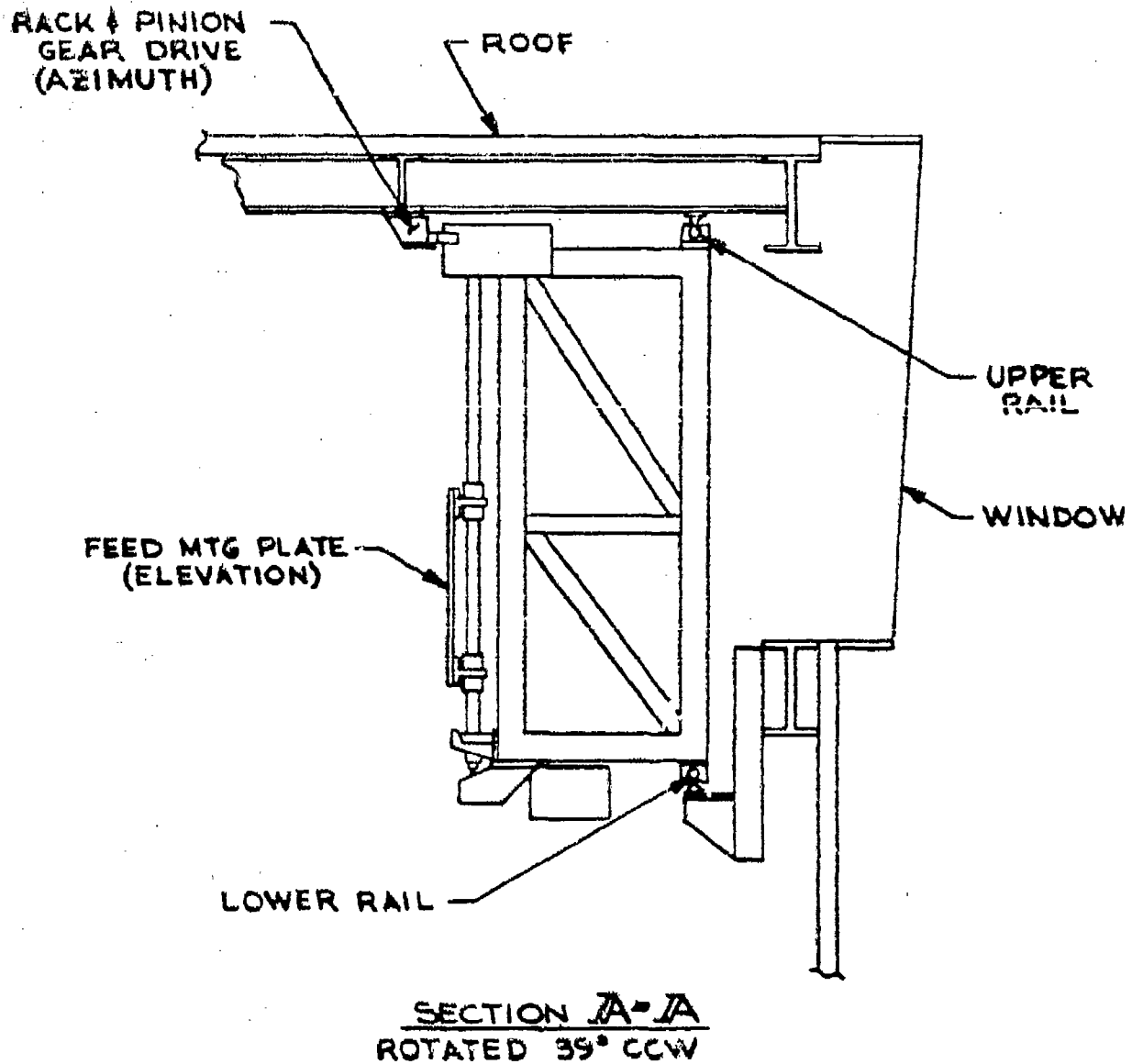


Figure 6-8. Orthogonal View of Feed Transport
Mechanism Support

6.3 STRUCTURAL DESIGN CONSIDERATIONS

The most difficult structural design problem is to obtain a single antenna structure package that is suitable for all potential sites and environmental criteria. Only minor modifications in the antenna support and feed tower structures can be made to suit the individual station requirement.

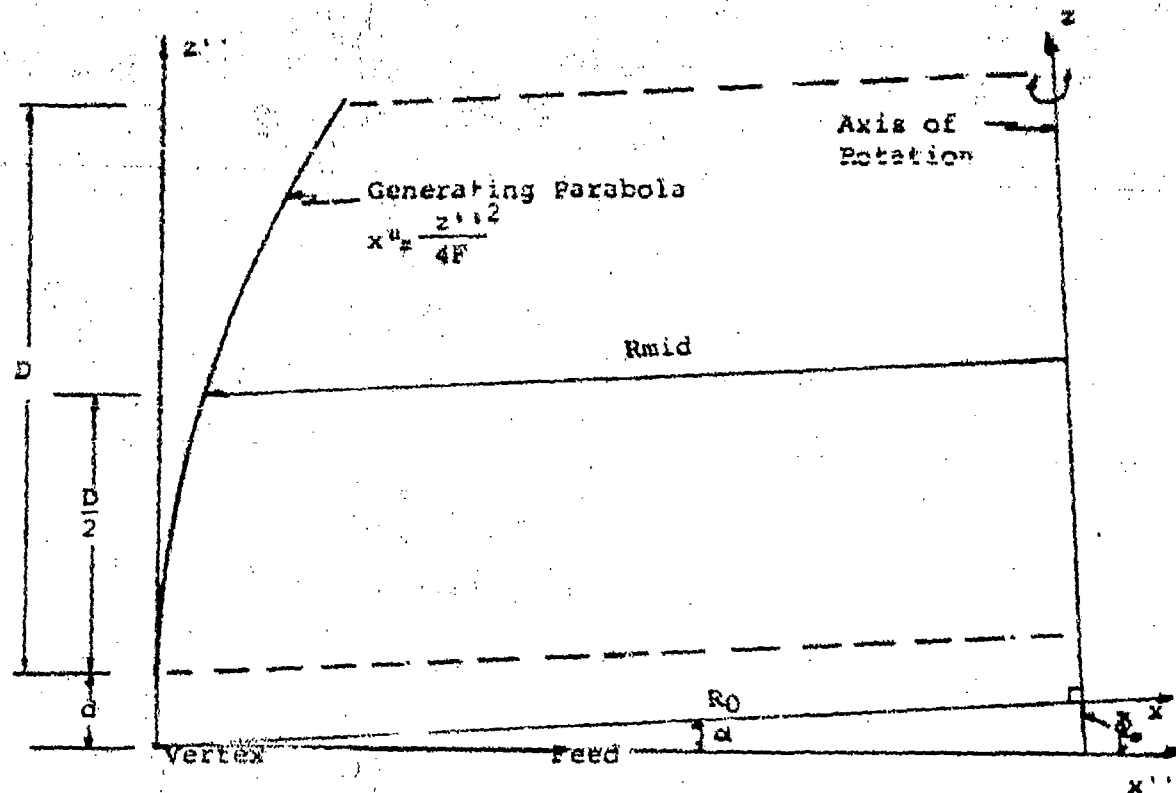


Figure 6-9. Reflector Geometry

As defined by the RF transmission data (Figure 6-9), the reflector geometry is symmetric about the axis of revolution. Across the parabolic arc the curvature of each section is unique. Thus, the cost of fabricating the individual molds or mandrels

can be reduced by minimizing the number of parabolic panels. However, other considerations including handling, storage, and shipping become important, especially as the aperture diameter size increases. Figure 6-10 shows the configuration that is considered optimum based on a tradeoff study. For a reflector in the 27-ft-aperture-diameter range, a configuration of four parabolic and eight circular sections appears to be advantageous in terms of weight and complexity.

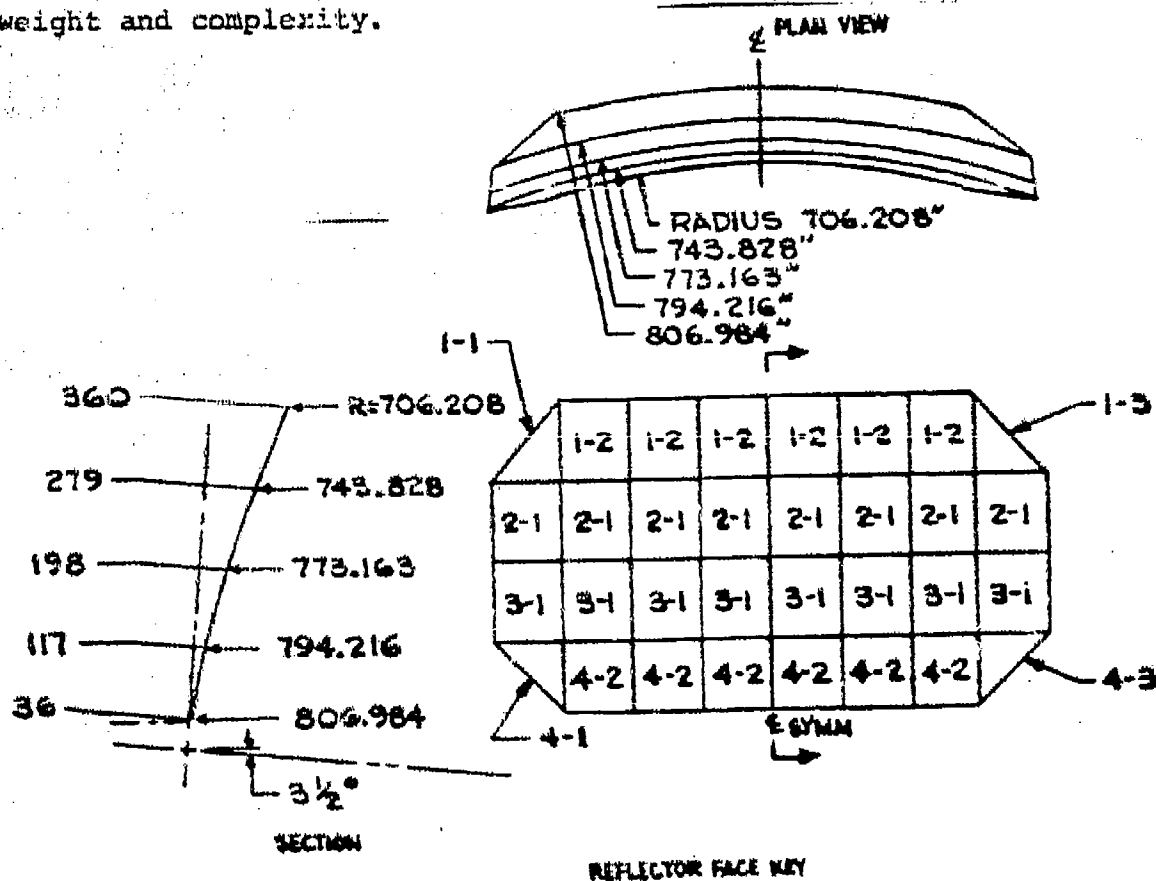


Figure 6-10. 27-ft MBTA Reflector Panel Configuration

The backup structure for this panel configuration requires a support at each panel corner, adequate stiffness, modularity, reasonable weight, simply erectable connections, and

universal applicability. Figure 6-3 shows the primary vertical members. A triangular spine truss is rotated about the axis of revolution, and a vertical truss is built around the spine at each circular panel section. The vertical members are stabilized by secondary horizontal trusses also following the curvature of the axis of revolution. Additional diagonal bracing is added during structural analysis to obtain the required structural stiffness and mechanical performance. Figure 6-11, which shows a typical backup truss, indicates the location of diagonal members and vertical and horizontal trusses. The reflector surface would be tied into the backup truss through adjustable support mechanisms to enable the maintenance of proper panel alignment and contour and thermal stress relief between the aluminum panels and steel members.

A 3-point pickup support enables perfect alignment of the elevation and tilt angles of the reflector during erection. However, for a structure of 60 x 27 ft or more, the stiffness of only three supports would be inadequate to maintain performance even at lower frequencies. Consequently, a minimum of four support points has been adopted. The configuration shown in Figure 6-12 has the required stiffness for the 27-ft reflector at most locations under all specified conditions. For earth stations for which a more extreme positioning or tighter rms tolerance is required, a support of six or more points might be necessary (Figure 6-13).

The feed transport building is assumed to be a pre-engineered environmental enclosure for a cost-effective structure. To ensure that environmental effects do not result in beam deformation, the feed mechanism support is assumed to be independent of the enclosure's foundation. The minimum building size of 12 ft on a side accommodates other mechanical and electrical equipment and provides work room around the transport mechanism.

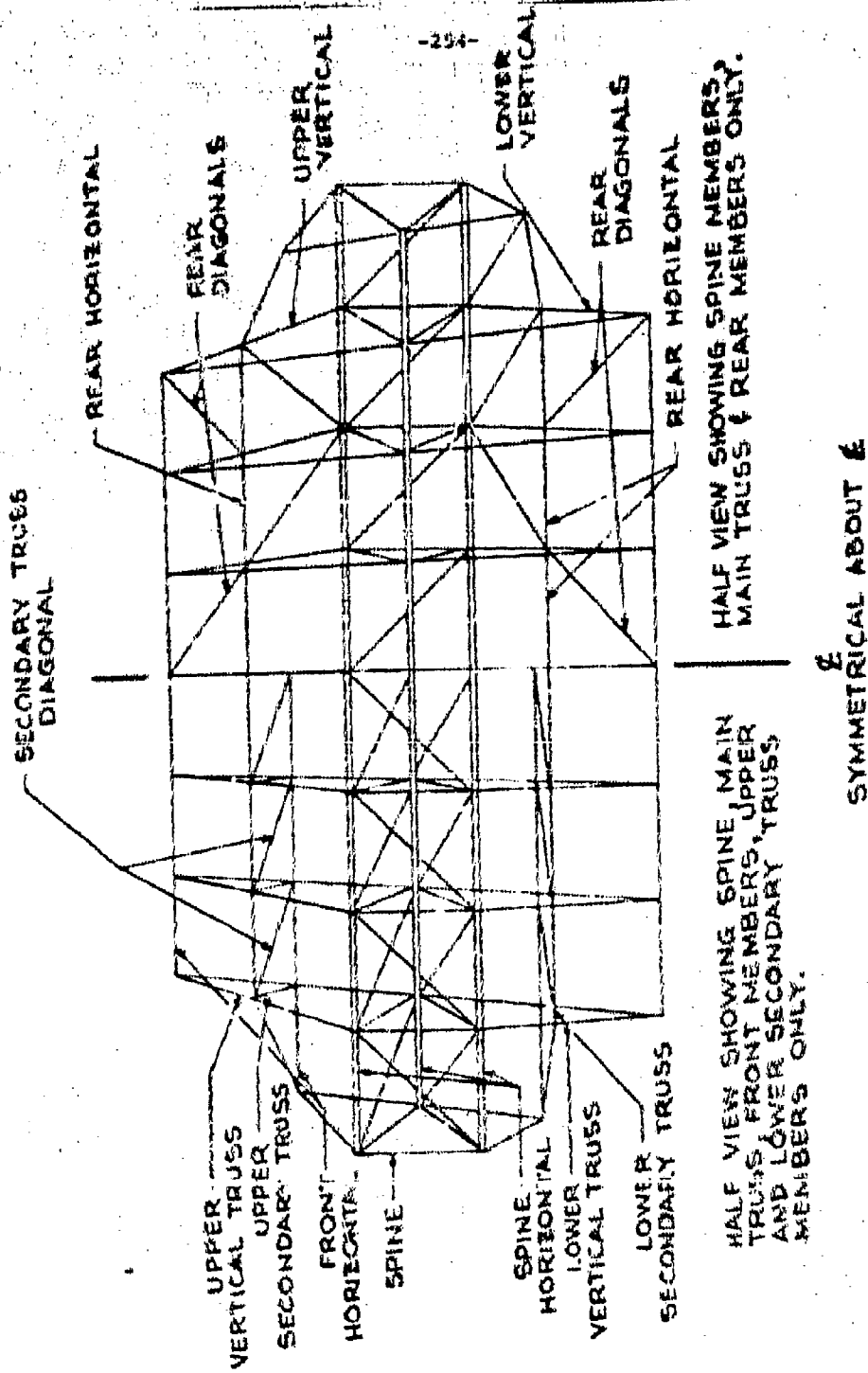


Figure 6-11. Detail of Backup Truss Members

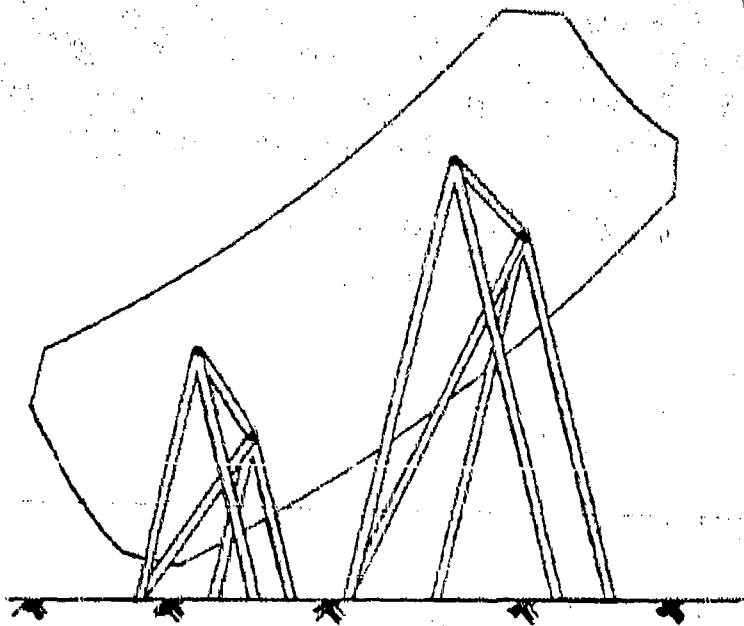


Figure 6-12. 4-Point Pickup Support Structure

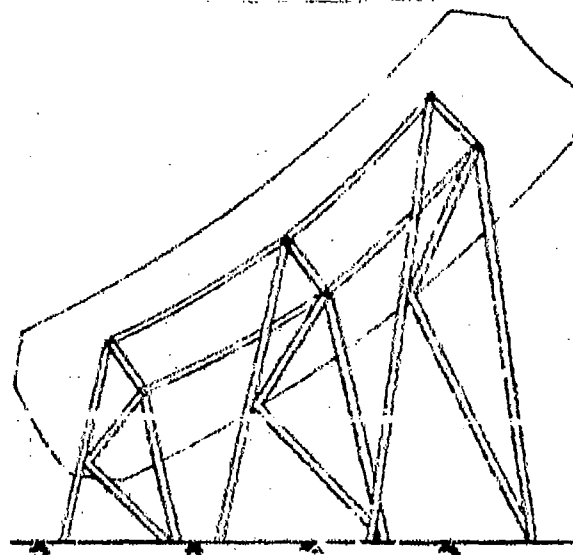


Figure 6-13. 6-Point Pickup Support Structure

6.4 APPLIED LOADS ANALYSIS

To design a universally applicable torus antenna, the basic system specifications have been used to define the required loading conditions for all members and the necessary RF performance of the final structure under those conditions. The basic forces applied to the MBTA structural model to test its performance are wind, gravity, and temperature variations. Of these three, wind loading is by far the most severe design condition.

6.4.1 GRAVITY

The deflection of the structure under its own weight is calculated alone and in combination with the other forces. Since gravity is a static load, its effects can be offset by applying a corrective deflection at each of the panel support points during erection.

6.4.2 WIND

The operational, degraded operational, and survival wind loads are defined in the specifications as 45, 60, and 125 mph, respectively. Wind forces are applied to the structure by calculating the wind pressure on the reflector panels according to the relationship²⁶

$$P = qC_D V^2 \quad (6-9)$$

where

V = wind velocity in mph

C_D = discharge coefficient = 1.4

q = dynamic air pressure = 0.00256

The net force applied to each joint of the backup structure is the wind pressure times the projected panel surface area in the direction of the load. Both front and side wind forces are calculated to determine the worst-case conditions for design. The global X and Y axes are used to define front and side wind directions. Figure 6-14 demonstrates the variation in projected wind surface area with change in station location.

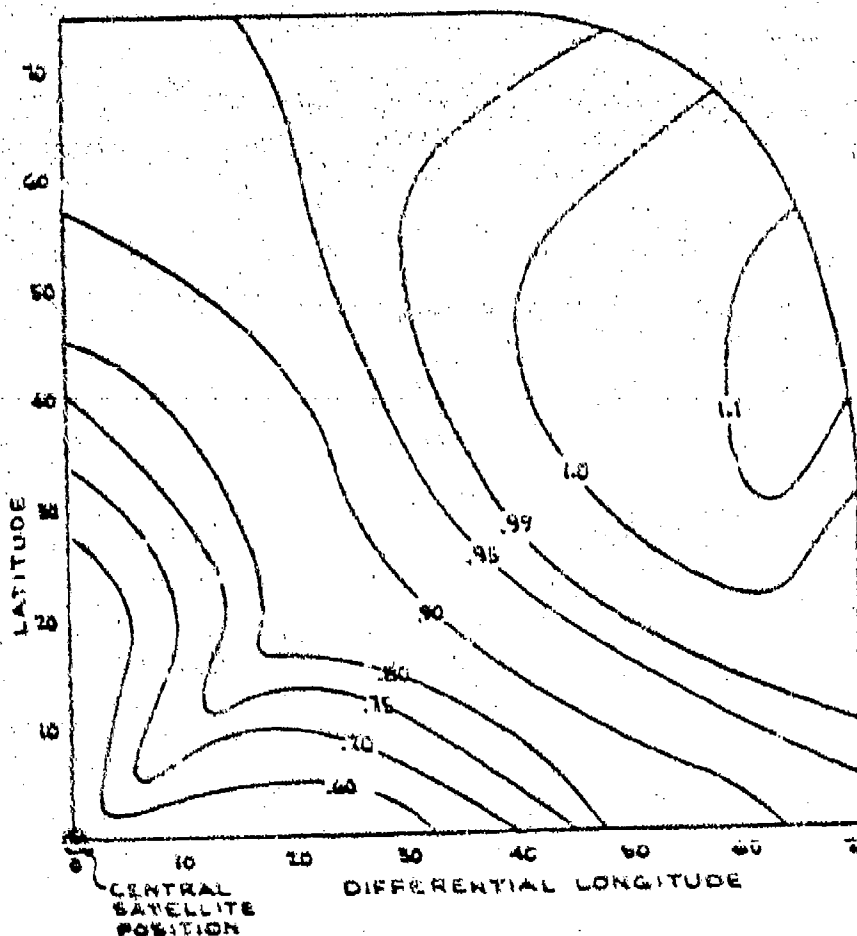


Figure 6-14. Normalized Projected Area $[A/(W \times D)]$

6.4.3 TEMPERATURE

Structural deflections due to a 10°F (5.5°C) differential temperature between the front surface (reflector joints) and the backup and support structures are calculated. This loading condition represents the case in which solar reflection warms up the exposed reflector surface faster than the sheltered structural members, for example, in the early morning.

6.5 ALLOWABLE DEFORMATION AND TILT ERROR BUDGET

6.5.1 SURFACE rms

Manufacturing tolerances, rigging adjustments, and deflections due to gravity, wind, and thermal loads are sources of surface deformation. For a first design iteration the total allowable rms error budget, ϵ_T , is split equally among the three separate categories, manufacturing (ϵ_m), erection (ϵ_r), and environment (ϵ_e), since their effects are uncorrelated²⁷:

$$\epsilon_T = \sum_{i=1}^n [\epsilon_i^2]^{1/2} = [\epsilon_m^2 + \epsilon_r^2 + \epsilon_e^2]^{1/2} \quad (6-10)$$

The total environmental rms error is the sum of the deflections of the panel surface (ϵ_p) and the backup/support structures (ϵ_s) due to wind, thermal, and gravity forces:

$$\epsilon_e = [\epsilon_p^2 + \epsilon_s^2]^{1/2} \quad (6-11)$$

Manufacturing and rigging rms errors are considered as a total for the whole system.

The basic MBTA required gain of 54 dB at 7.25 GHz calls for a minimum operational rms surface tolerance of 0.040 in. (1 mm), including 0.023-in. (0.58-mm) deformation due to each of the manufacturing, erection, and environmental effects. If these effects are kept equal, the deflection due to wind, temperature, and gravity is limited to 0.016 in. (0.41 mm) each for the panels and support structure. Ideally the deflection of the structure under its own weight is corrected during erection, and the distortions due to differential temperature are relatively small. Consequently, the majority of the environmental errors can be budgeted to the wind load deformations.

6.5.2 POINTING ERROR

The possible sources of pointing error are wind, gravity, and thermal deflections of the support structure; alignment errors during erection of the antenna; and displacements of the feed. Deflection of the feed structure itself can be eliminated by separating the foundation and supports of the feed mechanism and the feed tower. Thus, the feed travel is not subjected to displacement due to wind loads on the building walls or thermal distortions in its controlled environment. Adjustments of the feed can be used to compensate for the lateral displacement of the reflector structure and reduce the pointing error. Hence, displacements due to overall MBTA pointing error are subtracted from the total displacement at each point to obtain the uncorrected rms surface error.

6.6 STRUCTURAL MODEL

The RF transmission data define the generating parabolic toroidal surface²⁶:

$$z^4 - 8Fz^2 - 16F^2(x^2 + y^2) + 16(FR)^2 = 0 \quad (6-12)$$

where x , y , and z are calculated via transformation equation (6-3). The four basic parts of the torus antenna are the reflector surface panels, the backup truss, the support structure, and the concrete foundation. Since the backup, support, and foundation are dependent on the panel size, and number and type of corner supports, design iterations were first performed on a typical reflector surface panel to optimize its parameters.

6.6.1 PANELS

Panel optimization involved finding a practical design of minimum cost and weight. The factors influencing the design were material type, fabrication, assembly techniques, transportability, and erection ease. It was decided to limit the design to established fabrication techniques, easily available materials, and common overall size and weight. The maximum panel dimension was chosen as 9 ft to accommodate shipping size limitations. Aluminum was used as the basic surface material due to its good strength-to-weight ratio, availability, good RF characteristics, relatively low cost, and the large number of fabrication houses familiar with its use in curved panels. For ease of erection it was decided to limit backup structure connections to simple supports at each corner point.

For large panels, the advantages in terms of cost were as follows:

- a. few manufacturing mandrels,
- b. less joints for simpler erection procedures,
- c. greater alignment control, and
- d. a simpler backup structure.

For smaller panels the advantages were as follows:

- a. light weight for ease of shipping and handling,
- b. greater stiffness for each panel.
- c. ease of manufacture, and
- d. lower cost per unit area.

In addition, the following panel material configuration tradeoffs were considered:

- a. solid aluminum plate,
- b. thin aluminum plate backed with corrugated aluminum sheet,
- c. thin aluminum plate with aluminum stiffeners, or
- d. aluminum honeycomb with aluminum face skins.

To determine the optimum plate size and configuration, the maximum rms deviation is defined as

$$c_{rms}^2 = \frac{\delta_{max}^2}{3} \quad (6-13)$$

where δ_{max} is the maximum allowable panel deflection. From the error budget, δ_{max} is 0.014 in. (0.089 cm) and 0.028 in. (0.176 cm), respectively, for 20- and 40-mil overall rms tolerances in 45-mph winds.

For simplicity, the plates are assumed to be flat for the initial sizing. This is a conservative assumption since curved plates have greater rigidity than flat plates. The deflection of corner-supported square plates is defined as²⁹

$$\delta_{max} = \alpha \frac{qa^4}{D} \quad (6-14)$$

where

- α = function of edge stiffness = 0.0249
- q = uniform wind load = 0.050 lb/in² (0.034 N/cm²)
- a = side dimension
- D = plate stiffness = $Eh^3/[12(1 - \nu^2)]$
- E = 10^7 psi (7×10^6 N/cm²), the aluminum modulus of elasticity
- ν = Poisson's ratio = 0.3
- h = plate equivalent thickness

The resultant equivalent plate thickness required for various rms surface tolerances is shown in Figure 6-15. This figure indicates that the minimum total weight is 22.5 psf (1089 N/cm²) for a solid aluminum 8-ft square plate configuration vs 8.9 psf (427 N/m²) for a 4-ft plate. The equivalent plate thickness for corrugated honeycomb or beam-stiffened thin plates is

$$h_{equiv} = \sqrt[3]{12I} \quad (6-15)$$

where I is the section area moment of inertia per unit length.

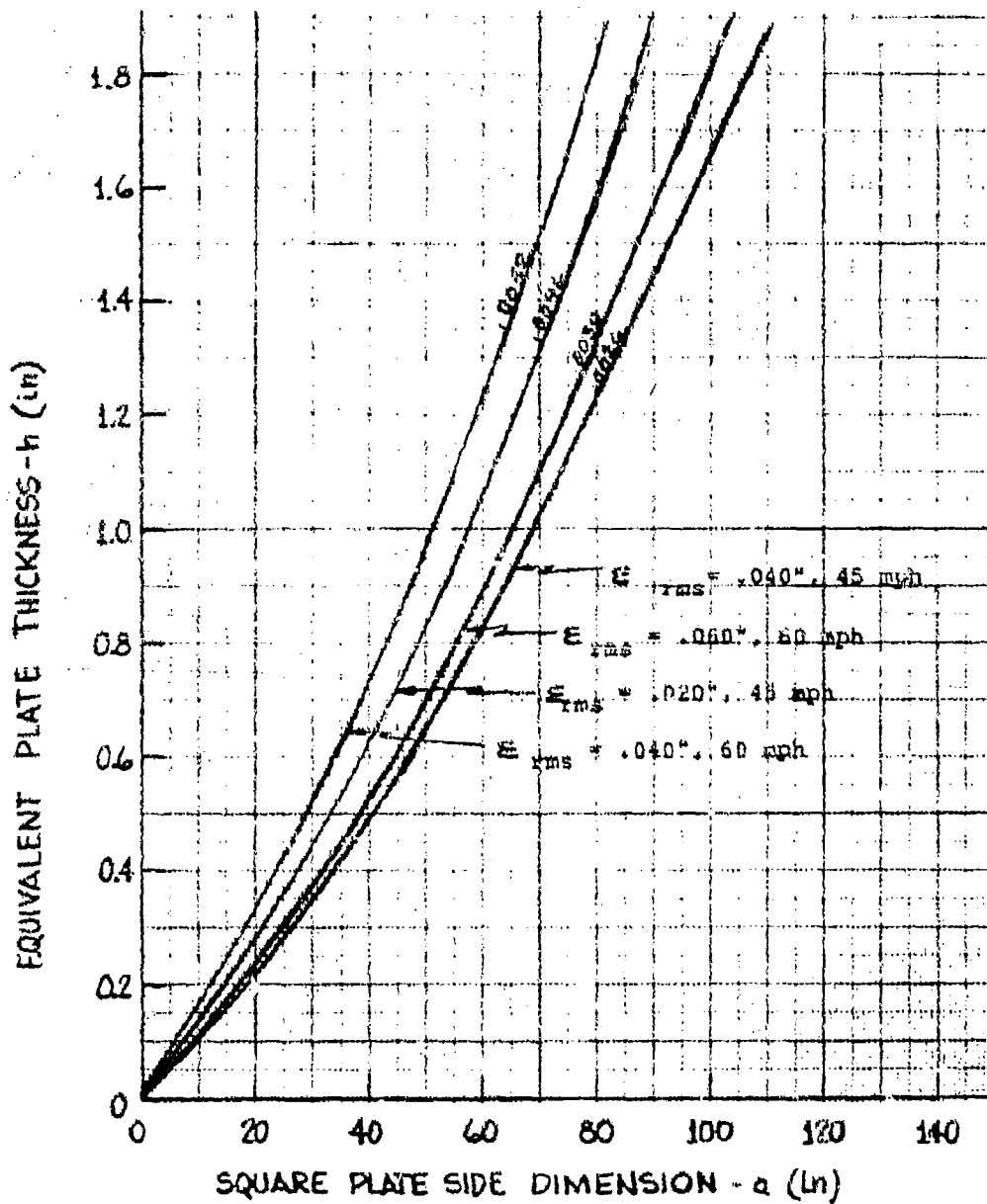


Figure 6-15. Equivalent Plate Thickness

Figure 6-15 indicates the critical relationship of panel size to surface tolerance. Since the 60-mph curve dominates in both cases, the recommended maximum panel sizes appear to be 8 and 6 ft for the 40- and 20-mil cases, respectively. Some examples of equivalent stiffened plates are shown in Figure 6-16. For a typical 8-ft square plate, the section moment of inertia required to meet the 60-mph surface tolerance criteria at 60 mph would be 0.42 in³/in. (2.7 cm³/cm).

Regardless of configuration, the thinnest aluminum face sheet used was 0.060 in. (0.152 cm) to protect the reflector surface from permanent deformation due to the impact of hailstones or other moderate size particles.^{27, 30} Based on a maximum panel dimension of 9 ft (2.7 m), several reflector configurations were analyzed (Figure 6-17). To reduce wind deflections on the structure, the four corner panels were shaped to eliminate unnecessary surface area. The configuration of three parabolic panel sections would require irregularly shaped corner panels to accomplish the area reduction without gain loss. Simple triangular corner panels can be used with four parabolic panel sections to minimize area reduction.

6.6.2 BACKUP STRUCTURE

Based on the results of the panel optimization, a stiff, lightweight, universal support was needed for the reflector. To add commonality to both the backup structure and the reflector, the main structural frame is a basic vertical truss structure tied to the panels at each corner point. The generating truss is rotated about the axis of revolution of the reflector. Additional stiffness is obtained by tying each vertical frame together via horizontal trusses and diagonal bracing. Given the latitude and

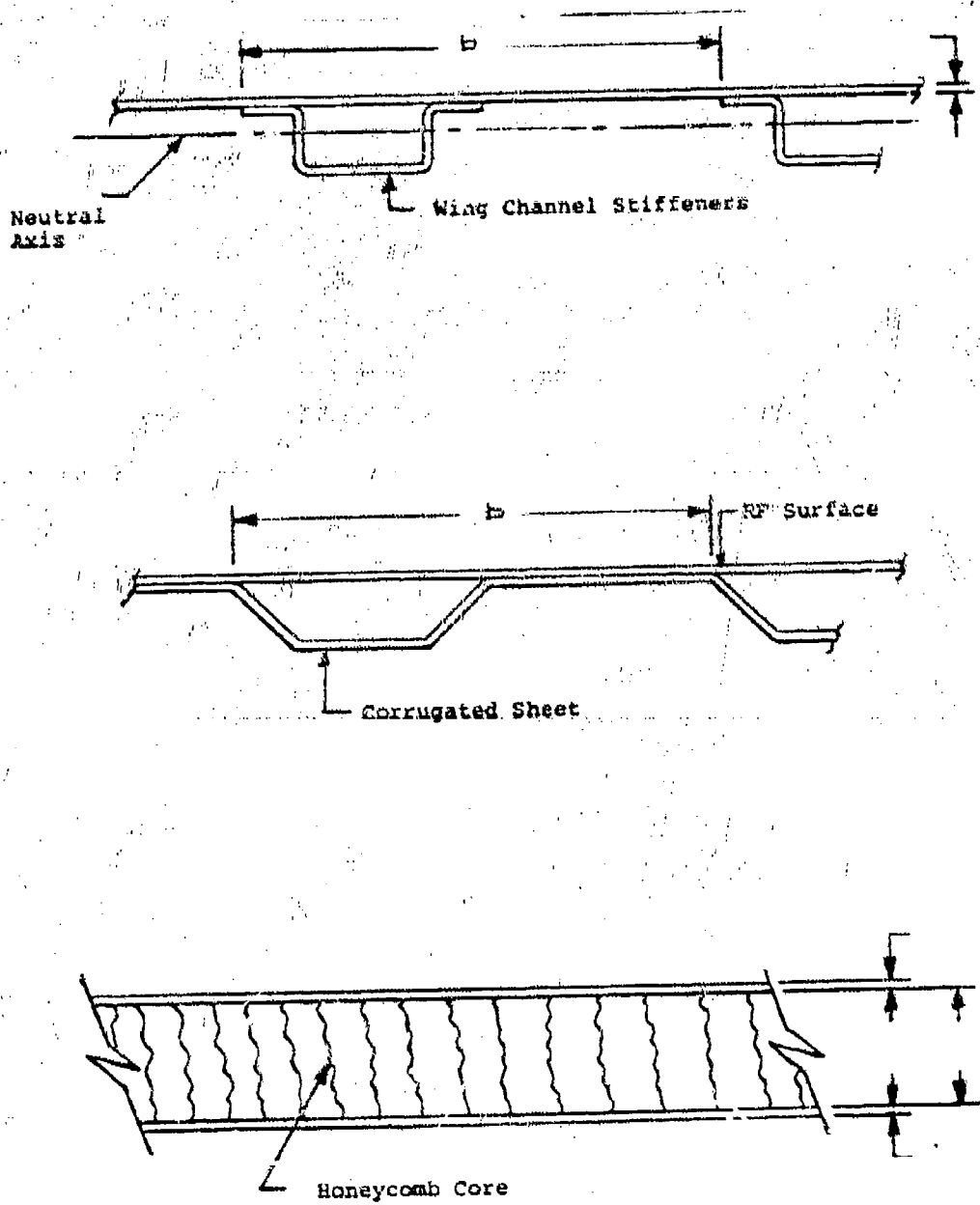
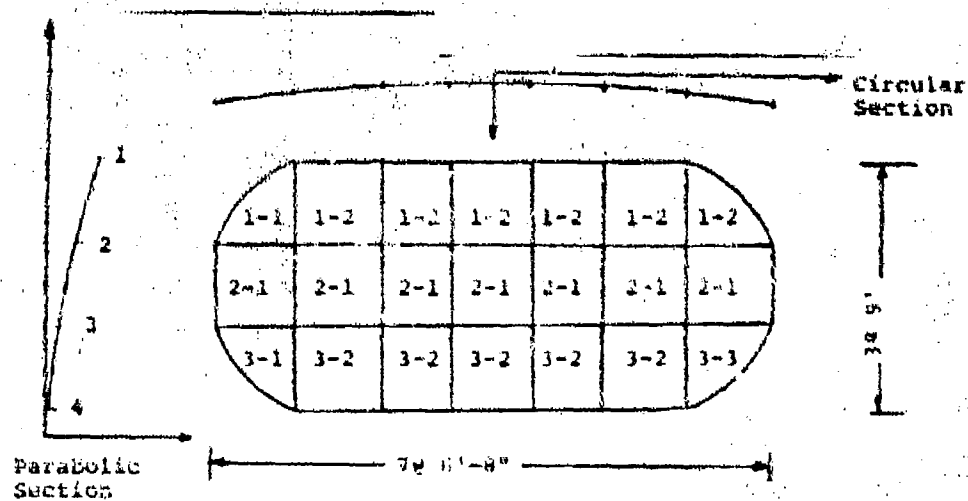
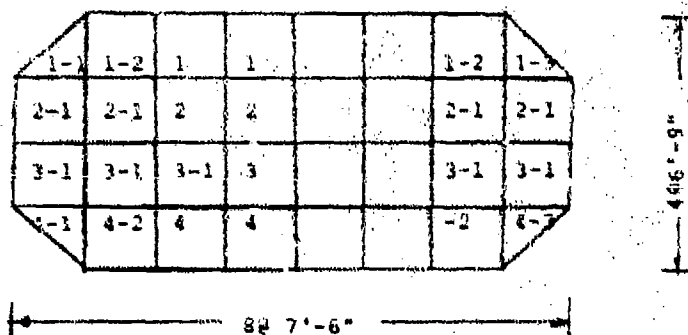


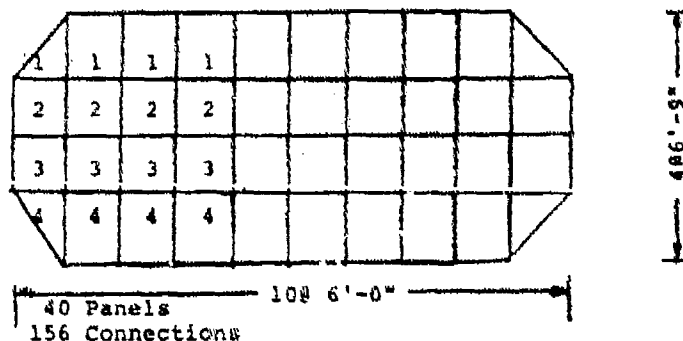
Figure 6-16. Reflector Panel Cross Section



21 Panels
80 Connections



32 Panels
124 Connections



40 Panels
156 Connections

Figure 6-17. Panel Configurations

longitude at the desired earth station location, the backup structure and reflector panels are then rotated into the global coordinate system via transformation equation (6-7). Some typical configurations considered for the generating vertical truss are shown in Figure 6-18.

After panel analysis design iterations, it was decided to use a 4 x 8 panel reflector surface as the baseline configuration. The panel layout shown in Figure 6-19 was chosen for design iterations. The nine vertical trusses required for this configuration are supported by the main spine truss generated as a curve about the axis of rotation of the reflector.

All members in this analysis are A36 structural steel in commonly available sizes. Ideally the reflector surface panels are attached to the truss at each corner by rods with adjustment mechanisms to make alignment corrections during erection.

A 4-point attachment to the support structure was used for the initial design iterations. A detailed view of the backup structure reduced from a NASTRAN plot for the 27-ft MBTA is shown in Figure 6-20.

6.6.3 SUPPORT POINTS

The type of support members is determined by the required stiffness of the torus structure in its operational position. The structural stiffness in turn is a function of the number and spacing of pickup and foundation points, the unbraced length of the steel members, and their relative configuration. Thus, each location requires a unique support structure to accommodate its antenna positioning.

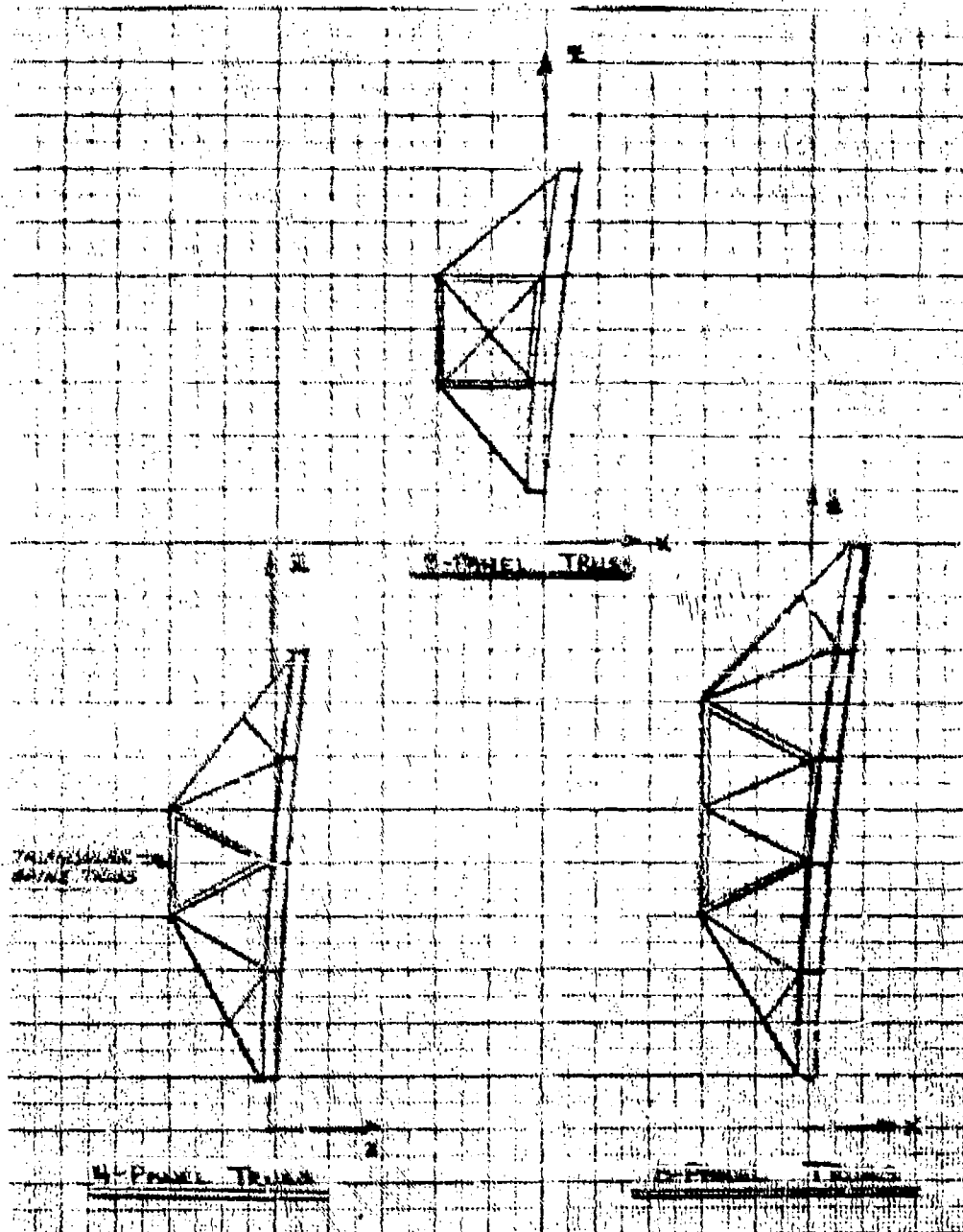


Figure 6-18. Vertical Truss Configurations

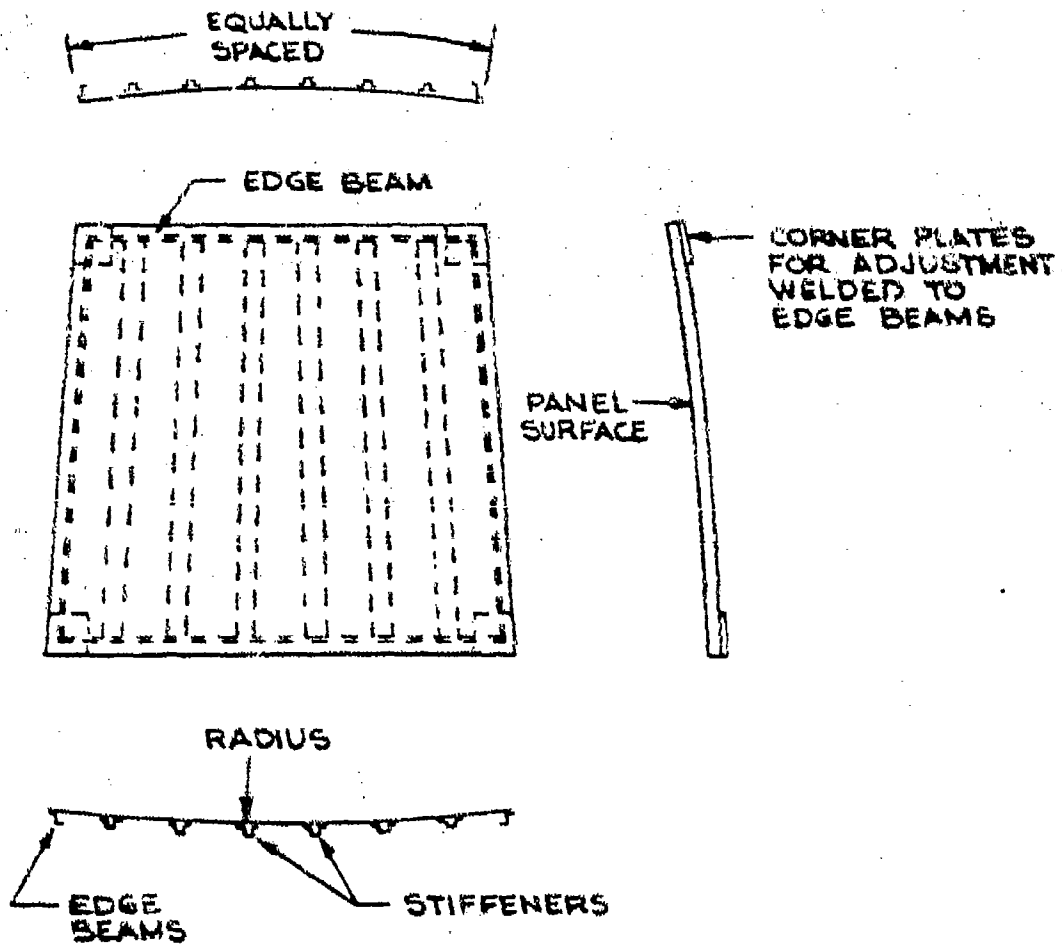


Figure 6-19. Typical Panel Layout

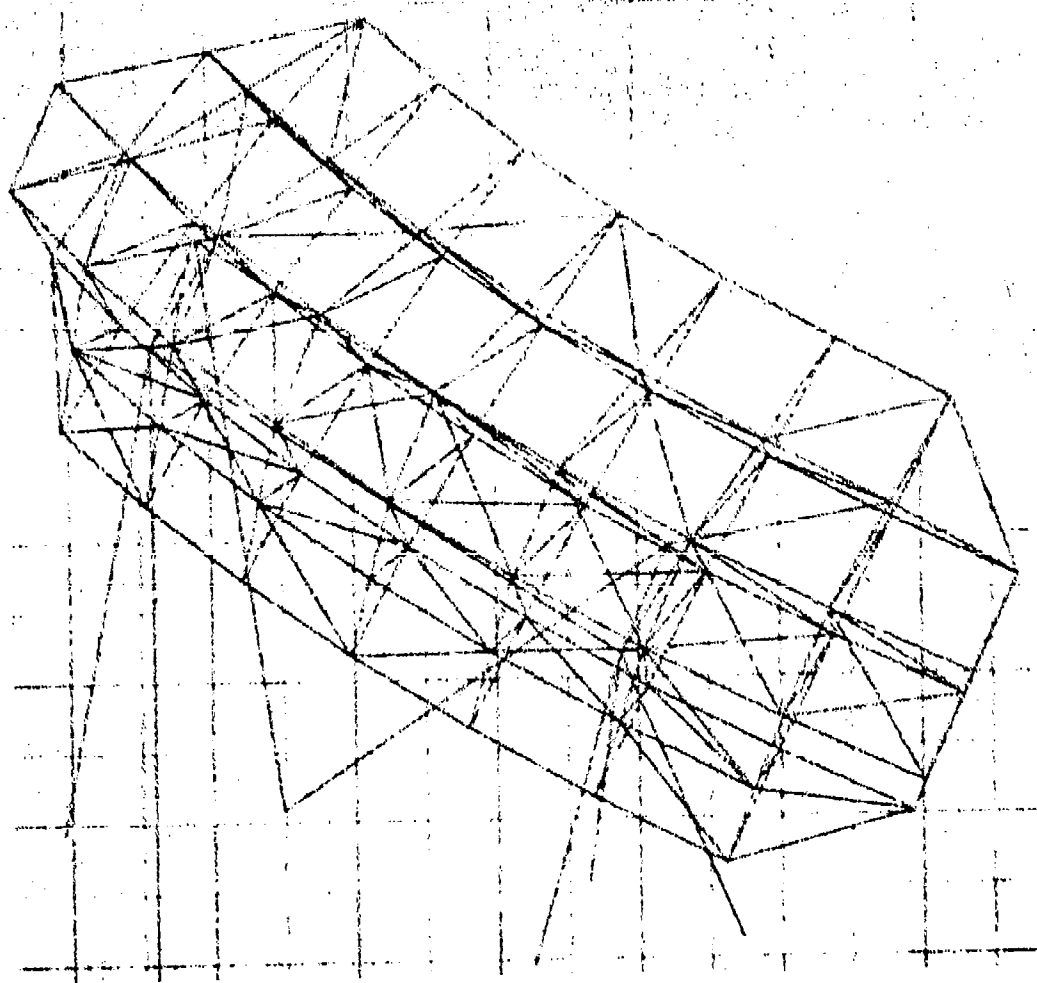


Figure 6-20. NASTRAN Plot of Backup Structure

The simple 7-member steel support structure shown in Figure 6-21 was used for design iterations of the basic MBTA antenna. It uses a lower tripod as the main static load carrying member. The dynamic wind load is transmitted through the V and A frames to ground. The V frame can also serve as a pivot mechanism for correcting the tilt of the antenna during erection. This particular support system is not a self-standing structure; the backup structure member assembly must be included to achieve overall stability.¹¹

Figure 6-11 shows a stable and less flexible support structure. This configuration might be necessary at sites where the most severe wind load overturning moments occur, or where, because of the extreme length of the V and A frame members and the required antenna size or extreme site location, the 6-member design is unconservative.

Figure 6-22 shows the stiffness requirements of the same reflector translated to different locations. The projected area times maximum reflector height is normalized to its surface area times the aperture height to give a measure of the relative wind loading deformation problem. It can be seen that the dynamic deflections at the Mt. Margret location are potentially six times as severe as those at the Ascension Island location.

6.7

STRUCTURAL LAYOUT

The MBTA-11 program, developed at COMSAT Labs, establishes the precise geometrical coordinates of antenna panels, backup, support structures, and feeds based on optimum RF parameters and site location. The main part of the program lays out the panel and panel support geometry, front and side wind loads,

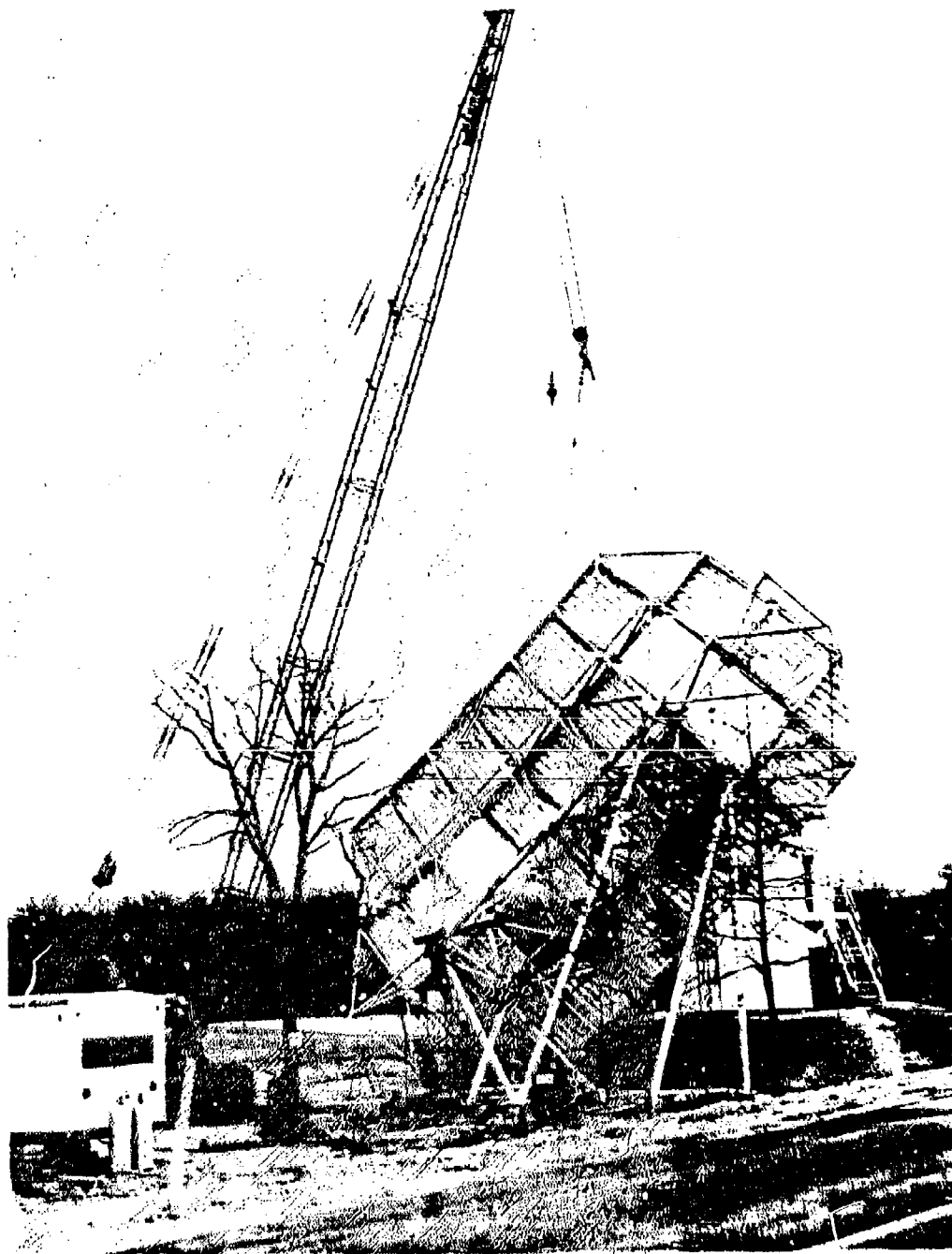


Figure 6-21. View of COMSAT UET Torus
Antenna During Construction

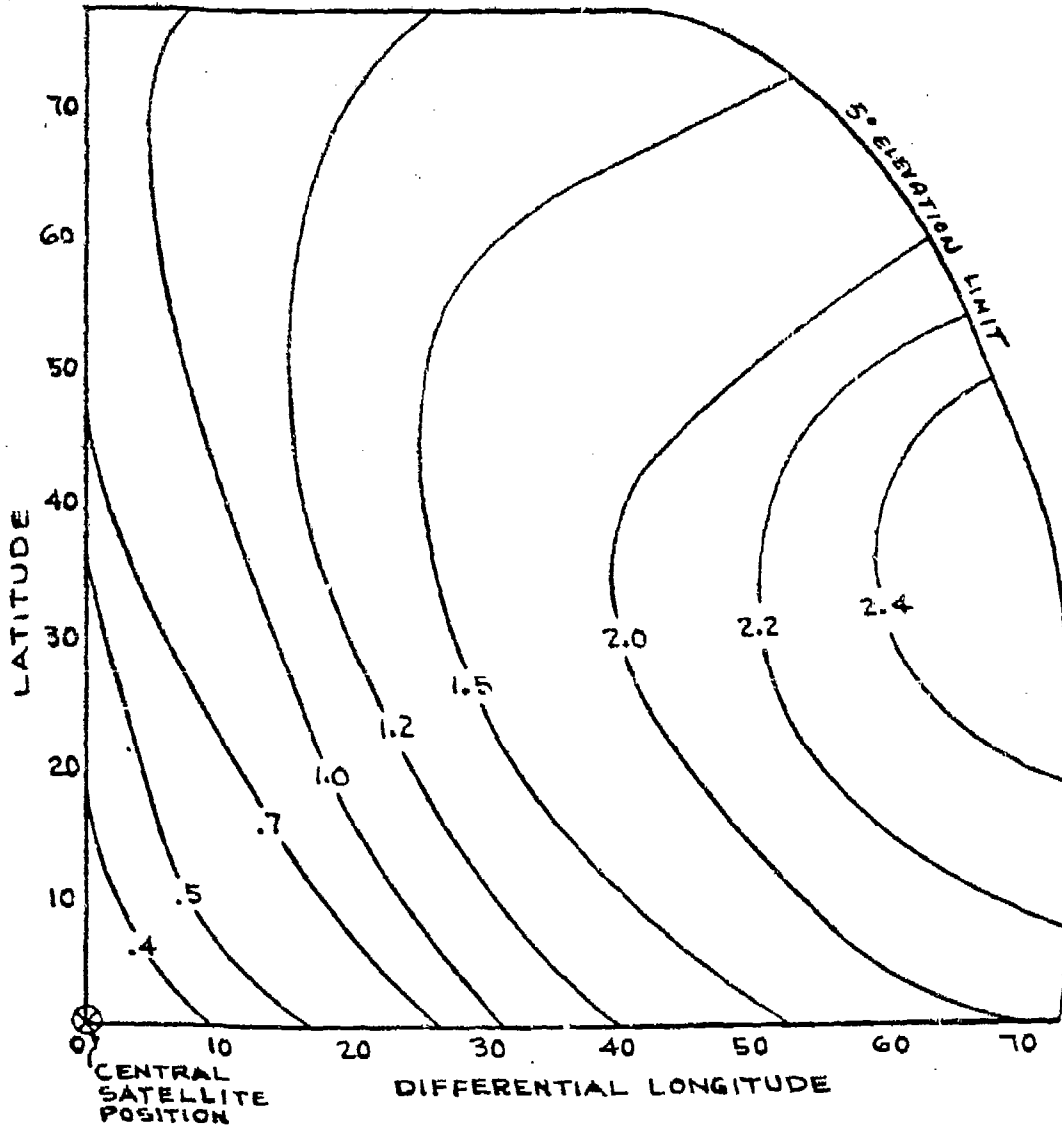


Figure 6-22. Normalized Wind Moment Area
 $[(A \times H) / (W \times D^2)]$

and transmitted panel weight to the corner points. All calculations are performed in the local (RF parameter) coordinate system and translated to the global (site-dependent) coordinate system. Subroutines within MBTA-11 determine the local coordinates of the desired backup and support structures. These routines are kept separate to simplify programming changes to accommodate a new configuration truss system, foundation layout, or pickup point designation.

MBTA-11 outputs the NASTRAN grid point sequencing for the individual panel shape, as shown in Figure 6-23, and for the backup truss, pickup points, and foundation supports, as shown in Figures 6-24 and 6-25. MBTA-11 also details necessary drafting and surveying information, including the actual arc and chord lengths of the panels as well as the relative location of the feeds from the reflector, referenced to the generating paraboloid vertex.³²

6.8 LOAD ANALYSIS

All environmental loads are generated in the MBTA-11 program. Based on results from panel design iterations, a projected panel weight per square inch is input. The program calculates the equivalent concentrated mass at each panel/truss support point. Thermal loads are generated based on a 10°F (-12°C) temperature at the panel support points and a 0°F (-18°C) temperature at all other structural joints.

Wind loads are generated based on the projected panel area in the plane perpendicular to the direction under consideration. The wind load vector is always assumed to be parallel to ground for simplicity. In reality, it rarely goes above 10° to the horizontal. Wind loads are calculated in the local coordinate

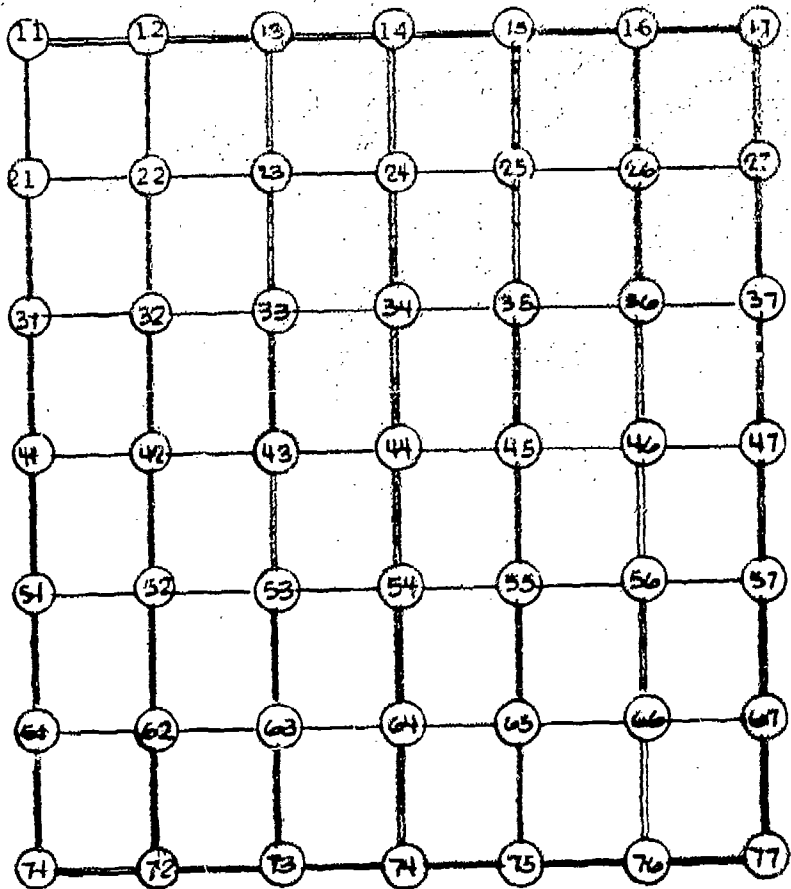
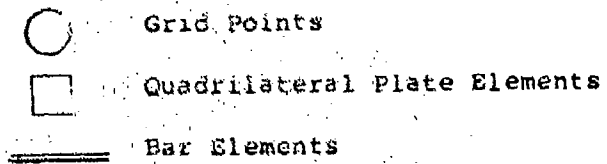


Figure 6-23. NASTRAN Plate Element Numbering

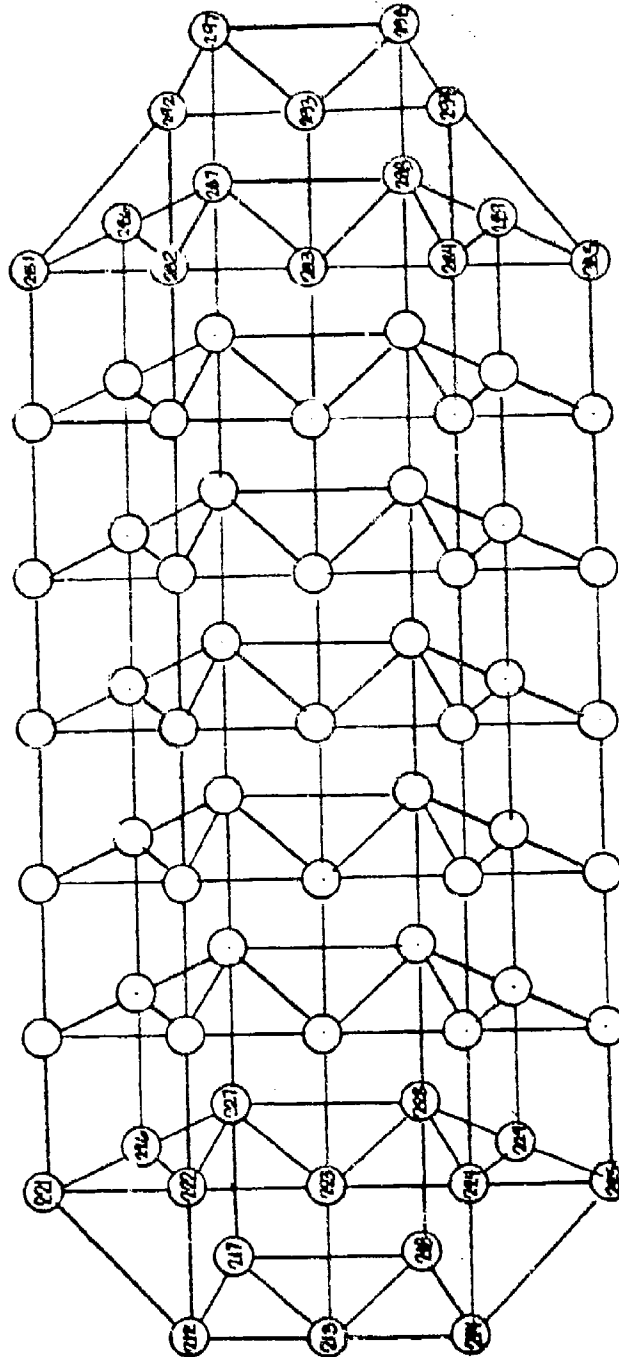


Figure 6-24. NASTRAN Backup Truss Grid Point Numbering Scheme

system and reduced in proportion to the cosine of the elevation angle in the aperture plane to determine the horizontal-to-beam (HTB) wind loads. The wind forces are also generated perpendicular to the global -X and +Y axes to determine the overturning and torsional effects of front and side wind forces.

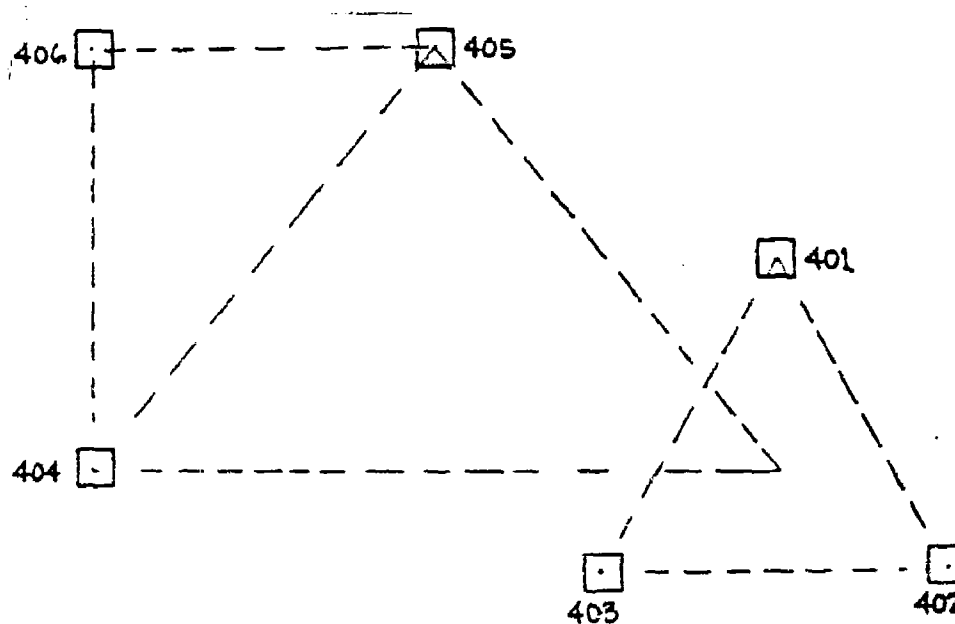


Figure 6-25. NASTRAN Foundation Grid Point Layout

The environmental loading cases are enumerated in Table 6-2. In addition to gravity and thermal conditions, effects of wind forces of 45, 60, and 125 mph, corresponding to operational, degraded operational, and survival conditions, are calculated.

Since wind tunnel tests are not available for the toroidal antenna, the exact wind pressure coefficients are not known for this shape. A review of the literature pertaining to tests on more common structural shapes indicates that a discharge

Table 6-2. NASTRAN Load Cases

Gravity Loading
45-mph Front (-X Axis) Wind Gusts
60-mph Front Wind Gusts
125-mph Front Wind Gusts
10° Differential Temperature (front to back)
45-mph Side (-Y Axis) Wind + Gravity + Differential Temperature
60-mph Side Wind + Gravity + Differential Temperature
125-mph Side Wind + Gravity + Differential Temperature
125-mph Side (+Y Axis) Wind + Gravity + Differential Temperature
45-mph Front Wind + Gravity + 10° Differential Temperature
60-mph Front Wind + Gravity + 10° Differential Temperature
125-mph Front Wind + Gravity + Differential Temperature

coefficient of 1.4 for the front wind is conservative.^{26,33} This also demonstrates one advantage of a relatively flat toroidal reflector over the curved paraboloid. Wind tunnel tests performed on parabolic reflectors indicate that a discharge coefficient of at least 1.7 is used for safe design. This represents a relative increase of 21 percent relative to the wind loads over a toroidal reflector³⁴ of equal area.

6.9 STATIC ANALYSIS

Given the grid point sequencing and load case cards from MBTA-11, a structural model for bar and rod members is generated for the NASTRAN input deck based on the truss and support structure layouts in Figures 6-24 and 6-25. All rotational degrees of freedom are eliminated from the model to simulate a totally pin-connected structure. This use of bolt- or pin-type connections permits a structure that is easy to assemble and dismantle as required.

The backup truss was modeled by CBAR³⁵ members, hence permitting the use of elements with triaxial stiffness. Since a primarily uniaxially stiff structural member such as tubing is required for the basic 7-member support, the support members were modeled by CROD³⁵ members. Additional bracing members were included as necessary during analysis. In conjunction with the surface rms results, the stiffness of beams in some locations was increased while the area and moment of inertia (MOI) of others were reduced. All selected areas and MOI values correspond to real members in the Manual of Steel Construction. The primary backup truss members were mainly double-angle beams, the secondary diagonal bracing members were single-angle beams and the support structure members were extra strength round tubing.

During static analysis iterations, as shown in Figure 6-26, there were two criteria for the final design. First the rms deflection was checked for each case. If the allowable surface tolerance for the operational or degraded performance cases was exceeded, additional stiffness was provided or extra members were included. Secondly, the structural stresses on members at the survival loads were checked. Any member exceeding the yield stress limit or buckling stress criteria was stiffened accordingly.

The yield stress for the backup truss and support members was assumed to be 36,000 psi for A36 steel. With a margin of safety, 24,000 psi was considered the maximum allowable bending stress. For long unbraced members the maximum allowable stress was determined from the buckling criterion¹⁶

$$F_a = \frac{12\pi^2 E}{23(Kl/r)^2} \quad (6-16)$$

where

- F_a = allowable axial stress
- E = modulus of elasticity
- Kl = unbraced length
- r = section radius of gyration

In most static analysis iterations, deflection was the governing criterion for sizing the backup truss members. The maximum bending stress determined the size and layout of the pickup point members between the backup truss and support structures, and the buckling criteria governed the design of the support members due to their long unbraced length.

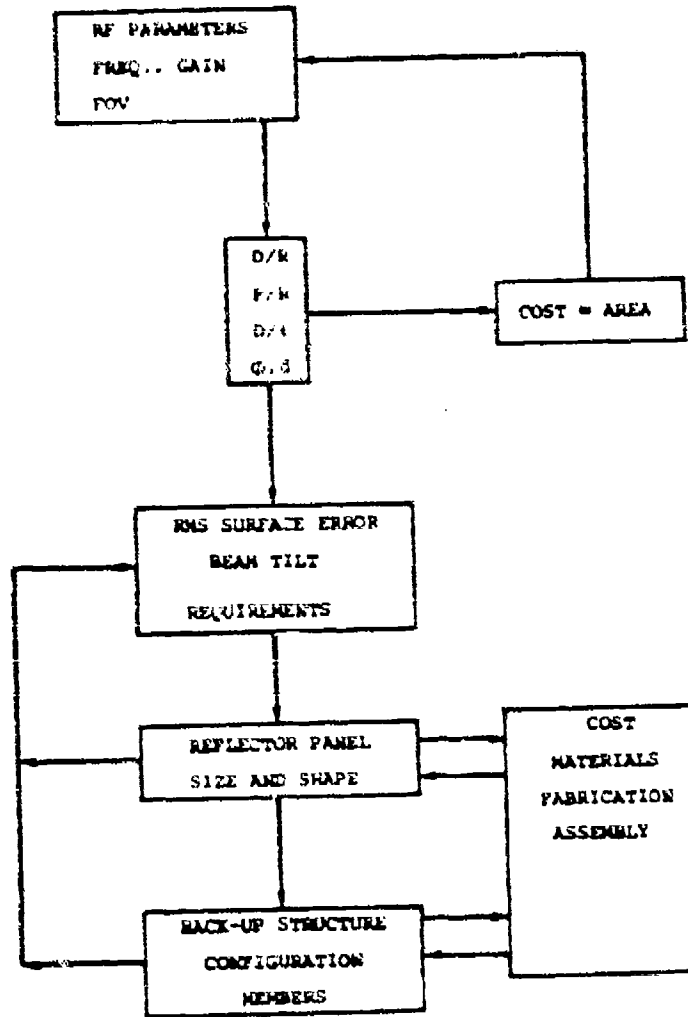


Figure 6-26. Flow Chart of Design Iterations

6.10 DYNAMIC ANALYSIS

Although static analysis was the primary solution of interest during this study, the NASTRAN normal mode analysis is also useful. To determine the wind velocities at which the natural frequency of a structure will cause resonant vibration of the reflector, the fundamental natural frequency must be known. The relationship between these parameters is defined by the nondimensional Strouhal member¹¹:

$$S = \frac{n_1 D}{V_1} \quad (6-17)$$

where

- n_1 = natural frequency in Hz
- V_1 = wind velocity at resonance
- D = structural diameter

The fundamental frequency of the 27-ft MBTA is 12 Hz. Assuming a Strouhal number between 0.15 and 0.20 results in critical wind velocities between 1100 and 1470 mph; hence, there should be few difficulties with resonant vibration. To prevent problems at the maximum design winds of 125 mph, the natural frequency should be at least a half power beam width above the critical frequency, or about 2 Hz. Even for 200-mph wind, the 12-Hz fundamental frequency is well above critical.

6.11 ERROR ANALYSIS

The MBTA-12 program was developed to calculate the rms surface deflections of the MBTA surface based on NASTRAN results. The grid point deflections for NASTRAN are punched on cards as

well as printed. The punch cards of the original undeformed location of the reflector surface grid points and deflection output comprise the input of MBTA-12.

The surface rms error is defined as

$$e_{rms} = \left[\frac{\sum_{i=1}^n c_i^2}{n} \right]^{1/2} \quad (6-18)$$

where c_i is the deflection at individual surface points. Due to the antenna tilt correction capability of the feed mechanism, the deflections due to angular movements of the structure as a whole are not included in the rms error calculation. Hence, a deformed surface fitting expression is needed. The simplest method is to calculate the best fit parabola for each vertical section cut and calculate the individual section tilt at that location. However, this method omits the horizontal aperture tilt as well as the relationship between sections. Therefore, a surface fitting relationship based on equation (6-12), the exact expression for the parabolic toroidal surface, is used. To simplify the results the square root of the sum of the squares (SRSS) deflection is calculated from

$$D_i = \left[d_{x_i}^2 + d_{y_i}^2 + d_{z_i}^2 \right]^{1/2} \quad (6-19)$$

and applied as a single x-axis deflection. This assumption is realistic, since in most cases the largest deformation occurs parallel to the x-axis due to front wind loads.

Equation (6-12), which is expressed in the form

$$\epsilon_i = A_1^2 \frac{z_i^4}{16} - A_1 \frac{z_i^2}{2} - A_2 (x_i^2 + y_i^2) + 1 \quad (6-20)$$

where ϵ_i is the function error to be minimized, has been divided by $16 F^2 R^2$ to minimize computational error on the IBM-360 computer. Curve fitting by the least squares method is performed based on a minimization of the sum of the deviations squared³⁷:

$$S = \sum_{i=1}^n \epsilon_i^2 \quad (6-21)$$

If S is a minimum, then $(\partial S / \partial A_1) = 0$ and $(\partial S / \partial A_2) = 0$. These expressions reduce to two equations in which A_1 and A_2 are solved for the best surface fit.

The tilted surface x_i values are then derived by substituting back into the original equation. Horizontal and vertical surface tilts are measured from the new x coordinates and the old y and z coordinates. The rms deflection is then derived from the difference between the deflected x_i coordinate and the tilted surface x_i , as shown in Figure 6-27.

The left local, center local, and right local rms values are given as well as the overall rms surface tolerance. The local values are perhaps a more accurate measure of the gain loss of the antenna, since these areas are covered by a single beam illumination rather than the whole reflector surface.

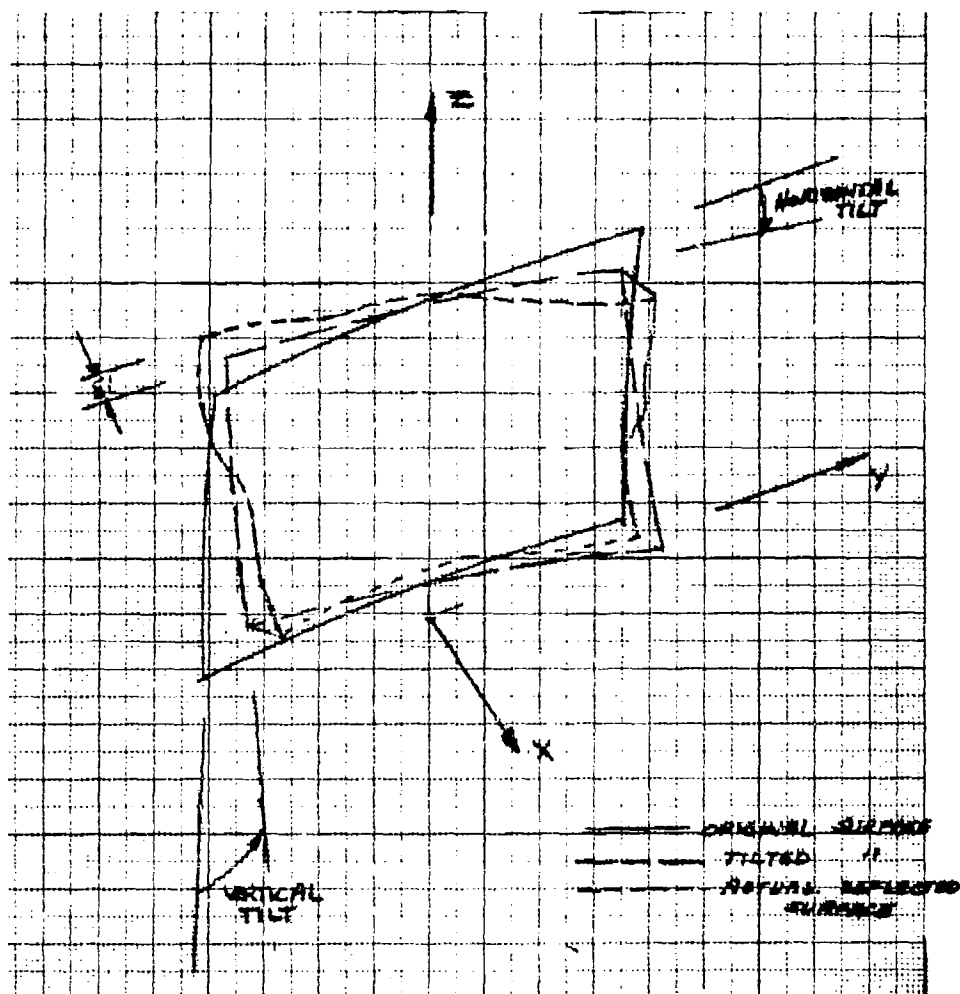


Figure 6-27. Surface Tilt and rms Deformation

7. COST ESTIMATES FOR A RECOVERABLE MBTA

The cost data presented in this section for various antenna sizes are based on a central satellite location of 333° east longitude, an earth station located at COMSAT Labs, a field of view angle of 30°, and a surface generation angle (ϕ_0) of 93.5°. All parameters used to determine cost estimates are output from the program MBTA-11. These parameters include the reflector width (W), which is used with the aperture diameter (D) to determine the antenna surface area, the maximum reflector height; the feed arc length and depth; and the corresponding dimensions of the feed building. In all cases ground level is assumed to be 5 ft below the lowest point on the reflector.

Fabrication costs include the costs of reflector surface panels and backup truss and support members. As shown in Figure 7-1, these costs are a function of surface area and rms surface tolerance. The RF panels are assumed to be stretch-formed aluminum, approximately eight feet on a side, over unidirectional stiffeners and edge beams. Only the support member length changes with station location. Since the cost of the extra length of steel required at different sites is negligible relative to the total cost, it was not included in that total cost.

Estimated erection costs are given as a function of surface area only in Figure 7-2. Unlike fabrication costs, erection costs are not scaled for surface tolerance since accurate placement of all members is required.

The antenna foundation costs are scaled from the volume of concrete (24 yd³) which is assumed to be necessary to support the COMSAT UET antenna (32 x 55 ft) on moderate to good soil. The foundation size is assumed to be proportional to the

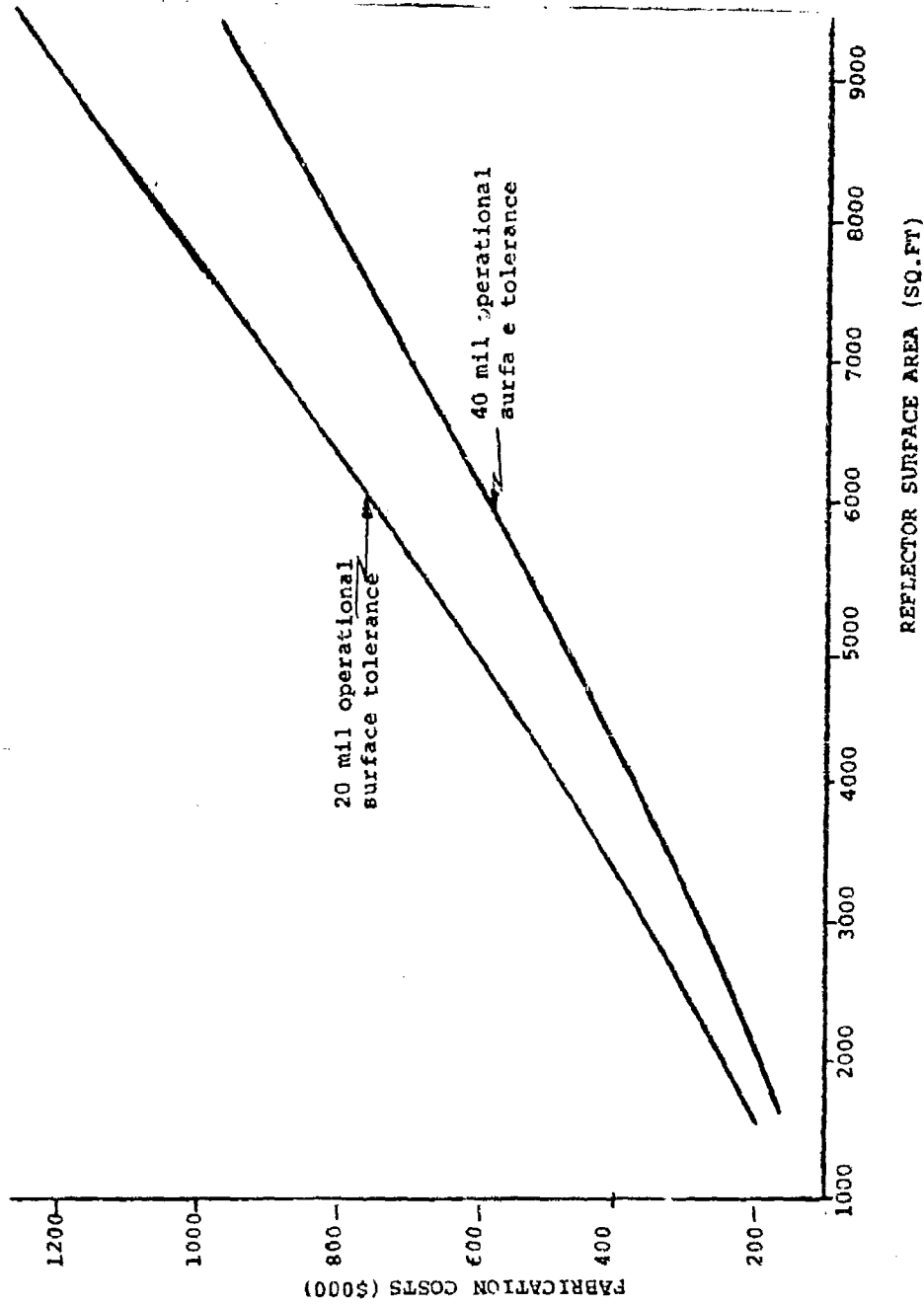


Figure 7-1. Fabrication Costs vs Surface Area

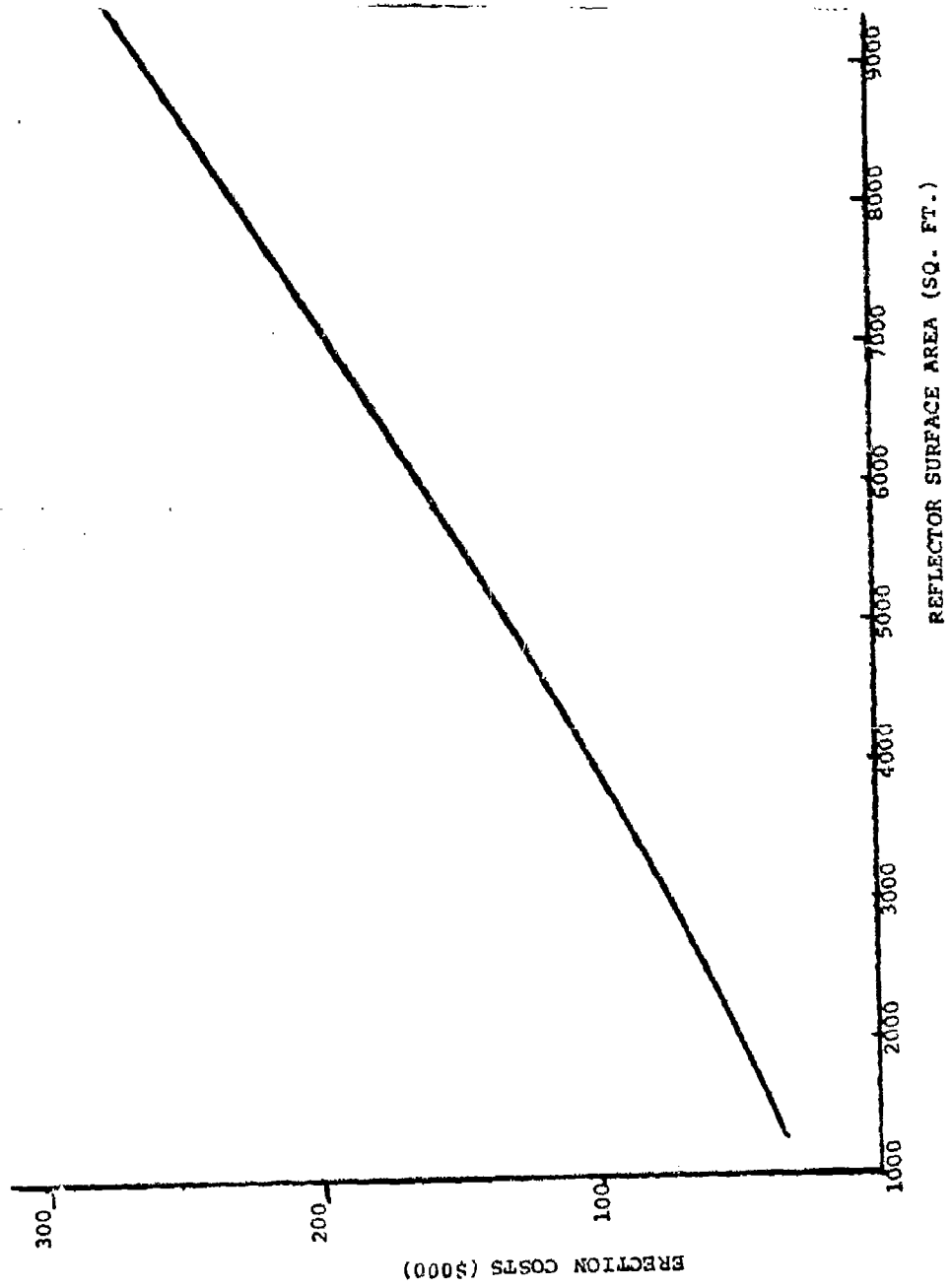


Figure 7-2. Erection Costs vs Surface Area

area and overall height of the reflector. Since the type of soil at any two sites varies greatly in bearing capacity, the cubic yardage assumed for this estimate should not be taken as an exact guideline. Cost per cubic yard was taken from building construction cost data for 1977 based on estimated amounts of excavation, forms, concrete, and reinforcement required per footing.³⁸

The feed transport mechanism cost is quoted as a constant \$12,000 independent of aperture size, since the rails and support steel work are included in the building price estimate. The transport cost is based on an actual mechanism designed, built, and tested at COMSAT Labs.

The feed building costs include those of the transport rails and support structure, a pre-engineered environmental enclosure, and separate foundations for the transport and building. The rail and mechanism support costs are estimated from values for the width and height of the feed arc. Figures 7-3 and 7-4 show these parameters as a function of location for a 27-ft reflector with $D/R = 0.4$. The feed building is assumed to be several feet larger than the transport dimensions with a minimum of 12 ft on a side. For simplicity, ground level is assumed to be the same as that of the reflector. Estimates are based on prices for pre-engineered buildings, steel work, and concrete from 1977 construction cost data with 30-percent additional cost included for extra mechanical or electrical work.³⁸

De-icing costs are included for DCA's information. Figure 7-5 shows that the cost asymptotically approaches \$22/ft² due to the high initial equipment investment required. COMSAT's experience indicates that this equipment will not be necessary at the majority of DCA sites. Hence, the cost of de-icing is included after the subtotal.

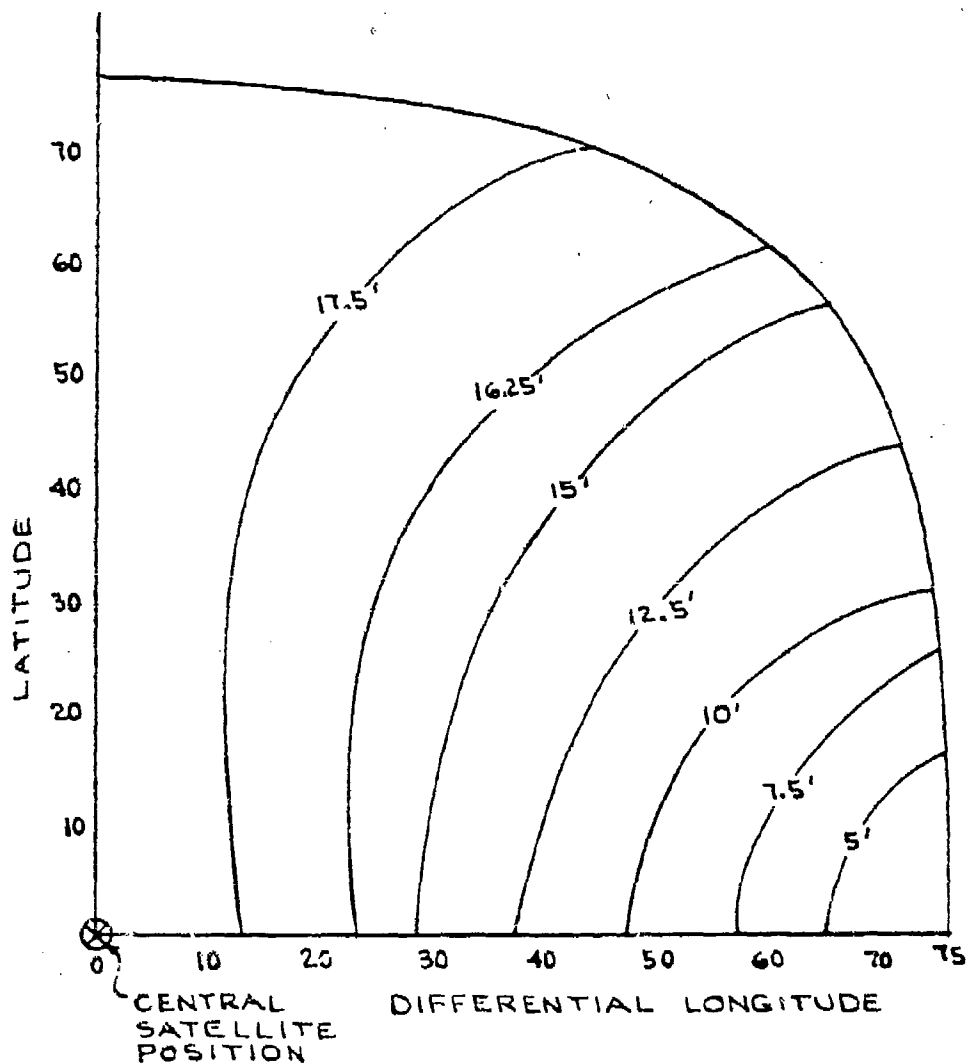


Figure 7-3. Width vs Location

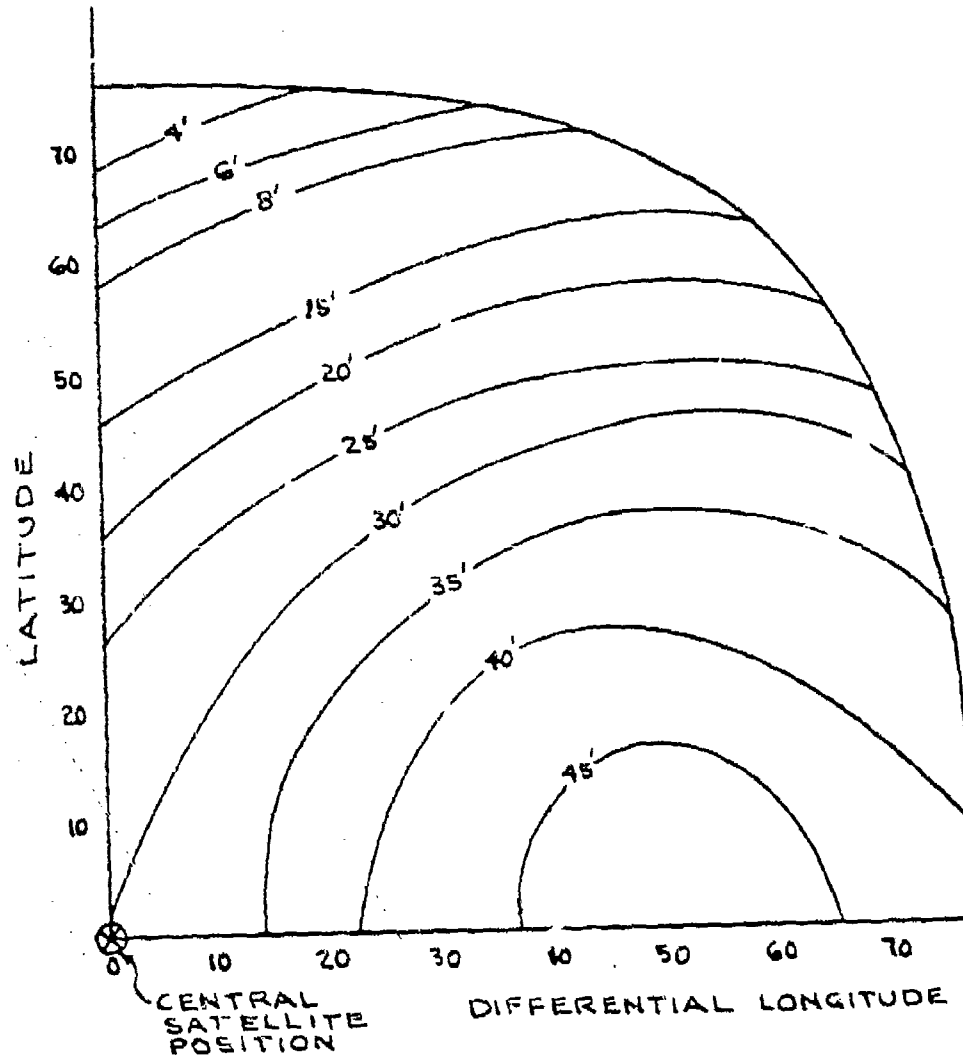


Figure 7-4. Height vs Location

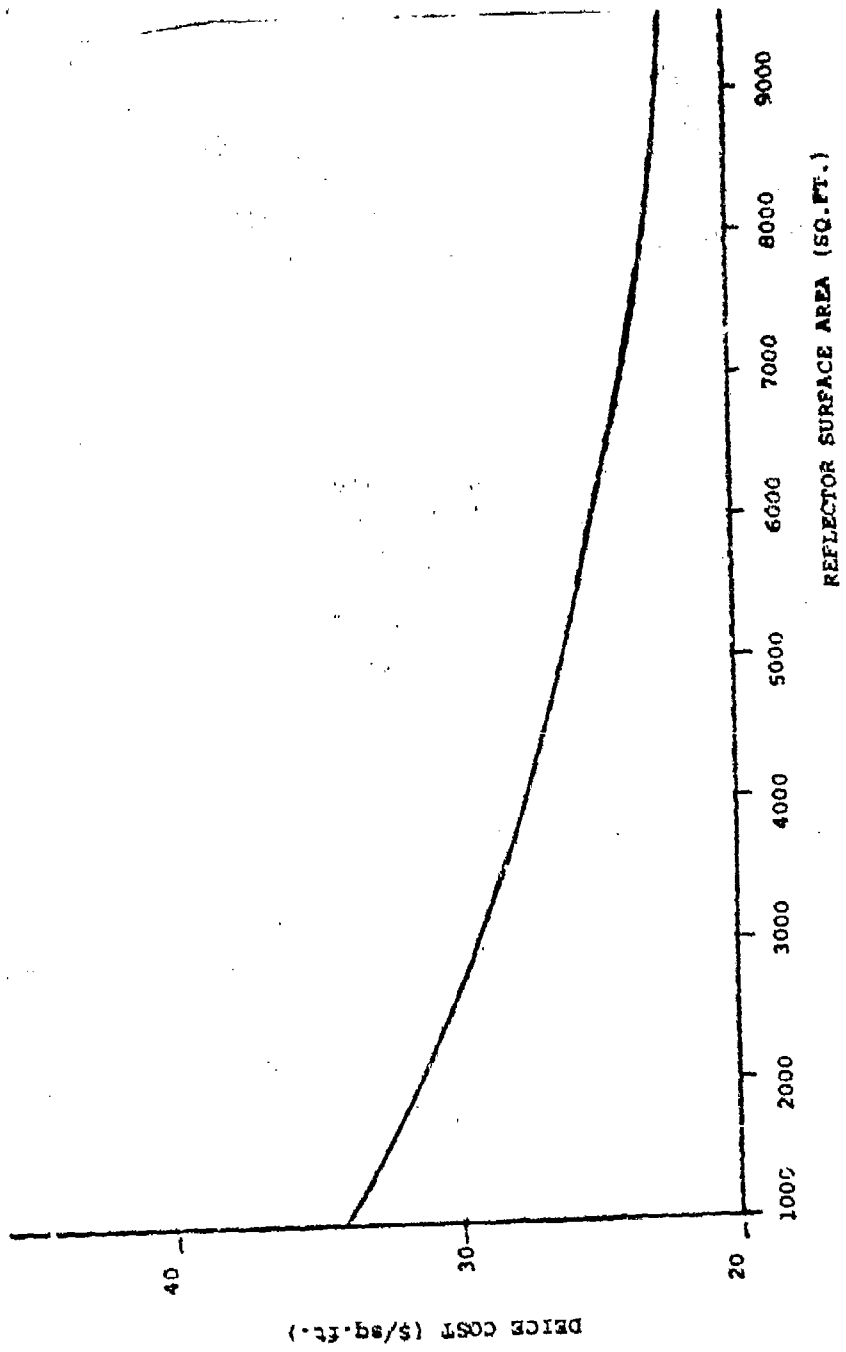


Figure 7-5. De-icing Costs per Square Foot vs Surface Area

Table 7-1 lists the cost estimates for three separate antenna aperture sizes, as shown in Figure 7-6. The basic antenna for this study is the 27-ft reflector, which provides 54-dB gain in the 7/8-GHz band with 0.040-inch rms surface tolerance. The cost of this reflector is compared with the cost of the same reflector with a 0.020-inch surface tolerance, which would be required for the 20/30-GHz operational frequency bands. The subtotal costs in Table 7-1 indicate that the decrease in allowable rms error increases the costs by about 20 percent. Cases 2 and 3 correspond to the required gain of 59 dB in the 7/8-GHz band. Both 48- and 65-ft-diameter reflectors meet the RF requirements. However, comparison of the antenna costs in Figure 7-7 indicates that the antenna with the smallest surface area satisfying the electrical requirements is also the least expensive. The cost of obtaining 0.020-inch surface tolerance at these aperture sizes is included for comparison only.

Table 7-2 lists the costs of the basic 27-ft reflector at several locations. Due to the universal design, fabrication, transport mechanism, and de-icing costs remain constant for all sites. Erection costs are scaled slightly above a fixed base cost, depending on the maximum reflector height. The largest change in cost is associated with the building parameters, since the orientation of the feed window varies radically with the site. The parameters on which the cost estimates are based are shown in Figures 7-8 and 7-9 for the site of interest. In terms of erection prices, a 27-ft reflector at the COMSAT Labs location is considered to be the baseline antenna. All building estimates are based on the aforementioned structural criteria.

Comparison of the subtotal costs of antennas at the various sites indicates that a small fraction (<10 percent) of the total cost is involved in site-dependent work. A far greater cost increase results from a change in the aperture size or a decrease in the allowable rms surface tolerance.

Table 7-1. MBTA Dimensions and Cost (FOV = 30°,
center frequency = 7.25 GHz)

	Case 1		Case 2		Case 3	
	Surface Tolerance		Surface Tolerance		Surface Tolerance	
	0.040-in.	0.020-in.	0.040-in.	0.020-in.	0.040-in.	0.020-in.
	Dimensions					
Reflector						
Aperture Diameter, D (ft)	27	27	48	48	65	65
Aperture Width, W (ft)	60	60	126	126	141	141
Maximum Height (ft)	62	62	124	124	142	142
Aperture Area, W x D (ft ²)	1585	1585	6045	6045	9186	9186
D/R	0.4	0.4	0.3	0.3	0.4	0.4
F/R	0.483	0.483	0.491	0.491	0.483	0.483
Gain (dB)	54	54	59	59	59	59
Antenna Foundation (yd ³)	28	28	214	214	372	372
Feed Building						
Width (ft)	12	12	17	17	17	17
Length (ft)	20	20	38	38	38	38
Height (ft)	41	43	88	88	92	92
Foundation (yd ³)	4	4	12	12	12	12
Feed Transport						
Width (ft)	14	14	33	33	33	33
Height (ft)	11	11	27	27	27	27
	Cost					
Fabrication	160	200	580	760	940	1200
Erection	40	40	160	160	265	265
Foundation	6.2	6.2	48.0	48.0	83.0	83.0
Building	7.0	7.0	24.0	24.0	25.0	25.0
Transport	12	12	12	12	12	12
Subtotal	<u>225</u>	<u>265</u>	<u>824</u>	<u>1004</u>	<u>1325</u>	<u>1605</u>
De-icing	52	52	151	151	207	207
Total	277	317	975	1155	1532	1812

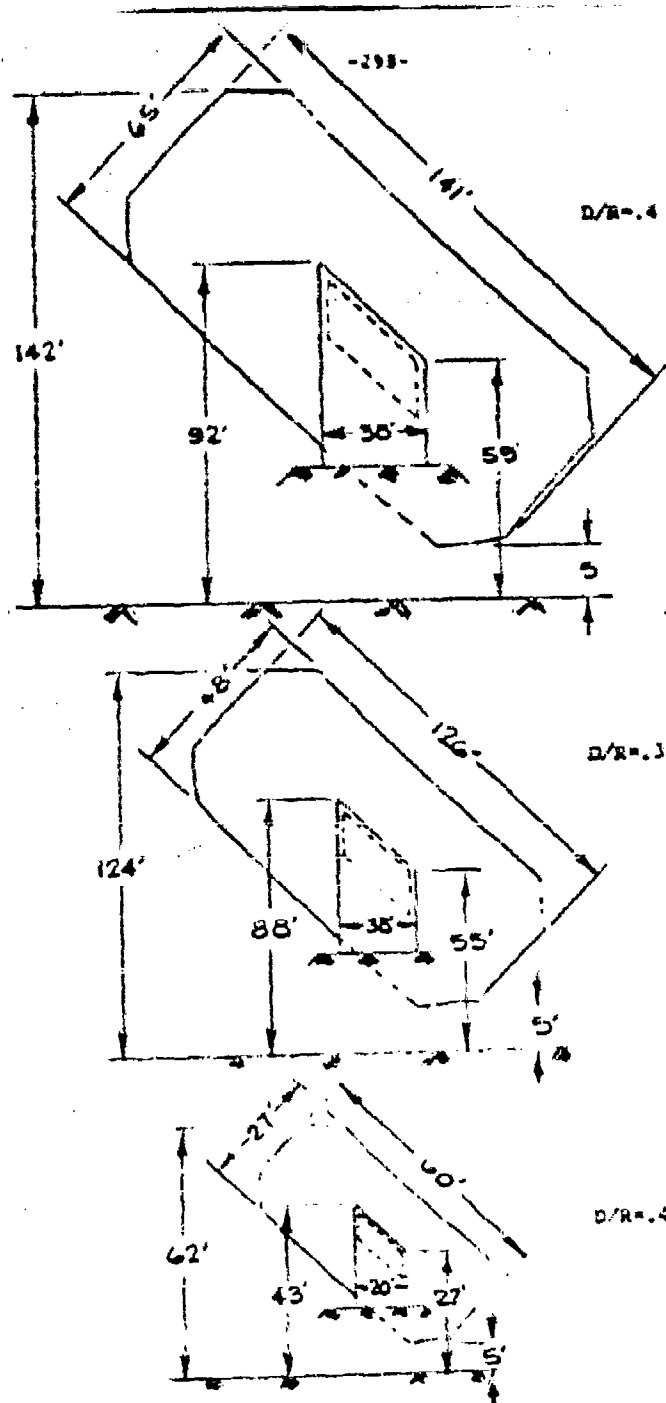


Figure 7-6. Sizes of Several MBTA Reflectors at COMSAT Labs

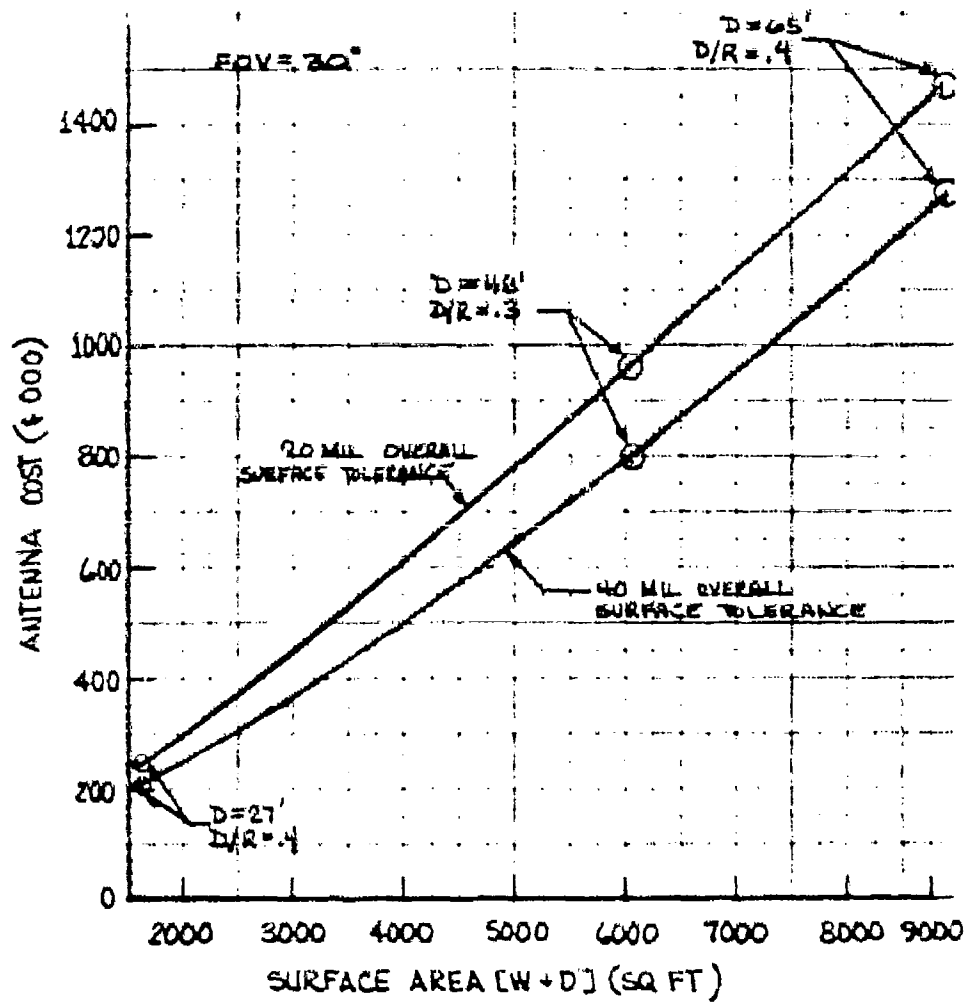
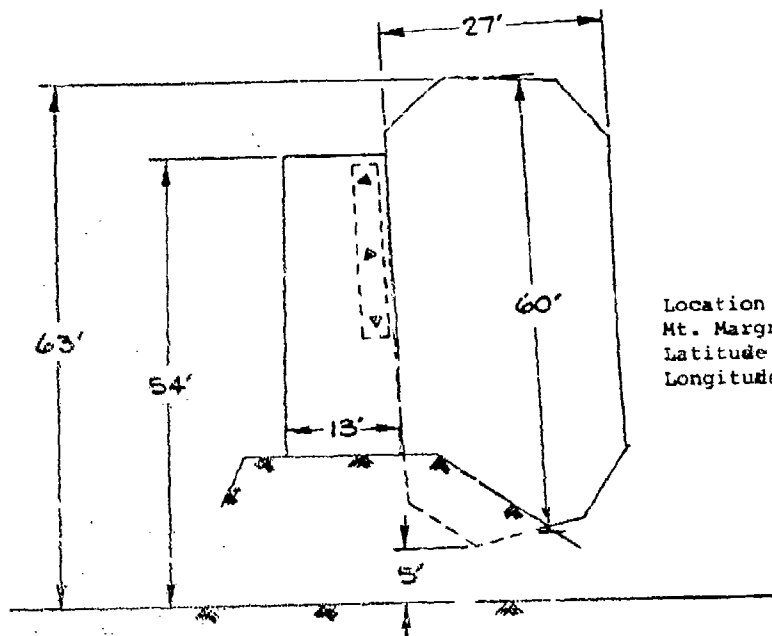
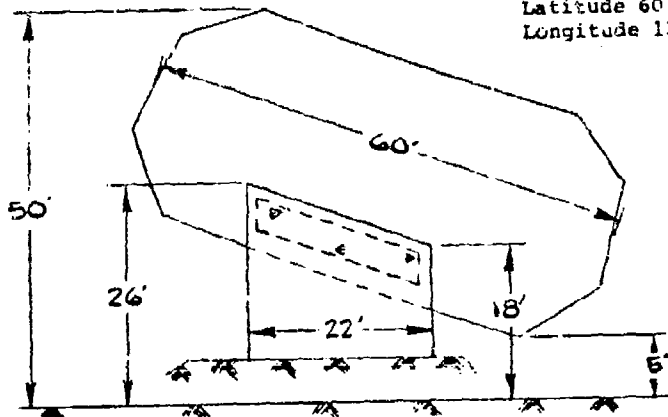


Figure 7-7. Antenna Cost vs Surface Area

Table 7-2. 27-ft MBTA Dimensions and Cost at
Several Locations

Parameter	Mt. Margret	Sweden	Iceland	Ascension Island
	Dimensions			
Latitude (deg)	-2	60	66	7
E. Longitude (deg)	37	13	340	346
Reflector Height (ft)	63	50	35	29
Reflector Foundation (yd ³)	29	23	16	13
Feed Building				
Width (ft)	12	12	12	22
Length (ft)	12	22	24	15
Height (ft)	54	26	14	44
Foundation (yd ³)	3	5	5	6
Feed Transport				
Width (ft)	6	17	18	17
Height (ft)	17	6	1	5
	Cost (\$K)			
Fabrication	160	160	160	160
Erection	40	36	31	29
Foundation	6	5	4	3
Building	6	6	5	8
Transport	12	12	12	12
Subtotal	224	219	212	213
De-icing	52	52	52	52
Total	276	271	264	265

Central Satellite Location 333 East Longitude all cases
 Earth Station Location 2
 Sweden
 Latitude 60 North
 Longitude 13 East



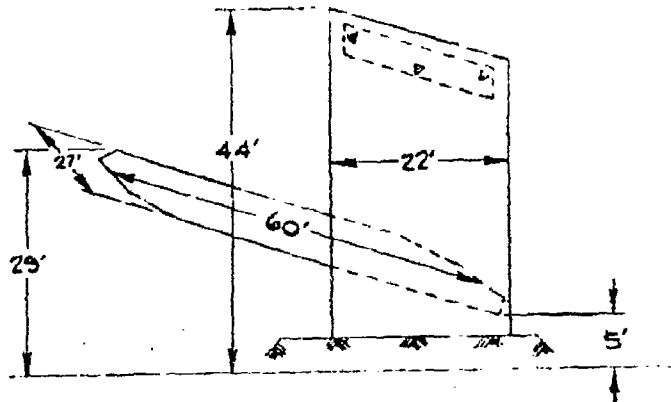
Location 1:
 Mt. Margret
 Latitude 2 South
 Longitude 37 East

Figure 7-8. Views of 27-ft MBTA at Locations 1 and 2

Multiple Beam Torus
Antenna Study

COMSAT Labs

Earth Station Location 4: Ascension Island
Latitude 7 North
Longitude 346 East



Earth Station Location 3: Iceland
Latitude 66 North
Longitude 340 East

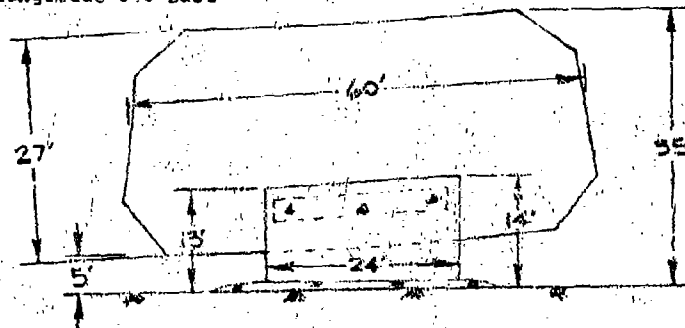


Figure 7-9. Views of 27-ft MBTA at Locations 3 and 4

8. REFERENCES

1. K. S. Kelleher and N. H. Hibbs, "A New Microwave Reflector," NRL Report 4141, Naval Research Laboratory, May 11, 1953.
2. G. D. M. Peeler and D. H. Archer, "A Toroidal Wave Reflector," IRE Convention Record, Institute of Radio Engineers Meeting, 1954, pp. 242-247.
3. L. J. Dolan, "Final Report on Recent Studies on Toric Reflectors," Radiation Engineering Laboratory Report No. 118, RADC-TR-59-231, December 1, 1959.
4. L. Pollack and W. Sones, "An Unattended Earth Terminal for Satellite Communications," COMSAT Technical Review, Vol. 4, No. 2, Fall 1974, pp. 205-230.
5. G. Hyde, R. Kreutel, and L. Smith, "The Unattended Earth Terminal Multiple-Beam Torus Antenna," COMSAT Technical Review, Vol. 4, No. 2, Fall 1974, pp. 231-262.
6. A. Abu-Taha, "Structural Analysis of the Unattended Earth Terminal Antenna," COMSAT Technical Review, Vol. 4, No. 2, Fall 1974, pp. 263-282.
7. R. Kreutel, Jr., et al., U.S. Patent 3,852,763.
8. G. Hyde, "A Novel Multiple-Beam Earth Terminal Antenna for Satellite Communications," IEEE 1970 International Conference on Communications, San Francisco, California, June 8-10, 1970, Conference Proceedings, Paper No. 70-CP-386-COM, pp. 38-24-38-33.

9. W. J. English and R. W. Kreutel, "Torus Antenna Pointing and Mounting Parameters," COMSAT Laboratories Interoffice Memorandum TCLT/72-2040, June 13, 1972.
10. R. Kreutel, "On Optimizing the Field of View of Toroidal Earth Station Antennas," COMSAT Laboratories Interoffice Memorandum TCLT/69-3168, May 13, 1969.
11. R. Price, "High-Performance Corrugated Feed Horn for the Unattended Earth Terminal," COMSAT Technical Review, Vol. 4, No. 2, Fall 1974, pp. 283-302.
12. R. W. Gruner and W. J. English, "A C.P. Reference Standard Antenna System for Satellite or Earth Station Applications," 1975 International IEEE/AP-S Symposium, June 2-4, 1975.
13. R. W. Kreutel, "Effective Surface Tolerance of Offset-Fed Reflector Antenna," COMSAT Laboratories Interoffice Memorandum TCLT/73-2004, January 4, 1973.
14. W. L. Cook and G. Hyde, "A General Purpose Interactive Antenna Analysis Program," 1973 G-AP International Symposium, Boulder, Colorado, August 22-24, 1973, Tech Program, pp. 91-94.
15. R. W. Kreutel, "Reflector Surface Area of Torus Antenna," COMSAT Laboratories Interoffice Memorandum TCLT/71-2038, April 14, 1971.
16. D. F. DiFonzo, W. J. English, and J. A. Janken, "Polarization Characteristics of Offset Reflectors with Multiple Element Feeds," 1973 G-AP International Symposium, August 22-24, 1973.

17. T. S. Chu and R. H. Turrin, "Depolarization Properties of Offset Reflectors," IEEE Transactions on Antennas and Propagation, Vol. AP-21, May 1973, pp. 339-345.
18. W. Korvin, "Performance Characteristics of a Multiple Beam Torus Antenna System Based on an Experimental Program," COMSAT Laboratories Technical Memorandum CL-26-72, March 1972.
19. G. Hyde, W. Korvin, and R. Price, "A Fixed Multiple Beam Toroidal Reflector Antenna Operating at Frequencies Above 12 GHz," IEEE International Conference on Communications, Montreal, Canada, June 11-14, 1971, Conference Proceedings, pp. 27-11-27-16.
20. R. Gruner, A. Williams, and F. Frey, "Calculated and Measured Data for the Phase Corrected Toroidal Antenna System," COMSAT Laboratories Technical Memorandum CL-38-75, April 22, 1975.
21. W. J. English, "Aberration-Correcting Feed Systems for Large Aperture Multiple-Beam Torus Antennas," International IEEE AP-S Symposium, June 20-24, 1977.
22. S. L. Wu and A. Ishimaru, "Fields in the Focal Region of a Parabolic Torus Reflector," 1970 AP-S International Symposium Digest, pp. 438-445.
23. N. Amitay and H. Zucker, "Compensation of Spherical Reflector Aberrations by Planar Array Feeds," 1970 AP-S International Symposium Digest, pp. 408-415.

24. H. Meyerhoff and B. Magenheim, "Mounting of Ground Station Torus Antenna," COMSAT Laboratories Interoffice Memorandum CP-61, May 26, 1970.
25. "11/14 GHz U.S. Earth Station Study Subsystem and Propagation Study," unpublished COMSAT Laboratories Study, December 15, 1976.
26. ASCE Task Committee on Wind Forces, Paper No. 3269, Transactions ASCE, Vol. 126, Pt. 2, pp. 1124-1198.
27. Simpson, Gumpertz and Heger, Inc., "Structural Design Study for a Fixed Toroidal Earth Station Antenna," COMSAT Contract No. CSC-CC-249, December 1970.
28. W. J. English, "INTELSAT V Preliminary Design Review - Selenia Antennas," COMSAT Laboratories Interoffice Memorandum MWL/72-2000, January 3, 1977.
29. Timoshenko and Woinowsky-Krieger, Theory of Plates and Shells, New York: McGraw-Hill, 1959.
30. The Aluminum Association, "Engineering Data for Aluminum Structures," Section 3, Aluminum Construction Manual, 1972.
31. L. V. Smith, Jr., "Structural Concept Development of Multiple Beam Torus Antenna," COMSAT Laboratories Technical Memorandum CL-35-73, November 2, 1973.

32. A. Abu-Taha, "NASTRAN Structural Analysis of the RET Torus Antenna," COMSAT Laboratories Technical Memorandum CL-34-73, December 1, 1973.
33. C. J. Richards, Mechanical Engineering in Radar and Communications, Van-Nostrand Reinhold Co., 1969.
34. H. Hirst and K. E. McKee, "Wind Forces on Parabolic Antenna," Andrew Corporation Report.
35. McCormick, Nastran Users Manual, Level 15, National Aeronautics and Space Administration, 1972.
36. American Institute of Steel Construction, Inc., Manual of Steel Construction, 1970.
37. I. S. Sokolnikoff and Redheffer, Mathematics of Physics and Modern Engineering, 2nd Edition, New York: McGraw-Hill, 1958.
38. Building Construction Cost Data, 35th Annual Edition, Robert Snow Means Co., Inc., 1977.

APPENDIX A. PROGRAM DESCRIPTIONS

The computer programs used to perform the calculations for the study program are as follows:

- a. MBTA-1 calculates pointing and geometrical parameters given v and λ ;
- b. MBTA-2 calculates the field of view (FOV) as a function of W/D for fixed D/R , F/R , offset, and generating axis angle;
- c. MBTA-3 calculates optimum generating axis angle and rotation axis unit vector components;
- d. MBTA-4 calculates the general exact beam pointing angle $\phi(\phi_0)$ and rotation vector \hat{u} as a function of ϕ_0 , ϕ_A , v , and λ ;
- e. MBTA-5 calculates the gain loss versus normalized surface tolerance (ϵ/λ) for fixed feed offset angles;
- f. MBTA-6 calculates the gain loss of the MBTA versus rms surface tolerance, ϵ (mils), for fixed feed offset angles;
- g. MBTA-7 calculates the aperture plane phase error characteristics of the MBTA ($\phi_0 = 90^\circ$);
- h. MBTA-9 calculates the locus of parabolic plane scanned beam feed positions and the associated scan angle;
- i. MBTA-10 calculates the feed phase center position relative to the parabolic focus given a desired spherical plane scan angle, θ_s , and furnishes the direction cosines for the feed pointing;
- j. MBTA-11 calculates the relative coordinates of the antenna reflector surface, possible feed locations, and backup truss, support structure, and foundation joint members; and

- k. MBTA-12 calculates the beam pointing error in the azimuth and elevation planes and the rms surface deformations at each vertical and horizontal cross section.

MBTA-11 takes the mechanical specifications, aperture diameter (D), ratios D/R (DR) and F/R (FR), field of view angle (β), offset dimension (H), and site-dependent earth station latitude, east longitude, central satellite east longitude, and surface generation angle (α) to determine the relative coordinates of the antenna reflector surface, possible feed locations, and backup truss, support structure, and foundation joint members. To determine individual panel corner points and truss and pickup point locations, the number of parabolic and circular panel points, vertical truss points, and desired pickup points must be used as input.

The output of MBTA-11 consists of the elevation (ξ) and azimuth (Ω) angles of the reflector; the local (site-independent) and global (site-dependent) coordinates of the generating parabola, vertical truss, panel and truss points, pickup, feed, and foundation; the panel arc and chord lengths for manufacturing; and the approximate panel weights (based on assumed weight per unit area). The local and global front and side wind forces for 45-, 60-, and 125-mph wind velocities are generated as well as thermal and gravity forces if required. Print output is always given, with the quantity determined by some of the input parameters. Punch output can be requested for the NASTRAN input cards for truss and panel point (GRID) locations and gravity (GRAV), wind (FORCE), and thermal (TEMP) loads. The transformation vector (CORD) between the global and local coordinate systems is also given to enable either set of outputs to be used as desired.

Program MBTA-12, written at COMSAT Laboratories, takes as input the ideal surface coordinates from MBTA-11 and the NASTRAN displacement vector punch output. It calculates the beam pointing error in the azimuth and elevation planes and the rms surface deformations at each vertical and horizontal cross section. For each case, the output includes the SRSS deflection at each backup truss point and the resultant tilts and local rms values. MBTA-12 calculates the best fitting toroidal surface to the deflected points. The beam pointing error is calculated as the angular difference between the ideal surface and the fitted surface. The rms error is a measure of the difference between the deflected and the fitted surface.

```

PROGRAM (REAL)
  PROGRAM CALCULATES THE BEAR POINTING AND MEASURING
  PARAMETERS GIVEN THE ANTENNA LATITUDE (NORTH) AND
  RELATIVE (EAST) LONGITUDE
  REAL N, LAT
  PI=4.0*ATN(1.0)
  RATIO OF GEOSYNCHRONOUS SATELLITE/EARH ANGLES-R
  R=6.61
  READ THE BEAR/NORTH/LATITUDE AND RELATIVE/EAST/LONGITUDE IN BEAR
  BEARS(S,SLAT,PLAN)
  R=COILATOP/100.0
  P=COILONGOP/100.0
  C=OUT
  THE LOCAL ELEVATION AND AZIMUTH ANGLE OF THE BEAR POINTING
  DIRECTION-EL AND AZ
  EL=100.0*PI*ATAN(RATIO*(R+COILATOP/100.0))
  AZ=100.0*PI*ATAN(RATIO*(R+COILONGOP/100.0))
  WRITE(S,EL,AZ)
  SATELLITE ANGLE TO THE BEAR-ORBIT
  DATA=100.0*PI*ATAN(RATIO*(R+COILATOP/100.0))
  WRITE(S,DATA)
  ANTENNA PLANE TILT ANGLE FROM HORIZONTAL-ATILT
  ATILT=100.0*PI*ATAN(RATIO*(R+COILATOP/100.0))
  C((R+COILONGOP/100.0))
  WRITE(S,8*ATILT)
  STOP
  END
  
```

```

List
00010 CC
00020 CC
00030 CC
00040 CC
00050 CC
00060 C
00070 C
00080 C
00090 C
00100 C
00110 C
00120 C
00130 C
00140 CC
00150 CC
00160 C
00170 C
00180 C
00190 C
00200 C
00210 C
00220 C
00230 C
00240 C
00250 C
00260 C
00270 C
00280 C
End of Data
  
```

```

1001 PROGRAM:RSTA-2;
1002 PROGRAM TO CALCULATE THE FIELD OF VIEW(FOV) OF THE
1003 FRONT FED RTDA AS A FUNCTION OF (U/D) FOR FINED
1004 (D/R), (F/R), (F/D), (F/D), AND PHIB.
1005 THE APPROXIMATE EXPRESSION IS  $FOV = (180/\pi) \times$ 
1006  $(D/R) \times ((U/D) - 1) \times (R/D)$  WHERE R IS THE RADIUS
1007 OF CURVATURE TO THE VERTEX OF THE PARABOLA AND
1008 D IS THE EFFECTIVE RADIUS OF CURVATURE TO THE
1009 CENTER OF THE APERTURE.
1010 REAL LDBS
1011 PI=4./ATAN(1.)
1012 STR=PI/180.
1013 READ(5,*)RDB, LDB, PHIB, FR
1014 WRITE(6,*)RDB, LDB, PHIB, FR
1015 THE RATIO OF EFFECTIVE RADIUS AT APERTURE CENTER
1016 TO R IS RCOR
1017 RCOR=1.+COS(PHIB*STR)/RDB+.5*(1-RCOR)
1018 (LDB*(LDB+.5)*RCOR/(4.*FR)
1019 DO 10 J=3,8
1020 J0=(J-1)/2.
1021 ARG1=(LDB*J0)/2.*RCOR
1022 ARG2=(RDB)/2.*RCOR
1023 ARG3=ARG1/(SIN(1.-ARG1/2))
1024 ARG4=ARG2/(SIN(1.-ARG2/2))
1025 FOV=2.*SIN(PI*(ARG1+ARG3)-ATAN(RDB/L))
1026 WRITE(6,*)FOV
1027 STOP
1028 END

```

END OF DATA


```

1151 C C C C
00010 C
00020 C
00030 C
00040 C
00050 C
00060 C
00070 C
00080 C
00090 C
00100 C
00110 C
00120 C
00130 C
00140 C
00150 C
00160 C
00170 C
00180 C
00190 C
00200 C
00210 C
END OF DATA

```

A-8

```

PROGRAM(NBTA-5)
PROGRAM TO CALCULATE THE GAIN LOSS OF THE NBTA US
NORMALIZED RMS SURFACE TOLERANCE AT FIXED NBTA
FEED OFFSET ANGLES
PI=4.14159(1.)
DO 10 J=10,60,10
FEED OFFSET ANGLE=ROSF
ROSF=(J-10.)
ROSF=ROSF*PI/180.
DO 20 I=1,10
NORMALIZED RMS SURFACE TOLERANCE=EL
EL=I/100.
Y=4.14159(ROSF))**2
Y=EXP(-X)
GAIN LOSS IM DB-GI
GI=10.*LOG10(Y)
WRITE(6,*)ROSF,EL,G1
CONTINUE
STOP
END

```

```

00015 C
00016 C
00017 C
00018 C
00019 C
00020 C
00021 C
00022 C
00023 C
00024 C
00025 C
00026 C
00027 C
00028 C
00029 C
00030 C
00031 C
00032 C
00033 C
00034 C
00035 C
00036 C
00037 C
00038 C
00039 C
00040 C
00041 C
00042 C
00043 C
00044 C
00045 C
00046 C
00047 C
00048 C
00049 C
00050 C
00051 C
00052 C
00053 C
00054 C
00055 C
00056 C
00057 C
00058 C
00059 C
00060 C
00061 C
00062 C
00063 C
00064 C
00065 C
00066 C
00067 C
00068 C
00069 C
00070 C
00071 C
00072 C
00073 C
00074 C
00075 C
00076 C
00077 C
00078 C
00079 C
00080 C
00081 C
00082 C
00083 C
00084 C
00085 C
00086 C
00087 C
00088 C
00089 C
00090 C
00091 C
00092 C
00093 C
00094 C
00095 C
00096 C
00097 C
00098 C
00099 C
00100 C
00101 C
00102 C
00103 C
00104 C
00105 C
00106 C
00107 C
00108 C
00109 C
00110 C
00111 C
00112 C
00113 C
00114 C
00115 C
00116 C
00117 C
00118 C
00119 C
00120 C
00121 C
00122 C
00123 C
00124 C
00125 C
00126 C
00127 C
00128 C
00129 C
00130 C
00131 C
00132 C
00133 C
00134 C
00135 C
00136 C
00137 C
00138 C
00139 C
00140 C
00141 C
00142 C
00143 C
00144 C
00145 C
00146 C
00147 C
00148 C
00149 C
00150 C
00151 C
00152 C
00153 C
00154 C
00155 C
00156 C
00157 C
00158 C
00159 C
00160 C
00161 C
00162 C
00163 C
00164 C
00165 C
00166 C
00167 C
00168 C
00169 C
00170 C
00171 C
00172 C
00173 C
00174 C
00175 C
00176 C
00177 C
00178 C
00179 C
00180 C
00181 C
00182 C
00183 C
00184 C
00185 C
00186 C
00187 C
00188 C
00189 C
00190 C
00191 C
00192 C
00193 C
00194 C
00195 C
00196 C
00197 C
00198 C
00199 C
00200 C
END OF DATA

PROGRAM(BETA-B)
PROGRAM TO CALCULATE THE GAIN LOSS OF THE BETA US
RMS SURFACE TOLERANCE(MILS) AT A FIXED FEED
OFFSET ANGLE
PI=4.8ATAN(1.)
FEED OFFSET ANGLE -AOSF
READ(5,*)AOSF
AOSFR=AOSF*PI/180.
FREQUENCY -F
READ(5,*)F
ANDA=11.81/F
DO 10 J=10,70,10
RMS SURFACE TOLERANCE -E(INCHES)
E=(J-10)/1000.
X=(4.8PI*E*F)/(AOSFR/ANDA)**2
Y=EXP(-X)
GAIN LOSS IN DB -G1
G1=10.*LOG10(Y)
WRITE(6,*)AOSF,F,ANDA,E,G1
GO TO 5
STOP
END

```

```

PROGRAM MBTA-7
APERTURE TO CALCULATE THE PHASE ERRORS OVER THE
APERTURE PLANE OF AN OFFSET META. THE GENERATING
AXIS ANGLE IS 90 DEGREES.
THIS PROGRAM PROVIDES A MEANS OF OPTIMIZING THE
META GEOMETRICAL PARAMETERS
(XC,0,0) OF THE PROJECTED APERURE IS TAKEN AS THE
PHASE REFERENCE(XD=LD+BD/2 IS THE CENTER)
REAL LD
PI=4.*ATAN(1.)
READ THE DIAMETER-BD,OFFSET-LD,DIAMETER+RADIUS-RL
DIAMETER/RADIUS OF CURVATURE-DR,AND FOCAL DISTANCE/
RADIUS-FR
NOTE LD=BD/2 GIVES A SYMMETRIC GEOMETRY(XD=0)
READ(5,*)BD,LD,BL,DR,FR
WRITE(6,*)BD,LD,DL,DR,FR
READ THE PHASE REFERENCE POINT-NC
READ(6,*)XC
XCD=XD/BD
READ THE FEED POSITION RELATIVE TO THE
PARABOLIC FOCUS-(XF,YF,ZF)
READ(5,*)XF,YF,ZF
XFD=XF/BD
YFD=YF/BD
ZFD=ZF/BD
XD,XFD ARE APERURE AND FEED COORDINATES NORMALIZED
TO THE DIAMETER
RD=1./DR
DO 10 I=1,11
XD=LD/BD+(I-1.)/10.
DO 20 J=1,11
YD=(J-1.)/20.
C1=(RD-XD**2/(4*FR*RD))
C2=SQRT(C1**2-YD**2)
C3=XCD**2/(4*FR*RD)
C4=(C3-FR*RD-ZFD)**2
APERURE PLANE PHASE ERROR-DPH
DPH=360*DL*(SQRT((XD-XFD)**2+(YD-YFD)**2+(RD*(1.-FR)-C2-ZFD)**2)
C3+C2-RD-SQRT((XCD-XFD)**2+C4)+DZ)
X=ND*BD
Y=YD*BD
APERURE COORDINATES AND RELATIVE PHASE ERROR
WRITE(6,*)X,Y,DPH
CONTINUE
GO TO 5
STOP
END

```

```

FI.FORT(NTAB)
00010 C PROGRAM(NTAB)
00020 C PROGRAM TO CALCULATE THE PHASE ERRORS OVER THE
00030 C APERTURE PLANE OF AN OFFSET MIRA WITH ARBITRARY
00040 C GENERATING AXIS ANGLE. THIS PROGRAM PROVIDES A
00050 C MEANS OF OPTIMIZING THE GEOMETRICAL PARAMETERS
00060 C OF THE DATA
00070 C (XC,C,Q) OF THE PROJECTED APERTURE IS TAKEN AS
00080 C THE PHASE REFERENCE (XC-LB-BD/2 IS THE CENTER)
00090 C PI=4.E5*(PI)
00100 C READ THE GENERATING AXIS ANGLE-PHIS
00110 C READ(S,2)PHIS
00120 C PHIS=PHIS*PI/180.
00130 C REAL LB
00140 C READ THE DIAMETER-BD, OFFSET-LD, RADIUS/RADIUS-RL,
00150 C DIAMETER/RADIUS OF CURVATURE-RS, AND FOCAL DISTANCE/
00160 C RADIUS OF CURVATURE-FL
00170 C NOTE THAT LB=BD/2 GIVES A SYMMETRIC GEOMETRY (XC=0)
00180 C READ(S,3)LD,DL,DL,FL
00190 C WRITE(S,2)LD,DL,DL,FL
00200 C READ THE PHASE REFERENCE POINT-XC
00210 C READ(S,1)XC
00220 C XCB=XC/BD
00230 C READ THE FEED POSITION RELATIVE TO THE PROBABLIC
00240 C FOCUS-(XF,VF,ZF)
00250 C READ(S,3)XF,VF,ZF
00260 C XF=XF/FL
00270 C VF=VF/FL
00280 C ZF=ZF/FL
00290 C RB=1./DL
00300 C RO IS 1./10.
00310 C XB=LB/BD+(1.-1.)/10.
00320 C YB=(1.-1.)/20.
00330 C RB=RD)/RADIUS(PHIS)-XCB*ZB/SIN(PHIS)/(4.E5*ZB)
00340 C ZB=RB/SIN(PHIS)-FB*RS/XCB*OS(PHIS)/4.E5*(PHIS)
00350 C C=ZB*(1./RADIUS-YB*ZB)/SIN(PHIS)
00360 C Z1=XCB*ZB/(4.E5*ZB)
00370 C APERTURE PLANE RELATIVE PHASE ERROR-DPH
00380 C DP=ABS(1./C)*SQRT((XC-XCB)DL*(1.-VF)ZB*(ZB-ZF)DL)
00390 C C=ZB*(1.-1.)-SQRT((XCB-XB)DL*(1.-VF)ZB*(ZB-ZF)DL)
00400 C C=ZB*(1.-1.)
00410 C X=ZB*DP
00420 C Y=ZB*DP
00430 C WRITE(S,1)X,Y,DPH
00440 C CONTINUE
00450 C GO TO 5
00460 C STOP
00470 C END
00480 C

```



```

1111
00010 C PROGRAM(NTA-10)
00020 C THIS PROGRAM CALCULATES THE FEED PHASE CENTER POSITION
00030 C RELATIVE TO THE FOCUS GIVEN THE DESIRED SCAN ANGLE(TNS),
00040 C IT ALSO FURNISHES THE DIRECTION COSINES FOR THE FEED
00050 C POINTING PARAMETERS.
00060 C PI=4. SATAN(1.)
00070 C ACR=PI/180
00080 C READ THE DIMETER-D, D/R, F/R, PH10 PARAMETERS
00090 C READ(S,8)D,BI,FR,PH10
00100 C READ THE FEED OFFSET ANGLE-TWOF
00110 C READ(S,8)THOFF
00120 C READ THE DESIRED SCAN ANGLE
00130 C READ(S,8)TNS
00140 C PH10=PI*THOFF
00150 C THOFF=THOFF/ACR
00160 C TNS=THNS*ACR
00170 C AI=BI(1.-FR)/BI
00180 C XI=AI*BI*BI(1.-FR)/BI
00190 C YI=-AI*BI*BI(1.-FR)/BI
00200 C ZI=-AI*BI*BI(1.-FR)/BI
00210 C D=COSINE OF LOCAL POINTING VECTOR
00220 C XI=BI*BI(1.-FR)/BI
00230 C YI=BI*BI(1.-FR)/BI
00240 C ZI=BI*BI(1.-FR)/BI
00250 C D=COS(TNS)
00260 C XI=BI*BI(1.-FR)/BI
00270 C YI=BI*BI(1.-FR)/BI
00280 C ZI=BI*BI(1.-FR)/BI
00290 C D=COS(TNS)
00300 C XI=BI*BI(1.-FR)/BI
00310 C YI=BI*BI(1.-FR)/BI
00320 C ZI=BI*BI(1.-FR)/BI
00330 C D=COS(TNS)
00340 C XI=BI*BI(1.-FR)/BI
00350 C YI=BI*BI(1.-FR)/BI
00360 C ZI=BI*BI(1.-FR)/BI
00370 C D=COS(TNS)
00380 C XI=BI*BI(1.-FR)/BI
00390 C YI=BI*BI(1.-FR)/BI
00400 C ZI=BI*BI(1.-FR)/BI
00410 C D=COS(TNS)
00420 C XI=BI*BI(1.-FR)/BI
00430 C YI=BI*BI(1.-FR)/BI
00440 C ZI=BI*BI(1.-FR)/BI
00450 C D=COS(TNS)
00460 C XI=BI*BI(1.-FR)/BI
00470 C YI=BI*BI(1.-FR)/BI
00480 C ZI=BI*BI(1.-FR)/BI
00490 C D=COS(TNS)
00500 C XI=BI*BI(1.-FR)/BI
00510 C YI=BI*BI(1.-FR)/BI
00520 C ZI=BI*BI(1.-FR)/BI
00530 C D=COS(TNS)
00540 C XI=BI*BI(1.-FR)/BI
00550 C YI=BI*BI(1.-FR)/BI
00560 C ZI=BI*BI(1.-FR)/BI
00570 C D=COS(TNS)
00580 C XI=BI*BI(1.-FR)/BI
00590 C YI=BI*BI(1.-FR)/BI
00600 C ZI=BI*BI(1.-FR)/BI
00610 C D=COS(TNS)
00620 C XI=BI*BI(1.-FR)/BI
00630 C YI=BI*BI(1.-FR)/BI
00640 C ZI=BI*BI(1.-FR)/BI
00650 C D=COS(TNS)
00660 C XI=BI*BI(1.-FR)/BI
00670 C YI=BI*BI(1.-FR)/BI
00680 C ZI=BI*BI(1.-FR)/BI
00690 C D=COS(TNS)
00700 C XI=BI*BI(1.-FR)/BI
00710 C YI=BI*BI(1.-FR)/BI
00720 C ZI=BI*BI(1.-FR)/BI
00730 C D=COS(TNS)
00740 C XI=BI*BI(1.-FR)/BI
00750 C YI=BI*BI(1.-FR)/BI
00760 C ZI=BI*BI(1.-FR)/BI
00770 C D=COS(TNS)
00780 C XI=BI*BI(1.-FR)/BI
00790 C YI=BI*BI(1.-FR)/BI
00800 C ZI=BI*BI(1.-FR)/BI
00810 C D=COS(TNS)
00820 C XI=BI*BI(1.-FR)/BI
00830 C YI=BI*BI(1.-FR)/BI
00840 C ZI=BI*BI(1.-FR)/BI
00850 C D=COS(TNS)
00860 C XI=BI*BI(1.-FR)/BI
00870 C YI=BI*BI(1.-FR)/BI
00880 C ZI=BI*BI(1.-FR)/BI
00890 C D=COS(TNS)
00900 C XI=BI*BI(1.-FR)/BI
00910 C YI=BI*BI(1.-FR)/BI
00920 C ZI=BI*BI(1.-FR)/BI
00930 C D=COS(TNS)
00940 C XI=BI*BI(1.-FR)/BI
00950 C YI=BI*BI(1.-FR)/BI
00960 C ZI=BI*BI(1.-FR)/BI
00970 C D=COS(TNS)
00980 C XI=BI*BI(1.-FR)/BI
00990 C YI=BI*BI(1.-FR)/BI
01000 C ZI=BI*BI(1.-FR)/BI
END OF DATA
END

```